University of Bath

UNIVERSITY OF BATH

PHD

Composite ferroelectric materials for energy harvesting and storage applications

Roscow, James

Award date:
2018

Awarding institution:
University of Bath

[Link to publication](#)

Composite ferroelectric materials for energy harvesting and storage applications

submitted by

James Roscow

for the degree of Doctor of Philosophy

of the

University of Bath

Department of Mechanical Engineering

January 2018

COPYRIGHT

Signature of Author . . . .

James Roscow

Abstract

In this study composite ferroelectric materials have been investigated for their ability to harvest energy from mechanical vibrations via the piezoelectric effect, and store electrical energy as capacitor materials. A combination of modelling and experimental techniques have been used to understand the consequences of using multiphase materials for energy harvesting and storage applications, with particular focus on the significance of interactions between composite structure, electric field distributions and the effective material properties.

A detailed investigation into the properties of ferroelectric ceramic–air composites, such as porous barium titanate, is presented. Introducing isotropic, randomly distributed porosity into barium titanate was found to increase the energy harvesting figure of merit from $\sim$1.40 pm^2/N for the dense material to $\sim$2.85 pm^2/N at 60 vol.% porosity. Finite element modelling was used to better understand the poling behaviour of barium titanate with different porous structures (uniform, porous sandwich layer and aligned), enabling the design of materials with improved energy harvesting capabilities. Complex porous structures were found to have enhanced energy harvesting figures of merit, with maximum values achieved of 3.74 pm^2/N and 3.79 pm^2/N in barium titanate with a 60 vol.% porosity sandwich layer (overall porosity $\sim$34 vol.%) and highly aligned freeze cast barium titanate with 45 vol.% porosity, respectively. Dense and porous barium titanate samples were mechanically excited and the derived electrical energy used to charge a capacitor. The porous barium titanate was found to charge the reference capacitor more effectively than the dense material, demonstrating the benefits of introducing porosity into ferroelectric materials for energy harvesting applications.

Ferroelectric composites, in which either a conductive filler was added to a high permittivity ferroelectric matrix or a high permittivity ferroelectric phase was added to a low permittivity polymer matrix, were evaluated for their potential as a new generation of capacitor materials using finite element modelling. The studies suggested that the rise in effective permittivity due to the forming of composites is fundamentally linked to the rapid decline in dielectric breakdown strengths observed in composites, resulting in nearly all cases reported in the literature demonstrating a reduction in the energy storage figure of merit. It is concluded that future efforts into finding the next generation of energy storage materials should focus on single phase, or intrinsic, high permittivity materials rather than composite materials.

Acknowledgements

Contents

Chapter 1

Introduction

This thesis is comprised of six research papers (five published and one draft paper) on the general theme of composite ferroelectric materials for energy harvesting and storage applications. Four papers, including a literature review in Chapter 2, and research papers in Chapters 3,5 and 6, investigate the effect of porosity introduced into ferroelectric ceramics, such as barium titanate and lead zirconate titanate (PZT), on the functional properties and energy harvesting capabilities; the other two papers, both contained in Chapter 4, assess the suitability of composite ferroelectric materials for energy storage applications using finite element modelling techniques.

The link between these two strands of research is that the properties and performance of both types of composite depend heavily on the way electric fields distribute and concentrate within them when an external field is applied. Electric field concentrations have implications for the resultant properties of porous ferroelectric materials as they are subject to a key processing step known as *poling*, whereby a large electric field is applied across the sintered porous material in order to align polar domains within the active ferroelectric phase; the degree of net polarisation (domain alignment) affects the measured piezoelectric and pyroelectric properties. Similarly, the dielectric properties of energy storage composites may be enhanced compared to a single phase material due to electric field concentrations that occur when the material is subject to an applied voltage, but these same electric field concentrations may in turn reduce the effective breakdown strength compared to a homogenous single phase material. Understanding these structure–electric field interactions is fundamental to designing better materials for both energy harvesting and storage applications.

1.1 Note on format

The thesis contents in terms of chapters and papers is shown Fig. 1-1. Additional papers that relate to the research themes of the thesis but have not been included in the main document are shown in the third column. Each paper is preceded by a 'Context' section and a 'Summary' is included at the end of each chapter to contextualise how each paper relates to the overall research question and other chapters/papers within the thesis. Also included before each paper is a *Statement of Authorship* that outlines the candidates' contribution to the published research under the following headings:

1. Formulation of ideas

2. Design of methodology

3. Experimental work

4. Presentation of data in journal format.

The references for each paper are self-contained with a full bibliography in alphabetical order given at the end of the thesis. Supplementary information, experimental methods and model scripts are contained within the appendices; relevant appendices to each chapter/paper are referenced in the preceding *Context* sections.

Data access statements are given prior to each published paper that contains original experimental or modelling data, i.e. those in Chapters 3, 4 and 5.

The papers contained within this thesis have been reformated from their published form into single column, one-and-a-half spaced text for the benefit of the reader.

Chapter	Paper(s) contained in chapter	Related papers
Chapter 1: Introduction		
Chapter 2: Literature review	Roscow et al., *Porous ferroelectrics for energy harvesting applications*, Eur. Phys. J.: ST, 224 (2015) 2949-2966.	
Chapter 3: Manufacture and characterisation of porous barium titanate for energy harvesting applications	Roscow et al., *Manufacture and characterisation of porous ferroelectrics for energy harvesting applications*, Ferroelectr., 498 (2016) 40-46.	Roscow et al., *Understanding the peculiarities of the piezoelectric effect in macro-porous BaTiO$_3$*, Sci. Tech. Adv. Mater., 17 (2016) 769-776.
Chapter 4: Modelling electric field distributions in ferroelectric composites for electrical energy storage	a) H. Luo, Roscow et al., *Ultra-high energy density capacitor using high aspect ratio Na$_{0.5}$Bi$_{0.5}$TiO$_3$ nanofibres*, J. Mater. Chem. A, 5 (2017) 7091-7102. b) Roscow et al., *Breakdown in the case for materials with giant permittivity?*, Energy Lett., 2 (2017) 2264-2269.	D. Zhang, X. Zhou, Roscow et al., *Significantly enhanced energy storage density by modulating the aspect ratio of BaTiO$_3$ nanofibres*, Sci. Rep., 7 (2017) 45179.
Chapter 5: Poling behaviour of barium titanate with porous sandwich layers for energy harvesting applications	Roscow et al., *Modelling and fabrication of porous sandwich layer barium titanate with improved energy harvesting figures of merit*, Acta Mater. 128 (2017) 7091-7102.	Roscow et al., *Piezoelectric anisotropy and energy-harvesting characteristics of novel sandwich layer BaTiO$_3$ structures*, Smart Mater. Struct., 26 (2017) 105006.
Chapter 6: Poling behaviour of freeze cast porous barium titanate with enhanced piezoelectric energy harvesting properties	Roscow et al., *Freeze cast porous barium titanate with enhanced piezoelectric energy harvesting capabilities*, DRAFT PAPER.	Y. Zhang, M. Xie, Roscow et al., *Enhanced pyroelectric and piezoelectric properties of PZT with aligned porosity for energy harvesting applications*, J. Mater. Chem. A, 5 (2017) 6569-6580.
Chapter 7: Conclusions and further work		

Figure 1-1: Overview of thesis contents with reference to the research papers contained in each chapter in the second column and related papers not included in the thesis in the third column.
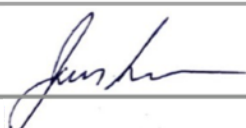
Chapter 2

Literature review

2.1   Context

The first paper presented in this thesis is a literature review that was written during the first year of the project. The work underpins the majority of the papers that are contained within this thesis with the exception of the work on energy storage composites in Chapter 4.

Statement of Authorship

This declaration concerns the article entitled:								
Porous ferroelectrics for energy harvesting applications								

Publication status (tick one)								
draft manuscript		**Submitted**		**In review**		**Accepted**		**Published** ✓
Publication details (reference)	Roscow et al., European Physical Journal: Special Topics **224** (2015) 2949-2966							
Candidate's contribution to the paper (detailed, and also given as a percentage).	The candidate contributed to/ considerably contributed to/predominantly executed the Formulation of ideas: Premise of work based on discussions with C.R. Bowen regarding research topic for PhD Design of methodology: Solely the candidate (100%) Experimental work: N/A Presentation of data in journal format: Solely the candidate (100%)							
Statement from Candidate	This paper reports on original research I conducted during the period of my Higher Degree by Research candidature.							
Signed						**Date**	30/11/17	

PAPER 1: Porous ferroelectrics for energy harvesting applications

J.I. Roscow[a], Y. Zhang[b], J. Taylor[c], and C.R. Bowen[a]

[a]*Department of Mechanical Engineering, University of Bath, Bath, UK*
[b]*Modern Training Center, Hunan University, Changsha, Hunan, PR China*
[c]*Department of Electrical and Electronic Engineering, University of Bath, Bath, UK*

Abstract

This paper provides an overview of energy harvesting using ferroelectric materials, with a particular focus on the energy harvesting capabilities of porous ferroelectric ceramics for both piezo- and pyroelectric harvesting. The benefits of introducing porosity into ferroelectrics such as lead zirconate titanate (PZT) has been known for over 30 years, but the potential advantages for energy harvesting from both ambient vibrations and temperature fluctuations have not been studied in depth. The article briefly discusses piezoelectric and pyroelectric energy harvesting, before evaluating the potential benefits of porous materials for increasing energy harvesting figures of merits and electromechanical/electrothermal coupling factors. Established processing routes are evaluated in terms of the final porous structure and the resulting effects on the electrical, thermal and mechanical properties.

1. Introduction

Interest in energy harvesting from ambient sources has grown in recent years with advances in microelectromechanical systems (MEMS) and wireless electronics [1, 2, 3]. Batteries are the current power source of choice for wireless sensors but their finite lifetime can quickly add to the maintenance cost of systems. Coupled with the fact that they are often used to monitor largely inaccessible and/or hostile areas, frequent replacement can be a difficult, time-consuming and expensive procedure. The ability to scavenge energy from the surrounding environment, be it through solar, thermoelectric, pyroelectric or piezoelectric devices, offers a potential mode of powering small-scale electronic devices without the need for cables to supply power or replacement of batteries. Alternatively, energy harvesting could be used to recharge batteries, significantly extending their lifetime and reducing problems associated with disposal [4]. Ferroelectric materials are of particular interest for energy harvesting due to their ability to convert energy from mechanical vibrations through the piezoelectric effect or from temperature fluctuations via the pyroelectric effect.

Ambient vibrations tend to coexist with the requirement to monitor structural health of components, meaning there is a vast resource of potentially harvestable energy that could be recaptured through piezoelectric devices. This area has received great interest in recent years, and as such a number of reviews are available that cover the various considerations that must be taken into account when designing a piezo-harvester [3, 5, 6]. Similarly, waste heat is a necessary by-product of all thermodynamic cycles implemented in power, refrigeration and heat pump processes. As one of the potential technologies for thermal energy harvesting, pyroelectric energy conversion is of interest since it offers a novel way to convert waste heat into electricity by alternatively heating and cooling a pyroelectric material. This approach has also attracted much interest in fields such as low-power electronics and wireless sensors [7, 8, 9].

There has been limited progress with respect to the properties of the active material in piezo- and pyroelectric devices since the discovery of lead zirconate titanate (PZT) with a composition close to the morphotropic phase boundary (MPB); single crystals such as lead magnesium niobate-lead titanate (PMN-PT) can exhibit piezoelectric coefficients an order of magnitude higher than PZT [10] but tend to be significantly more expensive to process than ceramic materials, as well as having size and shape limitations. In certain applications, such as SONAR and ultrasound imaging that exploit the piezoelectric effect, and thermal imaging using the pyroelectric response, the introduction of porosity has been found to yield beneficial properties, which will be discussed in detail later. However, the effect of porosity on the energy harvesting capabilities of ferroelectric materials has not been studied in depth. The potential benefits of controlled porosity will be discussed in this article for both piezoelectric and pyroelectric energy harvesting, as will processing routes for forming porous ferroelectrics and the resulting effects on properties due to the interconnected structure of the active and the passive phases.

2. Piezoelectric energy harvesting

Over the past two decades many examples of potential applications for piezo-harvesters have arisen in the form of concepts and prototypes to convert mechanical vibrations into useful electrical energy. Structural monitoring devices, such as sensors in rail sleepers [11] and tire pressure monitors [12], are subjected to vibrations in their ambient environment, allowing them to self-power their operation and wirelessly transmit information. Other examples of prototype piezo-harvesters include fitting multiple piezoelectric devices into the sole of a shoe [13] or into the straps of a backpack [14], recapturing energy from pressure fluctuations in fluids [15, 16], powering bio-MEMS inside the human body [17], using a piezoelectric membrane to convert acoustic energy to electrical energy in a thermoacoustic generator [18], as well as acoustic wave nanogenerators [19, 20].

The effective design of a piezoelectric harvester requires consideration and, in the final stages, optimisation of each component of the conversion system, from the input mechanical energy and how this is driven through the active material, to the output electrical signal and how this is converted to useful electrical power. The characteristics of the active material should also be considered so as to maximise the energy generated due to an applied mechanical stress. To do so with regards to energy harvesting requires a general understanding of the piezoelectric effect, which will now be described.

2.1. Piezoelectric effect

The piezoelectric effect, first discovered by Jacques and Pierre Curie in 1880, is the change in electric polarisation of a material due to an applied pressure. This change in polarisation leads to equal and opposite electrical charges forming on parallel surfaces generating a potential difference across the bulk material. This is known as the direct piezoelectric effect and is the basis for piezoelectric energy harvesting, as this voltage can be used to drive a current in an external circuit. Under short circuit conditions, which are the standard for measuring piezoelectric properties, the magnitude of charge developed, or the dielectric displacement, D_i, is proportional to the applied stress, σ_j, such that:

$$D_i = d_{ij}\sigma_j \tag{1}$$

where d_{ij} is the piezoelectric strain coefficient and the subscripts denote the direction of response (i) and application (j), using matrix notation. Alternatively, applying an electric field over a piezoelectric material induces a strain, which is the basis for actuating devices. This is known as the converse effect:

$$x_m = d_{im}E_i \tag{2}$$

where x is strain, E is electric field and the subscripts i and m denote application and response, respectively. High strain coefficients are desirable for actuator applications where large displacements are required. In applications that require the generation of a large voltage, such as a sensor, the open circuit voltage coefficient, g_{ij}, is of greatest importance:

$$g_{ij} = \frac{d_{ij}}{\varepsilon_{33}^{\sigma}} \tag{3}$$

where $\varepsilon_{33}^{\sigma}$ is the permittivity of the material at constant stress. Piezoceramics can be classed as 'hard' or 'soft', which describes the ease of domain motion and is therefore linked to the degree to which a material can be polarised. 'Hard' materials are difficult

to polarise, exhibiting low d_{ij} coefficients but higher g_{ij} values due to having lower permittivity, whereas 'soft' materials are characterised by high d_{ij} values but low g_{ij} due to high permittivities.

2.2. Piezoelectric energy harvesting figures of merit (FOMs)

Many vibration sources that arise in ambient environments, for example those associated with transport or industrial machinery, are low frequency (relative to the resonant frequency of ceramic materials) and random (in terms of frequency and amplitude), making it difficult to design for operation at one specific frequency. At a low frequency and off-resonance, a piezoelectric ceramic can be assumed to behave as a parallel plate capacitor [21]. Equations for the energy density of a material due to an applied stress, in terms of d_{ij} and g_{ij}, can be derived from simple capacitance equations. Starting with energy stored in a parallel plate capacitor, $U = \frac{1}{2}CV^2$, where C is capacitance and V is applied voltage, the energy density, u, of a piezoelectric is given by:

$$
\begin{aligned}
u &= \frac{1}{2}.d_{ij}.g_{ij}.\left(\frac{F}{A}\right)^2 \\
&= \frac{1}{2}.\frac{d_{ij}^2}{\varepsilon_{33}^\sigma}.\left(\frac{F}{A}\right)^2
\end{aligned}
\tag{4}
$$

where F is force and A is the area over which it is applied. Energy harvesters may work in either direct excitement mode (i.e. force is applied from the source directly to the material along the poling axis), 33, or bending mode [3] (e.g. using a mass cantilever system), 31, and energy harvesting FOMs can be defined accordingly [22]:

Direct mode:

$$
FOM_{33} = \frac{d_{33}^2}{\varepsilon_{33}^\sigma}
\tag{5}
$$

Bending mode:

$$
FOM_{31} = \frac{d_{31}^2}{\varepsilon_{33}^\sigma}
\tag{6}
$$

The change in energy density gives the total amount of potential energy available for harvesting and it is therefore of interest to maximise these parameters.

The electromechanical coupling coefficient, k^2, is related to the efficiency that a piezoelectric converts energy. For harvesting applications (given here for direct mode) a high FOM is desirable for a high coupling coefficient as:

11

$$k_{33}^2 = \frac{d_{33}^2}{\varepsilon_{33}^\sigma . S_{33}^E} \qquad (7)$$

where S^E is the elastic compliance of the material measured at constant electric field. Both these terms need to be optimised to maximise the capabilities of a piezoelectric used in an energy harvesting device.

When harvesting on-resonance a different FOM is defined for bending mode as [23]:

$$FOM_{on-resonance} = \frac{k_{31}^2 . Q_m}{S_{11}^E} \qquad (8)$$

where Q_m is the mechanical quality factor, which describes the damping behaviour of a system at the resonant frequency [24]. A high Q_m is favourable for on-resonance harvesters as only a small amount of the input energy is dissipated. However, when the input signal is random, a material with a high Q_m would only harvest energy in a narrow frequency range, thereby limiting its effectiveness. Materials with lower Q_m values are likely to perform better than those with high Q_m when used for broadband energy harvesting as they can operate over a larger frequency range.

The dielectric loss of a material, $\tan \delta$, is the amount of input energy dissipated due to internal losses that occur during a change in polarisation. In all piezoelectric energy harvesters, a low $\tan \delta$ is favourable so as to increase electromechanical coupling, k_{ij}^2 [23], and therefore the efficiency of conversion from mechanical to electrical energy.

Research into maximising these parameters has so far focussed on careful control of the composition of materials to obtain high d_{33} or d_{31} values and low permittivities in PZT-P(ZN)N (Pb[(Zn$_{0.4}$Ni$_{0.6}$)$_{1/3}$Nb$_{2/3}$]O$_3$) ceramics [25, 26], as well as the evaluation of common commercial materials for their energy harvesting potential using the previously discussed FOMs [22, 23]. The trade off between high piezoelectric strain coefficients and low permittivities has also been described at a system level, where it is found smart geometries of the active material can improve the performance of mass cantilever systems through a reduction in the capacitance [27, 28]. As yet, little research has focussed on the use of porous ferroelectrics for energy harvesting, despite the potential for a high energy harvesting FOM due to reduced permittivity caused by the introduction of porosity. This may be due to a simultaneous reduction in strain coefficient, d_{ij}, and an increase in compliance, S_{ij}^E. However, through careful control of microstructure via the processing route it may be possible to limit the negative effects so as to improve the piezoelectric energy harvesting capabilities of the materials.

3. Pyroelectric energy harvesting

The pyroelectric effect, discovered before piezoelectricity with the first scientific account by Louis Lemery published in 1717, although others had observed the phenomena earlier [29], was used by the Curie brothers to help determine the mechanism for the piezoelectric effect. Pyroelectric materials produce power from temperature fluctuations (dT/dt) and therefore have similarities to piezoelectric harvesters that convert mechanical oscillations ($d\sigma/dt$) into electricity. If a pyroelectric is heated ($dT/dt > 0$) there is a decrease in its spontaneous polarisation as dipoles lose their orientation due to thermal vibrations. This fall in the polarisation level leads to a decrease in the number of free charges bound to the material surface. If the material is under short circuit conditions an electric current flows between the two polar surfaces of the material. Similarly, if the pyroelectric is cooled ($dT/dt < 0$) the dipoles regain their orientation leading to an increase in the level of spontaneous polarisation, thus reversing the electric current flow under short circuit conditions as free charges are attracted to the polar surfaces. The change in polarisation, ΔP, due to a change in temperature, ΔT, depends on the pyroelectric coefficient, p, of a material such that [29]:

$$\Delta P = p\Delta T \tag{9}$$

As in piezoelectric materials, it is of interest to use materials with high pyroelectric coefficients for energy harvesting applications, which is demonstrated by examining the FOMs.

3.1. Pyroelectric energy harvesting FOMs

FOMs have been derived for the selection of pyroelectric materials based on consideration of the thermal and electrical circuits employed [7]. The FOMs are based on the generation of maximum current or voltage for a given power input for applications such as thermal imaging sensors [8, 9, 30].

To obtain a high voltage responsivity (F_v) due to a given input power, the following FOM should be maximised [31]:

$$\begin{aligned} F_v &= \frac{p}{c_E . \varepsilon_{33}^{\sigma}} \\ &= \frac{p}{\rho . c_p . \varepsilon_{33}^{\sigma}} \end{aligned} \tag{10}$$

where c_E is volume specific heat capacity, c_p is specific heat capacity and ρ is density.

High current responsivity (F_i) is required to maximise performance of infrared detection devices and is characterised by the following FOM [31]:

13

$$F_i = \frac{p}{c_E}$$
$$= \frac{p}{\rho.c_p} \tag{11}$$

The two FOMs above are often used for selection of materials for heat and infrared detection, but these are not to be confused with energy harvesting applications where generated power is of interest, as is the efficiency of the conversion of thermal to electrical energy.

Pyroelectric energy harvesting-specific FOMs have been proposed [32, 33, 34], including an electrothermal coupling factor that has been defined to estimate the effectiveness of thermal harvesting [32]:

$$k^2 = \frac{p^2.T_{hot}}{c_E.\varepsilon_{33}^\sigma}$$
$$= \frac{p^2.T_{hot}}{\rho.c_p.\varepsilon_{33}^\sigma} \tag{12}$$

where T_{hot} is the maximum working temperature. An energy harvesting FOM, F_E, has been proposed as [33]:

$$F_E = \frac{p^2}{\varepsilon_{33}^\sigma} \tag{13}$$

which has been widely used for materials selection and materials design [29, 35, 36]. A modified version that includes heat capacity is [34]:

$$F_E' = \frac{p^2}{\varepsilon_{33}^\sigma.c_E^2} \tag{14}$$

To achieve a better performance for pyroelectric harvesting, it is necessary to increase F_E or F_E', which requires a combination of properties, such as high pyroelectric coefficient, p, low permittivity, ε_{33}^σ, and low volume heat capacity, c_E.

The piezo- and pyroelectric materials for energy harvesting display certain similarities with regards to their respective FOMs, in that increases can be achieved by maximising the piezo-/pyroelectric coefficient whilst reducing the permittivity. There are a number of ways to enhance the functional performance of a dense material, including chemical modification (doping, substitution), the utilisation of promising perovskite components for the construction of phase diagrams and the employment of the single crystals and polymers. Due to the complexity of developing new formulations and the

14

high cost, low Curie temperature and poor mechanical properties of single crystals, the applications of the above materials are limited. Porosity offers a relatively low-cost alternative to increasing FOMs through a reduction in both permittivity and heat capacity, as will be explained in the next section.

4. Ferroelectricity

Ferroelectric materials have the ability to maintain a spontaneous polarisation, the orientation of which can be electrically switched [37]. This means that they exhibit both piezoelectric and pyroelectric properties as applying a force to or changing the temperature of a poled ferroelectric will change the magnitude of the polarisation, which, as described earlier, can be used to extract usable electrical energy. This phenomena arises from the crystal structure in which a non-centrosymmetric unit cell creates an electric dipole. All ferroelectrics exist in a paraelectric state above the Curie temperature, where a phase transition results in no electric dipole, giving the upper limit of their functional properties. Ferroelectric ceramics, such as PZT, exhibit excellent piezo- and pyroelectric properties and are therefore of great interest for all applications that utilise these effects. Ferroelectricity can also exist in crystalline polymers, with PVDF (polyvinylidene fluoride) of particular interest due to its functional properties, flexibility and processability [38]. Ferroelectric materials are a sub-group of pyroelectric materials, and all pyroelectric materials are piezoelectric [3].

As sintered, ferroelectric ceramics have a random orientation of domains (sub-grain regions with aligned dipoles) giving an overall polarisation of zero. Poling the material by applying a large electric field aligns the domains over the bulk material resulting in a net polarisation that remains when the field is removed. Applying a significantly large electric field in the opposite direction can reverse the direction of polarisation, leading to the characteristic hysteresis behaviour observed in all ferroelectric materials [37]. Heating above the Curie temperature causes a phase change to a centrosymmetric crystal structure, resulting in the loss of piezo- and pyroelectric properties. When cooled below the Curie temperature ferroelectrics must be repoled to restore their functional properties as domains again orientate randomly in their lowest stress configuration. PZT exhibits high functional properties as the composition is tailored close to the morphotropic phase boundary (MPB) so that two phases coexist in normal operating conditions, across a wide range of temperatures, greatly increasing the polarisability of the material. The high degree of polarisation, coupled with a relatively high Curie temperature (up to ~400°C), makes PZT the material of choice for most actuator and transducer applications, as well as being frequently employed in pyroelectric thermal imaging devices.

15
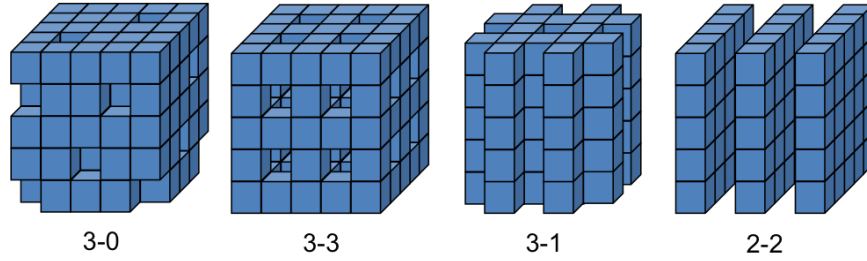
Figure 1: Examples of common connectivities of biphasic composites, e.g. ferroelectric ceramic-air materials, adapted from [48]. The first number refers to the connectivity of the ceramic phase (in blue) and the second to the connectivity of the porosity (represented as gaps in the structures).

4.1. Porous ferroelectric ceramics

Traditional processing routes have strived to obtain ceramics with very high relative densities (>95%) so as to maximise the mechanical properties, with porosity usually considered as a defect. Many functional properties, such as piezo- and pyroelectric coefficients in ferroelectrics, are also maximised when the relative density is close to maximum [39]. However, by introducing a second phase, either as porosity or polymer, it is found that certain coupled properties, such as the longitudinal and transverse piezoelectric effects, can be tuned somewhat independently of one another [40, 41]. The majority of research into porous piezoelectrics has been focussed in the field of ultrasonic transducers and low frequency (<100kHz) sensing devices such as hydrophones [42, 43, 44]. Most of the research into porous pyroelectrics has occurred in the last 15 years and has focussed on improving thermal imaging devices alongside side energy harvesting capabilities [45, 46, 47].

The connectivity of a ferroelectric composite determines the electrical, mechanical and thermal properties [48]. Newnham et al. [40, 41] defined the connectivity of a material with respect to the dimensionality of the interconnection of the individual phases, so that a two-phase material can be described by two numbers, the first of which refers to the piezoactive phase and the second to the passive phase. For example, PZT with 3-0 connectivity would have a continuous ceramic phase with isolated porosity. Although originally defined for piezocomposites, this notation is now commonly used for general composite engineering. The final connectivity of a porous ceramic is determined by the processing route. Fig. 1 shows a selection of common two-phase structures that can be achieved using the methods described in Section 4.2.

4.1.1. Effect of porosity on piezoelectric properties

Introducing porosity into piezoceramics is found to improve the hydrostatic response, measured by hydrostatic strain coefficient, d_h, and the hydrostatic voltage coefficient, g_h

16
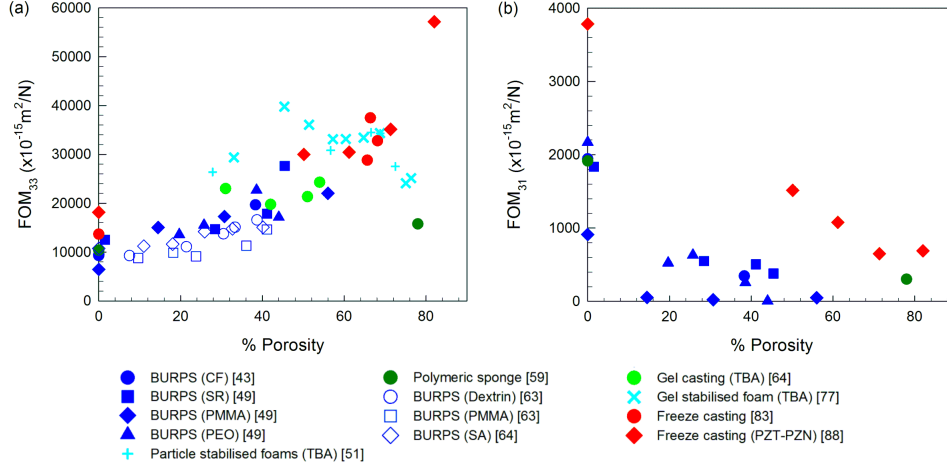
Figure 2: Reanalysed data from literature of (a) FOM_{33} as a function of porosity and (b) FOM_{31} as a function of porosity. Improvements of >300% are possible for linear vibration harvesting, highlighting the potential for energy harvesting. A decrease in FOM_{31} can be seen with increasing porosity, due to a corresponding decrease in d_{31}, meaning that porous materials would function less well in vibration harvester geometries that operate in bending mode without extra considerations for the placement of electrodes. Data are described in terms of processing route with PFA given in brackets, where CF is corn flour, SR is self-raising flour, PMMA is poly(methyl methacrylate), PEO is poly(ethylene oxide), SA is stearic acid and TBA is tert butyl alcohol.

[40, 44]. Perovskite piezoelectric ceramics, such as PZT, are characterised by a longi-tudinal and a transverse coefficient, d_{33} and d_{31}, respectively, and the hydrostatic strain coefficient can be written in terms of these: $d_h = d_{33} + 2d_{31}$. In dense ferroelectric ma-terials $d_{31} \sim \frac{1}{2}d_{33}$ leading to $d_h \sim 0$. Introducing porosity enables a partial decoupling of the longitudinal and transverse reactions so that d_{31} tends toward zero as porosity is increased to approximately 60vol%, with only a relatively small reduction in d_{33} [49]. Therefore, by introducing a second inactive phase into the piezoelectric material, a sig-nificant increase in the hydrostatic strain coefficient can be attained.

With regards to piezoelectric energy harvesting, the resulting structure must ensure that d_{33} maintains a high value, as the reduction in d_{31} has no benefit for direct mode harvesters and means that porous materials will not operate effectively in bending mode. This can be seen in Fig. 2, where data from past research into porous ferroelectrics for hydrophone applications has been reanalysed in terms of FOM_{33} and FOM_{31}. The benefits in direct mode are shown, with increases in FOM_{33} of >300%, whereas intro-ducing porosity is found to significantly decrease the bending mode response, FOM_{31}. Elastic compliance data are not readily available and so the electomechanical coupling coefficients of porous materials could not be analysed in the same way.

The hydrostatic voltage coefficient, g_h, is given by the term $g_h = d_h/\varepsilon_{33}^{\sigma}$. Dense

ferroelectrics exhibit high permittivities that reduce the voltage output due to an applied stress. The permittivity of ferroelectric ceramics is significantly reduced by the introduction of an inactive second phase as there is a lower volume of easily polarisable material within the composite. Therefore, the voltage generated due to hydrostatic pressure is increased in porous ferroelectrics, compared to their dense counterparts, through the combined reduction in $\varepsilon_{33}^{\sigma}$ and the increase in d_h. Examination of Eqn. (4-7) shows that lowering the permittivity is also of interest for maximising the energy harvesting capabilities of ferroelectric ceramics.

The acoustic impedance of a material, Z_A, determines the ratio of energy transmitted and reflected at the interface between the receiver and the surrounding environment [50]. In sensing devices such as hydrophones, impedances of devices should be closely matched to their working environment to ensure efficient energy transfer from one medium to another [39]. Water and biological tissue have an acoustic impedance of around 1-1.5 Mrayls and dense PZT has an impedance of around 30 Mrayls [49]. Introducing porosity reduces this value significantly, with impedances below 2 Mrayls reported for ~70% porous PZT [51], therefore providing a much better acoustic matching of piezoelectric devices when used in water, such as hydrophones, or on biological tissue, such as ultrasound scanners. This would also be advantageous for vibration or pressure fluctuation harvesting in these environments.

Another potential benefit of porosity for low frequency, off-resonance energy harvesting is the lower mechanical quality factors, Q_M, that porous ferroelectrics exhibit compared to dense ones [12, 52, 53]. A low Q_M material, such as porous PZT, has a broader peak at resonance than dense PZT, making it more suited for broadband energy harvesting at lower frequencies, i.e. the conditions for which the piezoelectric FOMs in Section 2.2 are derived.

The dielectric loss, tan δ, of a piezoelectric, is important for the efficient operation of transducers, such as energy harvesters, as it is related to the amount of energy dissipated during the energy conversion process. Several studies have found that introducing porosity can reduce tan δ compared to dense materials [54, 55, 56], which would be advantageous for increasing the conversion efficiency of devices using porous piezoelectrics as the active material.

The benefits of porous ferroelectric ceramics for applications such as hydrophones have been established over the past 30 years, with their superior hydrostatic response, improved acoustic matching and overall device sensitivity shown in numerous studies. In certain circumstances, such as in bending mode or on-resonance harvesters, dense ferroelectric ceramics offer a better route to high conversion efficiencies than porous materials. However, porous piezoceramics show promising properties for energy harvesting under certain conditions (low frequency, random excitation) due to their low

permittivity coupled with relatively high d_{33} values, as well as exhibiting low dielectric loss, tan δ, and mechanical quality factors, Q_m.

4.1.2. Effect of porosity on pyroelectric properties

As well as reducing the permittivity of ferroelectric ceramics, which has advantages for both piezo- and pyroelectric harvesting, the introduction of porosity also reduces the volume specific heat capacity, which has benefits for increasing pyroelectric FOMs (Eqn. (10-14)). The main application of pyroelectric materials is in infrared imaging devices, the principles of which are essentially the same as those required for energy harvesting. Three types of porous pyroelectric material have been explored for energy harvesting applications, including thin films [45, 57] with high FOMs resulting from the decreased heat capacity; bulk functionally graded materials (FGM) consisting of a porous layer with controlled porosity, which allows more control over the permittivity and heat capacity of the material [46, 47]; and uniform porous ferroelectric ceramics [58].

Lang et al. [58] observed that both piezoelectric and pyroelectric FOMs are improved in porous ferroelectric ceramics as a result of the reduced relative permittivity in porous PZT with 3-0 and 3-3 connectivities prepared by the burned out polymer spheres (BURPS) process (detailed in Section 4.2.2). It was reported that uniformly porous structures of pyroelectric ceramics have higher pyroelectric responsivities than the dense materials. Since porosity also decreases the volume heat capacity it leads to an improvement of the thermal response; however, it also decreases the electrical resistivity and pyroelectric coefficient [45]. This complex relationship between pyroelectric, dielectric and thermal properties means that there is potential to tune the porosity to achieve the optimum response for a given application. However, due to the poor mechanical properties of unaligned porous structures the machinability of such materials is relatively poor, limiting their use in devices for generating electric power from thermal fluctuations.

Controlling the porous structure is of interest for both piezo- and pyroelectric energy harvesting applications as it can give control over properties that affect FOMs. The processing route used to form porous ferroelectric materials ultimately determines their structure and functional properties, so an understanding of the strengths and limitations of the different methods available is important when designing a material for piezo- or pyroelectric energy harvesting. These will now be discussed with a focus on bulk porous ceramics.

4.2. Processing of porous ferroelectrics

4.2.1. Coral replamine

The initial work into piezocomposites used a coral replamine technique, whereby a cubic coral structure was impregnated under vacuum with wax [40]. The coral was dissolved away using acid to leave a wax negative that was then filled with PZT-slip, before drying and sintering to remove the wax and densify the PZT regions. The resulting structure had large pores that were then filled with epoxy resin, resulting in 3-3 connectivity, i.e. complete connectivity of both the PZT and epoxy phases. The large pore size increased the flexibility of the ceramic and an increase in hydrostatic strain and piezo- and pyroelectric voltage responses were noted. By heavily straining this material the PZT coral structure was cracked, isolating ceramic regions from one another, thereby creating a flexible 0-3 structure [41]. This simple method was used to evaluate the effect of introducing a second phase into a piezoelectric material, and succeeded in exhibiting the benefits for applications where a hydrostatic stress is applied. However, this method is not easy to scale up and so other methods for creating porous ceramics have been devised.

Most macroporous ceramic structures can be back-filled with a polymer phase to improve the mechanical properties of the material. Whilst using a polymer second phase does improve the hydrostatic piezoelectric properties, porous piezoelectric ceramics exhibit enhanced performance in terms of d_h and g_h compared with ceramic-polymer composites [59].

4.2.2. Burned out polymer spheres (BURPS)

The BURPS process is a method for creating 3-3 structures with relative ease and low cost [60]. A pore-forming agent (PFA) is added to the ceramic powder before the pressing stage and is burned out during the sintering process. The BURPS process can also be adapted for tape casting ceramics [47, 50], allowing scale-up of manufacturing as well as the manufacture of thick films in the range of 5-200 μm, which are also of interest for energy harvesting [61]. Sintering profiles are usually adjusted to include a dwell stage at the temperature at which the PFA sublimes. BURPS provides some control over the pore structure as the pore size is closely correlated to the size of the additive. Various studies have assessed the performance of different pore formers, such as poly(methyl methacrylate) (PMMA), poly(ethylene oxide) (PEO), self-raising flour, dextrin and poly(vinyl alcohol) (PVA) [49, 62, 63], with the main difference in structure resulting from pore size and morphology. A draw back of the BURPS process is that cracking of the ceramic bridges between the pores often occurs, thought to be due to aggressive burn off of the volatile species [64], which may reduce both mechanical and piezoelectric properties. Cracking has also been reported in samples using PMMA as a
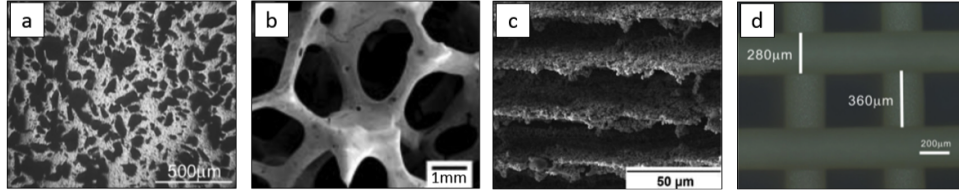
Figure 3: Porous microstructures formed using different processing routes including (a) 3-3 porous PZT formed via BURPS process with PMMA as PFA [63], (b) ~ 80% porous PZT formed via polymeric sponge method with 3-3 connectivity [59], (c) freeze cast alumina exhibiting 2-2 nacre-like structure aligned parallel to the poling direction [66] and (d) 3D printed 'woodpile' structure [67].

pore former, thought to be caused by relatively high stiffness of the PFA that leads to spring back after pressure has been released in the pressing stage, resulting in cracks perpendicular to the pressing direction [49, 62]. A limit to the amount of porosity obtainable, particularly for large, macro-PFAs, is usually 60-70% due to severe reduction in structural integrity above this point [59].

A limited degree of control over pore anisotropy and alignment is possible using the BURPS process by using irregular shaped PFAs [54, 64]. However, these tend to align perpendicular to the pressing direction, which is usually also the poling direction, and are found to lower both permittivity and piezoelectric coefficients. Modelling studies have shown that elongated pores aligned to the poling axis exhibit superior d_{33} coefficients in 3-3 structures compared with those aligned perpendicular to the poling direction, although were also predicted to exhibit higher permittivities [65]. It is likely that pore morphology could have a significant effect on energy harvesting capabilities of porous ferroelectric ceramics, however more sophisticated processing techniques are required to achieve desired structures.

4.2.3. Polymeric sponge

The effect of elongated pores aligned parallel to the poling direction has been studied by creating such structures via the polymeric sponge method [59, 68]. In the most basic method, a sponge is impregnated with ceramic slip before sintering removes the polymer, leaving a densified ceramic foam structure in its place. This comes under the broader category of sacrificial template methods [39]. By stretching and clamping the ceramic-soaked sponge during sintering the pores can be aligned, thereby providing a route to tailor the fraction of material in the polarisation direction and influencing the piezoelectric properties and permittivity [68]. The effect of pore morphology is discussed further in Section 4.2.8. This method was useful for evaluating the effect of pore anisotropy on piezoelectric properties [59], however incomplete sintering can lead to cracking in the ceramic struts, reducing the structural integrity and limiting its use for wider applications.

21

4.2.4. Gel casting

Gel casting was developed to form dense ceramics with superior shape retention from green to sintered form [69] but was adapted to synthesise porous materials with relatively high mechanical strength [70]. Ceramic powder is mixed with organic monomer binder and a dispersant in a solvent to form a slip. A commonly used pore former in gel casting is tert-butyl alcohol (TBA) [71, 72, 73, 74]. An initiator is added to begin polymerisation of the monomer, leading to in-situ formation of gel spheres that burn out during sintering, leaving spherical pores. Research into gel casting piezocomposites has been a reasonably recent phenomena and a comparison between gel casting and BURPS processes has shown gel casting to be advantageous, mainly due to the more uniform, spherical pores that can be obtained [64]. This will be discussed in more detail in Section 4.2.8 in terms of structural effects on electromechanical properties.

More recently, gel casting has been used in combination with the direct foaming method [51] and freeze casting [75]. In the direct foaming method, porosity is generated by mechanically frothing a ceramic slurry suspension to introduce air bubbles, prior to sintering [76]. This is a relatively low-cost method of forming porous ceramics but thermodynamic instability can cause a large distribution in pore sizes that may be mechanically unfavourable. Gel casting is used to increase the stability of foams, leading to a more even pore size distribution [77].

The processing methods described above are all used to generate 3-3 porosity, tending towards 3-0 as porosity levels are decreased, with pores randomly distributed through the bulk (schematics shown in Fig. 1). As has been shown previously in Section 2.2, piezoelectric ceramics for energy harvesting should ideally have the lowest possible compliance. There is an almost linear relationship between porosity and compliance in 3-3 ceramics [58, 63]. One possible way of improving the mechanical properties of porous ceramics is to utilise structures with the ceramic phase aligned in the direction in which the material is stressed.

4.2.5. Freeze casting

Freeze casting is a method for forming porous ceramics that has come to attention in the 15 years [78] and has the capability to form complex pore structures [79, 80]. Ceramic powders are mixed with dispersant and a solvent and cooled from one side to stimulate directional freezing of the solvent, which grow in dendrites that form at the cooled surface. These dendrites form the template for the porous structure. During solidification, ceramic particulates are forced into the channels between the crystallising solvent, leaving behind high density channels also aligned in the direction of freezing [81]. The freezing vehicle is then removed at low pressure so as not to degrade the unsintered ceramic. The resulting structure can be thought of as 3-1, with a fully in-

22

terconnected ceramic phase containing isolated pore channels (see Fig. 1), or 2-2, with a nacre-like structure (as shown in Fig. 3). For a given porosity, freeze cast ceramics exhibit superior mechanical properties to 3-3 structured materials when force is applied in the direction of alignment [82], which would be favourable for energy harvesting because of an increased electromechanical coupling coefficient, as well as making it easier to further process and handle the materials.

Freeze casting allows good control over porosity, simply by adjusting the solid loading in the slip [79, 81, 83, 84]. Altering the freezing agent can change the shape of the pore channels; camphene can yield pores with a near-circular cross section [81], whereas water tends to form flat ellipsoidal pores [56] and TBA produces hexagonal channels [85]. Freezing vehicles that allow room temperature processing, such as near-eutectic napthalene-camphor, have also been investigated [86]. The width of the pore channels [85] and ceramic walls [80] can be controlled by altering the degree of undercooling and the size of the ceramic particles in the slip [66]. Freeze casting is a promising processing route for piezocomposites as it enables control over the microstructure through relatively easy changes in freezing agent, solid loading and freezing temperature that may have benefits for the electromechanical properties. It may also allow high levels of porosity to be achieved (>80%) [80], whilst maintaining structural integrity.

Porous PZT with a 2-2 structure formed by freeze casting [87] has been found to exhibit higher a pyroelectric coefficient and a lower permittivity than that found in 3-3/3-0 PZT structures made using a BURPS process by Lang et al. [58]. The aligned structure may yield improved thermal properties for pyroelectric harvesting as well as superior compressive strengths (250-300%) [87] that have been found for these structures compared with 3-3 ceramic-air composites.

Most of the work on freeze cast porous ceramics has been on non-ferroelectric material systems, although in the last few years freeze casting has been shown to work with barium titanate [55, 56], PZT [53, 88] and PZT-lead zinc niobate (PZN) [84]. Notable results include reported d_{33} values of 81.8-93% of the dense value despite the porosity being over 65% [88], with d_{33} values at around 75% of dense values reported elsewhere for 82% porous samples [84]. This is typically much better than would be expected with 3-3 samples made by the BURPS process which often exhibit d_{33} values <60% of the dense value for similar levels of porosity [49]. However, the permittivity of porous materials usually correlates somewhat with the piezoelectric strain coefficient, and is therefore often found to be higher in freeze cast materials.

4.2.6. Printed porous structures

Another relatively recent development in the production of porous ceramics is the use of 3D printing technology, although it may be referred to under a number of dif-

ferent names, such as fused deposition technology (FDM) or solid freeform fabrication (SFF), for example [48, 89]. Ceramic slurry is mixed with a thermoplastic binder to make the filament, which is printed to form the desired structure. The green structure is then sintered to remove the thermoplastic and densify the ceramic phase. This can be used to form complex geometries and connectivities and, although early attempts led to relatively coarse (>250 μm) structures, advances in the technology mean microscale separations are possible [67]. Also, the use of 3D printing in combination with electrospinning technology can be used to form structures with nanoscale piezoelectric filaments [90]. Excellent control over the structure can be achieved using these methods so that good quality 3-1, 1-3 or 2-2 piezocomposites could be formed with properties tailored for energy harvesting.

4.2.7. Nanostructured porous materials

Advances in nanotechnology offer a route to form nanoscaled piezoelectric and ferroelectric structures for energy harvesting [91]. Currently the research has mainly focussed on materials such as piezoelectric zinc oxide [19] and ferroelectric lithium niobate [92] that exhibit the potential for high temperature operations and harvesting of acoustic energy. Production routes include the vapour-liquid-solid (VLS) process and photolithography to form arrays of nanowires on a conductive substrate such as gold. Materials such as lithium niobate exhibit ferroelectric properties to much higher temperatures, with a Curie temperature in excess of 1000°C, than more commonly used ferroelectric ceramics such as PZT and barium titanate, but have a significantly lower permittivity in their pure form ($\varepsilon_r < 100$), and therefore introducing porosity into structures is going to have less beneficial effect for energy harvesting. PZT nanowire arrays have been produced using a hydrothermal process [93], which has applications in the miniaturisation of harvesting devices and shows that high performance ferroelectric ceramics can be processed in this way.

Microporous PVDF thick films have also been investigated for their pyroelectric energy harvesting capabilities [45, 57]. Films ~50 μm thick were formed by hot-pressing a PVDF pellet before curing to remove volatiles and solvents, which yield a porous structure. These exhibited improved pyroelectric FOMs and electrothermal coupling coefficients than commercially available pure films. Similarly, 0-3 PZT-PVDF thick films formed using a spin casting process have been shown to have comparable pyroelectric FOMs to pure PZT thick films [94].

There has been increasing interest in the development of 0-3 piezocomposites using ceramic nanoparticles (NPs) embedded in an active PVDF matrix [95, 96] for small, flexible devices. Porosity, generated using sugar as a PFA, has been found to enhance the performance of the composites by increasing the compliance of the PVDF [95], which

24

may increase the stress transfer into the ferroelectric NPs. Introducing porosity may also enhance the piezoelectric behaviour as the micropores effectively form electret arrays [97]. This work, still in its early stages, has shown the potential for using porous PVDF films for energy harvesting, although interestingly the mechanism of enhanced performance appears different from that seen in porous piezoceramics, as it is not generally associated with a decrease in the permittivity.

4.2.8. Effect of pore morphology on properties

Pore size in 3-3 piezocomposites has been found to have little effect on the piezoelectric properties [49, 62], although macroporous structures have been found to exhibit lower permittivities than microporous ones [98]. The effect of pore size on the mechanical compliance has not been studied in detail, although there is some evidence to suggest that pore size has no effect on the Young's modulus of the material [63]. However, the general trend of an increase in compliance with increasing porosity is well established [50, 63].

Pore shape can have an effect on both the piezoelectric and mechanical properties. In the BURPS process, irregular pore shape can either be caused by an irregular shaped pore former or due to smearing of a soft volatile agent during pressing. In both cases, the long axis of the pores is usually aligned perpendicular to the pressing direction [54, 64]. The use of stearic acid as a pore former leads to irregular pore formation, with the relative permittivity being lower as a result [64], possibly due to stress concentrations leading to depolarising effects. The Young's modulus of materials with spherical pores has been found to be higher than materials with irregular pores, again thought to be because of stress concentrations [54].

4.2.9. Sintering temperature

A number of studies, using the different processing methods described above, have investigated the effect of sintering temperature on piezoelectric properties [50, 71, 73, 99]. In all cases, increasing the sintering temperature results in a denser microstructure, and therefore higher piezoelectric coefficients and permittivity, nullifying the positive effects of porosity with regards to energy harvesting and SONAR applications. The sintering temperature can be used as a mode of controlling the porosity in the structure rather than altering the level of PFA in BURPS [99] and could also be applied to tape/freeze casting. Altering the sintering temperature alongside other processing variables could be used to give added control over porosity volumes. An increase in grain size may be associated with higher piezoelectric coefficients [100] but this is difficult to achieve without also increasing density, which is likely to be associated with an increase in permittivity and is therefore unfavourable for ferroelectric ceramics for energy har-

vesting. At this stage the focus should be on understanding the structural relationships between the ceramic and the air phase, as this is likely to have a greater effect on overall performance, before considering the grain size when attempting to optimise the system.

5. Conclusions

Introducing porosity into ferroelectric materials, particularly high performance ceramics such as PZT, has the capability to increase both piezo- and pyroelectric off-resonance energy harvesting FOMs. High levels of porosity lead to a significant reduction in permittivity, which is of interest for both piezo- and pyroelectric energy harvesting, as well as reducing the volume specific heat capacity, which is favourable for pyroelectric harvesting. Lower Q_m values exhibited by porous piezoceramics also increase their appeal for broadband, off-resonance energy harvesting. However, the complex balance of properties required for high electromechanical and electrothermal coupling coefficients mean that porous structures must be carefully engineered to achieve the desired properties such as high d_{33} and low compliance and permittivity for piezo-harvesters, and high p, low heat capacity and low permittivity for pyro-harvesters.

Data from previous studies, presented in Fig. 2, has shown the potential for using porosity to increase piezoelectric harvesting FOMs, but more research is required to fully understand the effects this has on mechanical properties, in particular. Porosity has a detrimental effect on mechanical properties, even for freeze cast materials with excellent alignment of the ceramic phase. The significance of this effect needs to be investigated with regards to the electromechanical coupling coefficient, in which high FOMs are desirable but also low compliances, which will only be achievable in terms of porous ferroelectrics if careful attention is paid to the final structure of the material.

A variety of processing routes are available to produce ferroelectrics with complex structures that are suited to harvesting energy from thermal fluctuations and mechanical vibrations. The most promising of these includes freeze casting, which enables good alignment of both ceramic and porous phases thus yielding good properties tailored for energy harvesting, and new developments in printed and nanotechnology that may allow even better control over structure as well as enabling the production of very small energy harvesting devices.

References

[1] H. A. Sodano, D. J. Inman, G. Park, A Review of Power Harvesting from Vibration Using Piezoelectric Materials, The Shock and Vibration Digest 36 (2004) 197–205.

[2] K. A. Cook-Chennault, N. Thambi, A. M. Sastry, Powering MEMS portable devices-a review of non regenerative and regenerative power supply systems with special emphasis on piezoelectric energy harvesting systems, Smart Mater. Struct. (043001).

[3] C. R. Bowen, H. A. Kim, P. M. Weaver, S. Dunn, Piezoelectric and ferroelectric materials and structures for energy harvesting applications, Energy Environ. Sci. 7 (2013) 25–44.

[4] H. A. Sodano, Comparison of Piezoelectric Energy Harvesting Devices for Recharging Batteries, J. Intell. Mater. Syst. Struct. 16 (2005) 799–807.

[5] H. A. Sodano, G. Park, D. J. Inman, Estimation of Electric Charge Output for Piezoelectric Energy Harvesting, Strain 40 (2004) 49–58.

[6] S. P. Beeby, M. J. Tudor, N. M. White, Energy harvesting vibration sources for microsystems applications, Meas. Sci. Tech. 17 (2006) 175–195.

[7] I. Johnson, T. William, W. T. Choate, A. A. Davidson, Waste heat recovery: technology and opportunities in US industry, US Department of Energy.

[8] S. R. Hunter, N. V. Lavrik, S. Mostafa, S. Rajic, P. G. Datskos, Review of pyroelectric thermal energy harvesting and new MEMs-based resonant energy conversion techniques, Proc. Soc. Photo. Opt. Instru. Eng. 8377 (2012) 83770D–1–83770D–14.

[9] F. Y. Lee, A. Navid, L. Pilon, Pyroelectric waste heat energy harvesting using heat conduction, Appl. Therm. Eng. 37 (2012) 30–37.

[10] R. Zhang, B. Jiang, W. Cao, Elastic, piezoelectric, and dielectric properties of multidomain $0.67Pb(Mg_{1/3}Nb_{2/3})O_3$-$0.33PbTiO_3$ single crystals, J. Appl. Phys. 90 (2001) 3471–3475.

[11] M. G. Tehrani, G. Gatti, M. J. Brennan, D. J. Thompson, ENERGY HARVESTING FROM TRAIN VIBRATIONS, in: 11th International Conference on Vibration Problems, 2013.

[12] J. Lee, B. Choi, Development of a piezoelectric energy harvesting system for implementing wireless sensors on the tires, Energy Convers. Manage. 78 (2014) 32–38.

[13] N. S. Shenck, J. A. Paradiso, Energy scavenging with shoe-mounted piezoelectrics, IEEE Micro 21 (2001) 30–42.

[14] J. Granstrom, J. Feenstra, H. A. Sodano, K. Farinholt, Energy harvesting from a backpack instrumented with piezoelectric shoulder straps, Smart Mater. Struct. 16 (2007) 1810–1820.

[15] J. Allen, J. Smits, Energy harvesting eel, J. Fluids Struct. 15 (2001) 1–13.

[16] M. Deterre, E. Lefeuvre, E. Dufour-Gergam, An active piezoelectric energy extraction method for pressure energy harvesting, Smart Mater. Struct. 21 (2012) 085004.

[17] M. J. Ramsey, W. W. Clark, Piezoelectric energy harvesting for bio-MEMS applications, in: Proc. Soc. Photo. Opt. Instru. Eng., 2001, pp. 429–438.

[18] J. Smoker, M. Nouh, Energy harvesting from a standing wave thermoacoustic-piezoelectric resonator, J. Appl. Phys. 111 (2012) 104901.

[19] Z. L. Wang, J. Song, Piezoelectric nanogenerators based on zinc oxide nanowire arrays, Science 312 (2006) 242–247.

[20] S. N. Cha, S. M. Kim, H. J. Kim, J. Y. Ku, J. I. Sohn, Porous PVDF as effective sonic wave driven nanogenerators, Nano Lett. 11 (2011) 5142–5147.

[21] R. A. Islam, S. Priya, Realization of high-energy density polycrystalline piezoelectric ceramics, Appl. Phys. Lett. 88 (2006) 032903.

[22] S. Priya, Advances in energy harvesting using low profile piezoelectric transducers, J. Electroceram. 19 (2007) 165–182.

[23] S. Priya, Criterion for Material Selection in Design of Bulk Piezoelectric Energy Harvesters, IEEE Trans. Ultrason., Ferroelect., Freq. Control 57 (2010) 2610–2612.

[24] E. K. Akdogan, M. Allahverdi, A. Safari, Piezoelectric Composites for Sensor and Actuator Applications, IEEE Trans. Ultrason., Ferroelect., Freq. Control 52 (2005) 746–775.

[25] C.-H. Choi, I.-T. Seo, D. Song, M.-S. Jang, B.-Y. Kim, S. Nahm, T.-H. Sung, H.-C. Song, Relation between piezoelectric properties of ceramics and output power density of energy harvester, J. Eur.

Ceram. Soc. 33 (2013) 1343–1347.

[26] J. Hur, I.-T. Seo, D.-H. Kim, S. Nahm, J. Ryu, S. H. Han, C.-Y. Kang, S.-J. Yoon, Piezoelectric Ceramics for Use in Multilayer Actuators and Energy Harvesters, J. Am. Ceram. Soc. 97 (2014) 3157–3163.

[27] M. I. Friswell, S. Adhikari, Sensor shape design for piezoelectric cantilever beams to harvest vibration energy, J. Appl. Phys. 108 (2010) 014901.

[28] M. Stewart, P. M. Weaver, M. Cain, Charge redistribution in piezoelectric energy harvesters, Appl. Phys. Lett. 100 (2012) 073901.

[29] S. B. Lang, Pyroelectricity : From Ancient Curiosity to Modern Imaging Tool, Phys. Today 58 (2005) 31–36.

[30] Q. Zhang, A. Agbossou, Z. Feng, M. Cosnier, Solar micro-energy harvesting with pyroelectric effect and wind flow, Sens. Actuators, A 168 (2011) 335–342.

[31] C. R. Bowen, J. Taylor, E. LeBoulbar, D. Zabek, A. Chauhan, R. Vaish, Pyroelectric materials and devices for energy harvesting applications, Energy Environ. Sci. 7 (2014) 3836–3856.

[32] S. Krishnan, D. Ezhilarasi, G. Uma, M. Umapathy, Pyroelectric-based solar and wind energy harvesting system, IEEE Trans. Sustain. Energy 5 (2014) 73–81.

[33] V. Kotipalli, Z. Gong, P. Pathak, T. Zhang, Y. He, S. Yadav, L. Que, Light and thermal energy cell based on carbon nanotube films, Appl. Phys. Lett. 97 (2010) 124102.

[34] C. R. Bowen, J. Taylor, E. Le Boulbar, D. Zabek, V. Y. Topolov, A modified figure of merit for pyroelectric energy harvesting, Mater. Lett. 138 (2015) 243–246.

[35] S. B. Lang, D. K. Das-Gupta, Pyroelectricity: Fundamentals and Applications, in: Handbook of Advanced Electronic and Photonic Materials and Devices, 2001, pp. vol. 4, 1–54.

[36] R. W. Whatmore, Pyroelectric devices and materials, Rep. Prog. Phys. 49 (1986) 1335–1386.

[37] G. H. Haertling, Ferroelectric Ceramics: History and Technology, J. Am. Ceram. Soc. 82 (1999) 797–818.

[38] A. J. Lovinger, Ferroelectric Polymers, Science 220 (1983) 1115–1121.

[39] E. Mercadelli, A. Sanson, C. Galassi, Porous piezoelectric ceramics, in: E. Suaste-Gomez (Ed.), Piezoelectric Ceramics, InTech Open, 2010, Ch. 6, pp. 111–128.

[40] R. E. Newnham, D. P. Skinner, L. E. Cross, Connectivity and piezoelectric-pyroelectric composites, Mater. Res. Bull. 13 (1978) 525–536.

[41] D. P. Skinner, R. E. Newnham, L. E. Cross, Flexible Composite Transducers, Mater. Res. Bull. 13 (1978) 599–607.

[42] T. Arai, K. Ayusawa, H. Sato, T. Miyata, K. Kazutami, K. Keiichi, Properties of hydrophone with porous piezoelectric ceramics, Jpn. J App. Phys. 30 (1991) 2253–2255.

[43] S. Marselli, V. Pavia, C. Galassi, E. Roncari, F. Cranciun, G. Guidarelli, Porous piezoelectric ceramic hydrophone, J. Acoust. Soc. Am. 106 (1999) 733–738.

[44] E. Roncari, C. Galassi, F. Cranciun, G. Guidarelli, S. Marselli, V. Pavia, Ferroelectric ceramics with included porosity for hydrophone applications, Proceedings of the Eleventh IEEE International Symposium on Applications of Ferroelectrics (1998) 373–376.

[45] A. Navid, D. Vanderpool, A. Bah, L. Pilon, Towards optimization of a pyroelectric energy converter for harvesting waste heat, Inter. J. Heat Mass Trans. 53 (2010) 4060–4070.

[46] A. Navarro, R. W. Whatmore, J. R. Alcock, Preparation of functionally graded PZT ceramics using tape casting, J. Electroceram. 13 (2004) 413–415.

[47] C. P. Shaw, R. W. Whatmore, J. R. Alcock, Porous, Functionally Gradient Pyroelectric Materials, J. Am. Ceram. Soc. 90 (2007) 137–142.

[48] A. Safari, E. K. Akdogan, Rapid Prototyping of Novel Piezoelectric Composites, Ferroelectr. 331

(2006) 153–179.

[49] C. R. Bowen, A. Perry, A. C. F. Lewis, H. Kara, Processing and properties of porous piezoelectric materials with high hydrostatic figures of merit, J. Eur. Ceram. Soc. 24 (2004) 541–545.

[50] E. Roncari, C. Galassi, F. Craciun, C. Capiani, A. Piancastelli, A microstructural study of porous piezoelectric ceramics obtained by different methods, J. Eur. Ceram. Soc. 21 (2001) 409–417.

[51] W. Liu, J. Xu, Y. Wang, H. Xu, X. Xi, J. Yang, Processing and Properties of Porous PZT Ceramics from Particle-Stabilized Foams via Gel Casting, J. Am. Ceram. Soc. 96 (2013) 1827–1831.

[52] F. Craciun, C. Galassi, E. Roncari, A. Filippi, G. Guidarelli, Electro-elastic properties of porous piezoelectric ceramics obtained by tape casting, Ferroelectr. 205 (1998) 49–67.

[53] T. Xu, C.-A. Wang, Piezoelectric Properties of a Pioneering 3-1 Type PZT/Epoxy Composites Based on Freeze-Casting Processing, J. Am. Ceram. Soc. 97 (2014) 1511–1516.

[54] T. Zeng, X. Dong, C. Mao, Z. Zhou, H. Yang, Effects of pore shape and porosity on the properties of porous PZT 95/5 ceramics, J. Eur. Ceram. Soc. 27 (2007) 2025–2029.

[55] P. I. N. Li, Y. Pu, Z. Dong, P. A. N. Gao, Kaolinite as a Suspending Agent for Preparation of Porous BaTiO$_3$ Ceramics via Freeze Casting, J. Electron. Mater. 43 (2014) 459–464.

[56] G. Liu, T. W. Button, D. Zhang, Lamellar BaTiO$_3$ and its composites fabricated by the freeze casting technique, J. Eur. Ceram. Soc. 34 (2014) 4083–4088.

[57] A. Navid, L. Pilon, Pyroelectric energy harvesting using Olsen cycles in purified and porous poly(vinylidene fluoride-trifluoroethylene) [P(VDF-TrFE)] thin films, Smart Mater. Struct. 20 (2011) 025012.

[58] S. B. Lang, E. Ringgaard, Measurements of the thermal, dielectric, piezoelectric, pyroelectric and elastic properties of porous PZT samples, in: IEEE Conference on Electrical Insulation and Dielectric Phenomena, 2009, pp. 739–742.

[59] H. Kara, R. Ramesh, R. Stevens, C. R. Bowen, Porous PZT ceramics for receiving transducers, IEEE Trans. Ultrason., Ferroelect., Freq. Control 50 (2003) 289–296.

[60] K. Rittenmyer, T. R. Shrout, W. A. Schulze, R. E. Newnham, Piezoelectric 3-3 composites, Ferroelectr. 41 (1982) 189–195.

[61] R. A. Dorey, Integrated Powder-Based Thick Films for Energy Harvesting Devices, IEEE Sensors Journal 14 (2014) 2177–2184.

[62] B. P. Kumar, H. H. Kumar, D. K. Kharat, Study on pore-forming agents in processing of porous piezoceramics, J. Mater. Sci.: Mater. Electron. 16 (2005) 681–686.

[63] T. Zeng, X. Dong, S. Chen, H. Yang, Processing and piezoelectric properties of porous PZT ceramics, Ceram. Int. 33 (2007) 395–399.

[64] A.-K. Yang, C.-A. Wang, R. Guo, Y. Huang, Microstructure and Electrical Properties of Porous PZT Ceramics Fabricated by Different Methods, J. Am. Ceram. Soc. 93 (2010) 1984–1990.

[65] C. R. Bowen, H. Kara, Pore anisotropy in 3-3 piezoelectric composites, Mater. Chem. Phys. 75 (2002) 45–49.

[66] Y. Zhang, K. Zhou, J. Zeng, D. Zhang, Control of pore structures and sizes in freeze cast ceramics, Adv. App. Ceram. 112 (2013) 405–411.

[67] Y.-Y. Li, L.-T. Li, B. Li, Direct ink writing of 33 piezoelectric composite, J. Alloys Compd. 620 (2015) 125–128.

[68] M. J. Creedon, W. A. Schulze, Axially distorted 3-3 piezoelectric composites for hydrophone applications, Ferroelectr. 153 (1994) 333–339.

[69] A. C. Young, O. O. Omatete, M. A. Janney, P. A. Menchhofer, Gelcasting of Alumina, J. Am. Ceram. Soc. 74 (1991) 612–618.

[70] R. Chen, Y. Huang, C. A. Wang, J. Qi, Ceramics with ultra-low density fabricated by gelcasting: An

unconventional view, J. Am. Ceram. Soc. 90 (2007) 3424–3429.

[71] A.-K. Yang, C.-A. Wang, R. Guo, Y. Huang, C.-W. Nan, Effects of sintering behavior on microstructure and piezoelectric properties of porous PZT ceramics, Ceram. Int. 36 (2010) 549–554.

[72] A.-K. Yang, C.-A. Wang, R. Guo, Y. Huang, Effects of porosity on dielectric and piezoelectric properties of porous lead zirconate titanate ceramics, Appl. Phys. Lett. 98 (2011) 152904.

[73] W. Liu, J. Xu, R. Lv, Y. Wang, H. Xu, J. Yang, Effects of sintering behavior on piezoelectric properties of porous PZT ceramics, Ceram. Int. 40 (2014) 2005–2010.

[74] A.-K. Yang, C.-A. Wang, R. Guo, Y. Huang, C.-W. Nan, Porous PZT Ceramics with High Hydrostatic Figure of Merit and Low Acoustic Impedance by TBA-Based Gel-Casting Process, J. Am. Ceram. Soc. 93 (2010) 1427–1431.

[75] D. Zhang, Y. Zhang, R. Xie, K. Zhou, Freeze gelcasting of aqueous alumina suspensions for porous ceramics, Ceram. Int. 38 (2012) 6063–6066.

[76] A. R. Studart, U. T. Gonzenbach, E. Tervoort, L. J. Gauckler, Processing Routes to Macroporous Ceramics: A Review, J. Am. Ceram. Soc. 89 (2006) 1771–1789.

[77] W. Liu, L. Du, Y. Wang, J. Yang, H. Xu, Effects of foam composition on the microstructure and piezoelectric properties of macroporous PZT ceramics from ultrastable particle-stabilized foams, Ceram. Int. 39 (2013) 8781–8787.

[78] T. Fukasawa, M. Ando, Synthesis of Porous Ceramics with Complex Pore Structure by Freeze Dry Processing, J. Am. Ceram. Soc. 84 (2001) 230–232.

[79] T. Fukasawa, Z.-y. Deng, M. Ando, Synthesis of Porous Silicon Nitride with Unidirectionally Aligned Channels Using Freeze-Drying Process, J. Am. Ceram. Soc. 85 (2002) 2151–2155.

[80] S. Deville, E. Saiz, R. K. Nalla, A. P. Tomsia, Freezing as a path to build complex composites, Science 311 (2006) 515–518.

[81] K. Araki, J. W. Halloran, Porous Ceramic Bodies with Interconnected Pore Channels by a Novel Freeze Casting Technique, J. Am. Ceram. Soc. 88 (2005) 1108–1114.

[82] S. Deville, Freeze-Casting of Porous Ceramics: A Review of Current Achievements and Issues, Adv. Eng. Mater. 10 (2008) 155–169.

[83] Y. Zhang, L. Chen, J. Zeng, K. Zhou, D. Zhang, Aligned porous barium titanate/hydroxyapatite composites with high piezoelectric coefficients for bone tissue engineering., Mater. Sci. Eng. C 39 (2014) 143–9.

[84] S.-H. Lee, S.-H. Jun, H.-E. Kim, Y.-H. Koh, Fabrication of Porous PZT-PZN Piezoelectric Ceramics With High Hydrostatic Figure of Merits Using Camphene-Based Freeze Casting, J. Am. Ceram. Soc. 90 (2007) 2807–2813.

[85] L. Hu, C.-A. Wang, Y. Huang, C. Sun, S. Lu, Z. Hu, Control of pore channel size during freeze casting of porous YSZ ceramics with unidirectionally aligned channels using different freezing temperatures, J. Eur. Ceram. Soc. 30 (2010) 3389–3396.

[86] K. Araki, J. W. Halloran, Room-temperature freeze casting for ceramics with nonaqueous sublimable vehicles in the naphthalenecamphor eutectic system, J. Am. Ceram. Soc. 87 (2004) 2014–2019.

[87] Y. Zhang, Y. Bao, D. Zhang, C. R. Bowen, Porous PZT Ceramics with Aligned Pore Channels for Energy Harvesting Applications, J. Am. Ceram. Soc. 98 (2015) 2980–2983.

[88] R. Guo, C. A. Wang, A. Yang, Effects of pore size and orientation on dielectric and piezoelectric properties of 1-3 type porous PZT ceramics, J. Eur. Ceram. Soc. 31 (2011) 605–609.

[89] M. Allahverdi, S. C. Danforth, M. Jafari, A. Safari, Processing of advanced electroceramic components by fused deposition technique, J. Eur. Ceram. Soc. 21 (2001) 1485–1490.

[90] H. H. S. Chang, Z. Huang, Laminate composites with enhanced pyroelectric effects for energy harvesting, Smart Mater. Struct. 19 (2010) 065018.

[91] J. Briscoe, S. Dunn, Piezoelectric nanogenerators a review of nanostructured piezoelectric energy harvesters, Nano Energy 14 (2015) 15–29.

[92] R. W. C. Lewis, D. W. E. Allsopp, P. Shields, A. Šatka, S. Yu, V. Y. Topolov, C. R. Bowen, Nano-Imprinting of Highly Ordered Nano-Pillars of Lithium Niobate (LiNbO$_3$), Ferroelectr. 429 (2012) 62–68.

[93] S. Xu, B. J. Hansen, Z. L. Wang, Piezoelectric-nanowire-enabled power source for driving wireless microelectronics., Nat. Comms. 1 (2010) 93.

[94] M. Dietze, J. Krause, C.-H. Solterbeck, M. Es-Souni, Thick film polymer-ceramic composites for pyroelectric applications, J. Appl. Phys. 101 (2007) 054113.

[95] W. R. Mccall, K. Kim, C. Heath, G. L. Pierre, D. J. Sirbuly, Piezoelectric Nanoparticle Polymer Composite Foams, ACS Appl. Mater. Interfaces 6 (2014) 19504–19509.

[96] K. Kim, W. Zhu, X. Qu, C. Aaronson, W. R. McCall, 3D Optical Printing of Piezoelectric NanoparticlePolymer Composite Materials, ACS Nano 8 (2014) 9799–9806.

[97] P. Adhikary, S. Garain, D. Mandal, The co-operative performance of a hydrated salt assisted sponge like P(VDF-HFP) piezoelectric generator: an effective piezoelectric based energy harvester, Phys. Chem. Chem. Phys. 17 (2015) 7275–7281.

[98] Z. He, J. Ma, R. Zhang, Investigation on the microstructure and ferroelectric properties of porous PZT ceramics, Ceram. Int. 30 (2004) 1353–1356.

[99] T. Zeng, X. L. Dong, H. Chen, Y. L. Wang, The effects of sintering behavior on piezoelectric properties of porous PZT ceramics for hydrophone application, Mater. Sci. Eng. B 131 (2006) 181–185.

[100] K. Okazaki, K. Nagata, Effects of grain size effects and porosity on electrical and optical properties of PLZT ceramics, J. Am. Ceram. Soc. 56 (1973) 82–86.

2.2 Summary

The literature review identified several areas in which further research could add to the knowledge-base in the field of porous ferroelectric materials for energy harvesting applications. An overview of the processing routes discussed methods for producing various porous structures, in terms of pore shape, orientation and phase interconnectivity, and there was evidence in literature that the porous structure had a significant effect on the final properties of the material. However, the causes of such effects were not well understood. For example, freeze casting has been shown to produce porous materials with excellent mechanical properties due to the high degree of alignment of the two phases, yet no article satisfactorily explains why this type of structure also yields the excellent piezoelectric properties reported in freeze cast porous lead zirconate titanate (PZT).

Following the literature review, the objectives for the research project were defined as:

1. Understand the underlying causes of the effect of porosity, in terms of pore morphology and connectivity, on key material properties of porous ferroelectric materials, such as piezoelectric strain coefficients and permittivity.

   i) This will be achieved through the development of finite element models that can aid understanding of how the porous structure influences properties. Of particular interest is the effect the porous structure has on the poling process, a key stage in the production of ferroelectric materials that yields piezoelectric and pyroelectric behaviour.

2. Design, manufacture and characterise novel porous structures for energy harvesting applications that have been identified through the finite element modelling studies as those with potentially high piezoelectric energy harvesting figures of merit.

   i) Various processing methods will be utilized to achieve this objective including the burned out polymer spheres (BURPS) method, freeze casting and an adapted BURPS method to form layered structures.

3. Demonstrate the potential of porous ferroelectric materials for energy harvesting applications using materials manufactured during the project to harvest vibrational mechanical energy and convert into useful electric energy.

   i) Samples manufactured during the project will be mechanically excited and this mechanical energy converted into electrical energy via the piezoelectric effect. Samples with varying levels of porosity will be tested so as to compare the piezoelectric energy harvesting capabilities of dense and porous ferroelectric ceramics.

4. Adapt finite element models, discussed in the first objective, for composites that have a high permittivity fillers contained within a low permittivity matrix to assess the capabilities of these composites for energy storage applications.

i) This additional objective was not considered at the time of publication of the literature review but links to the understanding of how electric fields distribute in composites with phases with contrasting permittivities.

Chapter 3

Manufacture and characterisation of uniform porous barium titanate for energy harvesting applications

3.1 Context

The potential for the use of porous ferroelectric ceramics for energy harvesting applications was discussed in the literature review in Chapter 2, with reanalysed data from the literature demonstrating that energy harvesting figures of merit could be increased via the controlled introduction of porosity. One difficulty of comparing different experimental studies from the literature, particularly for ferroelectric ceramics, is that the material composition, microstructure resulting from the processing methods, and measurement techniques vary from study to study making it hard to definitively separate the variables, which is required to fully understand the role of porosity with different morphologies has on the effective material properties.

It was therefore necessary to produce ferroelectric ceramic samples with varying levels of uniformly distributed porosity using a well-known and robust manufacturing technique discussed in the literature review, the burned out polymer spheres (BURPS) method, so as to get a baseline data set to which subsequent work could be compared. This experimental study is the topic of the paper contained within this chapter.

As detailed in Chapter 1, Fig. 1-1, another publication is closely related to the work presented in this chapter: J. I. Roscow et al. *Understanding the peculiarities of the piezoelectric effect in macro-porous BaTiO₃*, Sci. Tech. Adv. Mater. **17** (2017), uses numerical modelling approaches that take into account the effect of 90° domain wall mobility on the piezoelectric properties. The experimental procedure and data are the same as in the work presented in this

chapter, although transverse piezoelectric coefficients, d_{31}, are also reported as a function of porosity.

Access the data from the following paper here: https://doi.org/10.15125/BATH-00451.

Statement of Authorship

This declaration concerns the article entitled:								
Manufacture and characterisation of porous ferroelectrics for energy harvesting applications								
Publication status (tick one)								
draft manuscript		**Submitted**		**In review**		**Accepted**		**Published** ✓
Publication details (reference)	Roscow et al., Ferroelectrics **498** (2016)							
Candidate's contribution to the paper (detailed, and also given as a percentage).	The candidate contributed to/ considerably contributed to/predominantly executed the Formulation of ideas: Solely the candidate (100%) Design of methodology: Solely the candidate (100%) Experimental work: Solely the candidate (100%) Presentation of data in journal format: Solely the candidate (100%)							
Statement from Candidate	This paper reports on original research I conducted during the period of my Higher Degree by Research candidature.							
Signed						**Date**	30/11/17	

PAPER 2: Manufacture and characterization of porous ferroelectrics for energy harvesting applications

J.I. Roscow[a], J. Taylor[b], and C.R. Bowen[a]

[a]*Department of Mechanical Engineering, University of Bath, Bath, UK*
[b]*Department of Electrical and Electronic Engineering, University of Bath, Bath, UK*

Abstract

Porous ferroelectric materials have been evaluated for their piezoelectric energy harvesting capabilities. Macro-porous barium titanate ($BaTiO_3$) ceramics were fabricated with a range of porosities using the burned out polymer spheres process. The pore fraction was tailored by mixing a pore forming agent with $BaTiO_3$ powder in varying amounts by weight before cold-pressing and pressureless sintering. Introducing porosity into the ferroelectric significantly increased the energy harvesting figure of merit; with a maximum of 2.85 pm^2/N obtained at ~40% relative density compared with ~1.0 pm^2/N for the dense material. The results demonstrate that introducing porosity into a piezoelectric provides an effective route to improving the vibration energy harvesting capability of these materials.

1. Introduction

Interest in energy harvesting devices has grown in recent years with a view that they can replace or prolong the lifespan of batteries used to power a range of low-power electronic devices, such as wireless sensor arrays [1]. Ferroelectric materials, such as lead zirconate titanate (PZT) and barium titanate ($BaTiO_3$), are of particular interest due to their effective piezoelectric and pyroelectric properties, which enable them to harvest energy from both mechanical vibrations and temperature fluctuations.

Porous ferroelectric ceramics, particularly PZT, have been extensively studied, but effort has focussed predominately on the development of porous piezoelectrics for hydrostatic sensor applications, such as active and passive SONAR [2]. This is due to superior hydrostatic piezoelectric strain and voltage coefficients, d_h and g_h, respectively, found in porous materials compared to dense materials. A reduction in relative density due to the introduction of porosity also reduces the acoustic impedance of transducers used in water or on biological tissue, thereby increasing the efficiency of energy transfer from one medium to another. These applications have dominated research into porous ferroelectrics to date, with little interest shown into the benefits for energy harvesting.

Energy harvesting FOMs have been derived for low frequency, off-resonance mechanical excitation of polycrystalline piezoelectric ceramics [3], conditions that mean the material can be assumed to behave as a parallel plate capacitor. The energy stored, u, in a material as a result of an applied stress is therefore equal to:

$$u = \frac{1}{2} d_{ij} g_{ij} . \sigma^2 \qquad (1)$$

where d is the piezoelectric strain coefficient, g is the piezoelectric voltage coefficient, σ is applied stress and subscripts i and j denote the direction of application and response, respectively. Eqn. 1 is derived from the energy stored in a capacitor ($U = \frac{1}{2}CV^2$) (where C is capacitance and V is applied voltage). If the force is applied along the poling axis, which convention defines as the 3-direction, the materials related FOM is [3]:

$$FOM_{33} = \frac{d_{33}^2}{\varepsilon_{33}^{\sigma}} \qquad (2)$$

where $\varepsilon_{33}^{\sigma}$ is the relative permittivity at constant stress. Previous studies have shown that only a small reduction in d_{33} occurs when the relative density is reduced to ~50% by the introduction of porosity, whilst there is a large decrease in the permittivity [4]. This indicates that there is potential to improve the energy harvesting FOM by introducing porosity as a second phase into ferroelectric ceramics. In addition to the FOM it is also beneficial to consider the impact of the presence of porosity on the electromechanical coupling coefficients, which determine the efficiency of energy conversion from mechanical to electrical energy, or vice versa. The longitudinal coupling coefficient is given by:

$$k_{33}^2 = \frac{d_{33}^2}{(\varepsilon_{33}^{\sigma} . S_{33}^E)} \qquad (3)$$

where S_{33}^E is the mechanical compliance in the 3-direction when a force is applied along the same axis. As a result there is a complex balance between the variation of d_{33}, $\varepsilon_{33}^{\sigma}$ and S_{33}^E with porosity.

The electromechanical properties of a piezo-composite, such as a porous ferroelectric, are highly dependent on the structure, which is classified by a two-digit notation first described by Newnham et al. [5]. The first digit refers to the active (piezoelectric) phase and the second to the inactive phase. The number assigned to each phase depends on the dimensionality of the interconnectivity and can range from zero (isolated particles) to three (full interconnection in all directions). A 3-3 piezo-composite therefore has a fully connected ceramic phase with fully open porosity distributed throughout. By changing the structure it is possible to tune the properties such as piezoelectric strain coefficients, permittivity and mechanical compliance, which in turn affect both the FOM Eqn. (2) and electromechanical coupling coefficient Eqn. (3).

In this work 3-3 barium titanate structures have been produced with a range of porosities so as to determine the potential benefits of porous materials for piezoelectric energy harvesting and the impact of porosity on the relevant figures of merit. Barium titanate has been chosen for this study because the processing is less complicated than that for PZT as the ceramics can be sintered in air.

2. Experimental

Barium titanate powder (Ferro, UK) was ball milled for 24 hours with zirconia media and distilled water. Dense and low porosity samples (3-20% open porosity) required the addition of a small amount of binder, polyethylene glycol (PEG) (Sigma Aldrich, UK), to the $BaTiO_3$ powder prior to the milling stage to enable crack-free pressing. After ball milling, the powder was dried over night before sieving through a 150 μm mesh. A range of porosities (10-72 vol.%) was obtained via the burned out polymer spheres (BURPS) method, whereby a volatile pore forming agent (PFA), PEG, was mixed with the sieved $BaTiO_3$ powder in varying proportions by weight. The PFA burned out during sintering to form ceramic structures with a high degree of open porosity. Dense samples were also produced with no additional PEG, other than that used as binder. The powder was uniaxially pressed at 300 MPa to form pellets 13mm in diameter and weighing 0.7 g. Pellets were sintered in air at 1300°C for two hours, including a two hour dwell stage at 400°C on the up-ramp to burn out the binder/PFA, with a ramp rate of ±60° C/h. XRD analysis was performed on a dense sample and a high porosity sample to confirm that a fully perovskite structure had formed. Samples were ground flat and cleaned in ethanol prior to determining the density and apparent porosity using the Archimedes method. Silver electrode paint (RS Components) was applied to all samples prior to corona poling in air at 115°C with a 14 kV field applied from a 35 mm point source. This poling procedure was chosen over poling in oil due to envisaged difficulties cleaning porous samples post-poling, as oil was likely to penetrate the porous structures. Piezoelectric strain coefficient, d_{33}, was measured using a *Take Control Piezometer System PM25*, which applies an alternating force of ±0.1 N at a frequency of 97 Hz and measures the electrical charge generated. The dielectric properties of the materials were measured using impedance spectroscopy (Solartron 1260 and 1296 Dielectric Interface) with an AC voltage of 100 mV applied over a frequency range of 0.1 Hz to 1 MHz and used to calculate the unclamped (constant stress) permittivity.

3. Results and discussion

Comparing data obtained via the Archimedes method for relative density and apparent porosity indicates that the connectivity of all pellets was a mixture of 3-0 and 3-3 connectivity. This was determined by subtracting the sum of the apparent (open) porosity (3-3) and the relative density from 100% to give the closed porosity (3-0). For the porous ceramic manufactured with ≥15 wt.% PFA there was significantly more open porosity than isolated porosity, as shown in Fig. 1 as a plot of PFA against the fraction of open porosity compared to the total porosity. Relatively good control over the final porosity/relative density was achieved using the BURPS process, although the process had to be altered for samples with <12.5 wt.% PFA due to difficulties obtaining crack-free pellets. The grain size in dense and two porous samples, with 40% and 60% relative densities, was investigated using scanning electron microscopy (SEM) and no significant change was identified in the bulk ceramic, with grain width generally in the range of 10-30 μm. In the immediate vicinity of a pore the grain size was found to decrease in both dense and porous samples, where the pores are thought to act as pinning sites, inhibiting grain growth.
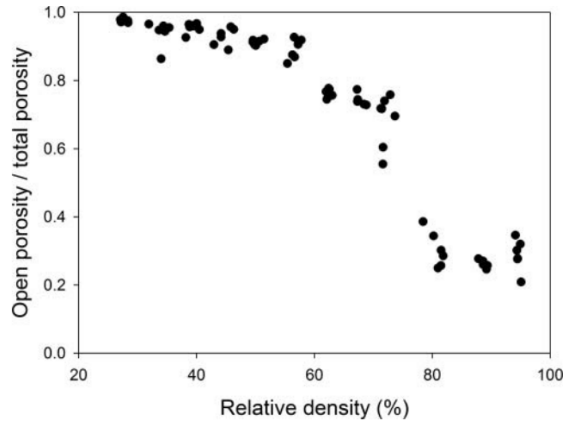
Figure 1: Fraction of open porosity in BaTiO$_3$ compared to the total porosity plotted against relative density. Data obtained via the Archimedes method. The high values of the open porosity/total porosity ratio at low relative density indicate that nearly all the porosity is open, i.e. pores are fully interconnected.
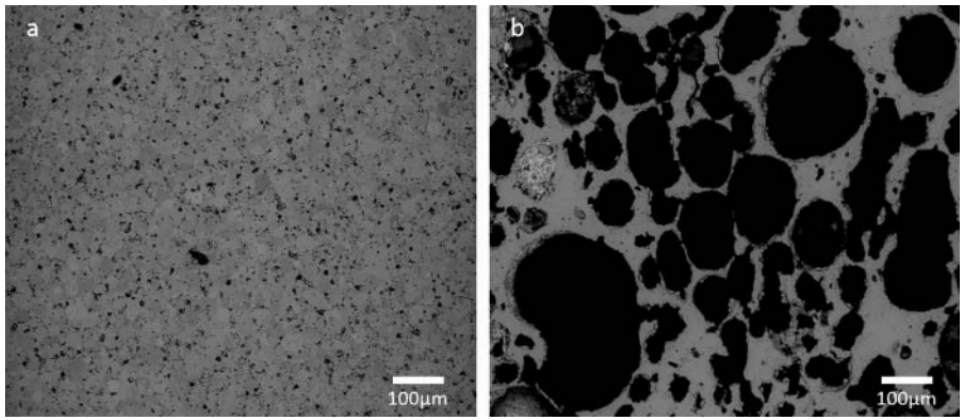
Figure 2: (a) Dense BaTiO$_3$ microstructure and (b) porous BaTiO$_3$ (~40% relative density) with spherical pores formed during burn off of the volatile additive, PEG.

Pores formed due to the burn off of the PFA were spherical in shape with diameters ranging between 100-400 μm. SEM images of samples with 95% and 40% relative density are shown in Fig. 2a and 2b, respectively.

The variation of d_{33} with porosity is shown in Fig. 3. As expected, the dense samples exhibited the highest piezoelectric strain coefficients, thought to be due to more complete poling of the samples. Reducing the relative density via the introduction of porosity is found to reduce the strain coefficient, although above ~40% the response remains relatively high at ~75% of the maximum d_{33} values achieved for dense BaTiO$_3$. This is a similar trend to that observed for porous PZT synthesised via the BURPS process [4, 6]. The large spread in data is attributed to difficulties in the poling procedure, which appears to be affected by ambient conditions, such as temperature and humidity, and controlling them in the experimental set up is not possible. The decrease in d_{33} in high porosity samples (<40% relative density) may be due to incomplete
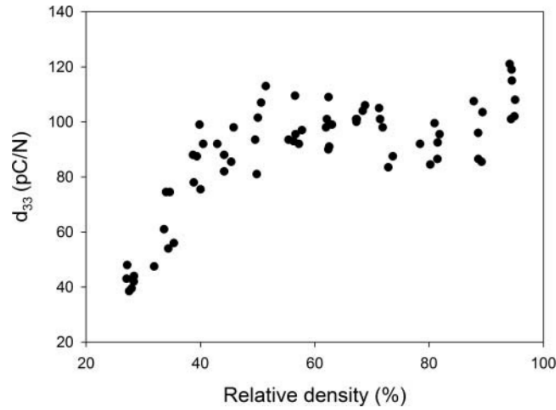
Figure 3: Variation of piezoelectric strain coefficient, d_{33}, with relative density. Values remain relatively high (>100pC/N) up to high porosity levels (~40% relative density).

poling of the BaTiO$_3$ phase caused by lower breakdown strength that occurs in highly porous dielectric ceramics and complex electric field distribution resulting from a mixture of low and high permittivity phases. Pores are also likely to increase stress concentrations that lead to depolarisation of the material [6] and also limit the grain size in their immediate vicinity, which is thought to inhibit domain motion [7], therefore reducing the achievable level of spontaneous polarisation. Slightly lower d_{33} values than might be expected were observed in samples with a relative density in the range of 75-90% theoretical. In order to produce crack-free samples in this range a small amount of binder was added to the BaTiO$_3$ powder prior to ball milling, which may have affected the microstructure or bulk structure in a way that supresses the piezoelectric response.

The permittivity of the porous ceramics was calculated from complex electrical impedance data measured across a range of frequencies and is reported here as the constant stress (unclamped) permittivity at 1 kHz as a function of relative density (Fig. 4). The permittivity was found to significantly decrease with the introduction of porosity, as the volume fraction of high permittivity BaTiO3 was reduced. This is in agreement with previous studies [4, 5, 6] and is one of the key reasons for investigating the effect of porosity on piezoelectric energy harvesters.

Fig. 5 shows the variation of piezoelectric energy harvesting FOM_{33}, calculated using Eqn. 2, against relative density. Low permittivities in high porosity samples, coupled with relatively high d_{33} values above 40% relative density, result in a broad peak in the FOM_{33} from 40-50% relative density. This is a similar phenomenon to that observed in porous PZT for hydrophone applications where $d_h.g_h$ reaches a maximum at a similar porosity [4]. Compared with dense BaTiO$_3$, a three-fold increase in the FOM_{33} is observed in these samples. At high porosities (<40% relative density), there is a fall in FOM_{33} despite very low permittivities measured in these samples; this is a result of the low d_{33} values of these highly porous materials.
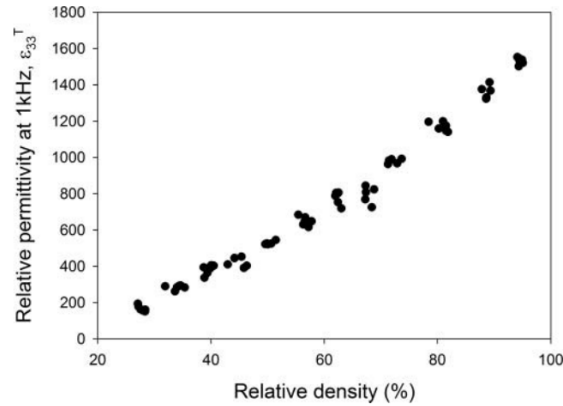
Figure 4: Variation in relative permittivity ($\varepsilon_{33}^{\sigma}$) with relative density. As porosity is increased (relative density decreased) permittivity decreases.
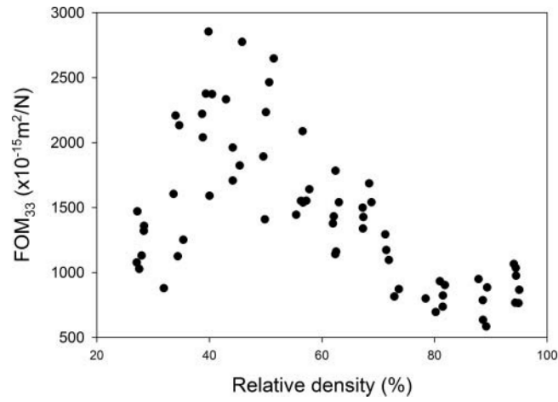
Figure 5: Energy harvesting figure of merit (FOM_{33}) calculated across full range of relative densities, using Eqn. 2. A broad peak is observed between 40 and 50% due to significant reductions in permittivity at this point but only relatively small reduction in d_{33}.

4. Conclusions

Porous BaTiO$_3$ has been synthesised using the BURPS process, with polyethylene glycol used as a volatile pore-forming species, and their potential for energy harvesting evaluated compared to conventional dense BaTiO$_3$. The relative density and open and closed porosity were characterised and microstructural analysis demonstrated that the porous composite structures changed from a 3-0 configuration (isolated pores) to a 3-3 configuration (interconnected pores) as the level of porosity was increased. The porous materials were characterised in terms of their piezoelectric and dielectric properties, which were then used to calculate a piezoelectric energy harvesting FOM_{33} for low frequency, off-resonance mechanical excitation. A maximum FOM_{33} of 2.85 pm^2/N was achieved at a relative density of ~40% (~60% porosity), a near three-fold increase compared with the dense samples. This significant improvement in the FOM_{33} was the result of a large reduction in permittivity at this porosity level along with a relatively small

reduction in d_{33}. The implication of this work is that for a given applied stress the energy generated within a material with an appropriate pore volume fraction can be significantly larger than its dense counterpart. Further investigation is required to determine the direct mode electromechanical coupling coefficient, k_{33}^2, of $BaTiO_3$ at different relative densities, which would show the effect of porosity on the efficiency of conversion from mechanical to electrical energy.

References

[1] C. R. Bowen, H. A. Kim, P. M. Weaver, S. Dunn, Piezoelectric and ferroelectric materials and structures for energy harvesting applications, Energy Environ. Sci. 7 (2013) 25–44.

[2] E. Mercadelli, A. Sanson, C. Galassi, Porous piezoelectric ceramics, in: E. Suaste-Gomez (Ed.), Piezoelectric Ceramics, InTech Open, 2010, Ch. 6, pp. 111–128.

[3] R. A. Islam, S. Priya, Realization of high-energy density polycrystalline piezoelectric ceramics, Appl. Phys. Lett. 88 (2006) 032903.

[4] C. R. Bowen, A. Perry, A. C. F. Lewis, H. Kara, Processing and properties of porous piezoelectric materials with high hydrostatic figures of merit, J. Eur. Ceram. Soc. 24 (2004) 541–545.

[5] R. E. Newnham, D. P. Skinner, L. E. Cross, Connectivity and piezoelectric-pyroelectric composites, Mater. Res. Bull. 13 (1978) 525–536.

[6] T. Zeng, X. Dong, S. Chen, H. Yang, Processing and piezoelectric properties of porous PZT ceramics, Ceram. Int. 33 (2007) 395–399.

[7] K. Okazaki, K. Nagata, Effects of grain size effects and porosity on electrical and optical properties of PLZT ceramics, J. Am. Ceram. Soc. 56 (1973) 82–86.

3.2　Summary

The experimental work into barium titanate with uniformly distributed porosity provides proof-of-concept to the idea that introducing porosity into ferroelectric ceramics can increase energy harvesting figures of merit, which is in agreement with the findings of the literature review. The key points of this chapter can be summarised as:

1. Porous barium titanate with fully interconnected ceramic and pore phases (i.e. 3-3 connectivity) was fabricated using the burned out polymer spheres (BURPS) process.

2. The introduction of porosity into barium titanate was found to increase the energy harvesting figure of merit from $\sim$1.0 pm^2/N for dense barium titanate to a maximum of 2.85 pm^2/N at 60 vol.% porosity.

This research provides a baseline set of data for the work presented in later chapters.

Chapter 4

Modelling electric field distributions in ferroelectric composites for electrical energy storage

This chapter consists of two papers regarding the use of ferroelectric composites for energy storage applications, with two commonly used approaches to produce materials with enhanced permittivity investigated here. Each paper has its own introduction and a combined summary of the work presented in the two papers is included at the end of the chapter.

4.1   Context, part 1

The first paper in this chapter, *Ultra-high discharged energy density capacitor using high aspect ratio $Na_{0.5}Bi_{0.5}TiO_3$ nanofibres*, was written in collaboration with a group from Central South University, Changsha, China and investigates the effect of introducing a ferroelectric ceramic with high permittivity ($\varepsilon_r = 377$) relative to the ferroelectric polymer matrix it is contained within ($\varepsilon_r = 10$). Section 3.3 of the paper details the modelling study that was carried out to investigate the effect of fill fraction, fibre aspect ratio and orientation, and the presence of an interphase to create a permittivity gradient between matrix and the inclusion, on the effective permittivity and dielectric breakdown strength of these materials. This modelling study was the first step to understanding how electric fields distribute within composite materials where the phases have contrasting permittivities, which, as will be discussed in later chapters, is also critical to understanding the properties of porous ferroelectric ceramics.
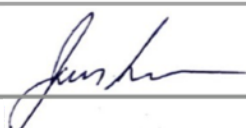
As detailed in Chapter 1, Fig. 1-1, another publication is closely related to the work presented in this chapter: D. Zhang, X. Zhou, J. I. Roscow et al. *Significantly enhanced energy storage density by modulating the aspect ratio of $BaTiO_3$ nanofibres*, Sci. Rep. **7** (2017) presents

a similar modelling study on the effect of BaTiO$_3$ fillers in a P(VDF-HFP) matrix. The study in this paper also investigates the effect of the separation distance between neighbouring high permittivity inclusions on the local electric field concentrations.

Supplementary information published alongside this paper can be found in Appendix A and the Ansys APDL script used for the single inclusion models is in Appendix B.

Access the data from the following paper here: https://doi.org/10.15125/BATH-00453.

Statement of Authorship

This declaration concerns the article entitled:									
Ultra-high discharged energy density capacitor using high aspect ratio $Na_{0.5}Bi_{0.5}TiO_3$ nanofibres									

Publication status (tick one)

draft manuscript		Submitted		In review		Accepted		Published	✓
Publication details (reference)		Luo, Roscow et al., Journal of Materials Chemistry A **5** (2017) 7091-7102							

Candidate's contribution to the paper (detailed, and also given as a percentage).	The candidate contributed to/ considerably contributed to/predominantly executed the Formulation of ideas: H. Luo & D. Zhang came up with the idea for the paper and experimental work, approach to modelling studies formulated by the candidate Design of methodology: Experimental methodology all designed and implemented by H. Luo and D. Zhang at CSU (0%). Modelling methodology designed solely by the candidate (100%) Experimental work: H. Luo et al. for experimental work, candidate for modelling studies (approx. 70/30 in terms of published work) Presentation of data in journal format: H. Luo et al. for experimental work, candidate for modelling studies (approx. 70/30 in terms of published work)
Statement from Candidate	This paper reports on original research I conducted during the period of my Higher Degree by Research candidature.
Signed	*[signature]* **Date** 30/11/17

PAPER 3: Ultra-high discharged energy density capacitor using high aspect ratio $Na_{0.5}Bi_{0.5}TiO_3$ nanofibres

H. Luo[a,b], J. I. Roscow[c], X. Zhou[a], S. Chen[d], X. Han[d], K. Zhou[a], D. Zhang[a], & C.R. Bowen[c]

[a]*State Key Laboratory of Powder Metallurgy, Central South University, Changsha, Hunan, China*
[b]*College of Chemistry and Chemical Engineering, Central South University, Changsha, Hunan, China*
[c]*Department of Mechanical Engineering, University of Bath, Bath, UK*
[d]*Key Laboratory of Polymeric Materials and Application Technology of Hunan Province, College of Chemistry, Xiangtan University, Xiangtan, Hunan, China*

Abstract

Ceramic/polymer nanocomposites are attractive for energy storage applications due to their ability to exploit the high permittivity of ceramic fillers and high breakdown strength of the polymer matrix. One challenge for the development of high performance nanocomposites based on ceramic particulates or fibres in a polymer matrix is that they often require a high volume fraction (>50%) to achieve a high permittivity, which is often at the expense of a reduction in dielectric strength and mechanical flexibility. In this paper we demonstrate by both experiment and finite element simulation that high aspect ratio nanofibre fillers offer an effective approach to achieve high energy density and dielectric strength. Lead-free ferroelectric $Na_{0.5}Bi_{0.5}TiO_3$ (BNT) nanofibres with a high aspect ratio (>200) are synthesized by a hydrothermal method and dispersed in a poly(vinylidene difluoride-co-hexafluoropropylene) (P(VDF-HFP)) matrix. The increased fraction of β-phase and the alignment of BNT nanofibres perpendicular to the direction of the applied electric field lead to an enhanced dielectric strength, compared to spherical BNT/P(VDF-HFP) nanoparticles and pure P(VDF-HFP), and experimental measurements are compared with numerical simulations. The results demonstrate that the nanofibre nanocomposites exhibited an ultra-high discharged energy density (12.7 J/cm^3) and provide an innovative approach to produce high-energy storage density materials.

1. Introduction

High power capacitors are widely applied in electronic devices with pulsed power such as radar, electric vehicles, mobile electronics, power electronics, lasers, and rail guns [1, 2, 3, 4, 5, 6, 7, 8]. However, these capacitors usually suffer from low energy density, hence they can only be applied in high cost and bulky electronic devices [9, 10]. The maximum discharged energy density (U) of linear dielectric materials is defined as:

$$U = \frac{1}{2}\varepsilon_0\varepsilon_r E_b^2 \tag{1}$$

where ε_0 and ε_r are the permittivity of vacuum and the material, respectively, and E_b is the breakdown electric field of the material. It is clear that the energy density is determined by

the E_b and ε_r of the dielectric material, and the E_b is a critical factor since U has a quadratic dependence on the E_b [5, 11, 12, 13].

In this regard, ceramic/polymer nanocomposites have been investigated since they have the potential to simultaneously optimize the two factors that determine the energy density by exploiting the high permittivity of ceramic fillers and the high breakdown strength of the polymer matrix [14, 15, 16]. It has been shown that the microstructural morphology and concentration of the ceramic fillers have a significant influence on the energy storage density of dielectric nanocomposites [17, 18, 19, 20]. In our previous work, 0-3 nanocomposites (0-dimensionally spherical nanoparticles dispersed in a 3-dimensionally connected polymer matrix) containing $BaTiO_3$ and $Pb(Mg_{1/3}Nb_{2/3})O_3PbTiO_3$ nanoparticles (NPs) dispersed in a poly(vinylidene difluoride-co-hexafluoropropylene), P(VDF-HFP), polymer matrix exhibited a significantly higher permittivity than pure P(VDF-HFP); however, the increased permittivity of the nanocomposite was at the expense of a decreased breakdown strength compared to the pure polymer matrix phase [9, 18]. The high volume fraction (>50 vol.%) of ceramic nanoparticle fillers that is needed to significantly increase the permittivity can also lead to the formation of defects, such as voids and cracks, in the 0-3 nanocomposite, as well as reduce the mechanical flexibility of the composites.

The complex balance between permittivity and breakdown strength is attributed to the presence of high local electric field concentrations, which are caused by the large contrast in permittivity between the ceramic and polymer matrix phase [21]. Recently, it was demonstrated that the use of high aspect ratio one-dimensional nanofibre fillers could be an effective approach to overcome the challenge of increasing the permittivity without leading to a corresponding decrease of breakdown strength and thereby improve the energy density of the nanocomposite [9, 17, 20, 22, 23]. The improvement is thought to be due to the increased permittivity of the high aspect ratio fillers, as demonstrated by theoretical models such as the Maxwell-Garnett model [17, 24]. The nature of the distribution of nanofibres in the polymer matrix and their orientation in perpendicular, parallel and random directions relative to the direction of the electric field significantly affects the electric field distribution in the nanocomposite. However, the influence of the morphology of the ceramic nanofibres or nanoparticles in the polymer matrix on the electric field distribution and the effective capacitance of the composites remains unclear. Most ceramic nanofibres/polymer composites in previous reports [11, 12] exhibited an increase in discharged energy density with an increase in the fraction of nanofibres; however the manufacture of high aspect ratio nanofibres continues to be a challenge [17]. Thus, it is of interest that dielectric nanocomposites possessing an ultra-high discharged energy density are formed using a relatively small fraction of nanofibres.

$Na_{0.5}Bi_{0.5}TiO_3$ (BNT) is considered to be an excellent lead-free ferroelectric ceramic with a d_{33} piezoelectric coefficient of approximately 80 pC/N and a high relative permittivity of approximately 500 at 1 kHz, which has attracted significant interest because of its potential to replace lead based piezoelectric materials [25, 26]. However, research on BNT/polymer composites, especially using the BNT nanofibres to create new nanocomposites for energy storage applications, remains limited.

In this paper, high aspect ratio BNT nanofibres and BNT nanoparticles are synthesized by a

simple hydrothermal method by controlling the temperature and NaOH concentration of the reaction. BNT nanofibres and nanoparticles will be examined as a filler introduced into a (P(VDF-HFP)) polymer matrix. To investigate the influence of BNT filler morphology on the permittivity and breakdown strength of the nanocomposites, the localised electric field distribution and capacitance of P(VDF-HFP) nanocomposites with BNT nanofibres and BNT nanoparticles for energy storage applications have also been simulated using a finite element approach (Ansys).

To enhance the adhesion between the fillers and matrix, the ceramic fillers were initially modified using dopamine, and FT-IR results indicate that the dopamine has led to modification of the BNT by condensation polymerization; the content of dopamine is 2.9 wt.%, which is related to the amount of BNT NFs, as shown in Fig. A1 (ESI) [18, 27]. The dielectric performance, discharged energy storage density and thermal management of the samples were investigated. This paper will show that the use of high-aspect-ratio BNT nanofibres led to an increased permittivity and high thermal conductivity. Of particular interest is that the discharged energy density of the nanocomposites increased significantly by introducing a low content of BNT nanofibres (2.37 vol.%), and the maximum energy density increased to 12.7 J/cm^3. This work therefore provides a practical route to achieve ultra-high energy storage density with a low level of BNT nanofibre loading.

2. Experimental methods

2.1. Materials

Chemicals were obtained from the following sources and used without further purification: dopamine hydrochloride (Alfa, 99%), P(VDF-HFP) (Aldrich, pellets with less than 15% of HFP), bismuth nitrate pentahydrate (Bi(NO$_3$)$_3$·5H$_2$O), sodium nitrate (NaNO$_3$), tetrabutyl titanate (Ti(OC$_4$H$_9$)$_4$), acetic acid (CH$_3$COOH), ethanol (CH$_3$CH$_2$OH) and N,N-dimethylformamide (DMF) were all purchased from Sinopharm, China; other reagents were all analytically pure.

2.2. Synthesis of BNT nanofibres and BNT particles

BNT nanofibres and BNT particles were obtained by controlling the hydrothermal reaction temperature and NaOH concentration, as reported in our previous study [28]. Specifically, 0.005 mol of Bi(NO$_3$)$_3$·5H$_2$O, 0.01 mol of NaNO$_3$ and 0.005 mol of Ti(OC$_4$H$_9$)$_4$ were dissolved in 7.5 mL of CH$_3$COOH, 2.5 mL of distilled water, and 10 mL of CH$_3$CH$_2$OH. The Bi(NO$_3$)$_3$·5H$_2$O and NaNO$_3$ solutions were then mixed with Ti(OC$_4$H$_9$)$_4$ solution, which subsequently formed a suspension with the addition of 10 M of NaOH solution and stirred for 1 h. The BNT nanofibres and particles were synthesized at 150°C for 48 h with a NaOH concentration of 10 M and 170°C for 48 h with a NaOH concentration of 10 M, respectively. The products were washed with distilled water several times and dried at 80°C in an oven.

2.3. Surface functionalization of BNT fillers using dopamine

Dopamine modified BNT was prepared using a method reported previously [18]. In a typical reaction, 2 g of BNT powder was dispersed in 20 mL of a mixture of 95:5 (v/v) ethanol/H$_2$O using an ultrasonic processor to increase the hydroxyl groups on the surface of the BNT. The
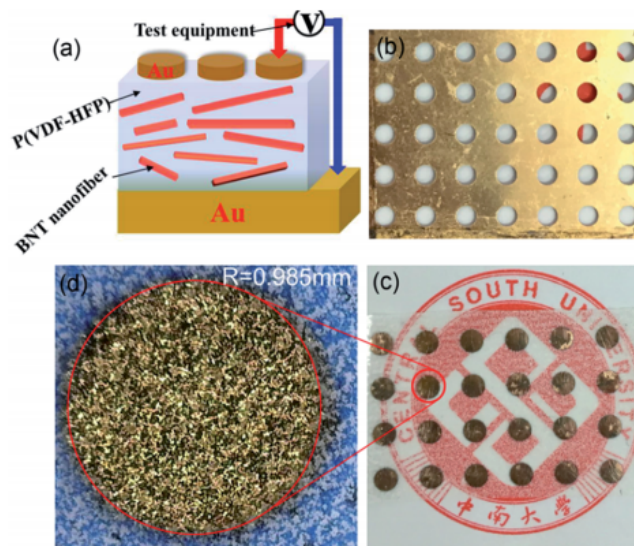
Figure 1: (a) Schematic illustration of BNT NFs/P(VDF-HFP) nanocomposites, (b) metal mask, (c) and (d) optical microscopy images of a P(VDF-HFP) film with 2 mm diameter gold electrodes, the gold regions correspond to a single high magnification electrode.

hydroxylated BNT was recovered by centrifugation and dried under vacuum at 60°C for 12 h, and was dispersed in 0.01 M dopamine hydrochloride aqueous solution, while stirring for 10 h at 60°C. The functionalized BNT was subsequently separated by centrifugation and rinsed repeatedly with excess deionized water, and finally dried overnight under vacuum at 60°C.

2.4. Preparation of BNT/P(VDF-HFP) nanocomposites

Surface functionalized BNT fillers were dispersed in a 70:30 (v/v) acetone/DMF hybrid solvent by sonication and stirring and then mixed with P(VDF-HFP) particles for further stirring and sonication for 48 h. The resulting suspension was then cast onto a clean glass surface, and dried at 80°C for 12 h under vacuum. The thickness of the final composite film was approximately 1020 μm. Gold electrodes were sputtered on both sides of the film using a mask with 2 mm diameter eyelets. Fig. 1 shows an illustration of the preparation approach of the flexible BNT nanofibre/P(VDF-HFP). The functionalized BNT NFs were dispersed in the P(VDF-HFP) nanocomposite film and gold electrodes were sputtered on both sides of the film to characterize the electrical properties for storage applications.

2.5. Characterisation

The crystal structure of the nanocomposites was examined in θ-2θ mode by X-ray diffraction (XRD, Rigaku D-Max/2550VB) utilizing Cu K$_\alpha$ radiation (λ = 1.5418 Å). Transmission electron microscopy (TEM) images were obtained from a JEOL JEM-2100 instrument operating at an accelerating voltage at 200 kV. The samples were prepared by dropping the sample solutions onto carbon coated copper grids and air-drying before measurement. Fourier-transform infrared (FT-IR) spectroscopy was performed with a Nicolet 6700 instrument over the range of

51

4000-450 cm^{-1} to determine the functionalization of the samples. Thermogravimetric analysis (TGA, NETZSCH STA 449) was conducted at a heating rate of 10°C/ min in a nitrogen flow (20 mL/min). Characterization of the morphology of the composites was performed by scanning electron microscopy (SEM, JSM-6390). Frequency-dependent permittivity and dielectric loss were measured using an Agilent 4294A LCR meter over a frequency range of 1 kHz to 10 MHz. Leakage current density, endurance testing, electric displacement-electric field (D-E) loops and leakage current were measured using a Precision Premier II ferroelectric polarization tester (Radiant, Inc.) and Delta 9023 furnace. The thermal diffusivity and conductivity of the nanocomposites were measured by a laser flash technique using a thermal constant analyzer (LFA427, Netzsch, Selb, Germany).

3. Results and discussion

3.1. Characterisation of BNT nanofibres and particles

Scanning electron microscopy (SEM) images of the BNT nanofibres and nanoparticles that were hydrothermally prepared are shown in Fig. 2a and b, respectively. The majority of the nanofibres exhibit a high aspect ratio (>200) with an average diameter of approximately 67 nm and average length of 17.78 μm; this was measured from 50 randomly selected nanofibres in an SEM image using ImageJ (Fig. 2d and e). The average diameter of the nanoparticles was measured using a laser particle size analyser and was found to be approximately 800 nm. The XRD pattern of BNT nanofibres and BNT nanoparticles is shown in Fig. 2c, where strong peaks at 2θ of 22, 31, 39, 45, 51 and 56° can be seen in the XRD pattern, which are attributed to the (100), (110), (111), (200), (210) and (211) characteristic peaks respectively of BNT with a pure monoclinic crystalline phase. All of the peaks matched well with the perovskite peaks found in the powder diffraction file database (JCPDS, 46-0001).

Fig. 3a shows a TEM micrograph of a typical single BNT nanofibre synthesized at 170°C for 48 h with NaOH concentration of 10 M showing a smooth surface with a diameter less than 100 nm. Fig. 3b shows the corresponding high resolution TEM (HRTEM) image. A fast Fourier transform (FFT) pattern of the BNT nanofibre is shown in the inset of Fig. 3b. The clear lattice fringes shown in Fig. 3b of 0.193 nm and 0.224 nm correspond to the (220) and (012) planes and illustrate that the as-synthesized nanofibres were single-crystalline. The parallel lattice spacing was approximately that of monoclinic BNT, which revealed that nanofibre growth was in the [110] direction. The FFT pattern shown in the inset of Fig. 3b further confirmed the monocrystalline nature of the nanofibre and the formation of monoclinic BNT.

3.2. Characterisation of the nanocomposites

It has been demonstrated that the presence of the polar β-phase in ferroelectric polymers such as P(VDF-HFP) is beneficial for increasing the permittivity and the piezoelectric/ferroelectric properties of the composite due to the large dipolar moment of this particular polar phase [29, 30, 31]. The introduction of ceramic fillers into the P(VDF-HFP) matrix led to the formation of a higher fraction of the b-phase by modification of the α-phase [32]. Fig. 4a shows the XRD
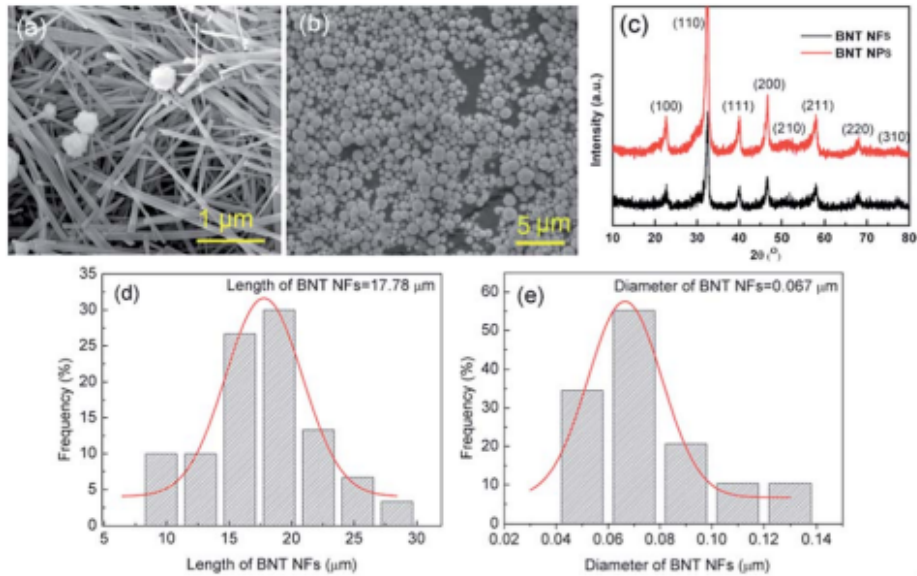
Figure 2: (a) and (b) SEM images, (c) XRD pattern of BNT nanofibres (NFs) and BNT nanoparticles (NPs), BNT NFs size distribution: (d) length of BNT NFs, (e) diameter of BNT NFs.

pattern of pure P(VDF-HFP), BNT NPs/P(VDF-HFP) and BNT NFs/P(VDF-HFP) nanocomposites. It can be seen that the pure (unfilled) P(VDF-HFP) exhibited peaks at $2\theta = 18.38°$, $19.96°$ and $26.6°$, which correspond to the α-phase [29, 31] with no β-phase detected. For the BNT nanoparticle/P(VDF-HFP) composite system, the peak of the α-phase at $2\theta = 19.56°$ is weakened, and the α-phase peaks at $2\theta = 18.38°$ and $26.6°$ both disappear after the introduction of the BNT nanoparticles, which is thought to be due to the addition of the crystalline BNT ceramic changing the crystallinity of the P(VDF-HFP) polymer.

It is notable that the peak at $2\theta = 20.74°$ that corresponds to the β-phase is observed in the XRD pattern of the BNT nanofibre/P(VDF-HFP) nanocomposite in Fig. 4a. Therefore, the introduction of one-dimensional ceramic fillers to P(VDF-HFP) appears to facilitate the formation of the polar β-phase, which can also be observed from the FT-IR results of the P(VDF-HFP) nanocomposites in Fig. A3a. This is in contrast to zero-dimensional nanoparticle fillers, and indicates that one-dimensional high aspect ratio ceramic fillers may be more effective in increasing the permittivity of nanocomposites due to the formation of the polar β-phase. In addition, one-dimensional ceramic fillers with a high aspect ratio have a larger dipole moment and lower surface energy compared to zero-dimensional particulates, which favours polarization and dispersion [16, 33].

To further investigate the influence of the introduction of the ceramic nanofibres on the crystallization of the polymer matrix, differential scanning calorimetry (DSC) curves of the BNT nanofibre/P(VDF-HFP) composites during the second heating circles are shown in Fig. 4b. The melting point (T_m) and crystallinity (χ_c) of the samples were obtained from DSC results, and the corresponding results are summarized in Table 1. It can be seen that the T_m is initially slightly in-
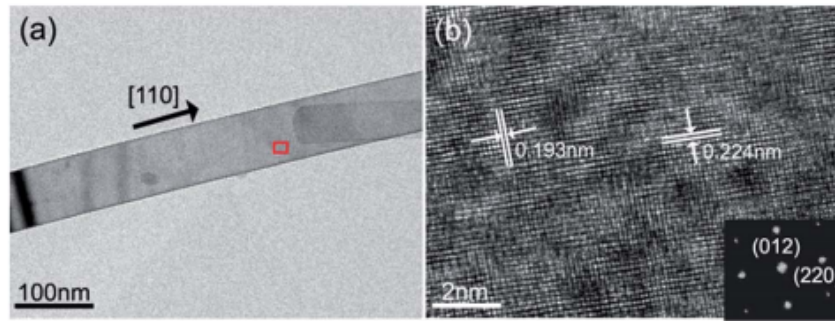
Figure 3: (a) TEM micrograph of a typical single BNT nanofibre and (b) HRTEM image of the BNT nanofibre. The inset image is the selected area electron diffraction (SAED) pattern of the BNT nanofibre.
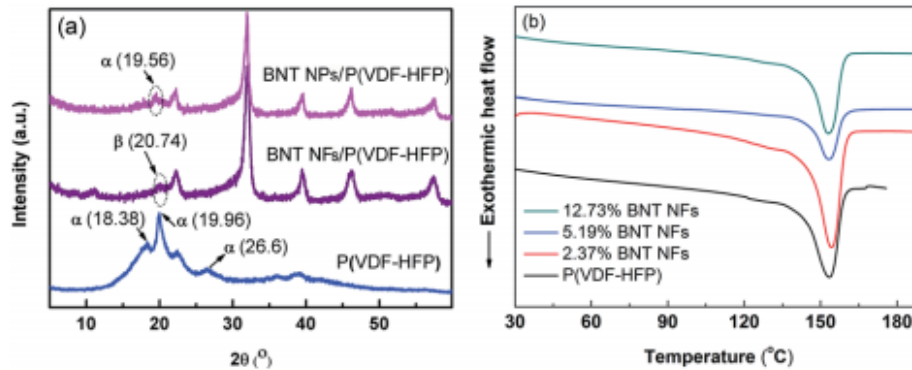
Figure 4: (a) XRD pattern of pure P(VDF-HFP), BNT nanoparticle/P(VDFHFP) and BNT nanofibre/P(VDF-HFP) nanocomposite, (b) DSC curves of the BNT NFs/P(VDF-HFP) samples during the second heating at the rate of 10°C/min under a N_2 atmosphere.

creased then decreased and the χ_c is decreased from 28.7% to 21.6% as the content of BNT NFs increased. The results can be explained by the following reasons. Firstly, the BNT nanofibres act as a new nucleation center, which can decrease the nucleation energy and increase the degree of crystallization of the P(VDF-HFP) matrix on the surface of the BNT nanofibres. Secondly, the introduction of BNT nanofibres decreases the degree of order of the P(VDF-HFP) matrix. Thus, the crystallinity and melting point of the nanocomposites increase with small amounts of BNT nanofibres, however they decrease as the filler loading is increased.

Figure 5a-c show SEM images of the surface morphology of the BNT nanofibre/P(VDF-HFP) composite, with increasing loading levels of 2.37 vol.%, 5.19 vol.% and 12.73 vol.% respectively. Fig. 5d shows a cross-section of the nanocomposite with 5.19 vol.% of BNT nanoparticles. The high aspect ratio BNT nano- fibres are observed in Fig. 5a-c, which are homogeneously dispersed and embedded in the polymer matrix. The formation of agglomerates, voids and cracks is not observed even when the BNT nanofibre loading is increased to 12.73 vol.%, as is shown in Fig. 5c. A similar view is shown in Fig. 5d, where the BNT nanoparticles are uniformly dispersed throughout the composite and tightly adhered to the surrounding

Table 1: The characterization result of P(VDF-HFP) with varied BNT NF contents from DSC curves[a]

Sample	T_m (K)	ΔH_m (J g^{-1})	χ_c (%)
P(VDF-HFP)	426.6	29.8	28.7
2.37% BNT/P(VDF-HFP)	427.7	31.2	30.0
5.19% BNT/P(VDF-HFP)	427.0	29.2	28.1
12.73% BNT/P(VDF-HFP)	426.5	22.5	21.6

[a]The T_m is determined by DSC during the second heating process. The crystallinity (χ_c) is calculated from the integration of the curves using the formula $\chi_c = \Delta H_m / \Delta H_m^*$ x 100%, where ΔH_{m*} (approximately 104 J g^{-1}) is the fusion enthalpy of PVDF with 100% crystallinity [34].
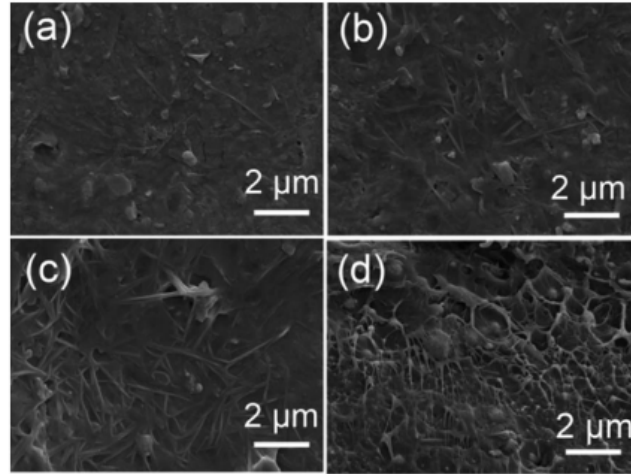
Figure 5: (a) SEM images of top surfaces of BNT nanofibre/P(VDF-HFP) nanocomposite films with various BNT loading levels, (a) 2.37 vol.%, (b) 5.19 vol.%, (c) 12.73 vol.%. (d) SEM cross-section of the nanocomposite with 5.19 vol.% BNT nanoparticles.

matrix. Since all the fillers are modified using dopamine (Fig. A1a) before being incorporated into P(VDF-HFP), the hydroxyl groups in dopamine form strong dipole-dipole interactions with the –F atoms from P(VDF-HFP). In addition, due to the strong electronegative nature of the –F atoms, hydrogen bonding (–F$\cdots$OH–) can be easily formed [29]. Therefore, the BNT nanofibres exhibit excellent dispersion and compatibility in the polymer matrix.

To assess the dielectric properties of the nanocomposites formed using BNT nanofibres and BNT nanoparticles, the frequency dependent permittivity, dielectric loss and electric conductivity of the nanocomposites with various loading levels of BNT nanofibres and BNT nanoparticles are shown over a frequency range of 500 Hz to 10 MHz in Fig. 6. It can be seen that the permittivity of the nanocomposite increased with increasing loading level of either BNT nanofibres or nanoparticles, as shown in Fig. 6a and c, respectively. It is also observed that the permittivity of the nanocomposite with BNT nanofibres is higher than the nanocomposite with BNT nanoparticles at the same volume fraction. This phenomenon is clearly observed in Fig. 6f; for example, at a filler loading level of 5.19 vol.% the permittivity of the BNT nanofibre composite is 15% higher than that of the BNT nanoparticle composite. In addition to the increased fraction
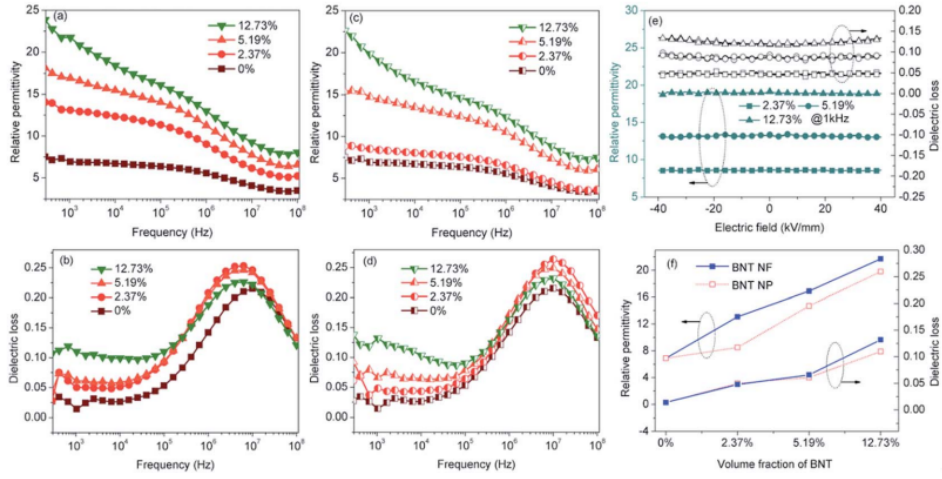
Figure 6: Frequency dependence of the (a) relative permittivity, (b) dielectric loss of the P(VDF-HFP) nanocomposites with BNT nanofibres; (c) relative permittivity and (d) dielectric loss of the nanocomposites with BNT nanoparticles at room temperature. Electric field dependence of the (e) relative permittivity and dielectric loss of the nanocomposites with BNT nanofibres; (f) comparison of the permittivities and dielectric loss at 1 kHz between the nanocomposites with BNT nanofibres and BNT nanoparticles as a function of BNT loading.

of the β-phase (Fig. 4a), the increased permittivity of the nanocomposites also arises from the Maxwell-Wagner-Sillars (MWS) interfacial effect, where the phase dependent permittivity ($\kappa(r)$) is defined as given below [11]:

$$\kappa(r) = \kappa^{\alpha}\alpha(r) + \kappa^{\beta}\beta(r) + \kappa^{\gamma}\gamma(r) + \kappa^{\eta}\eta(r) \tag{2}$$

where α, β, γ and η are the BNT nanofibre, BNT nanoparticles, P(VDF-HFP) matrix phases and the interfacial phase. The BNT nanoparticles have an average diameter of 869 nm, as shown in Fig. 2, and are therefore significantly larger than the BNT nanofibres (an average diameter of less than 100 nm), so that the BNT nanofibres have more interface area and interface polarization than the BNT nanoparticles for the same filler volume fraction. In addition, the permittivity of the nanocomposites gradually decreased with increasing frequency, and this trend is more obvious as the filler loading level increases; for example, the permittivity of the nanocomposite with 12.73 vol.% BNT nanofibres is 21.7 at 1 kHz and 13.0 at 1 MHz (Fig. 6a). A decrease in permittivity with increasing frequency has been observed to result from the existence of electrical conductivity in the material, which has been simulated using resistor-capacitor networks [35]. The properties are relatively independent of the magnitude of the applied electrical field, see Fig. 6e. The nanocomposites also exhibited improved thermal conductivity (Fig. A2) and increased tensile strength (Fig. A3b) compared to the pure matrix phase.

Fig. 7a shows the frequency dependence of electrical conductivity of the BNT NF nanocomposites with various filler loadings. It can be seen that the electrical conductivity increases with increasing frequency and filler loading; this indicates that the nanocomposites behave in a capacitative manner and all exhibit a relatively low electrical conductivity that is less than 6.8×10^{-7} S/m. The temperature dependence of the electric conductivity and permittivity of nanocompos-
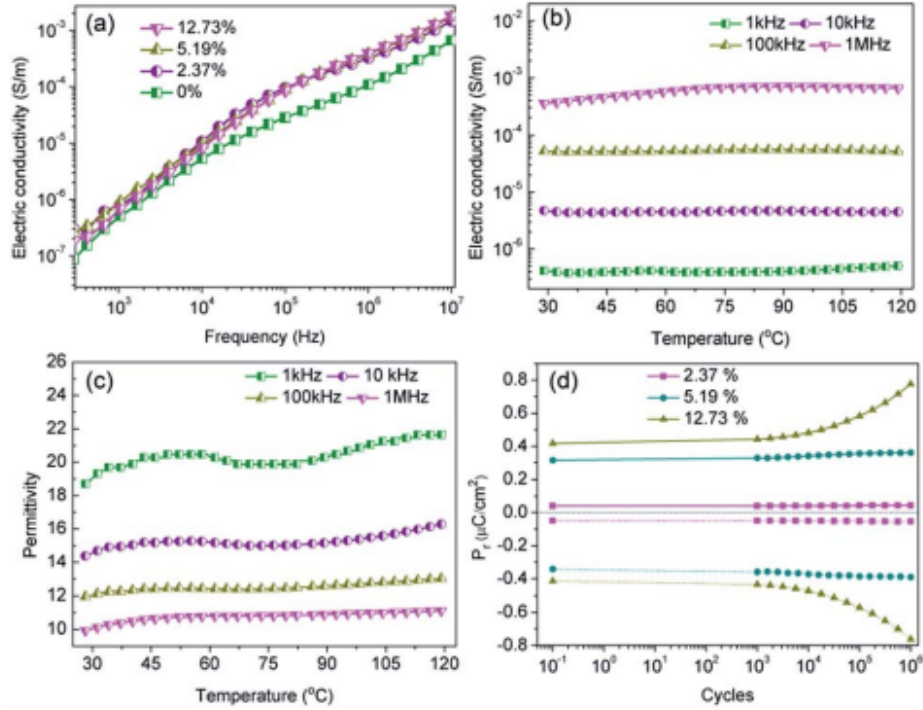
Figure 7: (a) Frequency dependence of the electric conductivity; temperature dependence of (b) electric conductivity, (c) relative permittivity of the nanocomposites with 12.73 vol.% BNT nanofibre at various frequencies; (d) endurance test of the nanocomposites with various BNT nanofibres with the electric field cycling and pulse field amplitude of 40 kV/mm.

ites with 12.73 vol.% BNT nanofibres at various frequencies is shown in Fig. 7b and c, respectively. The electric conductivity and permittivity of the nanocomposite were stable with a change in temperature, e.g. the electric conductivity was 5.3 x 10^{-5} S/m at 100 kHz at room temperature and 5.2 x 10^{-5} S/m when the temperature was increased to 120°C. The permittivity showed a similar phenomenon, which was 18.7 and 21.8 at room temperature and 120°C at 1 kHz respectively. These results demonstrate the excellent temperature stability of BNT NFs/P(VDF-HFP) composites in terms of electric conductivity and permittivity.

A high fatigue endurance is necessary for long-term stability during the capacitor charge-discharge cycling process [36, 37]. Thus, the residual polarization (P_r) of P(VDF-HFP) nanocomposites with various BNT NF loading levels was investigated as a function of the charge-discharge cycles up to 10^6 cycles with pulse heights of 40 kV/mm and pulse frequency fixed at 1 kHz. It can be seen in Fig. 7d that the P_r of the nanocomposites with 2.37 vol.% BNT nanofibres increased by only 6.1% after 106 switching cycles. However, the P_r was increased by 85.7% when the BNT nanofibre content was increased to 12.73 vol.% under the same cycling conditions. These results indicate that the P(VDF-HFP) nanocomposites with a low BNT nanofibre content possess superior cycling stability compared with the nanocomposites with a high BNT NF content, which are likely to exhibit a relatively high leakage current density due to the increased oxygen

vacancies in ABO_3-type perovskite structures [38].

The characteristic leakage current density-electric field curves with various BNT nanofibre contents, temperature and electric field were investigated and are shown in Fig. 8. The nanocomposite with a low BNT nanofibre content (2.37 vol.%) was an excellent insulating material for practical applications due to the low leakage current density of 1.47×10^{-7} A/cm^2 under 40 kV/mm at room temperature (Fig. 8a), which increased by more than two orders of magnitude (2.83×10^{-5} A/cm^2) when the BNT nanofibre content was increased to 12.73 vol.% (Fig. 8c). These results were consistent with the fatigue endurance test shown in Fig. 7d. However, the leakage current showed an obvious temperature diffusion phenomenon, especially when the filler content was low, e.g. the leakage current density of the nanocomposite with 2.37 vol.% BNT nanofibres was 1.47×10^{-7} A/cm^2, which was continuously increased to 3.20×10^{-6} A/cm^2 as the temperature increased from room temperature to 120°C under 40 kV/mm (Fig. 8a). These results may originate from the relatively low oxygen vacancy concentration and rapid free electron migration with temperature [36, 38, 39]. The leakage current density of the three samples showed an increase with an increase of the applied electric field (Fig. 8a-c). In the lower field region (<5 kV/mm), the current density rapidly increased with the applied electric field, whereas the current density showed a lower dependency on the field at higher applied fields. In addition, the nanocomposites exhibited an increased leakage current density as the loading level of the BNT nanofibres increased; for example, the leakage current densities of the nanocomposites with increasing nanofibre contents are 3.94×10^{-7} A/cm^2 (2.37 vol.%), 6.81×10^{-6} A/cm^2 (5.19 vol.%), 4.28×10^{-5} A/cm^2 (12.73 vol.%) at 40°C under 40 kV/mm. This is attributed to the high leakage current density of BNT and the defects and space charge introduced by the BNT nanofibre inclusions [40].

According to Eqn. 1 the breakdown strength is the key parameter to achieve a high discharge energy density for the composite. The breakdown strength of the BNT nanofibre/ P(VDF-HFP) composites with various volume fractions of fillers is shown in Fig. 9, which is analyzed with a two-parameter Weibull distribution function (Fig. 9a), using the equation:

$$P(E) = 1 - exp[-(E/E_0)^\beta] \tag{3}$$

The characteristic breakdown strength (E_0) is obtained when the cumulative probability of electric failure ($P(E)$) equalled 63.2% and β is the shape parameter, as shown in Table A1 [41]. As shown in Fig. 9a, the characteristic breakdown strength is determined from a fit of Eqn. 3 to at least eight individual breakdown measurements. As can be seen from Fig. 9a and b, the sample with 2.37 vol.% BNT nanofibres exhibited the highest breakdown strength of 458 kV/mm, which is higher than that of the pure (unfilled) P(VDF-HFP) polymer (398 kV/mm), a result that has also been reported elsewhere [34]. The breakdown strength decreases to 302 kV/mm when the filler loading is increased to 12.73 vol.%. As shown by Liu et al. [13], a low concentration of nanofibres improves the breakdown strength due to a number of reasons. Firstly, the homogeneous dispersion and strong adhesion of the high aspect ratio nanofibres after surface modification in the nanocomposite can reduce charge transfer and prevent the polymer chain from moving freely [11]. Secondly, the high aspect ratio nanofibres orientated parallel to the film surface direction

58
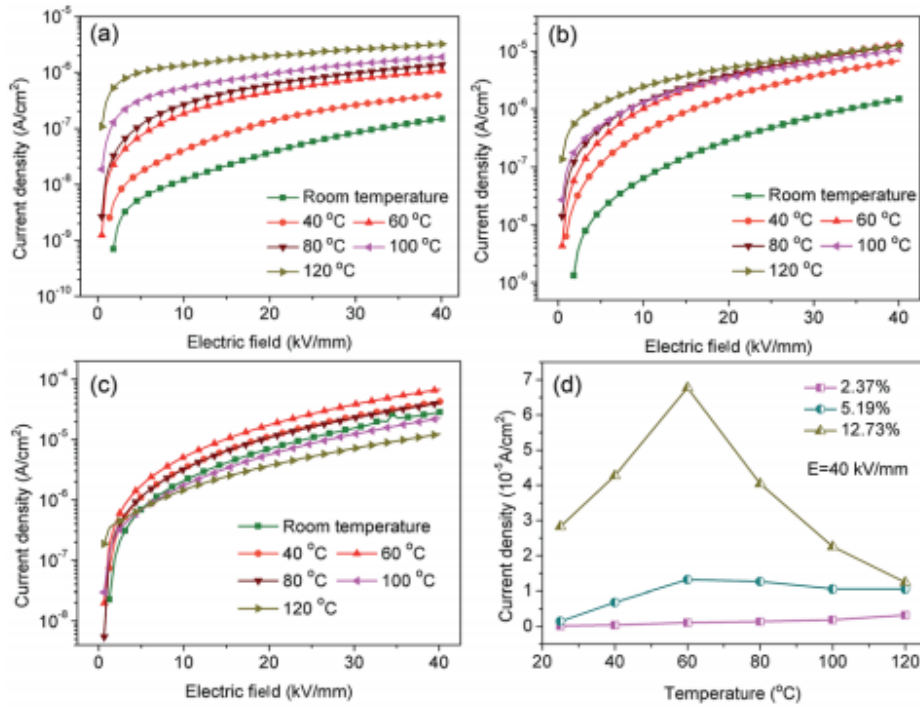
Figure 8: Leakage current density of the nanocomposites with (a) 2.37, (b) 5.19 and (c) 12.73 vol.% BNT nanofibres under different temperatures as a function of electric field; (d) current densities of the nanocomposites with various BNT nanofibre loading levels under different temperatures at $40\,\text{kV}\,\text{mm}^{-1}$ electric field.

during the solution casting process can endure a higher electric field vertical to the film surface direction (see Fig. A4) [5, 42]. Finally, the nanofibres also infuence the crystallization of the polymer, as seen in Fig. 4. The defects, such as the accumulation and voids in the nanocomposite, inevitably increased when the BNT nanofibre loading increased. The accumulated nanofibres in the nanocomposites can readily form a connected path for the free charge, and the voids will encapsulate the air, therefore, the breakdown strength was decreased. These results indicate that incorporation of a small loading level of BNT NF to the polymer matrix (2.37 vol.%) may be an effective method to achieve high energy densities.

The discharged energy density of the samples can be calculated from the electric displacement-electric field (D-E) loops. Fig. 10a shows the D-E loops of the nanocomposites with various loading levels of BNT at an electric field of 300 kV/mm, and the maximum D-E loops are shown in Fig. A5. As can be seen from Fig. 10a, the electric displacement of the nanocomposites increased with the loading level of BNT nanofibres at the same electric field, while the remnant displacement greatly increased. As a result, the nanocomposites with 12.73 vol.% BNT nanofibres showed a low energy density, which is shown in Fig. 10b. The nanocomposite with 2.37 vol.% BNT nanofibres have the largest discharged energy densities of 12.7 J/cm^3, which is more than three times that of the pure (unfilled) P(VDF-HFP). The significant increase in energy density is mainly due to the high breakdown strength and the high effective electric displacement
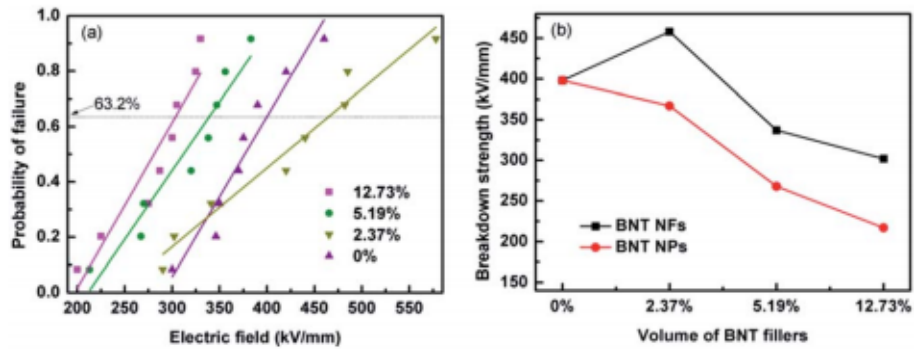
Figure 9: (a) Weibull distribution of the dielectric breakdown strength of nanocomposites filled with various BNT nanofibres, (b) variation of characteristic breakdown strength from Weibull distribution for samples with various volume fractions of fillers.
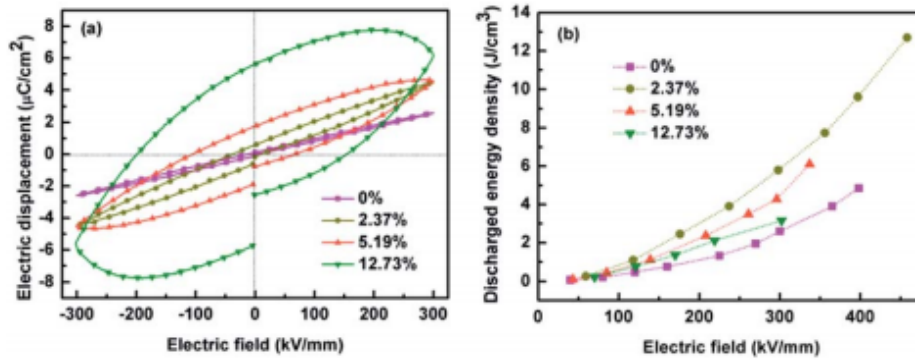
Figure 10: (a) *DE* loops of the nanocomposites with various loadings of BNT NFs at the electric field of 300 kV/mm, (b) discharged energy densities of the nanocomposites with the electric field.

shown in Fig. A6. Table 2 summarizes the previously reported dielectric nanocomposites with different ceramic nanofibres. The discharged energy density achieved in this work using a low content of $Na_{0.5}Bi_{0.5}TiO_3$ nanofibres is superior to the performance of nanocomposites reported elsewhere.

3.3. Modelling of composite dielectric materials

Finite element modelling of a single high permittivity inclusion in a low permittivity matrix was used to further understand the energy storage properties of the BNT/P(VDF-HFP) nanocomposites investigated experimentally. Rather than model a complex three-dimensional system, a series of simplified two dimensional models were created to examine the effect of the ceramic filling fraction, aspect ratio and angle of the high permittivity inclusion to the applied electric field direction on both the permittivity and breakdown strength of the nanocomposite. An additional model will be discussed which introduces a polar β-P(VDF-HFP) as an interphase between the matrix and the high permittivity inclusion. The modelling software used was Ansys v15.0 using a two dimensional four-node element type (PLANE13) for electrostatic analysis. In all

Table 2: Comparison of discharged energy storage density for dielectric composites with different nanofibre fillers

Matrix	Fillers (nanofibres)	Content of fillers (vol.%)	Breakdown strength (kV/mm)	Discharged energy density (J/cm³)	Ref.
P(VDF-TrFE)	$Bi_2O_3/Ba_{0.3}Sr_{0.7}TiO_3$	8.7	155	4.35	[5]
PVDF	$Ba_{0.4}Sr_{0.6}TiO_3$	7.5	~300	~5.5	[10]
PVDF	$SrTiO_3$	2.5	380	6.8	[13]
P(VDF-TrFE-CFE)	$BaTiO_3$	17.5	300	10.5	[20]
PVDF	$Ba(Zr_{0.3}Ti_{0.7})O_3$	7.5	~300	~5	[43]
PVDF	$Ba_{0.2}Sr_{0.8}TiO_3$	7.5	450	14.9	[44]
PVDF	TiO_2	7.5	300	~6.5	[45]
PVDF	$BaTiO_3@Al_2O_3$	2.5	380	7.1	[46]
P(VDF-CTFE)	$BaTiO_3$	3	280	8.4	[47]
P(VDF-HFP)	$Na_{0.5}Bi_{0.5}TiO_3$	2.37	458	12.7	This work

cases the matrix phase (α-P(VDF-HFP)) was modelled with a relative permittivity, $\varepsilon_r = 10$, and the inclusion was assigned the dielectric properties of BNT ($\varepsilon_r = 377$). It should be noted at this point that units and scales of length are in effect arbitrary in all the analyses so electrical loads applied to the models were selected so that the applied field in each case was unity.

The effective permittivity of the modelled composites was calculated by summing the electrostatic energy of each element and calculating the capacitance, and from this permittivity, using the relationship $C = Q/V$, where C is the capacitance, Q is the charge and V is the voltage. Electrical breakdown strength was not modelled directly but instead the maximum local electric field (E_f^{max}) within the composite due to the applied field for each geometry was recorded. The maximum applicable field for a single phase capacitive material, as discussed previously, is the breakdown strength, E_b; above this field the material will no longer store charge as it becomes electrically conductive. When high permittivity phases are introduced into a composite system, the electric field concentrates in the low permittivity phase [15, 16, 32], which is often the high breakdown strength phase; in the BNT/P(VDF-HFP) composite system explored here the low permittivity polymer phase has a higher breakdown strength.

If it is assumed that there is no change in the breakdown strength of the constituent phases in the creation of the composite, a concentration of electric field within the material is likely to lead to electrical breakdown at applied fields below E_b, such that the maximum field applied to the composite material must be modified by a concentration factor of $1/E_f^{max}$ so as to ensure the local field does not exceed the breakdown strength at any point within the composite. The effective breakdown strength of the composite can therefore be defined by the relationship:

$$E_b^{eff} = E_b/E_f^{max}. \tag{4}$$

Our initial model was designed to investigate the effect of filling fraction of the high permittivity BNT phase into the P(VDF-HFP) matrix. A circular BNT inclusion of varying radius (r = 1, 2, 3, 4, 5, 6, 7, 8, 9) was modelled in the center of a square P(VDF-HFP) matrix (20 x 20). A fine triangular finite element mesh was used that satisfactorily mapped the inclusion geometry and electrical loads were applied to the model at boundary lines to simulate electrodes in a parallel plate capacitor, thus generating an electric field across the geometry. An example of such a model can be seen in Fig. 11a which shows that the applied electric field tends to concentrate in the low permittivity matrix phase and is significantly smaller in the high permittivity inclusion. The results from this model for composite permittivity and the inverse of the maximum field (i.e.
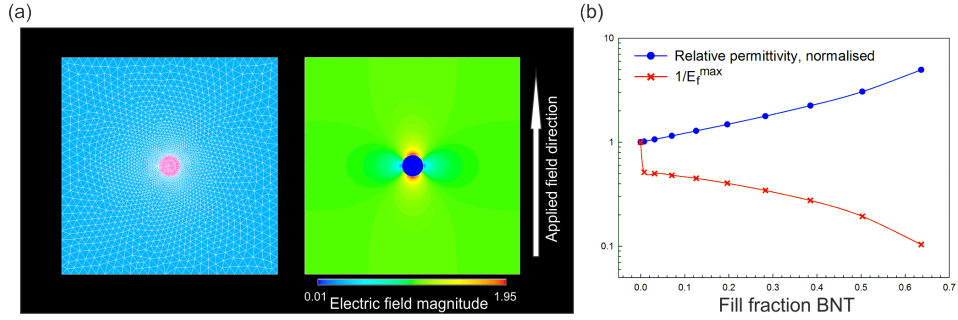
Figure 11: (a) Finite element model for high permittivity inclusion with an aspect ratio of unity and area fraction of 0.00785 with meshed geometry on the left and electric field distribution on the right after application of the electric field; field magnitude is normalized to the distribution in a single phase material (i.e. unity at all locations); (b) effect of area fraction of the high permittivity second phase on the composite permittivity (normalized) and the effective breakdown strength of the material, see Eqn. 4.

the factor by which the breakdown strength is modified in Eqn. 4) are shown in Fig. 11b. The data have been normalized with respect to the single phase matrix material to demonstrate clearly the effect of the high permittivity inclusions on the effective properties of the composites. It can be seen in Fig. 11b that introducing a high permittivity second phase increases the composite permittivity, however significant increases are not realized until the fill fraction exceeds 0.3 (30 vol.%) when the modelled permittivity is doubled compared with single phase P(VDF-HFP). As the electric field concentrates in the low permittivity phase to such an extent that the field in the high permittivity inclusion is close to zero, it appears that the increase in permittivity is linked to the concentration of the field in the low permittivity polymer phase, meaning that more charge, Q, is stored, as V in the relationship $Q = CV$ is effectively increased for the same overall volume. However, while there is an increase in permittivity, there is also a rapid increase in the maximum electric field at very low volume fraction of the high permittivity second phase, which is likely to lead to a reduction in the effective breakdown strength of the material. The highest fields are observed at the tips of the inclusion parallel to the applied field, as shown in Fig. 11a.

The model above clearly indicates that the inclusion of high permittivity particles can increase the effective permittivity but can also increase the maximum electric field and therefore reduce the breakdown strength, which is an important factor from Eqn. 1. The model is now adapted to investigate how the effective composite permittivity is affected by the aspect ratio of the high permittivity second phase and its orientation/angle relative to the applied electric field. The BNT inclusion was modelled as an ellipse with the aspect ratio defined as the ratio of the radii of the major and minor axes, with an aspect ratio of one being a circular inclusion. Fig. 12a shows example geometries of angle and aspect ratio; aspect ratios ranging from one to 10 have been investigated in this model. The inclusion was modelled in the center of a 20 x 20 P(VDF-HFP) matrix and the angle rotated from 0° (i.e. parallel to the applied field) to 90° (perpendicular to the applied field) in steps of 11.25°. In all cases the fill fraction of the BNT phase was constant at 0.00785. Electric field contour plots of fibre composites (aspect ratio = 10) are shown in Fig. 12b and c for angles with respect to a field of 0° and 90°, respectively, and demonstrate that the highest field concentrations occur in the polymer matrix in the vicinity of the high permittivity

inclusion, parallel to the field direction. The effect of aspect ratio and angle with respect to the field on the effective permittivity of the composite and the maximum local electric field is shown in Fig. 12d and e. The highest increase in the composite permittivity was found when high aspect ratio inclusions were aligned parallel to the applied field (Fig. 12d), however, this also caused significant increases in the local electric field at the sharp tips of the high permittivity inclusion (Fig. 12e). The normalized energy density for each case was calculated using the relationship $u_e^{norm} = \varepsilon_{norm}/(E_f^{max})^2$, where ε_{norm} is the composite permittivity normalized with respect to the permittivity of the single phase material, and is plotted in Fig. 12f as a function of angle for varying aspect ratios. The composite with high aspect ratio BNT NFs in the direction of perpendicular to the applied field is predicted as possessing the highest energy density, however, due to the reduction in $1/E_f^{max}$ with the addition of a high permittivity second phase no composite geometry improves on the energy density of the single phase material, shown as a dashed black line in Fig. 12f. Clearly for these composite systems, the introduction of the high permittivity phase increases the local electric field, which increases the effective permittivity (Fig. 12d) but also increases the local electric field (Fig. 12e), leading to reduced energy density (Fig. 12f).

In the models discussed to this point the nanoparticle composites (AR = 1) are predicted to have higher permittivity than high aspect ratio nanofibre composites (AR = 10 at 90°) aligned perpendicular to the field direction, which was not the case observed experimentally where the nanofibre composites had superior permittivity to the nanoparticle composites at the same volume fraction of BNT. To understand the reasons behind these results it was necessary to develop a third finite element model whereby a rectangular fibre of varying aspect ratio (AR = 12.5, 50, 200) and constant filling fraction (0.004) was contained in a rectangular matrix and a polar β-P(VDF-HFP) interphase with varying thickness was modelled between the matrix and the high permittivity inclusion. This is included due to the observation that the BNT nanofibre fillers in P(VDF-HFP) facilitate the formation of the polar β-phase, Fig. 4.

The rectangular model had dimensions of 100 x 500 and was meshed with square elements of equal size; Fig. 13a shows a close up image of the mesh surrounding the fibre. The size of the matrix was selected in this case to ensure that boundary effects did not influence the results as the fibre aspect ratio was increased. Three thicknesses of interphase layer on the surface of the fibre were investigated (element thickness = 0, 1, 2, where t = 0 has no interlayer) for the effect on electric field distribution in the composite and permittivity. The β-P(VDF-HFP) interphase was modelled with a relative permittivity of 15 [48], compared to a relative permittivity of 10 for the bulk matrix. Electric fields were applied perpendicular to the fibre direction as this was shown to be the best configuration for energy storage, as in Fig. 12c. Reported relative permittivity values for β-P(VDF-HFP) vary between 10 and 60 [49], which has an effect on the results of this model in terms of the composite permittivity, electric field concentration factor ($1/E_f^{max}$) and the normalized energy density, such that increasing the interphase permittivity leads to an increase in the overall permittivity but also increases the maximum local electric field concentration in the matrix, leading to a reduction in the normalized energy density compared to an interphase relative permittivity of 15, see Fig. A7.

A contour plot of the electric field distribution within a composite with an interphase thick-
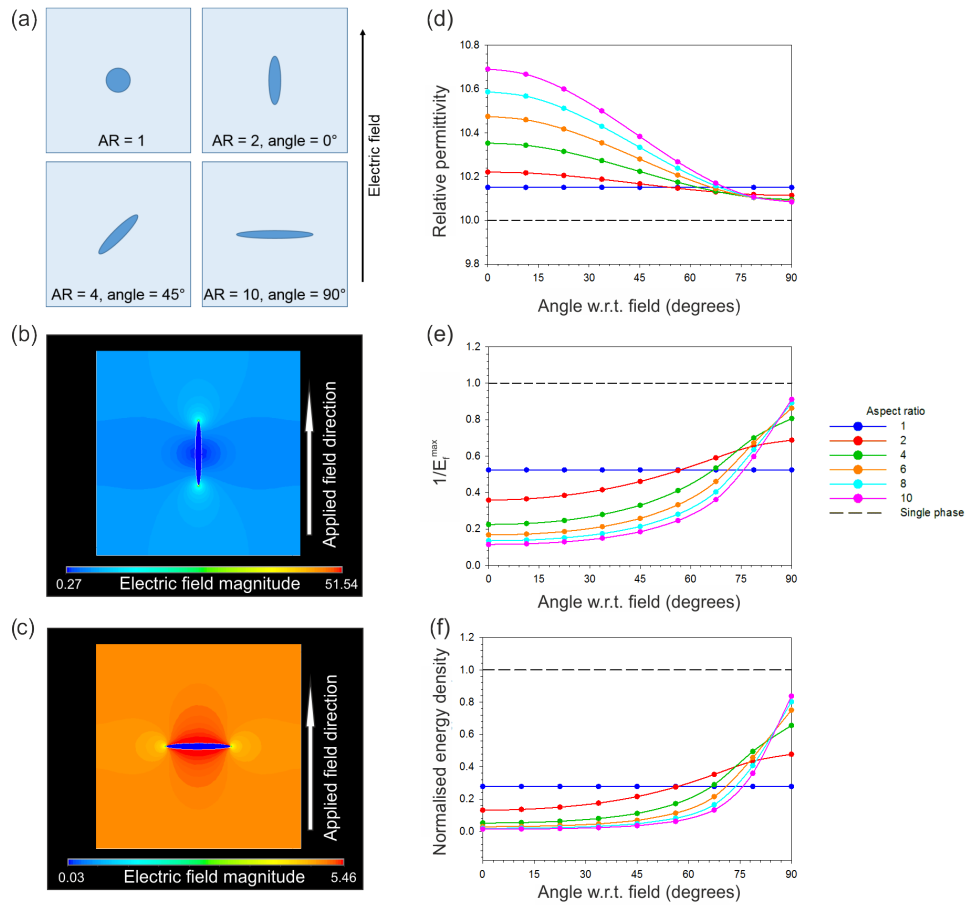
Figure 12: (a) Example geometries investigated via a finite element approach and their corresponding aspect ratios and angles with respect to the applied electric field; (b) and (c) electric field contour plots of fibres modelled parallel and perpendicular to the applied field, respectively, showing that field concentration occurs at sharp tips of the high permittivity phase but in the low permittivity matrix; (d), (e) and (f) effect of aspect ratio and angle on permittivity, field concentration factor ($1/E_f^{max}$) and energy density, respectively, normalized to the single phase material shown in all plots with a dashed black line.

ness of one element and a relative permittivity of 15 is shown in Fig. 13b. The presence of the interphase was found to increase the permittivity for all aspect ratios and permittivity was found to increase with increasing interphase thickness. High aspect ratio fillers yield the best improvements in permittivity, see Fig. 13c. This is due to the increase in the surface area of the fibre with aspect ratio and explains why the nanoparticle composites were found experimentally to exhibit a lower permittivity compared to the nanofibre composites at the same BNT volume fraction (see Fig. 6); the use of high aspect nanofibres simply led to a higher volume of the interphase compared to the nanoparticles, which experimentally had a significantly larger diameter than the fibres: 800 nm compared to 67 nm.

The presence of the higher permittivity β-P(VDF-HFP) interphase reduced the field concentration in the P(VDF-HFP) matrix compared to when there was no interphase, which can be seen
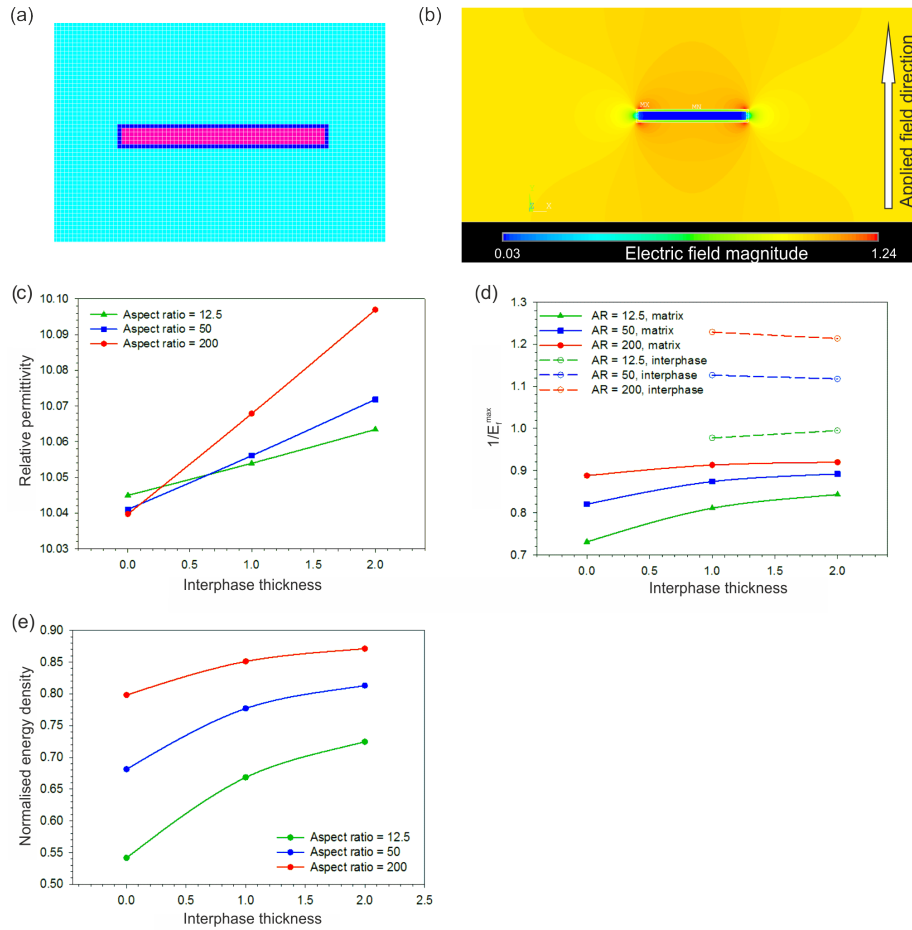
Figure 13: (a) High permittivity fibre (aspect ratio = 12.5, pink) with the β-P(VDF-HFP) interphase (one element thick, dark blue) in the P(VDF-HFP) matrix (cyan); (b) electric field contour plot of the fibre geometry shown in (a); effect of interphase thickness on (c) permittivity, (d) electric field concentration factor ($1 / E_f^{max}$) and (e) energy density when the interphase permittivity is 15.

from the data in Fig. 13d where the solid lines ($1/E_f^{max}$ in the matrix, colours denote varying aspect ratios) approach unity (i.e. no field concentration) as the interphase thickness is increased. It was also found that increasing the thickness of the β-P(VDF-HFP) layer reduced the field concentration within this phase and higher aspect ratios were also beneficial in this respect, this is indicated by the dashed lines in Fig. 13d. The effect of introducing an interphase on the electric field distribution of the composites may partially explain why experimentally an increase in breakdown strength was observed at low volume fractions of BNT nanofibres, see Fig. 9b, as the field concentrations are reduced due to the more gradual change in permittivity around the high permittivity inclusion. At higher BNT volume fractions the close proximity of neighboring nanofibres is likely to lead to field concentrations that negate the benefits of the nucleation of the interphase, hence the decline in breakdown strength observed experimentally above 2.37 vol.% volume fraction of BNT nanofibres. The increase in permittivity and reduction in field

concentration with the addition of the interphase leads to higher predicted energy densities than for the composites in all cases, with the best results seen for high aspect ratio fibres with a thick interphase, as shown in Fig. 13e.

4. Conclusions

This paper demonstrates that the use of a small volume fraction of high aspect ratio nanofibre fillers is an effective approach to achieve a nanocomposite architecture capable of achieving a high energy density and high dielectric strength. Lead-free high aspect ratio ferroelectric $Na_{0.5}Bi_{0.5}TiO_3$ (BNT) nanofibres and particles were synthesized by a hydrothermal method. The P(VDF-HFP) nanocomposite films with a variety of BNT nanofibres and nanoparticle loading levels (2.37, 5.19 and 12.73 vol.%) were obtained by casting and hot pressing. The relative permittivity of the nanocomposite continuously increased with the level of BNT nanofibre loading, while also maintaining a relatively low dielectric loss (<0.11). A small amount (2.37 vol.%) of BNT nanofibres introduced to the polymer matrix increased the fraction of the polar β-phase in the nanocomposite, which led to an increase of the permittivity. Due to the partial perpendicular distribution of BNT nanofibres to the applied electric field direction, the local electric field concentration was reduced, which was investigated in detail by finite element analysis (Ansys). The presence of high aspect ratio nanofibres with the treatment of surface modification and the alignment of nanofibres perpendicular to the applied electric field led to a high breakdown strength of 458 kV/mm for the nanocomposite with 2.37 vol.% BNT nanofibres with a corresponding large energy storage density of 12.7 J/cm^3. The thermal conductivity also increased to 0.67 W/m.K compared to the pure P(VDF-HFP) polymer (0.2 W/m.K). This research provides a novel nanocomposite approach to produce high energy storage density dielectric materials for advanced electronic and electrical power system applications.

References

[1] B. Chu, X. Zhou, K. Ren, B. Neese, M. Lin, Q. Wang, F. Bauer, Q. M. Zhang, A dielectric polymer with high energy density and fast discharge speed, Science 313 (2006) 334–336.

[2] M. N. Nadagouda, R. S. Varma, Green approach to bulk and template-free synthesis of thermally stable reduced polyaniline nanofibers for capacitor applications, Green Chem. 9 (2007) 632–637.

[3] D. R. Wang, T. Zhou, J. W. Zha, J. Zhao, C. Y. Shi, Z. M. Dang, Functionalized graphene-BaTiO$_3$/ferroelectric polymer nanodielectric composites with high permittivity, low dielectric loss, and low percolation threshold, J. Mater. Chem. A 1 (2013) 6162–6168.

[4] Q. Li, K. Han, M. R. Gadinski, G. Zhang, Q. Wang, High energy and power density capacitors from solution processed ternary ferroelectric polymer nanocomposites, Adv. Mater. 26 (2014) 6244–6249.

[5] P. Hu, Y. Song, H. Liu, Y. Shen, Y. Lin, C.-W. Nan, Largely enhanced energy density in flexible P(VDF-TrFE) nanocomposites by surface-modified electrospun BaSrTiO$_3$ fibers, J. Mater. Chem. A 1 (2013) 1688–1693.

[6] H. Luo, K. Zhou, C. Bowen, F. Zhang, A. Wei, Z. Wu, C. Chen, D. Zhang, Building Hierarchical Interfaces Using BaSrTiO$_3$ Nanocuboid Dotted Graphene Sheets in an Optimized Percolative Nanocomposite with Outstanding Dielectric Properties, Adv. Mater. Interfaces 3 (2016) 1–6.

[7] Q. Li, F. Liu, T. Yang, M. R. Gadinski, G. Zhang, L.-Q. Chen, Q. Wang, Sandwich-structured polymer nanocomposites with high energy density and great chargedischarge efficiency at elevated temperatures, Proc. Nation. Acad. of Sci. 113 (2016) 9995–10000.

[8] H. Tang, Z. Zhou, C. C. Bowland, H. A. Sodano, Synthesis of calcium copper titanate ($CaCu_3Ti_4O_{12}$) nanowires with insulating SiO_2 barrier for low loss high dielectric constant nanocomposites, Nano Energy 17 (2015) 302–307.

[9] H. Luo, D. Zhang, C. Jiang, X. Yuan, C. Chen, K. Zhou, Improved dielectric properties and energy storage density of poly(vinylidene fluoride-co-hexafluoropropylene) nanocomposite with hydantoin epoxy resin coated $BaTiO_3$, ACS Appl. Mater. Interfaces 7 (2015) 8061–8069.

[10] C. Jiang, D. Zhang, K. C. Zhou, X. F. Zhou, H. Luo, I. Abrahams, Significantly enhanced energy storage density of sandwich-structured $(Na_{0.5}Bi_{0.5})_{0.93}Ba_{0.07}TiO_3$ /P(VDFHFP) composites induced by PVP-modified two-dimensional platelets, J. Mater. Chem. A 4 (2016) 18050–18059.

[11] X. Hao, J. Zhai, X. Yao, Improved Energy Storage Performance and Fatigue Endurance of Sr-Doped $PbZrO_3$ Antiferroelectric Thin Films, J. Am. Ceram. Soc. 92 (2009) 1133–1135.

[12] L. Xie, X. Huang, K. Yang, S. Li, P. Jiang, "Grafting to" route to PVDF-HFP-GMA/$BaTiO_3$ nanocomposites with high dielectric constant and high thermal conductivity for energy storage and thermal management applications, J. Mater. Chem. A 2 (2014) 5244–5251.

[13] S. Liu, J. Zhai, Improving the dielectric constant and energy density of poly(vinylidene fluoride) composites induced by surface-modified $SrTiO_3$ nanofibers by polyvinylpyrrolidone, J. Mater. Chem. A 3 (2015) 1511–1517.

[14] L. Xie, X. Huang, Y. Huang, K. Yang, P. Jiang, Core-shell Structured Hyperbranched Aromatic Polyamide / $BaTiO_3$ Hybrid Filler for Poly (vinylidene fl uoride-tri fl uoroethylene- chloro fl uoroethylene) Nanocomposites with the Dielectric Constant Comparable to That of Percolative Composites, ACS Appl. Mater. Interfaces 5 (2013) 1747–1756.

[15] H. Tang, Z. Zhou, H. A. Sodano, Relationship between $BaTiO_3$ nanowire aspect ratio and the dielectric permittivity of nanocomposites, ACS Appl. Mater. Interfaces 6 (2014) 5450–5455.

[16] P. Kim, S. C. Jones, P. J. Hotchkiss, J. N. Haddock, B. Kippelen, S. R. Marder, J. W. Perry, Phosphonic acid-modified barium titanate polymer nanocomposites with high permittivity and dielectric strength, Adv. Mater. 19 (2007) 1001–1005.

[17] J. Li, P. Khanchaitit, K. Han, Q. Wang, New route toward high-energy-density nanocomposites based on chain-end functionalized ferroelectric polymers, Chem. Mater. 22 (2010) 5350–5357.

[18] H. Luo, C. Chen, K. Zhou, X. Zhou, Z. Wu, D. Zhang, Enhancement of dielectric properties and energy storage density in poly(vinylidene fluoride-co-hexafluoropropylene) by relaxor ferroelectric ceramics, RSC Adv. 5 (2015) 68515–68522.

[19] S. K. Patil, M. Y. Koledintseva, R. W. Schwartz, W. Huebner, Prediction of effective permittivity of diphasic dielectrics using an equivalent capacitance model, J. Appl. Phys. 104 (2008) 074108.

[20] H. Tang, Y. Lin, H. A. Sodano, Synthesis of high aspect ratio $BaTiO_3$ nanowires for high energy density nanocomposite capacitors, Adv. Energy Mater. 3 (2013) 451–456.

[21] C. Andrews, Y. Lin, H. A. Sodano, The effect of particle aspect ratio on the electroelastic properties of piezoelectric nanocomposites, Smart Mater. Struct. 19 (2010) 25018.

[22] X. Huang, T. Iizuka, P. Jiang, Y. Ohki, T. Tanaka, Role of Interface on the Thermal Conductivity of Highly Filled Dielectric Epoxy / AlN Composites, J. Phys. Chem. C 116 (2012) 13629–13636.

[23] X. Huang, C. Zhi, P. Jiang, D. Golberg, Y. Bando, T. Tanaka, Polyhedral oligosilsesquioxane-modified boron nitride nanotube based epoxy nanocomposites: An ideal dielectric material with high thermal conductivity, Adv. Funct. Mater. 23 (2013) 1824–1831.

[24] K. Roleder, I. Franke, A. M. Glazer, P. A. Thomas, S. Miga, J. Suchanicz, The piezoelectric effect in $Na_{0.5}Bi_{0.5}TiO_3$ ceramics, J. Phys: Cond. Matt. 14 (2002) 5399–5406.

[25] J. Suchanicz, Behaviour of $Na_{0.5}Bi_{0.5}TiO_3$ ceramics in the ac electric field, Ferroelectr. 209 (1998) 561–568.

[26] Y. Hou, Y. Deng, Y. Wang, H. Gao, Uniform distribution of low content $BaTiO_3$ nanoparticles in poly(vinylidene fluoride) nanocomposite: toward high dielectric breakdown strength and energy storage density, RSC Adv. 5 (2015) 72090–72098.

[27] X. Huang, P. Jiang, C. Kim, F. Liu, Y. Yin, Influence of aspect ratio of carbon nanotubes on crystalline phases and dielectric properties of poly(vinylidene fluoride), Eur. Polym. J. 45 (2009) 377–386.

[28] X. Zhou, C. Jiang, C. Chen, H. Luo, K. Zhou, D. Zhang, Morphology control and piezoelectric response of $Na_{0.5}Bi_{0.5}TiO_3$ synthesized via a hydrothermal method, Cryst. Eng. Comm. 18 (2016) 1302–1310.

[29] Y. Niu, Y. Bai, K. Yu, Y. Wang, F. Xiang, H. Wang, Effect of the modifier structure on the performance of barium titanate/poly(vinylidene fluoride) nanocomposites for energy storage applications, ACS Appl. Mater. Interfaces 7

(2015) 24168–24176.

[30] L. Xie, X. Huang, C. Wu, P. Jiang, Core-shell structured poly(methyl methacrylate)/BaTiO$_3$ nanocomposites prepared by in situ atom transfer radical polymerization: A route to high dielectric constant materials with the inherent low loss of the base polymer, J. Mater. Chem. 21 (2011) 5897–5906.

[31] X. Lin, P. Hu, Z. Jia, S. Gao, Enhanced electric displacement induces large energy density in polymer nanocomposites containing coreshell structured BaTiO$_3$ @TiO$_2$ nanofibers, J. Mater. Chem. A 4 (2016) 2314–2320.

[32] N. Guo, S. A. DiBenedetto, P. Tewari, M. T. Lanagan, M. A. Ratner, T. J. Marks, Nanoparticle, Size, Shape, and Interfacial Effects on Leakage Current Density, Permittivity, and Breakdown Strength of Metal Oxide-Polyolefin Nanocomposites: Experiment and Theory, Chem. Mater. 22 (2010) 1567–1578.

[33] S. Liu, J. Zhai, J. Wang, S. Xue, W. Zhang, Enhanced energy storage density in poly(vinylidene flouride) nanocomposites by a small loading of surface-hydroxylated Ba0.6Sr0.4TiO$_3$ nanofibers, ACS Appl. Mater. Interfaces 6 (2014) 1533–1540.

[34] J. Li, S. Tan, S. Ding, H. Li, L. Yang, Z. Zhang, High-field antiferroelectric behaviour and minimized energy loss in poly(vinylidene-co-trifluoroethylene)-graft-poly(ethyl methacrylate) for energy storage application, J. Mater. Chem. 22 (2012) 23468.

[35] D. P. Almond, C. R. Bowen, Anomalous power law dispersions in ac conductivity and permittivity shown to be characteristics of microstructural electrical networks, Phys. Rev. Lett. 92 (2004) 157601–1.

[36] C. W. Ahn, G. Amarsanaa, S. S. Won, S. a. Chae, D. S. Lee, I. W. Kim, Antiferroelectric Thin-Film Capacitors with High Energy-Storage Densities, Low Energy Losses, and Fast Discharge Times, ACS Appl. Mater. Interfaces 7 (2015) 26381–26386.

[37] M. H. Park, H. J. Kim, Y. J. Kim, T. Moon, K. D. Kim, Y. H. Lee, S. D. Hyun, C. S. Hwang, Study on the internal field and conduction mechanism of atomic layer deposited ferroelectric Hf$_{0.5}$Zr$_{0.5}$O$_2$ thin films, J. Mater. Chem. C 3 (2015) 6291–6300.

[38] X. J. Lou, Why do antiferroelectrics show higher fatigue resistance than ferroelectrics under bipolar electrical cycling?, Appl. Phys. Lett. 94 (2009) 072901.

[39] Y. Wang, K. F. Wang, C. Zhu, J.-M. Liu, Polarization fatigue of ferroelectric Pb(Zr$_{0.1}$Ti$_{0.9}$)O$_3$ thin films: Temperature dependence, J. Appl. Phys. 99 (2006) 044109.

[40] G. Wang, X. Huang, P. Jiang, Tailoring dielectric properties and energy density of ferroelectric polymer nanocomposites by high-k nanowires, ACS Appl. Mater. Interfaces 7 (2015) 18017–18027.

[41] P. Hu, Y. Shen, Y. Guan, X. Zhang, Y. Lin, Q. Zhang, C. W. Nan, Topological-structure modulated polymer nanocomposites exhibiting highly enhanced dielectric strength and energy density, Adv. Funct. Mater. 24 (2014) 3172–3178.

[42] C. A. Grabowski, S. P. Fillery, N. M. Westing, C. Z. Chi, J. S. Meth, M. F. Durstock, R. A. Vaia, Dielectric Breakdown in Silica-Amorphous Polymer Nanocomposite Films: The Role of the Polymer Matrix, ACS Appl. Mater. Interfaces 5 (2013) 5486–5492.

[43] S. Liu, S. Xue, S. Xiu, B. Shen, J. Zhai, Surface-modified Ba(Zr0.3Ti0.7)O$_3$ nanofibers by polyvinylpyrrolidone filler for poly(vinylidene fluoride) composites with enhanced dielectric constant and energy storage density, Sci. Rep. 6 (2016) 26198.

[44] H. Tang, H. A. Sodano, Ultra high energy density nanocomposite capacitors with fast discharge using Ba0.2Sr0.8TiO$_3$ nanowires, Nano Lett. 13 (2013) 1373–1379.

[45] H. Tang, H. A. Sodano, High energy density nanocomposite capacitors using non-ferroelectric nanowires, Appl. Phys. Lett. 102 (2013) 063901.

[46] S. Liu, J. Wang, B. Shen, J. Zhai, H. Hao, L. Zhao, Poly(vinylidene fluoride) nanocomposites with a small loading of core-shell structured BaTiO$_3$@Al$_2$O$_3$ nanofibers exhibiting high discharged energy density and efficiency, J. Alloys Compd. 696 (2017) 136–142.

[47] B. Xie, Q. Zhang, H. Zhang, G. Zhang, S. Qiu, S. Jiang, Largely enhanced ferroelectric and energy storage performances of P(VDF-CTFE) nanocomposites at a lower electric field using BaTiO$_3$ nanowires by stirring hydrothermal method, Ceram. Int. 42 (2016) 19012–19018.

[48] P. Martins, A. C. Lopes, S. Lanceros-Mendez, Electroactive phases of poly(vinylidene fluoride): Determination, processing and applications, Prog. Polym. Sci. 39 (2014) 683–706.

[49] V. Tiwari, G. Srivastava, Effect of thermal processing conditions on the structure and dielectric properties of PVDF films, J. Polym. Res. 21 (2014) 587.

4.2 Context, part 2

The second paper in this chapter questions whether energy storage composites formed of a conductive phase within a ferroelectric matrix are flawed in their design. A number of papers in recent years have reported on composite materials with 'giant' or 'colossal' measured permittivity, however, significant improvements in energy densities are yet to be realised using extrinsic material systems. The paper, titled *A breakdown in the case for materials with giant permittivity?*, builds on the modelling work presented in the first paper in this chapter, adapting it for conductive inclusions. Experimental and modelling data from literature was analysed and used to validate the finite element presented in this work. The paper provides more relevant conclusions to the findings of both modelling studies presented in this chapter but for clarity a combined summary of the findings is included at the end of the chapter.

Supplementary information published alongside this paper can be found in Appendix C.

Access the data from the following paper here: https://doi.org/10.15125/BATH-00454.

Statement of Authorship

This declaration concerns the article entitled:							
A breakdown in the case for materials with giant permittivity?							

Publication status (tick one)							
draft manuscript		**Submitted**		**In review**		**Accepted**		**Published**	✓

Publication details (reference)	Roscow et al., ACS Energy Letters **2** (2017) 2264-2269
Candidate's contribution to the paper (detailed, and also given as a percentage).	The candidate contributed to/ considerably contributed to/predominantly executed the Formulation of ideas: D.P. Almond and C.R. Bowen formulated idea for theme of paper from knowledge of literature in the field of conductor-ferroelectric composites. Use of our own model to fit with literature data was idea of the candidate (40% candidate) Design of methodology: Modelling and data fitting methodology was designed solely by the candidate (100%) Experimental work: Modelling studies and processing of data by candidate (100%), literature review a combination of all authors (33%) Presentation of data in journal format: Initial draft by C.R. Bowen and D.P. Almond, figures and work towards final draft by candidate (50%)
Statement from Candidate	This paper reports on original research I conducted during the period of my Higher Degree by Research candidature.
Signed		**Date**	30/11/17

PAPER 4: A breakdown in the case for materials with giant permittivity?

J.I. Roscow[a], C.R. Bowen[a], & D.P. Almond[a]

[a]*Department of Mechanical Engineering, University of Bath, Bath, UK*

Abstract

Despite the large number of papers published on 'giant' or 'colossal' permittivity composite, or 'extrinsic', materials for energy storage applications, significant improvements in energy densities remain elusive. One reason for this is that significantly enhanced permittivity (ε) in composite materials comes at the cost of greatly reduced breakdown strength (E_b), which is more important in terms of the energy storage density figure of merit, $\varepsilon.E_b^2$. In this commentary, data from literature is analysed and the underlying mechanism of the observed 'colossal' permittivity, particularly in metal-dielectric composites, is found to be electric field concentrations within the low permittivity matrix, which also act to reduce the breakdown strength of the material. These two effects appear to be fundamentally linked and it is therefore concluded that efforts should be spent searching for the next generation of 'intrinsic' high permittivity materials.

1. Introduction

There remains continued interest in the design and manufacture of heterogeneous materials with high permittivity; for example the so-called 'giant' or 'colossal' permittivity materials. These materials can be divided into two distinct classes. The first class are 'intrinsic' giant permittivity materials in which the dipolar response of the material has been enhanced; for example doped titania materials [1, 2, 3]. The second class can be classified as 'extrinsic' where a high effective permittivity is achieved by introducing electrical conductivity or creating a composite system that consists of a dielectric matrix with a random or ordered distribution of a conductive phase [4]. Specific examples of extrinsic composites with high permittivity include metal-loaded ceramics (cermets) including Mo-mullite [5] and Ag-bismuth zinc niobate [6], metal loaded ferroelectrics such as $BaTiO_3$ [7, 8], metal loaded glass [9] and metal- [10] and carbon-loaded [11, 12, 13] polymer matrices.

The reason for the interest in extrinsic materials is simple - the introduction of a conductive phase into a dielectric matrix creates a composite with an effective permittivity that is much higher than that of the matrix. Relative permittivity (ε_r) values of up to 10^5 have been reported in some composite systems. In many cases the permittivity and dielectric loss of the composite are characterised in detail, since the frequency dependent properties of materials are readily measured in the Hz to MHz range using frequency response analysers. It is common for publications related to the manufacture and characterisation of these high permittivity composites to highlight

their potential application as capacitor materials, including multi-layer and small volume high-performance capacitors. However, while the permittivity and dielectric loss is of importance it is insufficient to fully assess their potential for such applications since the dielectric strength, or breakdown strength, is also an important parameter. The selection of materials for capacitor applications has been well described by McLean [14] and is summarised below for the design of capacitors with high reliability, low cost and small size.

For small volume capacitor applications it is necessary to use the smallest amount of dielectric to meet the capacitance requirements. Considering a simple parallel plate capacitor, the overall capacitance (C) is:

$$C = \frac{A\varepsilon_r\varepsilon_0}{t} \tag{1}$$

where A is the plate area, t is the plate separation (thickness), ε_r is the relative permittivity of the dielectric medium and ε_0 is the permittivity of free space. The volume of the dielectric ($v_{dielectric}$) is:

$$v_{dielectric} = A.t \tag{2}$$

From Eqns. 1 and 2 the capacitance per unit volume (F /m^3) is therefore:

$$\frac{C}{v_{dielectric}} = \frac{\varepsilon_r\varepsilon_0}{t^2} \tag{3}$$

At this stage it is easy to assume that to achieve a high capacitance per unit volume a high permittivity is necessary; hence the interest in 'giant' permittivity materials. However to maximise the capacitance per unit volume, the thickness of the dielectric must also be as small. The minimum thickness is limited by the dielectric strength ($E_{dielectric}$) of the capacitor material. If the capacitor has a working voltage, V, the minimum thickness is $V/E_{dielectric}$. Substituting this into Eqn. 3 leads to:

$$\frac{C}{v_{dielectric}} = \varepsilon_r\varepsilon_0.\left[\frac{E_{dielectric}}{V}\right]^2 \tag{4}$$

Eqn. 4 shows that for a specific working voltage the capacitance per unit volume is proportional to a 'merit index' of $\varepsilon_r.(E_{dielectric})^2$. This clearly highlights that a low dielectric strength can lead to poor volume efficiency, even if the permittivity is high. Rearrangement of Eqn. 4 also provides a figure of merit for a capacitor with high energy density (J/m^3). Since the energy stored in a capacitor is $\frac{1}{2}CV^2$, the 'energy density' is given by:

$$\frac{\frac{1}{2}CV^2}{v_{dielectric}} = \frac{1}{2}\varepsilon_r\varepsilon_0.(E_{dielectric})^2 \tag{5}$$

and leads to the same merit index of $\varepsilon_r.(E_{dielectric})^2$ for maximum energy density.

Eqns. 4 and 5 clearly show that *both* relative permittivity and dielectric strength are important parameters for the selection of a material for capacitor applications. The dielectric strength cannot be ignored when considering potential materials for capacitor applications. In fact, the

$\varepsilon_r.(E_{dielectric})^2$ relationship in Eqn. 4 indicates that dielectric strength is a more important property than permittivity for high energy density capacitors. It is therefore of interest to examine the influence of the addition of a conductive phase on the permittivity, the dielectric strength and the $\varepsilon_r.(E_{dielectric})^2$ merit index of the dielectric.

2. Examples of extrinsic systems

Although a significant amount a data on frequency dependent permittivity and loss has been published on conductor-insulator composites and giant permittivity materials, there is much less data reporting both permittivity and dielectric strength. While the addition of a conductive phase increases the effective permittivity it can also have a deleterious effect on the dielectric strength as a result of the enhancement of local electric fields with the composite [11, 15]. Gyure et al. [16] have modelled the dielectric breakdown and permittivity of metal-loaded dielectrics and Duxbury et al. [17] considered rocket propellants mixtures that consisted of aluminium particles in a dielectric host due to a significant reduction of the breakdown field of the host due to the presence of aluminium particles. A variety of researchers have experimentally examined the dielectric strength and permittivity of Ni-BaTiO$_3$ composites [5, 8, 18].

Fig. 1 shows a graph of normalised variation of permittivity (solid symbols) and dielectric strength (open symbols) as a function of conductor volume fraction for a range of composite systems reported in the literature [7, 8, 11, 16, 17] that contain experimental measurements or modelling data. To simplify a comparison, the colour and symbol is the same for both permittivity and dielectric strength for each composite. For the limited number of publications where both permittivity and dielectric strength were reported as a function of conductor volume fraction, Fig. 1 clearly shows that the enhancement of permittivity is always at the expense of the dielectric strength.

It is of benefit to now calculate the $\varepsilon_r.(E_{dielectric})^2$ and $\varepsilon_r.(E_{dielectric})$ figures of merit as a function of conductor volume fraction for the data in the literature. For the data in Fig. 1, the permittivity and dielectric strength were not always available at the same conductor volume fractions; this was obtained by curve fitting of the data in Fig. 1 and calculating the relevant merit index across the range of volume fraction available for each data set. This was achieved using the general form: $f(x) = a.exp(bx) + c.exp(dx)$ of *MATLAB* Curve Fitting software, which had the best R-square values for the majority of data sets. It can be seen that for all data, other than that reported by Pecharromàn et al. [7] (see Fig. C1), the introduction of the conductor-phase leads to the volume efficiency figure of merit being reduced significantly compared to that of the filler free matrix, as the exponential rise in the permittivity coincides with a rapid reduction in the breakdown strength.

The data reported by Pecharromàn et al. [7] for Ni-BaTiO$_3$ is at variance to the trend observed in other work reviewed here, however, only one sample (volume fraction = 0.28) was calculated to have a figure of merit increased with respect to that of the matrix material; the data has been included in supplementary information Fig. C1. The reason for this appears to be a plateau in the breakdown strength close to the percolation threshold before a rapid decline as the volume fraction is increased above 0.28, whilst the permittivity increases exponentially. Breakdown

73
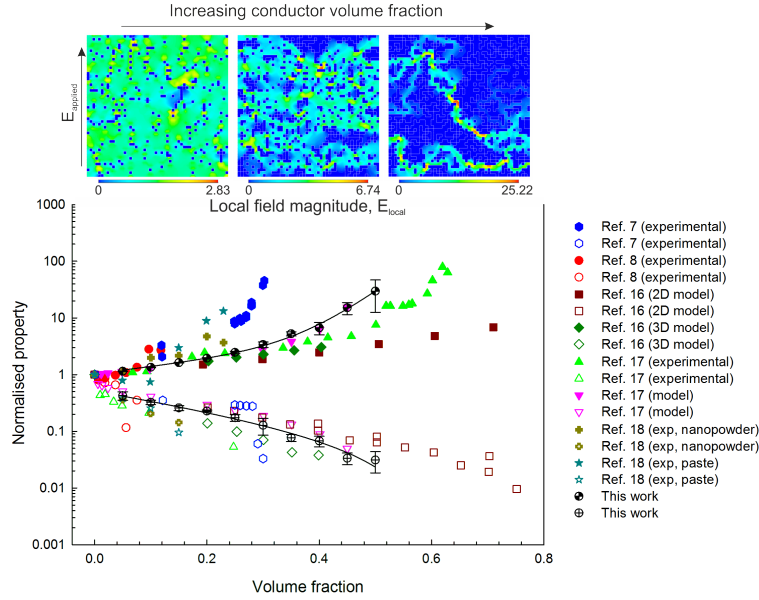
Figure 1: Graph showing permittivity (solid symbols) and dielectric strength (open symbols) as a function of conductor volume fraction normalised to the single phase matrix material. The colour and symbol type is the same for the permittivity and dielectric strength for each system. Electric field contour plots are shown above the graph for increasing conductor volume fractions. An increase in local field concentrations with increasing conductor fraction leads to a rise in permittivity (ε) and decrease in breakdown strength (E_b).

properties are highly susceptible to statistics of sample size close to the percolation threshold and so repeat tests would be useful to get a better idea of the reliability of this type of composite, however, it should also be noted that an energy density of 1.4 times that of $BaTiO_3$ as found here despite a 20-fold increase in the permittivity, is still far below commonly used capacitor materials, tantalum-based oxides for example [14]. A later study on Ni-$BaTiO_3$ composites from Saleem et al. [18] found the breakdown strength reduced at a faster rate than the permittivity increased, yielding a reduction in the figure of merit at all nickel volume fractions, as shown in Fig. 2. Nevertheless, it cannot be ignored that the composite in Pecharromàn et al. [7] breaks the general rule for extrinsic materials and demonstrates some potential that may require further investigation.

The data from the literature presented in Fig. 1 and Fig. 2 is supplemented by a 2D electrostatic finite element model (Ansys) we have developed to gain a better understanding of the mechanism behind the observed 'colossal' or 'giant' permittivity of metal-dielectric composites. A square mesh was divided into 50 x 50 equally sized square elements, which were initially assigned a nominal relative permittivity; $\varepsilon_r = 1$. 'Conductive' elements were selected at random and assigned a permittivity 10^6 higher than the matrix. This ensured that the electric field across the 'conductive' elements was effectively zero, i.e. the field we would expect across a conductor under equilibrium. An electric field ($E_{applied}$) was applied across the finite element matrix, and the capacitance measured from the stored electrical energy and the maximum local field magnitude (E_{max}) recorded. The effective permittivity was calculated from the capacitance and the
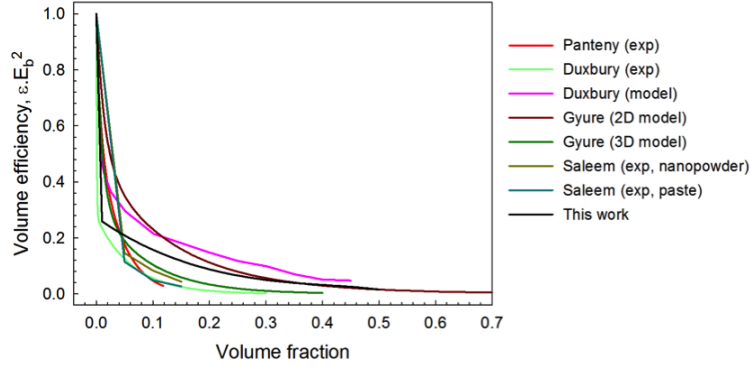
Figure 2: Energy storage material merit indices for energy density, $\varepsilon_r.(E_{dielectric})^2$, as a function of conductor volume fraction calculated from curve fitting equations obtained for data shown in Fig. 1.

normalised effective breakdown strength was predicted from the relationship:

$$E_b^* = \frac{E_{applied}}{E_{max}} \tag{6}$$

whereby breakdown was assumed to occur at the point of highest field concentration and would cascade onwards from the weakest point. For the filler free matrix the electric field is homogeneous and $E_{applied} = E_{max}$; however, we will see that the introduction of the conductive elements into a dielectric matrix leads to electric field concentrations. Dielectric breakdown in the composite was assumed to occur in the dielectric phase, as a conductor is effectively in a permanent state of 'breakdown', and so the maximum field applied to the composite compared to the matrix as a single phase must be reduced by a concentration factor, $1/E_{max}$, therefore allowing calculation of the effective breakdown strength, E_b^*, of the composite. It should be highlighted that the modelling approach ignores the potential of the filler introducing additional defects, which could reduce breakdown strength even further [19].

Electric field contour plots of models with conductor volume fractions of 0.1, 0.3 and 0.5 are shown in Fig. 3 to demonstrate the influence of conductor additions on the electric field distribution throughout the composite. As the volume fraction of conductive material in the dielectric matrix increases the electric field becomes increasingly more inhomogeneous and the maximum local electric field increases; see the contour maps at the bottom of Fig. 3. This leads to a reduction in the breakdown strength of the material, which can be seen in the lower trend line in Fig. 1 from the model data. The electric field concentrations within the matrix act to increase the stored energy due to an applied field, therefore leading to a significant increase in measured effective permittivity, see the model data in the upper trend line in Fig. 1. Good agreement is observed between our model and other reported experimental and modelling data. The modelled energy density figure of merit also decreases with increasing conductor fraction, as can be seen in Fig. 2. For conductor volume fractions > 0.4 the permittivity may be considered 'colossal' since the effective permittivity is an order of magnitude higher than that of the matrix. However, it should be highlighted there has been no change in the ability of the constituent phases themselves

75
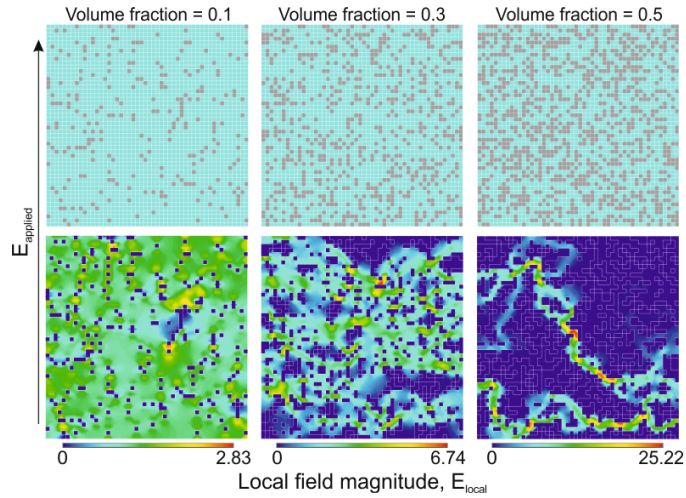
Figure 3: Finite element model of two phase composites with varying volume fraction of conducting phase. Top images show example random distribution of conductor (grey) in dielectric matrix (cyan) and bottom images are corresponding contour plots after application of normalised external electric field ($E_{applied} = 1$). For a filler-free matrix E_{local} at all locations.

to store more energy, since their permittivities remain constant, and the observed increases in effective permittivity are at the expense of forming areas of high local electric field which would significantly reduce breakdown strength.

The network model discussed previously is based on a random distribution of equiaxed conductive fillers within a dielectric matrix. One method that has been proposed to reduce electric field concentrations and avoid a reduction in breakdown strength in composites is to alter the aspect ratio and angle of the filler with respect to the direction of the working field. In particular, the alignment of high aspect ratio nanofibres perpendicular to the direction of applied field has been considered and has been used in systems containing high permittivity fillers [20, 21, 22, 23]. To examine this approach for metal-dielectric composites we now consider a single conductive particle at a fixed volume fraction ($\varepsilon_r = 10^6$, area fraction = 0.00785) within a dielectric matrix ($\varepsilon_r = 1$). We then vary its aspect ratio and orientation (θ) with respect to the applied electric field; when $\theta = 0°$ the filler particle is aligned parallel to the applied field and when $\theta = 90°$ the particle is orientated perpendicular to the applied field. Electric field contour maps of these conditions for an aspect ratio of eight are shown in Fig. 4a. The results for the effect of angle and aspect ratio on E_b^*, normalised permittivity and energy density ($\varepsilon.(E_b^*)^2$) are shown in Fig. 4b - d, respectively, calculated using the methods discussed previously. The dashed line in Fig. 4b - d represents the property of the filler free matrix material.

We can see in Fig. 4b that high aspect ratio inclusions aligned perpendicular to the applied field give rise to composites with the highest breakdown strength as this orientation results in the lowest field concentrations, see also Fig 4a. The worst breakdown strength is found when high aspect ratio particles are aligned parallel the applied field. However, whatever the orientation of the conductive filler relative to the applied field, or its aspect ratio, the breakdown strength is always lower than that of the single phase filler-free matrix in which the field is homogenous at
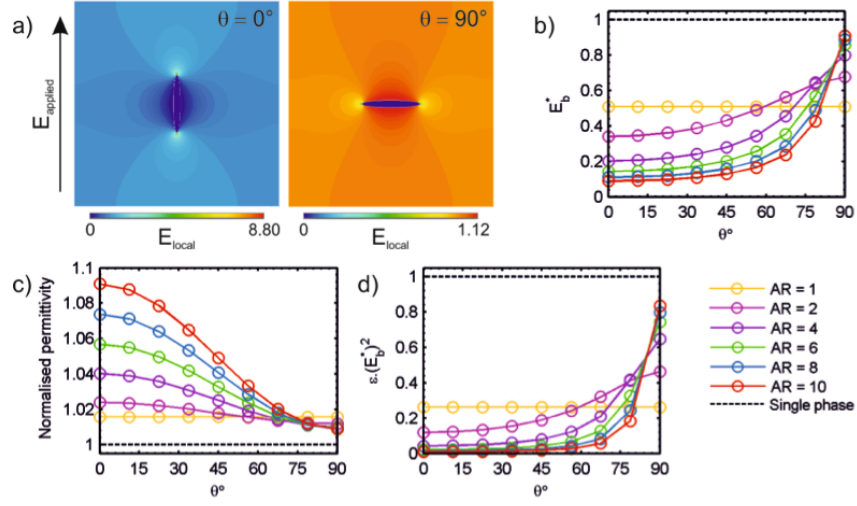
Figure 4: a) Example contour maps of electric field distribution for a single conductive inclusion with high aspect ratio (AR = 8) and angle with respect to applied field ($\theta = 0°$ (left) and 90° (right)) contained within a dielectric matrix; and variation of b) effective breakdown strength, E_b^*, c) permittivity and d) energy density, $\varepsilon.(E_{dielectric})^2$, with changing angle and aspect ratio of single inclusion.

all points in the matrix. The opposing trend is observed for the permittivity, Fig. 4c, which is unsurprising since field concentrations are beneficial to the effective permittivity but detrimental to dielectric strength. In this case, the highest permittivity is achieved when high aspect ratio inclusions are aligned parallel to the applied field since this leads to the highest field concentrations. Despite the high permittivity, this composite geometry has the lowest breakdown strength and the volume energy density is significantly reduced (<1%) compared to the matrix, see Fig. 4d. Since the $\varepsilon.(E_{dielectric})^2$ figure of merit for energy density depends on the square of the breakdown strength, the inclusion of conductive fillers of any orientation or aspect ratio reduces the energy storage capabilities of the composite compared to the matrix material, see Fig 4d.

The use of high permittivity fillers in an effort to enhance permittivity also leads to similar effects in terms of changes in permittivity and dielectric strength [20, 21, 22, 23, 24, 25, 26]; this is due to the high permittivity additions also forming electric field concentrations in the lower permittivity host. Introducing an interphase between matrix and high permittivity filler, through surface functionalisation of the filler [21, 22, 23, 24, 25] or using the filler to enhance the crystallisation of the polymer matrix [27] and thereby improve its dielectric strength may provide a route to reducing the problem, although it is unlikely to remove the problem completely as any high permittivity or conductive filler essentially behaves as a defect. The use of relatively low permittivity oxide fillers such as TiO_2 [28] and ZrO_2 [29] ($\varepsilon_r < 50$) with similar permittivity to a ferroelectric polymer matrix have been shown to have higher breakdown strength than nanocomposites with high permittivity fillers [15]; however there appears to be little reward in terms of enhancement of dielectric properties towards giant permittivity.

To conclude, we have shown that extrinsic giant or colossal permittivity materials are unlikely to be candidate materials for multi-layer and small volume high-performance capacitors.

Conductive fillers increase the effective permittivity of a conductor-dielectric composite by creating local electric field concentrations within the material. However, these internal electric field enhancements are limited in practice to the magnitude of the breakdown field strength of the filler free dielectric matrix. Consequently, the maximum field that can be applied to the composite, its effective breakdown field strength, will be reduced in magnitude from that of the filler free dielectric matrix. Since the enhanced permittivity in extrinsic materials originates from local internal electric field enhancements, it is impossible to produce composite configurations that achieve a giant permittivity without reducing the effective dielectric strength of the material. In fact, emphasis should be placed on the development of materials with 'giant' or 'colossal' $\varepsilon.(E_{dielectric})^2$ or $\varepsilon.(E_{dielectric})$ merit indices. This work indicates the properties of extrinsic materials, both obtained experimentally and through modelling, to have merit indices that are poorer than the corresponding filler free dielectric matrix materials. Hence it is recommended that the search for genuinely useful giant or colossal dielectric materials is confined to devising means of enhancing the intrinsic dielectric properties of materials.

References

[1] W. Hu, Y. Liu, R. L. Withers, T. J. Frankcombe, L. Norén, A. Snashall, M. Kitchin, P. Smith, B. Gong, H. Chen, J. Schiemer, F. Brink, J. Wong-Leung, Electron-pinned defect-dipoles for high-performance colossal permittivity materials, Nat. Mater. 12 (2013) 821–826.

[2] C. C. Homes, T. Vogt, Colossal permittivity materials: Doping for superior dielectrics, Nat. Mater. 12 (2013) 782–783.

[3] Z. Li, X. Luo, W. Wu, J. Wu, Niobium and divalent-modified titanium dioxide ceramics: Colossal permittivity and composition design, J. Am. Ceram. Soc. 100 (2017) 3004–3012.

[4] H. Du, X. Lin, H. Zheng, B. Qu, Y. Huang, D. Chu, Colossal permittivity in percolative ceramic/metal dielectric composites, J. Alloys Compd. 663 (2016) 848–861.

[5] C. Pecharromán, J. S. Moya, Experimental evidence of a giant capacitance in insulator-conductor composites at the percolation threshold, Adv. Mater. 12 (2000) 294–297.

[6] S. George, J. James, M. T. Sebastian, Giant Permittivity of a Bismuth Zinc Niobate–Silver Composite, J. Am. Ceram. Soc. 90 (2007) 3522–3528.

[7] C. Pecharroman, F. Esteban-Betegón, J. F. Bartolome, S. López-Esteban, J. S. Moya, New Percolative BaTiO$_3$ -Ni Composites with a High and Frequency-Independent Dielectric Constant (e = 80,000), Adv. Mater. 13 (2001) 1541–1544.

[8] S. Panteny, C. R. Bowen, R. Stevens, Characterisation of barium titanate-silver composites, part I: Microstructure and mechanical properties, J. Mater. Sci. 41 (2006) 3837–3843.

[9] J. Huang, H. Zheng, Z. Chen, Q. Gao, N. Ma, P. Du, Percolative ceramic composites with giant dielectric constants and low dielectric losses, J. Mater. Chem. 19 (2009) 3909–3913.

[10] X. Huang, P. Jiang, L. Xie, Ferroelectric polymer/silver nanocomposites with high dielectric constant and high thermal conductivity, Appl. Phys. Lett. 95 (2009) 242901.

[11] H. Stoyanov, D. Mc Carthy, M. Kollosche, G. Kofod, Dielectric properties and electric breakdown strength of a subpercolative composite of carbon black in thermoplastic copolymer, Appl. Phys. Lett. 94 (2009) 232905.

[12] A. Luna, J. Yuan, W. Néri, C. Zakri, P. Poulin, A. Colin, Giant Permittivity Polymer Nanocomposites Obtained by Curing a Direct Emulsion, Langmuir 31 (2015) 12231–12239.

[13] J.-K. Yuan, S.-H. Yao, Z.-M. Dang, A. Sylvestre, M. Genestoux, J. Bai1, Giant Dielectric Permittivity Nanocomposites: Realizing True Potential of Pristine Carbon Nanotubes in Polyvinylidene Fluoride Matrix through an Enhanced Interfacial Interaction, J. Phys. Chem. C 115 (2011) 5515–5521.

[14] D. A. McLean, Dielectric Materials and Capacitor Miniaturization, IEEE Trans. Parts, Mater. and Packag. 3 (1967) 163–169.

[15] Z.-M. Dang, J.-K. Yuan, S.-H. Yao, R.-J. Liao, Flexible Nanodielectric Materials with High Permittivity for Power Energy Storage, Adv. Mater. 25 (2013) 6334–6365.

[16] M. F. Gyure, P. D. Beale, Dielectric breakdown in continuous models of metal-loaded dielectrics, Phys. Rev. B 46 (1992) 3736–3746.

[17] P. M. Duxbury, P. D. Beale, H. Bak, P. A. Schroeder, Capacitance and dielectric breakdown of metal loaded dielectrics, J. Phys. D: App. Phys. 23 (1990) 1546.

[18] M. Saleem, J. S. Song, S. J. Jeong, M. S. Kim, S. Yoon, I. S. Kim, Dielectric response on microwave sintered BaTiO$_3$ composite with Ni nanopowder and paste, Mater. Res. Bull. 64 (2015) 380–385.

[19] J. Y. Li, L. Zhang, S. Ducharme, Electric energy density of dielectric nanocomposites, Appl. Phys. Lett. 90 (2007) 132901.

[20] H. Tang, Y. Lin, C. Andrews, H. A. Sodano, Nanocomposites with increased energy density through high aspect ratio PZT nanowires, Nanotech. 22 (2011) 15702.

[21] S. Wang, X. Huang, G. Wang, Y. Wang, J. He, P. Jiang, Increasing the Energy Efficiency and Breakdown Strength of High-Energy-Density Polymer Nanocomposites by Engineering the Ba0.7Sr0.3TiO$_3$ Nanowire Surface via Reversible AdditionFragmentation Chain Transfer Polymerization, J. Phys. Chem. C 119 (2015) 25307–25318.

[22] X. Zhang, W. Chen, J. Wang, Y. Shen, L. Gu, Y. Lin, C. W. Nan, Hierarchical interfaces induce high dielectric permittivity in nanocomposites containing TiO$_2$@BaTiO$_3$ nanofibers, Nanoscale 6 (2014) 6701–6709.

[23] S. Liu, J. Zhai, Improving the dielectric constant and energy density of poly(vinylidene fluoride) composites induced by surface-modified SrTiO$_3$ nanofibers by polyvinylpyrrolidone, J. Mater. Chem. A 3 (2015) 1511–1517.

[24] X. Zhang, Ultrahigh Energy Density of Polymer Nanocomposites Containing BaTiO$_3$ @TiO$_2$ Nanofibers by Atomic - Scale Interface Engineering, Adv. Mater. 27 (2015) 819–824.

[25] S. Liu, S. Xue, S. Xiu, B. Shen, J. Zhai, Surface-modified Ba(Zr0.3Ti0.7)O$_3$ nanofibers by polyvinylpyrrolidone filler for poly(vinylidene fluoride) composites with enhanced dielectric constant and energy storage density, Sci. Rep. 6 (2016) 26198.

[26] H. Tang, H. A. Sodano, Ultra High Energy Density Nanocomposite Capacitors with Fast Discharge Using Ba 0.2 Sr 0.8 TiO$_3$ Nanowires, Nano Lett. 13 (2013) 1373–1379.

[27] H. Luo, J. Roscow, X. Zhou, S. Chen, X. Han, K. Zhou, D. Zhang, C. Bowen, Ultra-high Discharged Energy Density Capacitor using High Aspect Ratio Na$_{0.5}$Bi$_{0.5}$TiO$_3$ Nanofibers, J. Mater. Chem. A 5 (2017) 7091–7102.

[28] J. Li, S. I. Seok, B. Chu, F. Dogan, Q. Zhang, Q. Wang, Nanocomposites of ferroelectric polymers with TiO$_2$ nanoparticles exhibiting significantly enhanced electrical energy density, Adv. Mater. 21 (2009) 217–221.

[29] C. Zou, D. Kushner, S. Zhang, Wide temperature polyimide/ ZrO$_2$ nanodielectric capacitor film with excellent electrical performance, Appl. Phys. Lett. 98 (2011) 082905.

4.3 Summary

In this chapter ferroelectric composites have been evaluated for their suitability for electrical energy storage applications. Modelling studies, presented across two papers, have been used to explain results observed experimentally. The key points from this research can summarised as:

1. Energy storage composites were modelled using a finite element approach to assess their energy storage capabilities in terms of the permittivity (ε) and dielectric breakdown strength (E_b), from which a figure of merit ($\varepsilon.E_b^2$) was calculated to allow comparison between different composite structures. Two types of these composites were investigated: (i) those with high permittivity fillers contained within a low permittivity matrix, and (ii) those with conductive fillers (modelled as effectively infinite permittivity inclusions) in a high permittivity matrix.

2. Due to the difference in permittivity between the two phases the electric field preferentially concentrates in the low permittivity matrix phase. For very large differences, such as for the conductive fillers, no electric field forms in the high permittivity/conductive phase when an external field is applied. The field concentrates in the matrix around the high permittivity second phases resulting in an increase in local field compared to the applied field, causing a reduction in effective breakdown strength, a phenomenon commonly observed experimentally for both types of ferroelectric composite. A second phase with contrasting permittivity to the matrix therefore acts as a defect rather than improving the energy storage capabilities due to the breakdown strength of the material being the dominant property in the merit index.

3. The local electric fields across the high permittivity/conductive inclusions are very low in both composites investigated due to the permittivity contrast and it is therefore concluded that the associated rise in permittivity (relatively modest for the first type of composite, often deemed 'giant' or 'colossal' for the second) is a result of the local field concentrations in the matrix phase, rather than the inherent charge-storing ability of the second phase. This means the rise in permittivity and reduction in breakdown strengh, two competing properties in terms of enhancing the energy storage figure of merit, appear to be fundamentally linked.

4. Modelling studies on the effect of the aspect ratio and angle with respect to applied field of the second phase inclusions demonstrated that the highest increases in permittivity occured for long fibres aligned parallel to the field but the electric field concentrations in the matrix made these the worst geometries in terms of breakdown strength and energy storage figure of merit. High aspect ratio inclusions aligned perpendicular to the applied field were found to yield the highest figures of merit for the composite systems. The best figures of merit in all cases, however, were found for the single phase materials, such was the detrimental effect of the high local field concentrations on the dielectric strength.

5. Increases in breakdown strength observed in the experimental studies in the first paper in this chapter are thought to be due to the introduction of the high permittivity, high aspect ratio nanofibres enhancing crystallisation of the matrix. This constitutes an intrinsic change in the properties of the matrix material that was only partially considered in the model in which an interphase was introduced between the matrix and the filler. The results from this investigation showed some promise, although the predicted figure of merit was still below that of the single phase material.

Porous ferroelectric ceramics are also subject to electric fields after sintering as they need to be poled in order to induce the net remanent polarisation that leads to both piezoelectric and pyroelectric behaviour, properties which can then be exploited to harvest ambient energy. The studies presented in this chapter informed the research presented in subsequent chapters on porous ferroelectrics, particularly the single pore models.

Chapter 5

Poling behaviour of barium titanate with a porous sandwich layer for energy harvesting applications

5.1 Context

The paper presented in this chapter, *Modelling and fabrication of porous sandwich layer barium titanate with improved energy harvesting figures of merit*, demonstrates the potential for porous sandwich layer structures for energy harvesting applications due to their low permittivity and high longitudinal piezoelectric strain coefficients. Numerical models are presented that account for the complex poling distribution of porous ferroelectric materials that is caused by the difference in permittivity between the ferroelectric matrix and the pores. Good agreement with experimental data is achieved. This work builds on the experimental work presented in Chapter 3 and the finite element modelling studies in Chapter 4.

As detailed in Chapter 1, Fig. 1-1, another publication is closely related to the work presented in this chapter: J. I. Roscow et al. *Piezoelectric anisotropy and energy harvesting characteristics of novel sandwich layer $BaTiO_3$ structures*, Smart Mater. Struct. **26** (2017), details the anisotropic properties of porous sandwich layer barium titanate that are beneficial for sensor applications. Numerical modelling studies are used that take into account the effect of 90° domain wall mobility on the piezoelectric properties of these 'composite-in-composite' materials. The experimental procedure and data are the same as in the work presented in this chapter, although transverse piezoelectric coefficients, d_{31}, are also reported as a function of porosity.

Supplementary information published alongside this paper can be found in Appendix D and

the Ansys script for modelling porous sandwich layer materials is included in Appendix E. Access the data from the following paper here: https://doi.org/10.15125/BATH-00452.

Statement of Authorship

This declaration concerns the article entitled:								
Modelling and fabrication of porous sandwich layer barium titanate with improved energy harvesting figures of merit								
Publication status (tick one)								
draft manuscript		**Submitted**		**In review**		**Accepted**		**Published** ✓

Publication details (reference)	Roscow et al., Acta Materialia **128** (2017) 207-217
Candidate's contribution to the paper (detailed, and also given as a percentage).	The candidate contributed to/ considerably contributed to/predominantly executed the Formulation of ideas: Solely the candidate (100%) Design of methodology: Experimental methodology designed by the candidate (100%), modelling methodology designed in conjunction with R.W.C Lewis (co-author) (30% candidate contribution to method design, post processing solely the Experimental work: candidate) Solely the candidate (100%) Presentation of data in journal format: Solely the candidate (100%)
Statement from Candidate	This paper reports on original research I conducted during the period of my Higher Degree by Research candidature.
Signed		Date	30/11/17

PAPER 5: Modelling and fabrication of porous sandwich layer barium titanate with improved energy harvesting figures of merit

J.I. Roscow[a], R.W.C. Lewis[b], J. Taylor[c], & C.R. Bowen[a]

[a]*Department of Mechanical Engineering, University of Bath, Bath, UK*
[b]*Renishaw Plc., Wooton-under-Edge, Gloucestershire, UK*
[c]*Department of Electrical and Electronic Engineering, University of Bath, Bath, UK*

Abstract

This paper demonstrates that porous 'sandwich' structures can provide an effective route for the design and optimisation of piezoelectric materials for energy harvesting applications, which is becoming an increasingly important technology for self-powered wireless networks and sensors. A numerical model is presented that accounts for the complex poling distribution throughout a layered ferroelectric and helps to develop a detailed understanding of the relationship between the geometry of the porous structure and the poling characteristics of porous ferroelectric materials, with good agreement with experimental data. Novel layered barium titanate ceramics were fabricated whereby dense outer layers surround a highly porous sandwich layer, and for specific layer geometries an unusual condition was achieved where the longitudinal piezoelectric strain coefficients (d_{33}) increased as the thickness of the porous layer and total porosity level of the layered structure increased. The permittivity ($\varepsilon_{33}^{\sigma}$) decreased with increasing thickness and increasing porosity level of the porous layer due to the presence of a low permittivity air phase. These two factors in combination led to an increase in the longitudinal energy harvesting figure of merit, $d_{33}^2/\varepsilon_{33}^{\sigma}$, for the layered structure, with a maximum of 3.74 pm^2/N when the relative thickness of the porous layer was 0.52 and the porosity within this layer was ~60 vol.%. This harvesting performance of these novel structures is much larger than both dense barium titanate (1.40 pm^2/N) and barium titanate with randomly distributed porosity at the same 60% volume fraction (2.85 pm^2/N).

---

1. Introduction

There is significant interest in the use of ferroelectric materials for energy harvesting applications due to their inherent ability to convert energy from mechanical vibrations and thermal fluctuations, via the piezoelectric and pyroelectric effects, respectively, to electrical energy. A variety of figures of merit (FOMs) have been devised to assist with the selection of piezoelectric materials for energy harvesting applications. When a piezoelectric is subjected to mechanical vibrations at low frequencies (<<100 kHz) and away from the electromechanical resonance (i.e. off-resonance) the relevant FOM is given by [1]:

$$FOM_{ij} = \frac{d_{ij}^2}{\varepsilon_{33}^{\sigma}} \tag{1}$$

where d_{ij} is the relevant piezoelectric strain coefficient associated with the direction of stress relative to the poling direction (such as d_{33} or d_{31}), $\varepsilon_{33}^{\sigma}$ is the permittivity at constant stress, σ, and subscripts i and j follow conventional piezoelectric matrix notation. The FOM_{ij} is derived from capacitor energy storage equations ($E = \frac{1}{2}CV^2$, where E is stored electrical energy, C is capacitance and V is potential difference across a capacitor) and effectively describes the change in stored electrical energy within a piezo-active material when a stress is applied. Another important factor for effective piezoelectric energy conversion is the electromechanical coupling factor, k_{ij}^2, which takes into account the mechanical properties of the material and describes the efficiency of conversion from mechanical to electrical energy:

$$k_{ij}^2 = \frac{d_{ij}^2}{\varepsilon_{33}^{\sigma}.S_{33}^E} \qquad (2)$$

where S_{ij}^E is the mechanical compliance at constant electric field. From Eqn. 1 and 2 it can be seen that optimum materials for energy harvesting mechanical loads should have high piezoelectric strain coefficients, low permittivity and low compliance.

One approach to reduce significantly the effective permittivity of piezoelectric composites is to introduce a low permittivity phase, such as air or a polymer ($\varepsilon_{33}^{\sigma} \sim$ 1-10), into the high permittivity ferroelectric ceramic; e.g. lead zirconate titanate (PZT, $\varepsilon_{33}^{\sigma} \sim$ 1000-3500, depending on composition) and barium titanate (BaTiO$_3$, $\varepsilon_{33}^{\sigma} \sim$ 1500) [2]. This has been achieved by introducing randomly distributed porosity throughout the ferroelectric microstructure [2] and has led to an increase in the longitudinal mode energy harvesting figure of merit, FOM_{33} [3], where d_{ij} = d_{33} in Eqn. 1 and 2. The FOM_{33} increases as porosity is introduced into the material since there is a large reduction in permittivity and a relatively small decrease in d_{33}. By understanding the reasons behind the reduction in d_{33} and permittivity in porous ferroelectrics it is possible to design porous structures that yield further increases in the relevant FOMs, and will be discussed throughout this paper.

1.1. Poling of ferroelectrics

Ferroelectric ceramics, such as PZT and BaTiO$_3$, exhibit no bulk piezo- or pyro-electric properties when manufactured by traditional methods such as compaction of powders and heat-treatment at high temperature, known as sintering. This is due to the random distribution of domains as the polycrystalline material cools, post-sintering, below the Curie temperature and it relaxes to its lowest energy state, resulting in zero net polarisation [4]. To align the ferroelectric domains so as to yield the net polarisation required for ferroelectric ceramics to exhibit piezoelectric behaviour the material has to be 'poled', whereby a large static electric field is applied across the material, usually at elevated temperatures close to the Curie point where the domains are more mobile. A ferroelectric material will become poled in the direction of the applied field, when the local electric field, E_f, (i.e. within a grain or domain) is greater than the coercive field, E_c, i.e. when $E_f > E_c$. In a dense single phase ferroelectric, E_f is homogenous, leading to a fully poled structure if the applied field is sufficiently large and greater than E_c. However, when a second phase with a different permittivity is introduced into the microstructure of the material
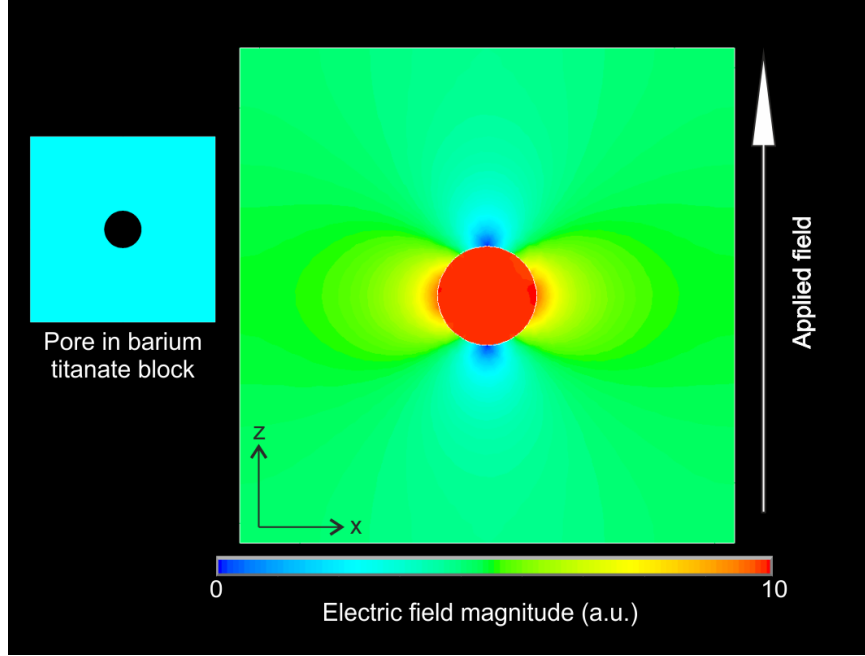
Figure 1: Contour plot of local electric field magnitude (arbitrary units) due to an applied field across a two dimensional finite element model whereby a circular pore of low permittivity is contained within a high permittivity barium titanate matrix. Blue regions represent areas of low field in the BaTiO$_3$ phase that may result incomplete poling in a porous ferroelectric material.

the electric field will tend to concentrate in the low permittivity phase, in particular the pores of a porous ferroelectric material.

To illustrate this effect, the complex electric field distribution in a porous ferroelectric material is demonstrated in Fig. 1, which shows a two-dimensional finite element (FE) model of a single pore (relative permittivity, $\varepsilon_{33}^{\sigma} = 1$) in barium titanate ($\varepsilon_{33}^{\sigma} = 1500$) with a static electric field applied. This simulates the electric field distribution within a porous ferroelectric material during the poling process. A high electric field concentration (red contour in Fig. 1) is observed within the low permittivity pore while the field in the ceramic phase varies with location. Regions of low electric field (blue contour in Fig. 1) are observed in the immediate vicinity of the pore parallel to the direction of the applied field, which in a ferroelectric material may lead to incomplete poling in these regions. This phenomenon can be described by an adaptation of Gauss law where the electric field, E_f, is related to the relative permittivity by the relationship [5]:

$$E_f = \frac{q}{A.\varepsilon_0.\varepsilon_r} \tag{3}$$

where q is charge, A is area and ε_0 is the permittivity of free space. In a two phase material where $\varepsilon_1 \neq \varepsilon_2$ (subscripts denote phase), the electric field will not have the continuous and linear path that is present in a dense ferroelectric material during the poling procedure. As a consequence of the field concentrating in the low permittivity air phase, porous ferroelectrics are difficult to pole,

which reduces the effective piezoelectric response, and d_{ij}, of the material. Previous work has shown a gradual decrease in d_{33} as the porosity levels increase to 50-60 vol.%. Beyond 60 vol.% porosity there is a rapid decrease in d_{33} with increasing porosity [3, 6]. The decrease in d_{33} at high porosities is due to incomplete poling of the ferroelectric phase and cannot be counteracted by simply increasing the poling field, as high electric fields will eventually lead to electrical breakdown in either the air or in the ferroelectric ceramic.

A further consideration for designing porous ferroelectric ceramics is the increase in the elastic compliance, S_{33}^E, associated with the introduction of porosity, which is approximately proportional to the amount of porosity present for randomly distributed porosity [7]; the influence of spherical porosity on compliance of ceramics has been described in detail elsewhere [8, 9]. Therefore, despite the potential benefit of introducing porosity into ferroelectric ceramics for energy harvesting applications due to the significant reduction in permittivity, careful consideration of the porous structure is necessary to achieve improvements in harvesting FOMs and electromechanical coupling factors (see Eqn. 1 and 2).

One potential approach to improving both the mechanical and piezoelectric properties of porous piezoelectric composites is to consider porous piezoelectric 'sandwich layer' structures, where the porous layer is formed between two outer dense piezoelectric layers. A porous sandwich layer structure can be described in this case by two variables. Firstly, the relative thickness of the porous layer, which is defined as follows:

$$
\begin{aligned}
t_p^{rel} &= thickness\ of\ porous\ layer/total\ thickness \\
&= \frac{t_{porous}}{t_{porous} + 2t_{dense}}
\end{aligned}
\tag{4}
$$

based on the upper and lower dense layers being the same thickness, and secondly the porosity of the porous layer, discussed here in terms of volume percentage (vol.%). It should also be noted that in this paper, when comparing to previous work involving materials with uniformly distributed porosity [3], it is necessary to refer to the relative density, ρ_{rel}, of the overall ceramic structure. A relative density of unity is a ceramic with zero porosity (in reality pressureless sintered ceramics are typically $\rho_{rel} > 0.95$), such that the overall volume fraction of porosity, v_p, can be determined from $v_p = 1 - \rho_{rel}$.

2. Ferroelectric sandwich structures

The majority of previous research into porous sandwich structures and functionally graded porous ferroelectrics has focussed on the reduction in bulk permittivity leading to increased detection sensitivity for pyroelectric applications [10, 11, 12, 13]. In this case the porosity (typically less than 16 vol.% bulk porosity) acts to increase a variety of pyroelectric figures of merit, including the pyroelectric energy harvesting FOM, $F_E' = p^2/(\varepsilon_{33}^\sigma.c_e^2)$ [14], where p is the pyroelectric coefficient. The increase in F_E' is due to a reduction in permittivity, although there is also a decrease in the pyroelectric coefficient as the level of porosity is increased. The significant

reductions in permittivity are also of interest for piezoelectric energy harvesting, see Eqn. 1 and 2.

Work on piezoelectric sandwich layers of PZT for hydrophone applications also found that permittivity is reduced by the addition of a porous layer, which increases the voltage generated due to an acoustic pressure and the dense outer layers were found to improve the bending strength compared to PZT ceramics with uniformly distributed porosity [15]. Introducing graded porosity yielded enhanced acoustic matching, beneficial for hydrophone applications, as well as increasing the piezoelectric anisotropy leading to improved hydrostatic piezoelectric properties [16, 17]. Compared to dense PZT, the addition of a porous inter-layer with ~25 vol.% porosity led to a decrease in d_{33}, but it was significantly higher than a ceramic with the same volume fraction of uniformly distributed porosity [15].

The reported work on sandwich structures is experimental and no models have been presented that demonstrate an understanding of the impact of the complex electric field distribution, such as that shown in Fig. 1, in these structures during poling and the effect on the resulting piezoelectric properties. Such a study is necessary to understand the effect of a layered porous structure on both the energy harvesting FOM and the electromechanical coupling factor for harvesting and other transducer applications.

A variety of manufacturing methods have been used to create functionally graded and layered porous structures. Spin coating of $Pb_{0.8}La_{0.1}Ca_{0.1}Ti_{0.975}O_3$[12] and deposition from a solution of $(Na_{0.85}K_{0.15})_{0.5}Bi_{0.5}TiO_3$ [13] has been used for producing thin films (≤500 nm) of ferroelectric materials with enhanced pyroelectric FOMs. Tape casting has been used effectively to create PZT-based thick films (~1 mm) with alternating dense and porous layers [10, 11, 15] and porosity gradient materials [16]. Sequential compaction of individual layers provides a route to produce ferroelectric ceramic structures with thickness >1 mm [17].

In this work barium titanate ceramics with porous sandwich layer structures have been evaluated both numerically and experimentally for their energy harvesting capabilities, with particular attention paid to the effect of the relative thickness of the porous inter-layer and the porosity level of the inter-layer on the relevant properties and performance figures of merit. The properties of these structures are compared to that of dense and uniformly distributed porous barium titanate used to create the layers. Barium titanate was used in this investigation rather than PZT so as to enable comparison to previous data [3].

3. Finite element modelling

3.1. Models of porous ferroelectric ceramics

A variety of models exist that were designed to evaluate the effect of introducing a low permittivity second phase (such as air or a polymer) into ferroelectric ceramics (usually PZT) on the piezoelectric and dielectric properties [18, 19, 20, 21, 22, 23, 24, 25, 26, 27, 28, 29]. A common assumption in such models, often based on the unit cell approach, is that the ferroelectric material is fully poled, irrespective of the porosity levels. This is a simplification that leads to a disagreement between the models and experimental data, as highlighted by Fig. 1 where we see a complex field distribution in the high permittivity phase due to the presence of a pore can result

in a partially poled material, and therefore lower effective piezoelectric properties of a porous ferroelectric ceramic. A more accurate approach for modelling porous piezoelectric ceramics was found using a finite element model that accounted for this complex electric field distribution within a porous ferroelectric during the poling process [6].

In this paper the approach proposed by Lewis et al. [6] has been further developed to investigate how the addition of a porous layer between two dense layers to form a sandwich structure affects the poling behaviour of these materials. By developing a detailed understanding of how the effective longitudinal piezoelectric response, d_{33}, and permittivity changes with the porous layer thickness and the level of porosity after the poling process, it is possible to design porous structures with significantly improved properties for energy harvesting applications.

3.2. Modelling methodology

A finite element (FE) approach has been used whereby a three dimensional cubic mesh with 27,000 elements (30 x 30 x 30) was arranged into dense outer layers and a porous inter-layer, see Fig. 2. Models were created where varying levels of inter-layer porosity were achieved by changing the ratio of cells randomly assigned with the properties of either unpoled $BaTiO_3$ ceramic [30] or air; the outer layers were assumed to be fully dense (i.e. no pores). The $BaTiO_3$ elements in the model can be thought of as representing multi-grain, and therefore multi-domain, regions that have no net polarisation when the geometry is initially generated so as to simulate the properties of sintered ferroelectric ceramics prior to poling. The relative porous layer thickness, t_p^{rel}, defined in Eqn. 4, was varied from $0 \geq t_p^{rel} \geq 1$, such that when $t_p^{rel} = 0$ the structure is fully dense and when $t_p^{rel} = 1$ the structure has uniformly distributed porosity with no dense layers. The increment at which t_p^{rel} was varied was as close to 0.1 as possible, whilst maintaining the sandwich layer in the middle of the structure, meaning that at certain values the step was displaced by $\frac{1}{30}$, i.e. 0.1 became 0.13.

Once the network of cells used to create the sandwich structure had been generated, electrodes were simulated by coupling the voltage degrees of freedom at the upper and lower faces of the three-dimensional model. An electric field (0.6 MV/m) that was higher than the coercive field ($E_c = 0.5$ MV/m [31]) was applied between the electrodes to simulate the poling procedure and the local electric field analysed in each element. The poling electric field was selected as it gave a good fit to the experimental data for $BaTiO_3$ with uniformly distributed porosity, from Ref. [3], using the porous network model detailed in Ref. [6]. The use of higher poling fields results in an overestimation of effective piezoelectric properties at high porosities, see Supplementary Information Fig. D1. Elements in which the local field in the z-direction, E_f^z, was greater than the coercive field, E_c, of $BaTiO_3$ became poled in this direction. Early versions of the porous network model allowed poling of elements in six possible directions (-x, x, -y, y, -z and z) [6], analogous to the six tetragonal poling directions in a unit cell of $BaTiO_3$ [32], however, it was found that the effect of elements poled in directions other than the z-direction on the effective d_{33} was negligible (a maximum of 1.5% of the elements poled in the z-direction for any given geometry) and so the model was simplified to only pole elements in the z-direction. Input data of compliance, permittivity and piezoelectric properties for the coupled-field FE model is
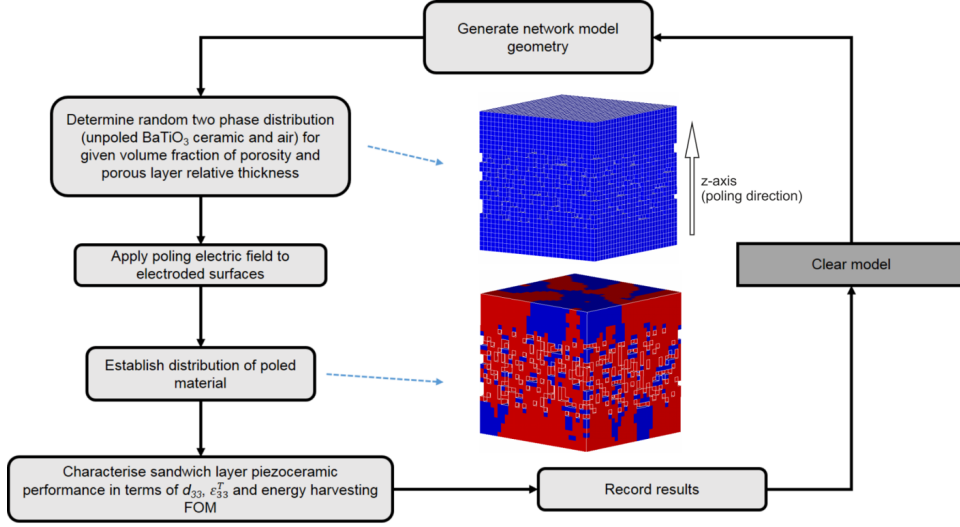
90

Figure 2: Flow diagram of finite element modelling process using Ansys APDL. The upper image in the centre of the diagram shows the network geometry of unpoled BaTiO₃ ceramic (blue regions) and pores in the layer 'sandwiched' between two outer dense layers. The lower image shows the poled geometry where red regions represent poled BaTiO₃ and blue regions remain unpoled.

Table 1: Material input data of poled BaTiO₃ where c_{ij}^E is the stiffness matrix (GPa), e_{ij} is used to define the piezoelectric coefficient matrix (C/m²) and $\varepsilon_{11}^S/\varepsilon_0$ is the relative permittivity at constant strain.

C_{11}^E	C_{12}^E	C_{13}^E	C_{33}^E	C_{44}^E	e_{31}	e_{33}	e_{15}	$\varepsilon_{11}^S/\varepsilon_0$	$\varepsilon_{33}^S/\varepsilon_0$
150.0	66.0	60.0	146.0	44.0	-4.35	17.5	11.4	1115	1260

contained in Table 1 poled material [30] and an E_c value of 0.5 MV/m was used [31]. The permittivity of the unpoled BaTiO₃ ($\varepsilon_r = 1187.5$) is an average of the constant strain permittivity of poled BaTiO₃ in the 1- and 3-directions. After establishing the distribution of material poled in the z-direction a potential difference, V, was applied between the electrodes of the poled model and the resulting strain used to calculate the effective piezoelectric strain coefficient, d_{33}. The effective permittivity was calculated from the charge (Q) developed at the electrodes and using the relationship $Q = CV$, where C is capacitance.

3.3. Modelling results

Figures 3, 4 and 5 show the modelled data for the piezoelectric d_{33} coefficient, permittivity (ε_{33}^σ) and FOM_{33} as a function of porous layer relative thickness (t_p^{rel}), respectively. The data is averaged from 30 runs at each t_p^{rel} and layer porosity and is shown for the porosity level of 10-60 vol.% in the centre porous layer. Layer porosities of greater than 60 vol.% could not be investigated as this led to a high fraction of 'floating' BaTiO₃ elements, i.e. those surrounded completely by air. These high porosity fractions are also difficult to manufacture (as discussed in the experimental section).

Fig. 3 shows that at low inter-layer porosity levels (≤20 vol.%) there is no significant variation in d_{33} across the full range of t_p^{rel}. However, as the porosity is increased to 30 vol.% and 40
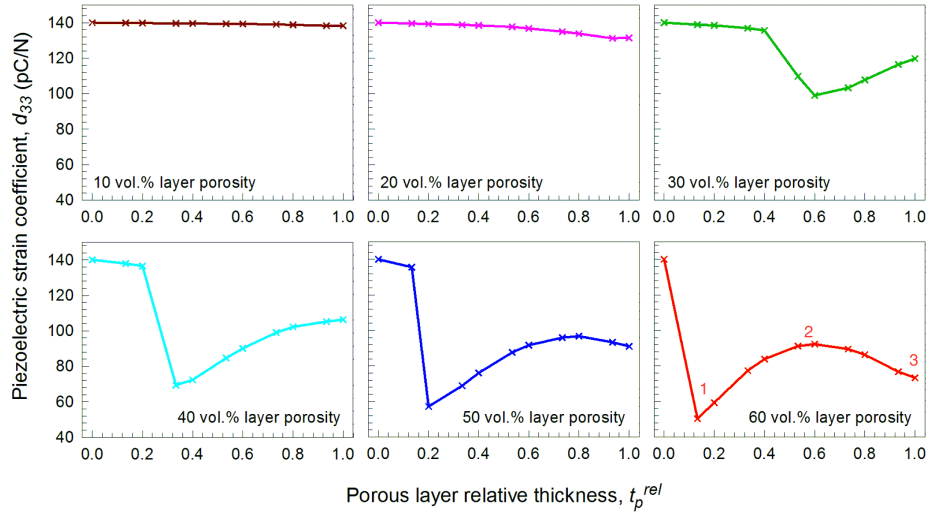
Figure 3: Finite element model data showing the effect of porous layer relative thickness and inter-layer porosity on longitudinal piezoelectric strain coefficient, d_{33}.

vol.% a large decrease in d_{33} is observed as the porous layer relative thickness (t_p^{rel}) is gradually increased from zero. Past the local minima an increase in d_{33} is then observed with increasing t_p^{rel}. For sandwich layer structures with high porosity inter-layers (50 and 60 vol.%) the d_{33} initially falls steeply as t_p^{rel} is gradually increased, before subsequently rising with further increases in t_p^{rel} and eventually reaching a local maxima of d_{33} before declining as t_p^{rel} is further increased toward unity, where we have a uniformly distributed porous BaTiO$_3$. The model prediction of effective d_{33} of the multi-layered structure is intrinsically linked to the fraction of material poled, which can be seen in Fig. 6 where both d_{33} and fraction of BaTiO$_3$ poled in the z-direction are plotted as a function of porous layer thickness and for different layer porosities. The paths followed by both curves are very similar with maximum points occurring at the same relative thickness for all layer porosities. The effective d_{33} appears to be dependent on other factors as well as the fraction of poled material, such as its distribution throughout the structure, but the trend is quite clear when porosity is uniformly distributed throughout the structure, which is shown in Fig. D2. The physical origin of the turning points on the plot discussed in detail later.

The relative permittivity gradually decreases as the relative porous layer thickness increases and the fraction of low permittivity porosity in the inner layer increases, see Fig. 4. The model indicates that the relative permittivity of the overall structure is primarily a function of the amount of high permittivity BaTiO$_3$ material, i.e. the overall relative density, and is not significantly affected by the amount of material poled.

The predicted d_{33} and $\varepsilon_{33}^{\sigma}$ from the model were then used to calculate FOM_{33} using Eqn. 1 and results are shown in Fig. 5. In all cases, the uniformly distributed porosity material (i.e. t_p^{rel} = 1) has a higher FOM_{33} than the dense material (i.e. t_p^{rel} = 0); the value for the dense material is 1.53 pm^2/N. The layered structure at 60% porosity and t_p^{rel} = 0.73 has a FOM_{33} of 2.23 pm^2/N,
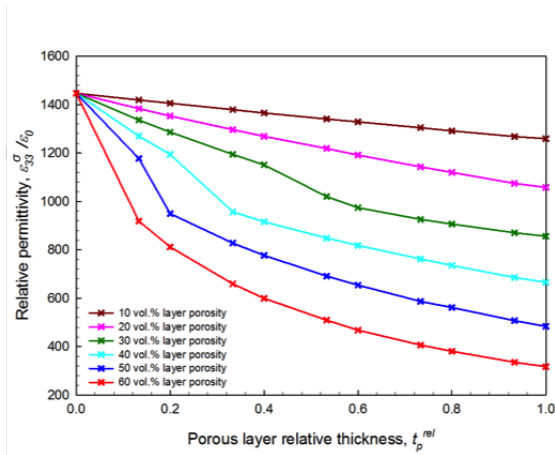
Figure 4: Finite element model data showing the effect of porous layer relative thickness and layer porosity on relative permittivity, which decreases with increasing porosity in all cases, i.e. both as layer thickness and layer porosity are increased.

which is higher than the value of 1.91 pm^2/N for the uniformly distributed porous material at $t_p^{rel} = 1$. This is a result of high d_{33} (Fig. 3) and low permittivity (Fig. 4). The high FOM_{33} indicates the potential of porous sandwich layer structures for piezoelectric energy harvesting applications.

3.4. Discussion

The unusual dependence of the d_{33} and FOM_{33} on relative porous layer thickness (Figs. 3 and 5) is a result of the complex poling behaviour of the structures at high layer porosities (≥ 30 vol.%), resulting in incomplete poling of the structure, (see also in Fig. 6). This can be better understood by analysing the local electric field in each phase (BaTiO$_3$ or air) in the FE model in both the dense and porous layers. Histograms of the electric field in BaTiO$_3$ z-direction (i.e. poling axis) during the poling process of the model at 0.6 MV/m are shown in Fig. 7 for a structure with a layer porosity of 60 vol.% and relative thickness values of 0.2, 0.6 and 0.93 (top, middle and bottom images of Fig. 7, respectively). Images of poled material distributions for corresponding sample geometries and porosity are shown in the histograms with blue regions representing unpoled BaTiO$_3$ elements and red regions are elements poled in the z-direction. A sandwich layer porosity of 60 vol.% was selected to demonstrate how the distribution of poled material changes with porous layer thickness shown in the histograms as the model predicts it has the greatest FOM_{33}; see Fig. 5. The dashed line at 0.5 MV/m indicates the coercive field, E_c: all BaTiO$_3$ elements subjected to fields greater than this value are poled in the z-direction, and contribute to the resulting piezoelectric d_{33} coefficient.

For a low thickness porous layer ($t_p^{rel} = 0.2$), ~80% of BaTiO$_3$ elements in the dense layers have a local z-field of $0.4 < E_f < 0.45$ MV/m, indicating a relatively homogenous field distribution but one that lies below the coercive field so that the BaTiO$_3$ in this layer remains largely unpoled, see the upper histogram and the poling distribution in the inset of Fig. 7. However, high field concentrations in the thin porous layer for both the BaTiO$_3$ and air phase are observed, but
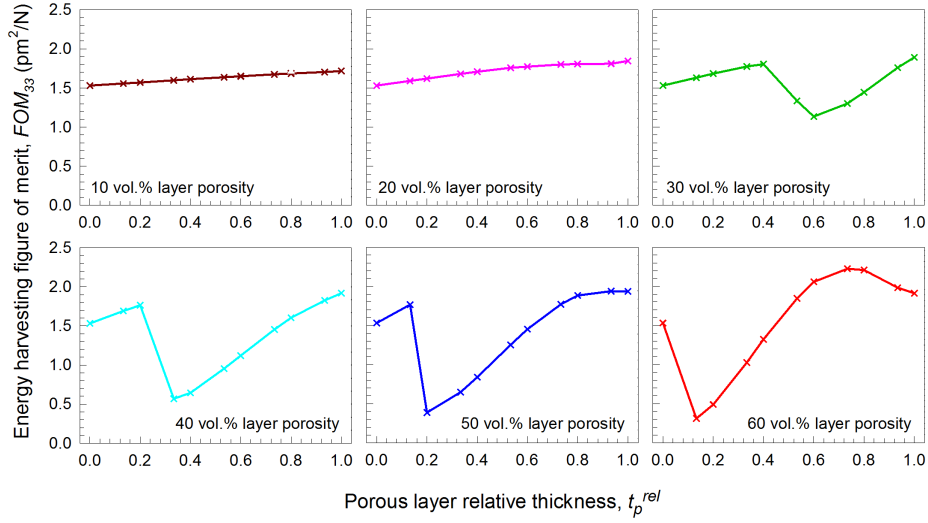
Figure 5: Finite element model data showing the effect of porous layer relative thickness and porosity level of layer on longitudinal energy harvesting figure of merit, FOM_{33} ($d_{33}^2/\varepsilon_{33}^\sigma$).

as the total number of polarizable elements in this thin region is low, the total volume fraction poled and d_{33} is low, see Fig. 6. When $t_p^{rel} = 0.6$ (middle histogram and poling distribution inset, Fig. 7) the electric field in the dense layer remains relatively homogenous, however there is a shift towards lower field strengths compared to $t_p^{rel} = 0.2$ so there is almost no poling of the dense BaTiO$_3$ layers. Once again the electric field concentrates in the central porous layer of lower permittivity, with the highest fields in the air phase. A more homogenous distribution of field in the porous layer is observed for $t_p^{rel} = 0.6$ compared to $t_p^{rel} = 0.2$ and over 50% of elements in this central layer are greater than the coercive field and are poled, leading to the increase in d_{33} for a layer porosity of 60 vol.% from $0.2 < t_p^{rel} < 0.6$, as seen in Fig. 6.

As the layer porosity is further increased to $t_p^{rel} = 0.93$ (lower histogram and poling distribution inset, Fig. 7) the field strengths in the dense layers shift to even lower magnitudes, such that no material is poled in the thin outer dense layers. This can be explained by examination of Fig. 1, whereby the regions above and below a low permittivity region (i.e. the pore in Fig. 1 or the porous layer in the layered structure) and parallel to the applied field are subject to the lowest electric fields and are not poled in the direction of the field. The field in the porous layer in both the BaTiO$_3$ and the air is the most homogenous for this thick porous layer, however, due to a the shift to lower field strengths, less than 25% of the BaTiO$_3$ volume in the porous layer is subjected to fields above E_c. As a result, the d_{33} decreases for $t_p^{rel} = 0.93$ compared to $t_p^{rel} = 0.6$.

These results indicate that the presence of a thin porous layer with high porosity leads to high field concentrations in both the BaTiO$_3$ and air in the porous layer, compared to when the porous layer is relatively thick. As a result of Gauss' Law (Eqn. 3), the electric field increasingly concentrates in the porous layer as the ratio between the effective permittivity of the dense and porous layers increases, i.e. as the porosity in the central layer increases. When the porosity in
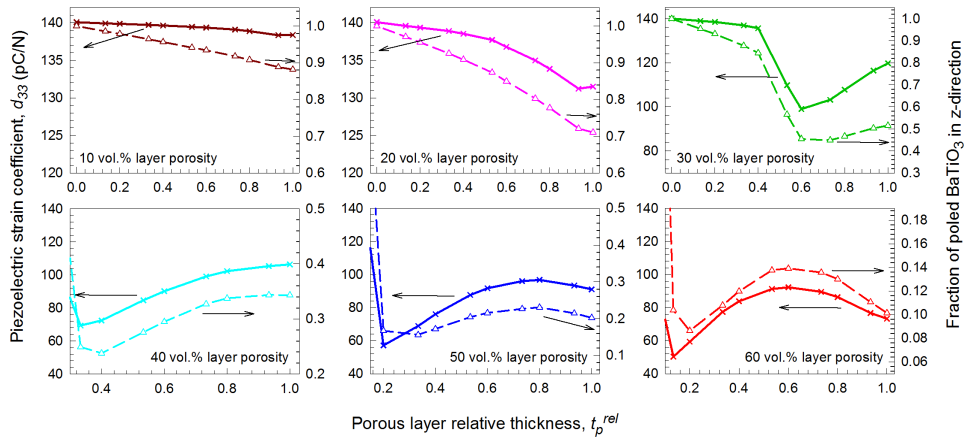
94

Figure 6: Finite element model data of effect of sandwich layer relative thickness and porosity on the d_{33} (left axes, solid lines) and fraction of poled BaTiO$_3$ in z-direction (right axes, dashed lines), demonstrating the link between the fraction of material poled in the z-direction and the effective piezoelectric properties of the material.

the inner layer is large ($\geq$ 30 vol.%), the high fields in the porous region for thin porous layers (i.e. low t_p^{rel}) result in a high fraction of ceramic in the porous layer becoming poled. However the volume of BaTiO$_3$ in the porous layer is low relative to the total volume material, hence there is a rapid decrease in d_{33} (Fig. 3, points 1 $\rightarrow$ 2). As the porous layer thickness and volume is increased, the electric field strengths in this layer decrease but are still sufficiently large to pole a high fraction of BaTiO$_3$ in this region, leading to an increase in d_{33} (Fig. 3, points 2 $\rightarrow$ 3). This phenomenon is only observed when the layer porosity is $\geq$ 30 vol.% so that there is a large difference between the effective permittivity of the dense and porous layers. When the porosity of the central layer is low (10 and 20 vol.%) the ratio of the permittivity of the dense and porous layers is also low, and while the electric field continues to concentrate in the porous layer the decrease in field in the dense layers is not sufficiently large to fall below the coercive field, E_c, so that most of the BaTiO$_3$ elements are poled, contributing to the high d_{33} values observed from 0 $\leq t_p^{rel} \leq$ 1 (see Fig. 6). At very high layer porosities ($\geq$ 50 vol.%) a peak value for d_{33} is observed before a decrease with further increases in t_p^{rel} as there is no longer a sufficient field concentration in the porous layer to pole a significant fraction of the BaTiO$_3$ material, thus leading to a decrease in d_{33} (Fig. 3, points 3 $\rightarrow$ 4).

4. Experimental

4.1. Fabrication of BaTiO$_3$ with porous sandwich layer

Sandwich layer structures were manufactured to compare with the modelling outputs. In order to fabricate the dense outer layers the starting powder was produced by ball milling barium titanate powder (Ferro, UK) with 5 wt.% binder, polyethylene glycol (PEG) (Sigma, UK) in distilled water for 24 h before drying and regrinding. To form the inner porous layer the burned out polymer spheres (BURPS) process was used, with the starting powder produced by dry-mixing
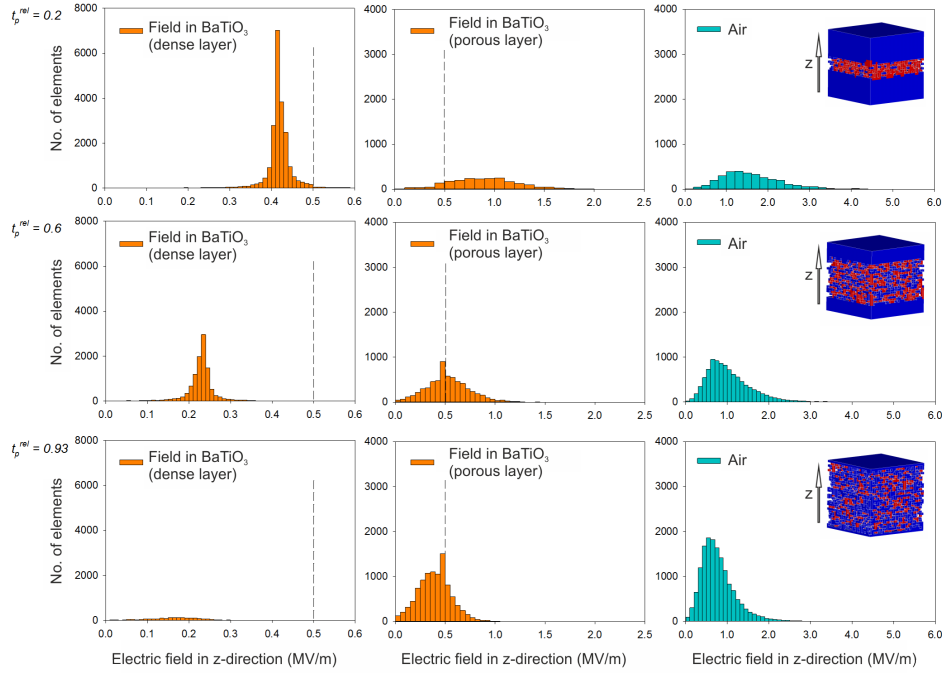
95

Figure 7: Histograms showing electric field distribution in elements of dense barium titante layer (left), barium titanate phase in the porous layer (centre) and air (right) for ~60 vol.% layer porosity at $t_p^{rel} = 0.2$ (top), $t_p^{rel} = 0.6$ (middle) and $t_p^{rel} = 0.93$ (bottom). The dashed vertical line at 0.5 MV/m represents the coercive field, E_c, of BaTiO$_3$; BaTiO$_3$ elements subjected to fields above this line are considered 'poled'. Typical distributions of unpoled BaTiO$_3$ elements (blue regions) and poled elements (red regions) are shown for each geometry as insets on the right.

the barium titanate powder with varying proportions of PEG (25 and 35 wt.%) to enable the production of layered structures with different sandwich layer porosities. Green barium titanate pellets (13 mm diameter) were formed by alternately adding dense and porous starting powder into the uniaxial pellet die, gently flattening the powder between each layer and pressing at 185 MPa. The ratio of the amount of dense and porous starting powder was varied to produce layers of different relative thicknesses whilst attempting to achieve similar final pellet dimensions. Pressureless sintering of the green ceramics was conducted in air at 1300°C for 2 h, which included a 2 h dwell stage on the up-ramp at 400°C to burn off the PEG pore forming agent. The ramp rate throughout the sintering process was 60°C/h. Post sintering, samples were ground flat and cleaned, silver electrodes were applied (RS Components, Product No 186-3600) and the layered structures were then subjected to corona poling in air at 115°C with a 14 kV field applied from a 35 mm point source. These processing conditions are similar to those detailed in Ref. [3] to allow comparison between fully dense, fully porous (uniform distribution of porosity) and the porous sandwich layer barium titanate, as in Fig. 2. Using >20 wt.% of PEG was found to reduce cracking during the pressing stage, such that producing samples with a lower inter-layer porosity was not achievable using the fabrication methods used in this investigation. Other methods, such as tape casting have previously demonstrated the potential for forming layered structures with
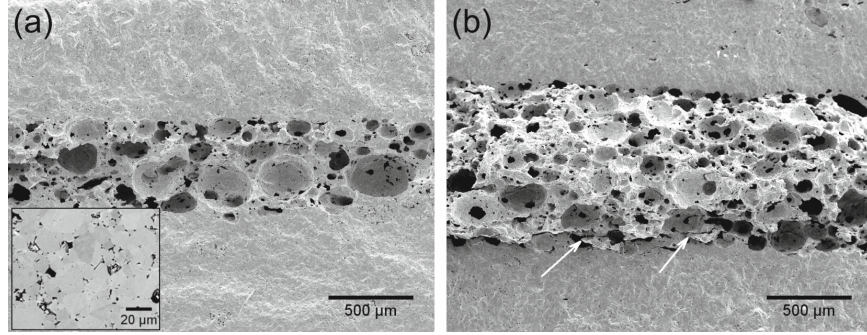
Figure 8: SEM of fracture surface of cross section of BaTiO$_3$ with porous sandwich layer (porosity $\sim$ 60 vol.%) with (a) porous layer thickness, t_p^{rel} $\sim$0.25 and relative density $\sim$80%; SEM of dense outer-layer shown as inset, and (b) t_p^{rel} $\sim$ 0.48, relative density $\sim$66% with small cracks at interface between middle and bottom layers (shown by arrows); the porous layer in this image is on a small angle with respect to the dense layers, which was a common occurrence.

inter-layer porosities of less than 30 vol.% [10, 11, 15]. Very high levels of porosity (>60 vol.%) cause a significant reduction in mechanical properties and so were not investigated.

Piezoelectric strain coefficients, d_{33} and d_{31}, were measured using a Take Control Piezometer PM25 system. The dielectric properties of the material were measured via impedance spectroscopy using a Solartron 1260 and 1296 Dielectric Interface over a frequency range of 1 Hz to 1 MHz, and reported in this paper at 1 kHz. Optical and scanning electron microscopy (SEM) were used to investigate the bulk laminate structure and the porous microstructure. The relative density and apparent porosity of the samples was measured using the Archimedean method.

The porous layer relative thickness, t_p^{rel}, was estimated from the average relative density measured of the dense layers ($\rho_{rel} = 0.93$) and the average relative densities of the porous layer as a result of the amount of pore former used in the starting powder from previous work [3]: ρ_{rel} = 0.40 for 35 wt.% PEG and ρ_{rel} = 0.50 for 25 wt.% PEG. This was compared to measurements taken from SEM images using ImageJ software and found to be a satisfactory estimate.

4.2. Structural characterisation of layered materials

After sintering, the relative density of the dense layers was found to be 0.93, slightly lower than the density achieved in the uniform dense material (ρ_{rel} = 0.95 [3]). This was likely to be due to the lower pressing force required to produce crack-free sandwich layered samples. SEM images of two sandwich-layered structures with two different thicknesses are shown in Fig. 8 (t_p^{rel} of $\sim$0.25 and $\sim$0.48). All samples were polycrystalline with grain sizes in the range of 10-30 μm; the microstructure from a dense layer with ρ_{rel} = 0.93 is shown as an inset to Fig. 8a. Despite lowering the pressing force some small cracks could be observed between layers perpendicular to the pressing direction in Fig. 8b, which are thought to form during sintering, where differences in shrinkage between the porous and dense layers can cause thermal stresses. An additional difficulty encountered during the preparation of samples was achieving layers exactly perpendicular to the pressing direction that may have had an effect on the repeatability of results; a porous sandwich layer with a small slanted orientation with respect to the parallel outer dense surfaces of the layered BaTiO$_3$ can be seen in Fig. 8b.
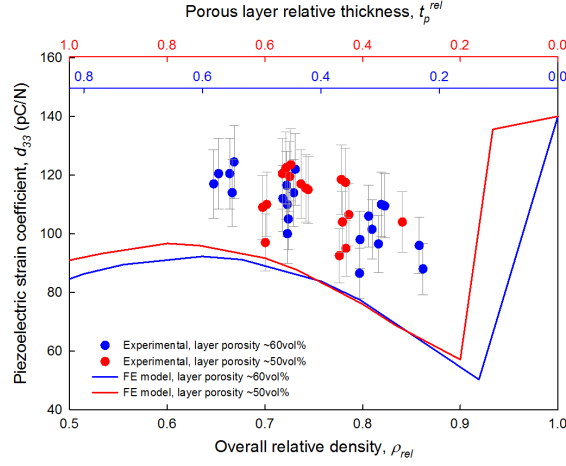
Figure 9: Comparison of experimental longitudinal piezoelectric coefficient, d_{33}, of BaTiO$_3$ porous sandwich layer structures with FE model. Data is shown across range of overall relative densities for layer porosities of 50 and 60 vol.%, in red and blue, respectively. Top axis in gives estimated porous layer relative thickness for corresponding relative density. Error bars at ±10% (accuracy of measurement device).

4.3. Piezoelectric strain coefficients, d_{33} and d_{31}

The measured longitudinal piezoelectric strain coefficient, d_{33}, exhibited a similar trend as predicted by the FE model and is shown in Fig. 9, as a function of both relative density (bottom x-axis) and porous layer relative thickness, t_p^{rel} (top x-axes with colours relevant to the data sets), for both 50 and 60 vol.% layer porosity for a poling voltage of 0.6 MV/m in the model. A comparison of the effect of using higher poling fields in the model (0.7 and 0.8 MV/m) for these sample conditions is shown in the supplementary information, Fig. D3, indicating that higher effective d_{33} values (i.e. more complete poling) may be achievable if it were possible to experimentally pole porous samples at larger electric fields. However, dielectric breakdown occurs at lower field strengths than for dense samples due to field concentrations around the pores, which is a practical limitation of processing these materials. The experimental data was found to be higher than in the model, which is thought to be due to differences in the applied fields between the model and during corona poling of the manufactured samples (i.e. the experimental samples exhibited a higher degree of poling than was observed in the model). Both experimental data and the model indicate the porosity of the sandwich layer was not found to have a significant influence on the d_{33} coefficients in the t_p^{rel} region studied, with maximum experimental values of >120 pC/N measured in structures with different porosity sandwich layers and overall relative density of ~0.70, values which are comparable to that of dense BaTiO$_3$ [3] (average d_{33} = 124.8 pC/N). These values are higher than d_{33} observed in uniformly distributed porous BaTiO$_3$ with similar levels of porosity as the inner layer (average of 86.8 pC/N for 60 vol.% porosity and 99.5 pC/N for 50 vol.% porosity [3]) and overall porosity of 32 vol.%, i.e. ρ_{rel} = 0.68 (average d_{33} = 102.4 pC/N).

The transverse piezoelectric coefficient, d_{31}, shown in Supplementary Information Fig. D4, also reduces with increasing layer thickness, and coupled with high d_{33}, values would lead to
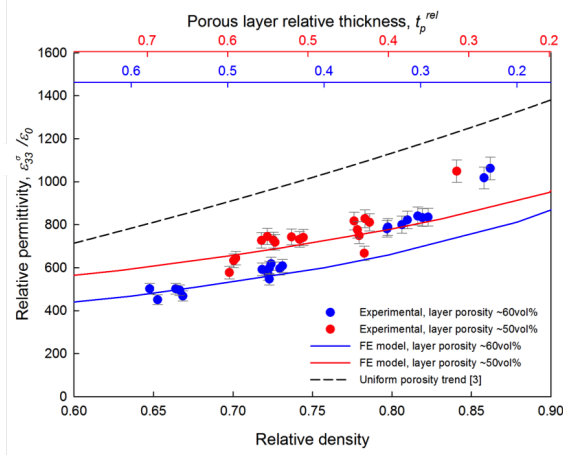
98

Figure 10: Comparison of relative permittivity, $\varepsilon^{\sigma}_{33}/\varepsilon_0$, measured from manufactured porous layer samples (points) with data from FE model (coloured lines) and samples with uniform porosity from previous study (dashed black line) [3]. Data is shown for two layer porosities, 50 and 60 vol.%, in red and blue, respectively. Porous layer relative thickness corresponding to layer both layer porosities are on the upper x-axes. Error bars of ±5% are attributed to measurement error of sample dimensions.

significantly improved hydrostatic piezoelectric coefficient, $d_h = d_{33} + 2d_{31}$; this may make layered porous structures of interest for use in other applications such as hydrostatic sensors (high d_h or g_h). It is of interest to note that the low d_{31} of the porous sandwich layers structures manufactured in this work make them unsuitable for 31-mode mode energy harvesters (FOM_{31}), such as cantilevers, where high d_{31} coefficients are necessary, see Eqn. 1 and 2.

4.4. Permittivity and FOM_{33}

The permittivity of porous sandwich layer structures reduced with increasing porous layer relative thickness and with an increase in the porosity level of the layer. This is shown in Fig. 10 as a function of relative density (bottom x-axis) and porous layer relative thickness (top x-axes with colours relevant to the data sets). The FE model (solid line in Fig. 10) provides a good fit the experimental data (points), particularly when $\rho_{rel} < 0.75$. Concentrating the porosity in a sandwich layer, rather than being uniformly distributed, was found to be beneficial in terms of reducing permittivity as can be seen by comparing the fit of the experimental data for uniformly porous BaTiO$_3$ (dashed black line), from Ref. [3], to the sandwich layer materials in Fig. 10. This may also be beneficial in terms of elastic compliance, S^E_{33}, as lower permittivities are observed in sandwich structures for the same overall volume of porosity than in uniform porous materials; further work is necessary to characterise any potential improvement in terms of compliance and the resulting effect on electromechanical coupling coefficient, k^2_{ij}, see Eqn. 2. The findings presented here indicate that tuning of the permittivity is possible by careful positioning of the porosity within the inner layer of the structure.

The longitudinal energy harvesting figure of merit, FOM_{33}, was calculated from the experimental d_{33} and $\varepsilon^{\sigma}_{33}$ data using Eqn. 1, and is shown in Fig. 11 as a function of relative density, alongside data obtained for BaTiO$_3$ with uniformly distributed porosity that is reported elsewhere [3]. The combined effect of high d_{33} values that are comparable to that of dense BaTiO$_3$

99

Table 2: Comparison of average and maximum longitudinal piezoelectric coefficients (d_{33}), relative permittivity ($\varepsilon_{33}^{\sigma}/\varepsilon_0$) and energy harvesting figure of merit (FOM_{33}) for dense, uniformly distributed porous (from previous investigation [3]) and layered porous barium titanate.

Sample type	Average relative density (%)	Sandwich layer relative thickness	Sandwich layer porosity (vol.%)	Average d_{33} (pC/N)	Max d_{33} (pC/N)	Average $\varepsilon_{33}^{\sigma}/\varepsilon_0$	Average FOM_{33} (pm²/N)
Dense	94.9			124.8	144.5	1527	1.31
Uniform porous	88.8			95.8	107.5	1362	0.76
	80.7			91.8	99.5	1170	0.81
	68.0			102.4	106.0	794	1.49
	62.4			98.0	109.0	759	1.43
	50.2			99.2	113.0	528	2.11
	39.2			88.9	99.0	377	2.37
	34.0			61.3	74.5	284	1.49
	27.7			42.5	48.0	167	1.22
Sandwich	86.0	0.15	60	92.0	96.0	1040	0.92
	81.5	0.23	60	104.7	110.0	826	1.50
	72.5	0.40	60	114.9	122.0	583	2.56
	66.0	0.52	60	119.3	124.5	484	3.34
	84.1	0.22	50	104.0	104.0	1049	1.16
	78.1	0.36	50	99.5	106.5	801	1.41
	73.5	0.46	50	118.1	123.5	732	2.15

(Fig. 9) and significant reductions in permittivity compared to both dense and uniform porous BaTiO$_3$ (Fig. 9) resulted in a maximum FOM_{33} = 3.74 pm²/N (layer porosity ~60 vol.%, t_p^{rel} = 0.52), which is a factor of 2.65 higher than the value for dense BaTiO$_3$ (FOM_{33} = 1.40 pm²/N) and 1.3 times higher than highest FOM_{33} for porous BaTiO$_3$ with uniformly distributed porosity (FOM_{33} = 2.85 pm²/N and ~60 vol.% porosity), see Fig. 11. Data for the measured d_{33}, $\varepsilon_{33}^{\sigma}$ and FOM_{33} is summarised in Table 2 for dense BaTiO$_3$, BaTiO$_3$ with uniformly distributed porosity and the layered structures manufactured for this work. The increase in FOM_{33} demonstrates the potential for ferroelectric porous sandwich layer structures for applications such as energy harvesting.

5. Conclusions

This paper describes the modelling, fabrication and characterisation of novel layered barium titanate ceramics that have been produced with dense outer layers and a porous 'sandwich' layer. Properties have been evaluated both numerically and experimentally for their energy harvesting capabilities and compared to both dense BaTiO$_3$ and BaTiO$_3$ with uniformly distributed porosity. It was found that d_{33} values increased with porous layer relative thickness in materials with high porosity layers, a counterintuitive phenomenon that has not been observed previously.

Finite element modelling was used to demonstrate that the increase in d_{33} with porous layer thickness, observed at high internal layer porosities ($\geq$30 vol.%), was due to complexities in the poling of these ferroelectric materials that caused them become only partially poled in the direction of the applied poling field. This effect was more pronounced in structures with a high porosity sandwich layer due to large differences in effective permittivity between dense and porous layers causing high field concentrations in the porous layer. The amount of polarizsable material
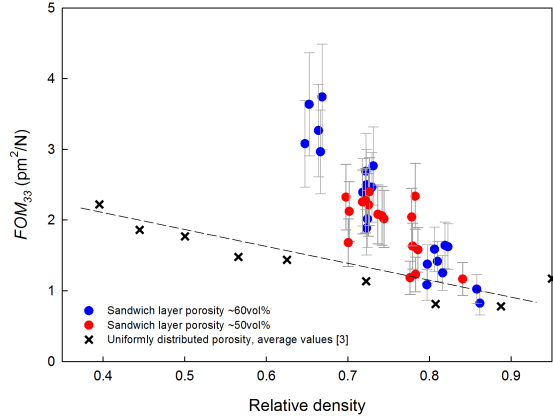
Figure 11: FOM_{33} ($d_{33}^2/\varepsilon_{33}^\sigma$) for manufactured porous sandwich layer BaTiO$_3$ (red and blue points for 50 and 60 vol.% layer porosity, respectively) as a function of relative density. Average values for uniform porous samples from previous study are shown for comparison. Dashed black line is an approximate trend of uniform porous data to act as a guide for the eye. Error bars at ±20% (cumulative error).

in the porous layer was found to be important with regard to measured piezoelectric properties in materials with high inter-layer porosities, such that increases in d_{33} were observed with increasing porous layer thickness, i.e. increased levels of porosity. This resulted in a predicted optimum layer porosity (60 vol.%) and relative thickness ($t_p^{rel} = 0.73$) to maximise the modelled energy harvesting figure of merit. Good agreement with experimental data was observed that could not have been predicted using a model that assumes the material is fully poled. The modelling approach developed in this paper has shown the importance of considering the complex distribution of poled material that is likely to occur when manufacturing and poling porous ferroelectric materials.

High longitudinal piezoelectric d_{33} coefficients, comparable to those measured in dense BaTiO$_3$ (~120 pC/N), were observed experimentally in porous sandwich layer structures using high porosity (≥50 vol.%) layers with a high porous layer thickness ($t_p^{rel} = 0.52$). The high d_{33}, coupled with the low permittivity, leads to high longitudinal energy harvesting figures of merit, FOM_{33}, that were found to improve on harvesting figures of merits measured in both dense and uniform porous BaTiO$_3$ by factors of 2.65 and 1.30, respectively. These significant improvements demonstrate the potential of porous sandwich layer ferroelectric ceramics to design high performance materials for energy harvesting and sensing applications.

References

[1] R. A. Islam, S. Priya, Realization of high-energy density polycrystalline piezoelectric ceramics, Appl. Phys. Lett. 88 (2006) 032903.

[2] R. E. Newnham, D. P. Skinner, L. E. Cross, Connectivity and piezoelectric-pyroelectric composites, Mater. Res. Bull. 13 (1978) 525–536.

[3] J. I. Roscow, J. Taylor, C. R. Bowen, Manufacture and characterization of porous ferroelectrics for piezoelectric energy harvesting applications, Ferroelectr. 498 (2016) 40–46.

[4] G. H. Haertling, Ferroelectric Ceramics: History and Technology, J. Am. Ceram. Soc. 82 (1999) 797–818.

[5] I. S. Grant, W. R. Phillips, Electromagnetics, in: Electromagnetics, 1990.

[6] R. W. C. Lewis, A. C. E. Dent, R. Stevens, C. R. Bowen, Microstructural modelling of the polarization and properties of porous ferroelectrics, Smart Mater. Struct. 20 (2011) 085002.

[7] T. Zeng, X. Dong, S. Chen, H. Yang, Processing and piezoelectric properties of porous PZT ceramics, Ceram. Int. 33 (2007) 395–399.

[8] R. W. Rice, Evaluation and extension of physical property-porosity models based on minimum solid area, J. Mater. Sci. 31 (1996) 102–118.

[9] A. P. Roberts, E. J. Garboczi, Elastic properties of model porous ceramics, J. Am. Ceram. Soc. 83 (2000) 3041–3048.

[10] A. Navarro, R. W. Whatmore, J. R. Alcock, Preparation of functionally graded PZT ceramics using tape casting, J. Electroceram. 13 (2004) 413–415.

[11] C. P. Shaw, R. W. Whatmore, J. R. Alcock, Porous, Functionally Gradient Pyroelectric Materials, J. Am. Ceram. Soc. 90 (2007) 137–142.

[12] Q. G. Chi, W. L. Li, W. D. Fei, Y. Zhao, Enhanced performance of sandwich structure $Pb_{0.8}La_{0.1}Ca_{0.1}T_{0.975}O_3$ thin film for pyroelectric applications, Mater. Lett. 63 (2009) 1712–1714.

[13] Q. Chi, J. Dong, C. Zhang, X. Wang, Q. Lei, Highly (100)-oriented sandwich structure of $(Na_{0.85}K_{0.15})_{0.5}Bi_{0.5}TiO_3$ composite films with outstanding pyroelectric properties, J. Mater. Chem. C 4 (2016) 4442–4450.

[14] C. R. Bowen, J. Taylor, E. LeBoulbar, D. Zabek, A. Chauhan, R. Vaish, Pyroelectric materials and devices for energy harvesting applications, Energy Environ. Sci. 7 (2014) 3836–3856.

[15] L. Palmqvist, K. Palmqvist, C. P. Shaw, Porous multilayer PZT materials made by aqueous tape casting, Key Eng. Mater. 333 (2007) 215–218.

[16] E. Mercadelli, A. Sanson, P. Pinasco, E. Roncari, C. Galassi, Tape cast porosity-graded piezoelectric ceramics, J. Eur. Ceram. Soc. 30 (2010) 1461–1467.

[17] D. Piazza, C. Capiani, C. Galassi, Piezoceramic material with anisotropic graded porosity, J. Eur. Ceram. Soc. 25 (2005) 3075–3078.

[18] H. R. Gallantree, Piezoelectric ceramic/polymer composites, British Ceramics Proceedings 41 (1989) 161.

[19] H. Banno, Effects of porosity on dielectric, elastic and electromechanical properties of $Pb(Zr, Ti)O_3$ ceramics with open pores: A theoretical approach, Jpn. J App. Phys., Part 1 32 (1993) 4214–4217.

[20] M. L. Dunn, M. Taya, Electromechanical properties of porous piezoelectric ceramics, J. Am. Ceram. Soc. 76 (1993) 1697–1706.

[21] C. R. Bowen, H. Kara, Pore anisotropy in 3-3 piezoelectric composites, Mater. Chem. Phys. 75 (2002) 45–49.

[22] F. Levassort, M. Lethiecq, R. Desmare, L. P. Tran-Huu-Hue, Effective electroelastic moduli of 3-3(0-3) piezocomposites, IEEE Trans. Ultrason., Ferroelect., Freq. Control 46 (1999) 1028–1034.

[23] C. R. Bowen, V. Y. Topolov, Piezoelectric sensitivity of $PbTiO_3$-based ceramic/polymer composites with 03 and 33 connectivity, Acta Mater. 51 (2003) 4965–4976.

[24] R. Ramesh, H. Kara, C. R. Bowen, Finite element modelling of dense and porous piezoceramic disc hydrophones., Ultrason. 43 (2005) 173–81.

[25] R. Kar-Gupta, T. A. Venkatesh, Electromechanical response of porous piezoelectric materials: Effects of porosity distribution, Appl. Phys. Lett. 91 (2007) 062904.

[26] S. Iyer, T. A. Venkatesh, Electromechanical response of porous piezoelectric materials: Effects of porosity connectivity, Appl. Phys. Lett. 97 (2010) 072904.

[27] K. S. Challagulla, T. A. Venkatesh, Electromechanical response of piezoelectric foams, Acta Mater. 60 (2012) 2111–2127.

[28] P. W. Bosse, K. S. Challagulla, T. A. Venkatesh, Effects of foam shape and porosity aspect ratio on the electromechanical properties of 3-3 piezoelectric foams, Acta Mater. 60 (2012) 6464–6475.

[29] S. Iyer, M. Alkhader, T. A. Venkatesh, Electromechanical Response of Piezoelectric Honeycomb Foam Structures, J. Am. Ceram. Soc. 97 (2014) 826–834.

[30] A. C. Dent, C. R. Bowen, R. Stevens, M. G. Cain, M. Stewart, Effective elastic properties for unpoled barium titanate, J. Eur. Ceram. Soc. 27 (2007) 3739–3743.

[31] D. Berlincourt, H. A. Krueger, C. Near, Properties of Morgan electro ceramic ceramics, Technical Publication TP-226, Morgan Electroceramics (1999) 1–12.

[32] G. H. Kwei, A. C. Lawson, Structures of the ferroelectric phases of barium titanate, J. Phys. Chem. 97 (1993) 2368–2377.

5.2   Summary

The research in this chapter further demonstrated the potential for porous ferroelectric materials for energy harvesting applications, building on the work in Chapters 2, 3 & 4. The key findings of this chapter can be summarised as:

1. A finite element model was developed that demonstrated that the introduction of porosity leads to complex field distributions during the poling process and results in incomplete poling of the ferroelectric material, building on earlier work by *Lewis et al. (2011)*. This is particularly important for the porous sandwich layer materials in which the high permittivity dense layers act to concentrate the field into the low permittivity porous layer. An optimum porous layer relative thickness of 0.73 and porosity of 60 vol.% was predicted to yield the highest figure of merit due to high longitudinal piezoelectric strain coefficients, d_{33}, resulting from a high fraction of material poled coupled with low permittivity.

2. The modelling studies were validated with experimental data obtained from samples fabricated by a modified burned out polymer spheres process. Although there were discrepencies between the model and the experimental work in terms of exact values, the observed trend in which d_{33} increased with increasing porosity was of significant interest for energy harvesting applications and had not been reported elsewhere previously. This behaviour could not have been predicted a model that did not consider the distribution of poled material with a porous ferroelectric material.

3. Concentrating porosity into a single layer was found to be an effective method for reducing permittivity at a faster rate than when porosity was uniformly distributed throughout the structure for a given overall porosity. This is of significance for energy harvesting and other applications that require high voltage (g) coefficients, such as SONAR devices.

4. A maximum energy harvesting figure of merit of 3.74 pm^2/N was measured in barium titante with an inner layer porosity of 60 vol.% and a relative layer thickness of 0.52, which was significantly higher than both the highest measured for dense barium titanate (1.40 pm^2/N) and uniform porous barium titanate (2.85 pm^2/N) as discussed in Chapter 3.

This work further demonstrated that careful control of porous structure is an effective method for tuning the material properties of ferroelectric ceramics for specific applications. The single pore model presented in the first part of the paper helped to explain the results from the more complex network model; both models are developed further in Chapter 6 to investigate the effect of pore morphology on the poling behaviour and piezoelectric properties of freeze cast barium titanate.

Chapter 6

Poling behaviour of freeze cast porous barium titanate with enhanced piezoelectric energy harvesting properties

6.1 Context

The final paper in this thesis investigates the properties of highly aligned porous barium titanate formed via the freeze casting method, which was highlighted in Chapter 2 as being a processing route of interest due to high d_{33} coefficients reported in the literature for freeze cast lead zirconate titanate (PZT) (*Guo et al. (2015), Lee et al. (2007), Lee et al. (2009), Zhang et al. (2015) and Zhang et al. (2017)*). Firstly, the single pore model is used to demonstrate the effect of pore aspect ratio and angle with respect to the poling field on the poling behaviour of porous ferroelectric materials. The porous network model used in Chapter 5 is adapted for freeze cast-type structures and freeze cast barium titanate was fabricated to provide experimental comparison with modelled data. Finally, a demonstration of the enhanced energy harvesting capabilities of porous ferroelectric ceramics is presented, with dense and porous barium titanate mechanically excited and the harvested electrical energy used to charge a capacitor.

As detailed in Chapter 1, Fig. 1-1, another publication is closely related to the work presented in this chapter: Y. Zhang, M. Xie, J. I. Roscow et al. *Enhanced pyroelectric and piezoelectric propeties of PZT with aligned porosity for energy harvesting applications*, J. Mater. Chem. A **5** (2017), demonstrates the potential of porous ferroelectrics for pyroelectric harvesting.

The freeze casting set up used to produce experimental samples in this chapter is discussed in more detail in Appendix F and the MATLAB script for generating 2-2 type structures is contained in Appendix G.

Statement of Authorship

This declaration concerns the article entitled:								
Freeze cast porous barium titanate with enhanced piezoelectric energy harvesting capabilities								
Publication status (tick one)								
draft manuscript	✓	**Submitted**		**In review**		**Accepted**		**Published**
Publication details (reference)	J.I. Roscow, Y. Zhang, M.J. Krasny , R.W.C. Lewis, J. Taylor, & C.R. Bowen							
Candidate's contribution to the paper (detailed, and also given as a percentage).	The candidate contributed to/ considerably contributed to/predominantly executed the Formulation of ideas: Solely the candidate (100%) Design of methodology: Experimental method designed by candidate (100%), modelling method designed by candidate in collaboration with R.W.C. Lewis (80% candidate), energy harvesting demonstration rig designed by M.J. Krasny Experimental work: Sample fabrication and characterisation by candidate (100%), energy harvesting experiments done by candidate in collaboration with M.J. Krasny (30% candidate) Presentation of data in journal format: Solely the candidate (100%)							
Statement from Candidate	This paper reports on original research I conducted during the period of my Higher Degree by Research candidature.							
Signed						**Date**		30/11/17

PAPER 6: Freeze cast porous barium titanate with enhanced piezoelectric energy harvesting capabilities

J.I. Roscow[a], Y. Zhang[a], M.J. Krasny[a], R.W.C. Lewis[b], J. Taylor[c], & C.R. Bowen[a]

[a]*Department of Mechanical Engineering, University of Bath, Bath, UK*
[b]*Renishaw Plc., Wooton-under-Edge, Gloucestershire, UK*
[c]*Department of Electrical and Electronic Engineering, University of Bath, UK*

Abstract

Barium titanate with highly aligned porosity, fabricated using the freeze casting method, is shown in this paper to improve the energy harvesting capabilities compared to the dense material. Energy harvesting is an important developing technology that may be used to develop a new generation of self-powered sensor networks. Two finite element models are presented that investigate (i) the effect of pore morphology and angle with respect to poling field, and (ii) the effect of common microstructural characteristics of water-based freeze cast ceramics, on the poling behaviour of ferroelectric materials and their resultant piezoelectric, dielectric and energy harvesting properties. Porous barium titanate was fabricated using the freeze casting method, producing highly aligned structures with excellent longitudinal piezoelectric strain coefficients, d_{33}, that compared well with the fully dense material: freeze cast barium titanate with 45 vol.% porosity was found to have a maximum d_{33} = 134.5 pC/N, compared to a maximum of d_{33} = 144.5 pC/N for dense barium titanate. The d_{33} coefficients of the freeze cast porous barium titanate were higher than barium titanate with uniformly distributed spherical porosity, which was predicted by the modelling study and thought to be due to more complete poling of the aligned structures. Introducing porosity resulted in large reductions in the constant stress permittivity ($\varepsilon_{33}^{\sigma}$) of the barium titanate leading to increases in energy harvesting figure of merit, $d_{33}^2/\varepsilon_{33}^{\sigma}$, with a maximum of 3.79 pm^2/N found for 45 vol.% porous barium titanate, significantly higher than that of dense barium titanate ($\sim$1.40 pm^2/N). Dense and porous barium titanate was mechanically excited on a shaker and the rectified current used to charge a capacitor, with the porous barium titanate found to charge the capacitor to a voltage of 234 mV compared to 96 mV for the dense material, a 2.4-fold increase, similar to that predicted by the respective energy harvesting figures of merit.

1. Introduction

Energy harvesting, the process of recapturing energy from ambient sources, such as mechanical vibrations and waste heat, and converting it to useful electrical energy, has received increasing attention in recent years with the development of low powered electronics and wireless sensor technologies [1]. Ferroelectric ceramics are of particular interest to this field due to their ability to directly convert vibrational energy to electrical energy via the piezoelectric effect and thermal fluctuations into electrical energy via the pyroelectric effect [2, 3]. Figures of merit for both piezoelectric and pyroelectric energy harvesting have been derived from the change of energy within a poled ferroelectric material due to an applied stress (piezoelectric) or change in temperature (pyroelectric). The piezoelectric harvesting figure of merit for off-resonance, low frequency (<<100 kHz) vibration is given by [4]:

$$FoM_{ij} = \frac{d_{ij}^2}{\varepsilon_{33}^\sigma} \qquad (1)$$

where d_{ij} is the piezoelectric strain coefficient (subscripts denote the direction of applied stress (j) with respect to the poling direction (i)) and ε_{33}^σ is the permittivity at constant stress. The pyroelectric energy harvesting figure of merit is given by [5]:

$$F_E' = \frac{p^2}{c_E^2 . \varepsilon_{33}^\sigma} \qquad (2)$$

where p is the pyroelectric coefficient and c_E is the volume specific heat capacity. Simple analysis of the figures of merit demonstrate that when selecting a ferroelectric material for energy harvesting from mechanical or thermal vibrations it should have a high piezoelectric strain or pyroelectric coefficient coupled with low permittivity. Generally speaking, ferroelectric materials with the highest piezo- and pyroelectric coefficients also have high permittivities, however, introducing porosity has been shown to provide a cost-effective way of tuning the properties of these materials by reducing the permittivity whilst maintaining a relatively high d_{33} [6].

As sintered, ferroelectric ceramics display no piezoelectric or pyroelectric properties as domains within the material are randomly orientated [7]. Ferroelectric materials are poled under electric fields after sintering to orientate domains, which exist below the Curie temperature, yielding a net polarisation that in turn leads to piezoelectric and pyroelectric behaviour. It has been shown previously that the decrease in piezoelectric response in porous ferroelectrics is largely due to difficulties poling these materials, as the poling field preferentially concentrates in the low permittivity pores leading to regions of ferroelectric material remaining unpoled when the field is removed [8, 9]. Understanding the effect of the porous structure on the poling behaviour of composite ferroelectrics may therefore aid the design of materials with low permittivity and high d_{33} coefficients. The processing method used to form porous ceramic structures determines the connectivity, distribution and alignment of the final porous structure [10], which as will be demonstrated in this paper can be utilised to improve piezoelectric energy harvesting capabilities of porous ferroelectric ceramics.

The introduction of porosity into ferroelectric ceramics such as lead zirconate titanate (PZT) and barium titanate (BaTiO$_3$) reduces the permittivity of the composite [11] and has been shown to be beneficial in terms of increasing figures of merit for a number of applications including piezoelectric hydrostatic acoustic sensors [12, 13, 14, 15, 16], pyroelectric thermal detection devices [17, 18] and, more recently, for both piezoelectric [6, 9, 19] and pyroelectric energy harvesting [20, 21]. The presence of high levels of uniformly distributed porosity (i.e. 3-3 or 3-0 type connectivity) lead to a relatively small decrease in d_{33} up to ~50 vol.% porosity before a steeper decline [14, 15, 16, 19]. The large reductions in d_{31} make porous materials unsuitable for energy harvesters that operate in this mode, i.e. bending mode cantilever devices. Freeze cast PZT-based materials with excellent alignment of both pore and ceramic channels (3-1 and 2-2 connectivity) have been shown to have higher d_{33} coefficients [20, 21, 22, 23, 24] than PZT with uniformly distributed porosity at similar levels of porosity [14, 15]. For example, freeze cast PZT with over 65 vol.% porosity was reported to have d_{33} values of up to 91% that of

the dense material, whilst the permittivity was found to be just a third that of dense PZT [22], yielding an exceptionally high piezoelectric energy harvesting figure of merit [6]. Ionotropic gelation is another recently developed processing route that has been used to produce highly aligned 3-1 porous PZT [25, 26], again with excellent potential for energy harvesting due to high d_{33} coefficients.

1.1. Effect of porous structure on poling and d_{33}

The inhomogeneous field distribution during the poling of porous ferroelectrics is thought to lead to incomplete poling of the system and a decrease in d_{33} compared to the dense material [8, 9]. This occurs as the electric field applied during poling preferentially concentrates in the low permittivity phase, a condition of Gauss' law [27]. There have been several recent investigations into the effect of pore shape, orientation and connectivity on the electric field distribution and polarization-switching dynamics in dielectric materials [28, 29, 30, 31]. Porous structures with ideal 3-1 connectivity have been shown via finite element analysis to have homogenous electric field distributions throughout the material when an external field is applied parallel to the alignment direction of the dielectric phase [28]. In composites with 3-0 and 3-3 connectivity, an increase in porosity is found to reduce the local electric field in the high permittivity phase as the field preferentially concentrates in the pores [29], which partially explains the changes in polarisation-electric field (P-E) loops observed in PZT [21] and $(Pb,Nb)(Ti,Zr)O_3$ (PZTN) [29] with increasing porosity. A detailed study on the effect of pore aspect ratio and orientation with respect to applied electric field demonstrated that anisotropic pores cause broadening of P-E loops compared with isotropic pores when aligned perpendicular to the applied field, however, the least disruption to field was observed when elliptical pores were aligned to the field [30]. Experimental studies have demonstrated that anisotropic pores aligned perpendicular to the poling direction lead to lower d_{33} values than spherical pores [30, 32, 33], which is in agreement with the findings of the various theoretical studies [28, 29, 30, 31].

With regards to developing porous ferroelectrics for energy harvesting, structures that promote homogenous field distributions throughout the material with local fields close to the applied field in both the ceramic phase and the pores are likely to be easier to pole than structures with broad field distributions during the poling process. This would explain the high d_{33} coefficients reported for freeze cast porous piezoelectric materials with an orientated structure [20, 21, 22, 23, 24] compared with uniformly distributed porosity [14, 15] and is of benefit for piezoelectric materials for energy harvesting in terms of the relevant figure of merit, see Eqn. 1.

1.2. Effect of porosity on mechanical properties

Porosity increases the mechanical compliance [15, 34] and also decreases the strength of ceramics [35]. Aligning the high stiffness phase to the primary loading axis, as is the case of freeze cast porous ceramics, improves the mechanical properties compared to those in which porosity is uniformly distributed throughout the structure [36]. In order to harvest energy from mechanical loads porous ferroelectric ceramics must be sufficiently stiff and strong to survive their operating conditions, which is likely to be a further advantage, alongside high d_{33} coefficients, of using highly aligned freeze cast materials rather than those with uniformly distributed porosity.

In this paper both a single pore model and a porous network model are presented so as to evaluate the effect of porous structure on the resultant piezoelectric properties and energy harvesting behaviour. Barium titanate with highly aligned porosity has been produced via the freeze casting method to provide an experimental comparison to the observations from the modelling studies. Finally, a practical demonstration of the benefits of porosity on piezoelectric energy harvesting capabilities of ferroelectric ceramics is presented.

2. Single pore model

Finite element analysis has been used to demonstrate the effect of pore shape and orientation on the electric field distribution during the poling of a ferroelectric ceramic. A single elliptical pore with constant area fraction (A_f = 0.0785) and relative permittivity, ε_r = 1, was contained within a high permittivity barium titanate matrix, ε_r = 1500. The angle of the pore was varied from 0° (i.e. aligned to the field) to 90° (perpendicular to the field) and the aspect ratio varied from 1 to 10 (with an aspect ratio of one corresponding to a circular pore). An electric field greater than the coercive field of the barium titanate was applied to top and bottom boundary lines of the model to simulate the poling field across the material. The electric field in each element was analysed to determine whether the local field exceeded the coercive field (E_c = 0.5 kV/mm [37]), i.e. the necessary field to switch the orientation of a domain in a ferroelectric material. The applied field used in this model was selected as it provided good contrast between poled and unpoled regions; increasing the applied field (analogous to increasing the poling voltage) results in higher poled fractions of material, however, in real materials this is limited by electrical breakdown in the pores that discharges the poling field [38].

An example electric field contour plot for a pore orientated at 45° to the field with aspect ratio = 4, is shown in Fig. 1a, and the resulting distribution of poled material for a range of pore angles is shown in Fig. 1b. It can be seen from Fig. 1a that the electric field concentrates in the low permittivity pore and low field regions occur in the BaTiO$_3$ phase in immediate vicinity of the pore, parallel to the applied field. This results in varying fractions of the BaTiO$_3$ becoming poled as shown in Fig. 1b, in which the blue areas are those in which the local field is below the coercive field and therefore likely to remain unpoled. The variation in the fraction of barium titanate in which the field exceeds the coercive field, i.e. the fraction of poled material, is plotted as a function of pore angle with respect to field in Fig. 1c. High aspect ratio pores aligned parallel to the applied field yielded the highest fraction of poled material, whereas high aspect ratio pores aligned perpendicular to the poling field (angle = 90°) resulted in the lowest poled fraction, see Fig. 1b and c. If we were to extend the aspect ratio further we would reach the extreme case of parallel and series structures, i.e. a 3-1 or 2-2 composite in three dimensions. These results indicate the potential for achieving high degrees of poling in porous ferroelectric structures where pores have high aspect ratios and are aligned along or close to the poling axis, such as those achieved by the freeze casting process; this is discussed in more detail in Section 3.1. Achieving high fractions of poled material in porous ferroelectric materials has previously been shown to be closely linked to high d_{33} coefficients [8, 9].
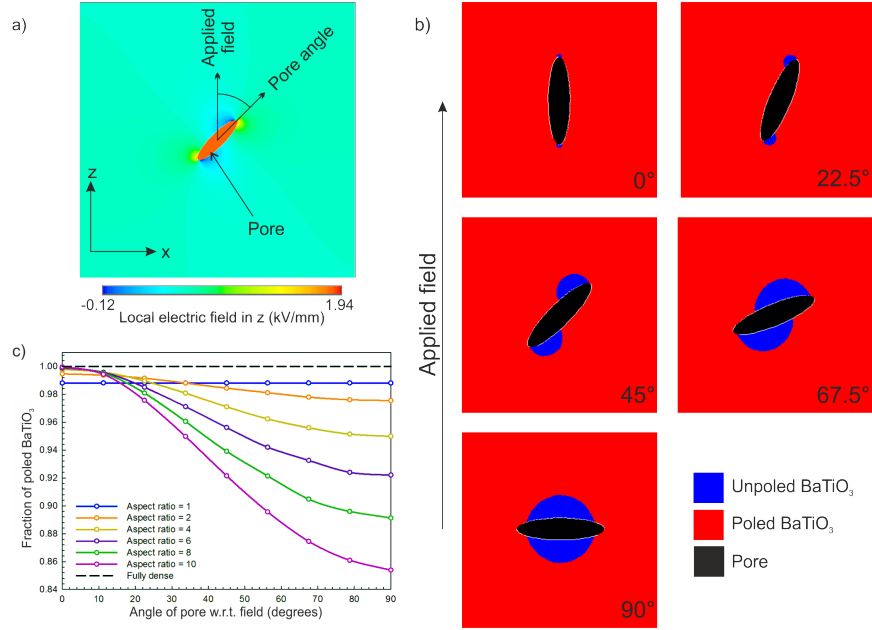
Figure 1: (a) Contour plot of electric field distribution in and around a single pore (aspect ratio, AR = 4, angle = 45°) contained within a barium titanate matrix; (b) regions of poled (red) and unpoled (blue) barium titanate with single pore (black) angle varyied from 0° to 90° with respect to applied field; and (c) effect of aspect ratio and angle of pore with respect to direction of applied field on the fraction of barium titanate poled in z-direction, i.e. the area in which the local field exceeds the coercive field of barium titanate (E_c = 0.5 kV/mm [37]).

3. Porous network model

We now expand upon the single pore model presented in Section 2 to investigate three dimensional aligned structures that are more closely linked to those formed via unidirectional freeze casting of water-based solutions. A porous network finite element approach has been implemented that has been used previously to describe the observed behaviour of lead zirconate titanate (PZT) with uniformly distributed porosity [8] and barium titanate with porous sandwich layer structures [9]. Firstly, however, it is necessary to understand the freeze casting process and the derived porous structures in more detail.

3.1. Freeze casting process

Freeze casting is a process whereby a liquid suspension of a solvent and ceramic particles is frozen before the solvent phase is sublimated under reduced pressure, i.e. converted from the solid phase directly to the vapour phase. As the solvent freezes the ceramic is ejected from the ice front, forming regions of compacted ceramic powder; when the frozen solvent is sublimated pores are left that have the morphology of the solvent crystals, hence the process often being referred to as 'ice-templating' [39, 40]. The ceramic powder compaction must then be sintered at high temperature to densify the ceramic walls. A variety of porous structures can be achieved through control of the freezing conditions and the properties of the liquid suspension, however, the majority of work to date in terms of freeze cast porous ceramics has focussed on highly
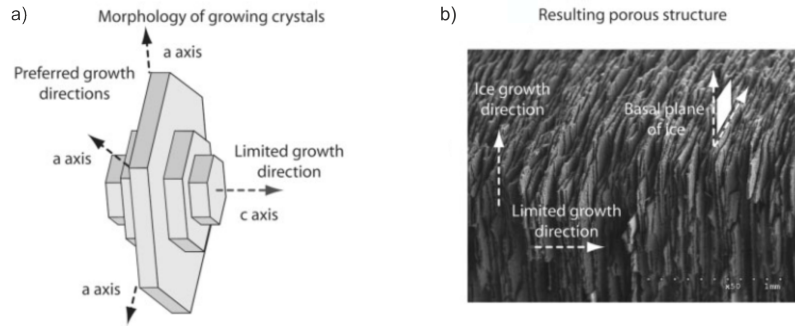
111

Figure 2: (a) Schematic diagram of hexagonal structure of ice showing preferential planes of crystal growth and (b) unidirectionally freeze cast porous alumina with lamellar structure, reproduced with permission from [41].

aligned structures that are beneficial in terms of their mechanical properties [36]. Similarly, the literature on freeze cast porous ferroelectric ceramics focusses on the fabrication and properties of porous structures aligned to the poling direction that, as previously discussed, are found to have high piezoelectric strain coefficients [21, 22, 23, 24]. The excellent alignment is achieved by unidirectional freezing of a suspension, which encourages the crystallising solvent to grow preferentially along the direction of the temperature gradient.

The solvent used in the liquid suspension is a key factor in determining the final porous structure of the freeze cast material. Water is the most commonly used solvent and is the focus of the porous structures modelled later in this section, although tetra-butyl alcohol and camphene have also been extensively researched [40]. The crystal structure and the crystal growth kinetics of the solvent determine the pore morphology of the freeze cast material. For example, ice has a hexagonal crystal structure and highly anisotropic growth kinetics such that crystals grow preferentially along their basal plane (see Fig. 2a) with limited dendritic growth perpendicular to this plane [41] yielding a lamellar 2-2 porous structure, as shown in Fig. 2b. During unidirectional freezing the basal plane of the ice crystals are aligned to the freezing direction, in effect growing in a two-dimensional sheet. As the ice grows the ceramic particles are ejected from the solidification front into channels between the sheets of ice, thus forming the characteristic lamellar 2-2 structure produced by water-based freeze casting [21, 39].

The temperature gradient provides the driving force for the directional growth of the crystallising solvent, meaning that high temperature gradients are favourable for producing highly aligned structures [40]. When the gradient, and therefore the driving force to directional growth, is too low the solvent crystals are more likely to tilt away from the primary freezing axis, resulting in less overall alignment [39]. Double-sided freezing set ups, whereby suspensions are frozen from both top and bottom surfaces simultaneously have been shown to improve alignment [20, 42].

The width of the lamellar ice channels can be controlled by adjusting the freezing rate, with finer pore structures achieved using faster rates [39]. Reducing the pore width of freeze cast materials has been shown to improve their mechanical strength compared to coarse structures

at the same porosity [36], however, freezing too fast leads to entrapment of particles within the ice, resulting in little or no pore alignment or long range order. On the other hand, using too slow a cooling rate can lead to unstable freezing conditions causing lateral growth of ice crystals between adjacent lamellae [43]. Some entrapment of particles within the ice is likely to occur, even under close-to-ideal conditions, that may form characteristic bridges between the ceramic lamellae, which are commonly observed in freeze cast structures [21].

The main factor controlling the final porosity of the material is the solid loading of the liquid suspension. Freeze casting has been used to create both highly dense ceramics (<1 vol.% porosity), using very slow freezing rates, and very high porosity materials, such as aerogels (>90 vol.% porosity) [40]. As solid loading is increased the viscosity of the suspension increases and redistribution of the ceramic particles away from the solidification front becomes more difficult [44], which may effect the long range order of the porous structure post-sintering.

The particle size also affects the resulting microstructure in several ways. For example, a small particle size will yield pores with a closer resemblance to the morphology of the solvent crystal, whereas larger particles tend to give less definition to the ceramic walls. Larger particles are also more likely to become engulfed by the ice front during freezing [41]. The density of the ceramic walls post-sintering is also affected by the initial particle size, with nano-sized particles yielding denser ceramic channels than micro-sized particles as smaller particles can both more closely pack together and tend to sinter more effectively [45]. As in dense ceramics formed by traditional processing routes, there is always some degree of porosity present in the ceramic channels of freeze cast materials.

3.2. Overview of modelling procedure

Freeze casting is a complex process and this article is not intended as a comprehensive review of the research conducted in this field. However, it is important to understand some of the difficulties that arise during freeze casting in order to model their behaviour in the context of the poling behaviour of ferroelectric materials. As discussed in Section 3.1, control of the process is essential to generate the desired structure, and even with relatively good control some 'defects' (defined in this sense as microstructural features which detract from an ideal 2-2 structure) are likely to be present, such as porosity in the ceramic channels and bridges forming in the pore channels; these two defects are commonly observed in water-derived freeze cast structures as shown in Fig. 3a and b. Another common defect in freeze cast materials is the tilt of ice crystals away from freezing direction if the temperature gradient falls, however, this has not been considered in this modelling study; it is clear from the single pore model in Section 2 this will have a detrimental effect on the fraction of material poled, see Fig. 1b and 1c.

For the purposes of this modelling study, an ideal structure for a porous freeze cast material can therefore be defined as a lamellar 2-2 structure with no porosity in the ceramic channels and no ceramic bridges in the pore channels. The model is not designed to model a complete bulk freeze cast material but instead focusses on the poling behaviour in regions of the material whereby the pore and ceramic channels are aligned parallel to one another; a transverse image of freeze cast barium titanate (i.e. freezing direction is out of plane) is shown in Fig. 3c with the boxes showing regions where lamellar ceramic/pore channels are parallel to one another. Two
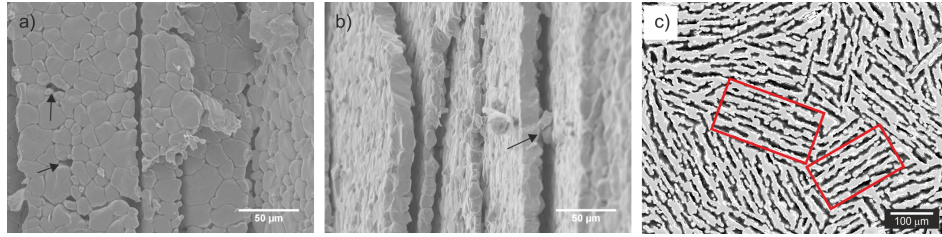
Figure 3: SEM images of porous barium titanate fabricated via unidirectional freeze casting with 30 vol.% solid loading in suspension (see Section 4.1 for more details) with examples of (a) porosity in the ceramic channels and (b) a bridge between adjacent ceramic lamellae, indicated in both images by arrows; the freezing direction is vertical in both images; and (c) SEM of porous barium titanate taken transverse to freezing direction (pores with dark contrast) with boxes indicating regions of freeze material whereby pore and ceramic lamellae are parallel, such as those modelled in Section 3.

kinds of defects were introduced in varying fractions to understand the effects of these on freeze cast ferroelectric materials: (i) the effect of porosity present in the ceramic lamellae that form in real freeze cast materials due to incomplete compaction or sintering of the ceramic powder on rejection from the solidification front of the solvent; and (ii) the effect of ceramic elements present in the pore channels, i.e. the ceramic bridges that form during freezing casting due to engulfment of particles by the ice front and unstable growth conditions. As with the single pore model the finite element analysis was conducted in Ansys APDL.

3.3. Defining the model geometry

A 30 x 30 x 30 mesh of cubic elements was used as the starting point for all structures (Fig. 4a) before designating pore channels (Fig. 4b). Bridges between and porosity within the ceramic channels was then introduced in randomly selected positions within the network (Fig. 4c). The fraction of porosity introduced into the ceramic channels was controlled by the parameter α_{cc} and the fraction of ceramic elements in the pore channels (i.e. the bridges) was controlled by the parameter α_{pc}. An ideal 2-2 structure with no porosity in the ceramic channels or ceramic in the pore channel therefore had both α_{cc} and α_{pc} equal to zero, i.e. the structure shown in Fig. 4b. The variables α_{cc} and α_{pc} were varied from zero to 0.3 and 0.4, respectively; this range was selected as it extends beyond the desirable levels of ceramic channel porosity and pore channel bridges in a freeze cast material, however, as will be seen from the results gives a good indication of the effect of the two types of 'defect' studied here on the poling behaviour and piezoelectric properties of freeze cast ferroelectric ceramics. Fig. 5 demonstrates the effect of varying α_{cc} (top row) and α_{pc} (bottom row) on porous structure; images are 2D slices taken parallel to the poling direction.

The pore channel width was kept constant at one element wide as increasing it did not significantly affect the poling behaviour and would have meant the presence of a ceramic element in the pore channel did not necessarily constitute a bridge between neighbouring lamellae. The spacing between the pore channels (i.e. the ceramic channel width) was varied to give additional control over the porosity, as in Fig. 5, where the top row have a ceramic channel width of three elements and the bottom row have a width of two. Once the porous network had been generated the ceramic elements were assigned the properties of unpoled barium titanate (elastic modulus =
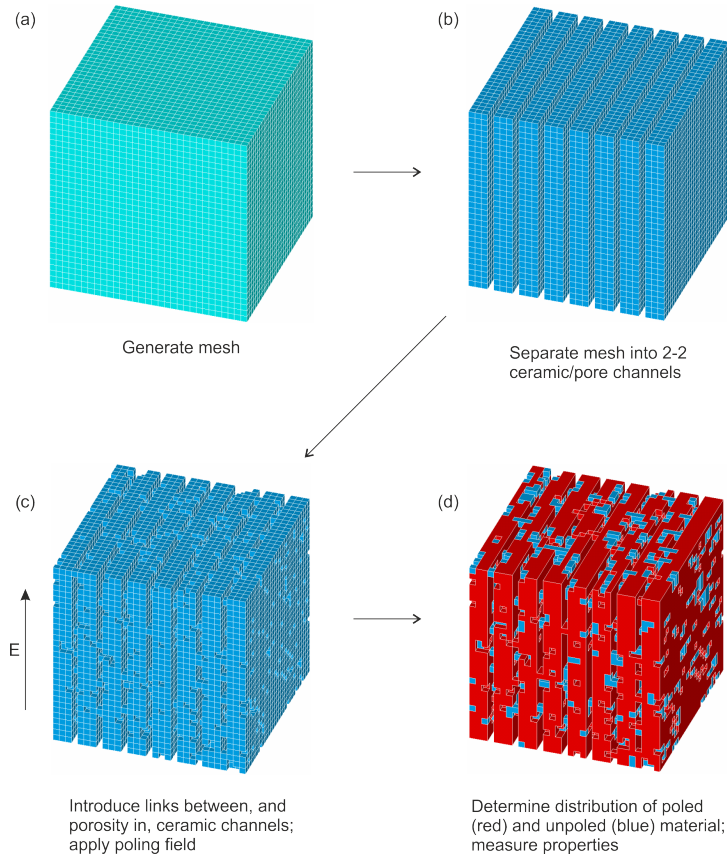
Figure 4: Schematic diagram of process to form porous network geometry in Ansys. (a) A cubic mesh with 30^3 elements was initially generated before (b) defining pore channels (i.e. an ideal 2-2 structure), (c) introducing porosity in the ceramic channels and bridges in pore channels and (d) applying a poling field to establish the distribution of poled and unpoled $BaTiO_3$ and porosity, and measuring the effective material properties.

120 GPa, Poisson's ratio = 0.3, ε_r = 1187.5 [46]) and pore elements were assigned the properties of air (elastic modulus = 0, ε_r = 1). The mesh size was deemed to yield a good balance between computing speed and reliability. As networks were generated randomly, five different structures were evaluated for each combination of α_{cc} and α_{pc} parameters.

The poling procedure was simulated to achieve a distribution of poled and unpoled barium titanate. Electrodes were 'applied' by coupling the voltages of the nodes at the top and bottom surfaces and applying a poling field between them, see Fig. 4c. Elements in which the local electric field exceeded the coercive field, i.e. $E_f > E_c$, were assigned the properties of poled barium titanate, as shown in Fig 4d in which red elements are those which have been poled and blue elements are those that remain unpoled. Once the distribution of poled material had been established the effective piezoelectric properties of the network were measured.
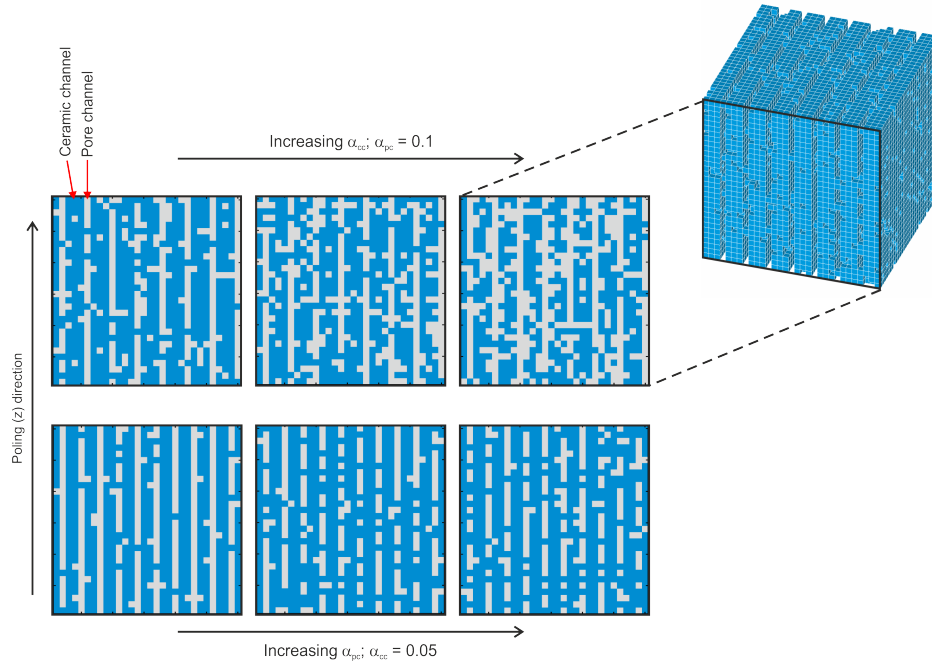
Figure 5: Cross-section images (see top right for reference) of modelled porous structures showing the effect of the variables, α_{cc}, i.e. the fraction of porosity in the ceramic channels, and α_{pc}, the fraction of ceramic in the pore channels on the porous structure; pores are light grey in colour and the ceramic phase is blue. The top three images have increasing α_{cc} with $\alpha_{pc} = 0.1$ and the bottom three images have increasing α_{pc} with $\alpha_{cc} = 0.05$. The ceramic channel width is wider in the top three images compared to the bottom three images, which allowed additional control over the overall porosity fraction.

3.4. Porous network model results

The results for the longitudinal piezoelectric strain coefficient are shown in Fig. 6 for varying ceramic fraction in the pore channel, α_{pc}, constant ceramic channel porosity, α_{cc}, and Fig. 7 for varying α_{cc}, constant α_{pc}; data has been fitted using second order polynomial functions to highlight general trends. Firstly, considering Fig. 6, increasing the fraction of barium titanate in the pore channels (increasing α_{pc}) resulted in a decrease in the measured d_{33} at a given porosity; the highest d_{33} values were achieved in structures with well-defined pore channels parallel to the poling (z) direction. This was due to regions of low field occuring in the immediate vicinity of a pore parallel the direction of the applied field (as can be seen in the single pore model, Fig 2), such that BaTiO$_3$ elements in the pore channels tended to be in low field regions and therefore remained unpoled, thus adding to the relative density of the material but not contributing to the measured d_{33}. The results shown in Fig. 7 are more intuitive and fit in with what is known from previous studies: increasing porosity within the ferroelectric channels (increasing α_{cc}) led to lower poled fractions being achieved that ultimately resulted in reduced d_{33} coefficients. A linear relationship between d_{33} and fraction of barium titanate poled was observed, see Fig. 7e, demonstrating the link between fraction poled and resulting piezoelectric response that has also been reported previously [8, 9].

A comparison between an ideal 2-2 ($\alpha_{cc}, \alpha_{pc} = 0$), modelled freeze cast structures (with vary-

ing ceramic channel porosity, α_{cc}, and ceramic in pore channel, α_{pc}) and uniform porous BaTiO$_3$ is shown in Fig 7. For an ideal 2-2 porous structure, d_{33} remained at 140 pC/N regardless of the porosity as the aligned structure promoted a homogenenous poling field meaning that all the BaTiO$_3$ elements were poled. At low α_{cc} and α_{pc}, i.e. close to an ideal 2-2 structure, the predicted d_{33} was higher than that of uniform porous barium titanate, as has been shown experimentally for highly aligned freeze cast porous PZT compared to PZT with uniform porosity manufactured by the BURPS process [14, 15, 21, 22, 23, 24]. However, when α_{pc} was increased, i.e. the pore channels became less well-defined and contained higher fractions of BaTiO$_3$, higher d_{33} coefficients were observed in the uniform porous structures compared to the 2-2 based materials, even when α_{cc} remained low, i.e. there was a low pore fraction within the ceramic BaTiO$_3$ channels. This indicates that in order to achieve high d_{33} coefficients clear pore channels are actually more important than having highly dense ferroelectric channels aligned in the poling axis. This was thought to be caused by a restriction of the strain in poled material due to the presence of unpoled material in the porous channels. For example, when an external field was applied a strain was induced in the highly poled dense channels but none directly in the stiff unpoled BaTiO$_3$ bridges in the pore channel. When there was a low fraction of unpoled ceramic in the pore channels (low α_{pc}) the highly poled, ceramic channels were relatively unrestricted in their expansion due to the applied field so that a high net piezoelectric response was observed across the material, i.e. a high d_{33} was recorded. However, when the fraction of ceramic in the pore channel was increased to $\alpha_{pc} > 0.2$ there was sufficient unpoled material in the pore channels to restrict the induced strain in the poled dense channels to such an extent that the measured net piezoelectric response of the structure due to an applied electric field fell below that of the material with uniformly distributed porosity, particularly when α_{cc}, i.e. the amount of porosity in the ceramic channels, was also increased, which resulted in a lower fraction of poled material in these channels. Having well-defined pore channels and long range order was therefore found to be beneficial in terms of promoting high d_{33} coefficients in the modelled freeze cast-type porous ferroelectric materials.

Selected permittivity data obtained from the porous network model are shown in Fig. 8a for constant pore channel ceramic fraction, α_{pc}, varying pore fraction in ceramic channels, α_{cc} and Fig. 8b for constant α_{cc}, varying α_{pc}, alongside the permittivity for an ideal 2-2 connected ($\alpha_{cc}, \alpha_{pc} = 0$) and uniform porous barium titanate. The ideal 2-2 structure followed a linear trend of a parallel rule of mixtures model [47] and as α_{cc} and α_{pc} approached zero, i.e. towards an ideal structure, the permittivity increased to what is effectively an upper bound. When $\alpha_{pc} > 0.1$ the permittivity of the freeze cast structure became close to that of the uniform porous barium titanate. Fig. 8c is included to show that at the limits of the parameters studied here, i.e. α_{cc} = 0.3, α_{pc} = 0.4, the permittivity of the aligned structure was actually lower than the uniform porous material. In terms of the energy harvesting figure of merit (Eqn. 1) a low permittivity is beneficial, however, these structures also had relatively low d_{33} coefficients.

Calculated figures of merit, $d_{33}^2/\varepsilon_{33}^\sigma$, for the modelled data are shown in Fig. 9. Introducing porosity was generally found to increase the figure of merit from the dense value of 1.50 pm^2/N, with the ideal 2-2 structure in effect providing an upper limit for the increases that could be achieved by forming highly aligned freeze cast barium titanate, assuming no microstructural
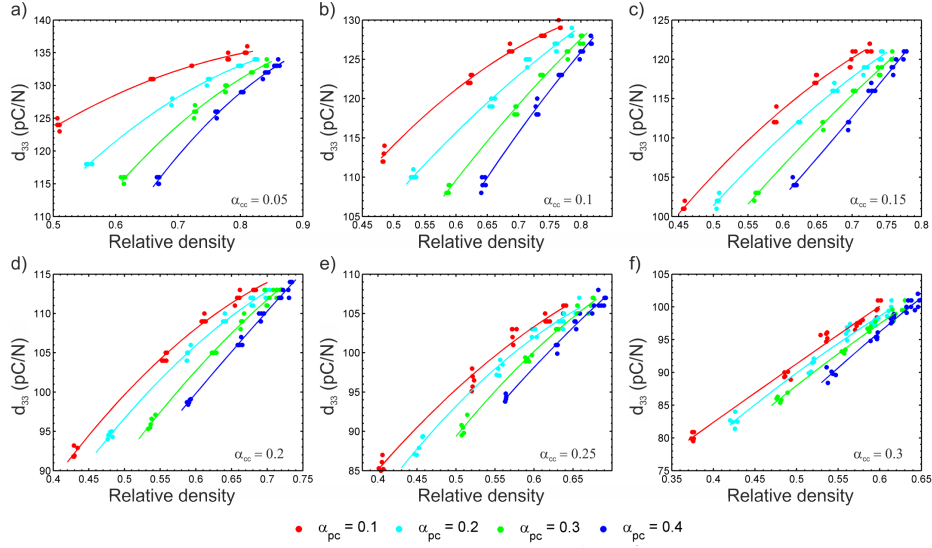
117

Figure 6: Effect of fraction of barium titanate in pore channel, α_{pc}, on the longitudinal piezoelectric strain coefficient, d_{33}, for increasing fractions of porosity in ceramic channel, α_{cc}, in (a) - (e). For a given α_{cc} and α_{pc}, the relative density of the modelled material was controlled by adjusting the width of the ceramic channels.

change in the porous material compared to the dense material (i.e. grain size and texturing, domain mobility, etc.). For example the uniform porous material was predicted to have an energy harvesting figure of merit of ~2 pm^2/N at 50 vol.% porosity, whereas for the ideal 2-2 structure the predicted figure of merit was ~3 pm^2/N at the same porosity, double that of the dense material. Having a low fraction of porosity in the ceramic channels (α_{cc}) and a low fraction of ceramic in the pore channels (α_{pc}) yielded high figures of merit compared to both dense and porous material due to the high piezoelectric strain coefficient, d_{33}, that resulted from high fractions of the ferroelectric phase becoming poled.

4. Experimental

4.1. Method

Barium titanate suspensions with varying solid loading contents (20, 25, 30, 32.5 vol.%) were prepared with commercial BaTiO$_3$ powder (particle size, d_{50} = 2.1 μm, *Ferro*, UK), 1 wt.% organic binder (polyethylene glycol, *Sigma*, UK) and dispersant (polyacrylic acid, *Sigma*, UK), and deionized water. A single-side freeze casting set up was used whereby the suspension was poured into a polydimethylsiloxane (PDMS) mould and placed onto a heat sink cooled by liquid nitrogen to -90°C. The mould used was open ended and so silver adesive tape was used to contain the suspension. Care was taken not to introduce air bubbles when filling the moulds. The ice was sublimated from the frozen bodies by freeze drying (*Mini Lyotrap*, *LTE Scientific*, UK) for 24 h. These were then sintered at 1300°C for 2 h with a 2 h dwell at 400°C to remove the organic binder; heating and cooling rates during the sintering process were ±60°C/h. Individual
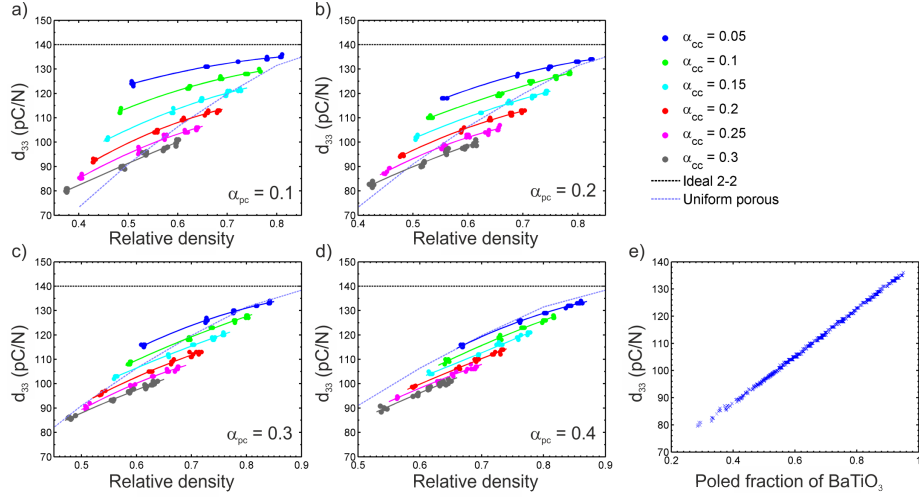
Figure 7: Effect of pore fraction in ceramic channel, α_{cc}, on longitudinal piezoelectric strain coefficient, d_{33}, for increasing fractions of ceramic in pore channels, α_{pc}, in (a) - (d) with comparison to an ideal 2-2 structure ($\alpha_{cc}, \alpha_{pc} = 0$) and barium titanate with uniformly distributed porosity, see black and violet dashed lines, respectively; and (e) shows the relationship between the fraction of barium titanate poled and the resulting piezoelectric strain coefficient, d_{33}.

samples were cut to ~2 mm thick from the sintered bodies at least 6 mm from the freezing surface. Samples were ground flat, cleaned and silver electrodes applied (*RS Components, Product No 186-3600*, UK). The ceramic powder and sintering profile were the same as those used in previous investigations [9, 19] to enable comparison between the properties of barium titanate with different porous structures.

The relative density and porosity of the sectioned pellets was measured via the Archimedean method [48]. The samples were corona poled in air with 14 kV applied from a 35 mm point source. Piezoelectric strain coefficients, d_{33} and d_{31} were measured 24 h after poling via the Berlincourt method using a *Take Control Piezometer PM25*. Impedance spectroscopy (*Solartron 1260* and *1296 Dielectric Interface*) was used to measure the permittivity. Microstructural analysis was undertaken using scanning electron microscopy (SEM, *JEOL JSM-6480LV*)

4.2. Microstructural analysis

SEM images of barium titanate freeze cast from suspensions with 20 vol.% initial solid loading (relative density, $\rho_{rel} = 0.45$) are shown in Fig. 10a and b and 30 vol.% solid loading samples ($\rho_{rel} = 0.55$) are shown in Fig. 10c and d. Comparing Fig. 10a and c it can be seen that the barium titanate freeze cast from the 30 vol.% suspension had more defined lamellar pore and ceramic channels than the samples cast from the 20 vol.% suspension. One possible reason for this is reducing the solid loading content resulted in significantly more shrinkage post-sintering (30% radial shrinkage for 20 vol.% suspension, 24% radial shrinkage for 30 vol.% suspension) that may have resulted in coalescing of adjacent ceramic lamellae. In addition, adjusting the solid loading of the suspension alters properties such as freezing temperature and viscosity [40] and therefore it may be that a better freeze cast structure could have been achieved if the freezing conditions were altered depending on the suspension properties. The grain size, which can be
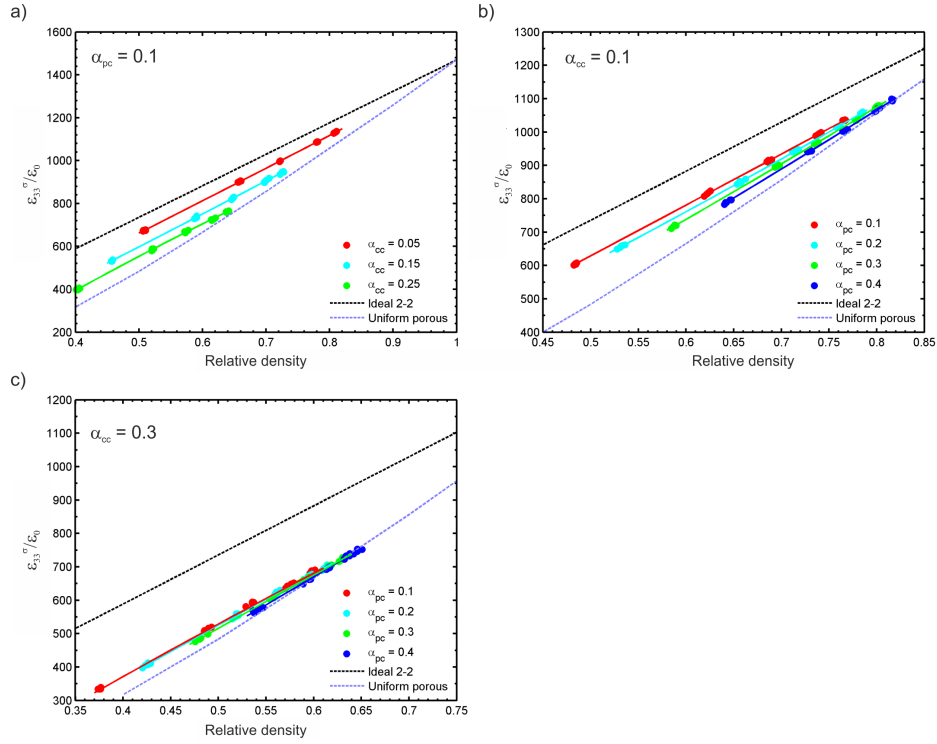
Figure 8: Variation of relative permittivity $\varepsilon_{33}^\sigma/\varepsilon_0$ with relative density for (a) varying ceramic channel porosity α_{cc}, α_{pc} = 0.1, (b) varying ceramic fraction in pore channel α_{pc}, α_{cc} = 0.1, and (c) varying ceramic fraction in pore channel α_{pc}, α_{cc} = 0.3. The relative permittivity for an ideal 2-2 structure (α_{cc}, α_{pc} = 0) and uniformly distributed porous barium titanate as a function of relative density are shown for comparison (black and violet dashed lines, respectively) in all figures.

clearly seen in Fig. 10b and c, did not change significantly with varying solid loading content or resulting porosity with grains generally between 10 and 30 μm, which was similar to previous studies into the effect of porous structure on the energy harvesting properties of barium titanate [9, 19].

A combination of transverse images (i.e. perpendicular to freezing direction), shown in Fig. 11, and polished images of the sample cross-sections (i.e. the direction shown in Fig. 10), were used to calculate the average ceramic and pore channel width of the freeze cast barium titanate. Transverse pore structures of three solid loadings (20, 30 and 32.5 vol.%) with corresponding relative densities of ρ_{rel} = 0.45, 0.55 and 0.62 are shown in Fig. 11a-c, respectively. Increasing the solid loading content led to an increase in ceramic channel average width, which was found to be ~9 μm for barium titanate cast from 20 vol.% suspension compared to ~15 μm for 30 and 32.5 vol.% initial solid loading. Comparing the average ceramic wall thickness measured from transverse images in Fig. 11 to the SEMs in Fig. 10 it appears the ceramic channels were generally 1-2 grains thick and seemed to have a degree of anisotropy as the ceramic channel width was smaller than the typical grain size that can be seen looking side-on at ceramic walls, as in Fig. 10b and d; this indicates that freeze casting may also cause some degree of texturing
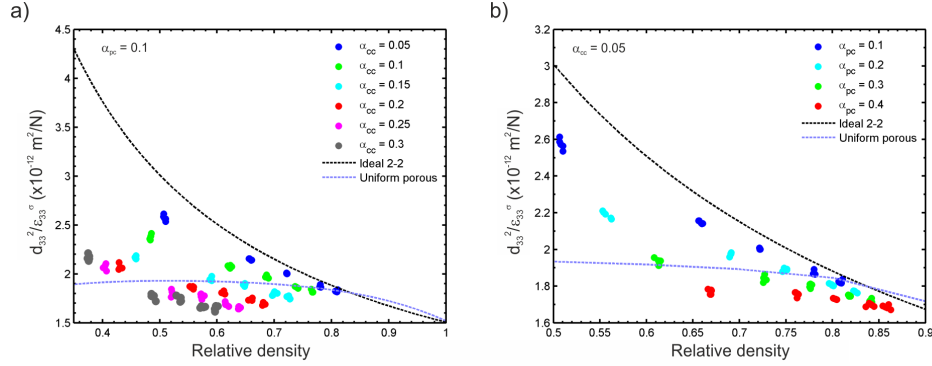
120

Figure 9: Modelled data showing effect of (a) variation of ceramic channel porosity, α_{cc}, at constant pore channel ceramic fraction (α_{pc} = 0.1) and (b) variation of pore channel ceramic fraction, α_{pc}, at constant ceramic channel porosity (α_{cc} = 0.05) on the longitudinal energy harvesting figure of merit of porous barium titanate, $d_{33}^2/\varepsilon_{33}^\sigma$. The figure of merit for an ideal 2-2 structure (α_{cc}, α_{pc} = 0) and uniformly distributed porous barium titanate as a function of relative density are shown for comparison (black and violet dashed lines, respectively) in both figures.

within the ceramic phase that may be of interest to study further. Pore channel width peaked for the 30 vol.% barium titanate at ~14 μm, with both the 20 and 32.5 vol.% material having a pore channel width of <10 μm although it is thought this is due to differing mechanisms. Firstly, as previously discussed, low solid loading samples experienced higher shrinkage during sintering, which may have lead to a reduction in the pore channel width as neighbouring ceramic lamellae shrunk closer together. The samples cast from suspensions with high solid loading contents had less solvent and more ceramic, which is likely to give relatively thicker ceramic channels compared to the pore channels, as observed here.

4.3. Results and discussion

The measured d_{33} data for freeze cast barium titanate are plotted in Fig. 12a as a function of relative density alongside data for uniform porous (3-3) barium titanate manufactured via the BURPS process [19]. The d_{33} coefficients of the freeze cast materials were consistently higher than for the materials with uniform porosity, with a maximum of 134.5 pC/N measured in barium titanate with a porosity of 45 vol.% (relative density, ρ_{rel} = 0.55), which was 93% that of the dense BaTiO$_3$, where the maximum measured d_{33} was 144.5 pC/N, and can be seen to be higher than the d_{33} of the uniform porous samples across the whole range of relative densities. This was a similar trend to that observed in the finite element models, see Fig. 6 and 7, in which the highly aligned structures had superior piezoelectric strain coefficients to the uniform porous samples. The spread in data indicates there was some variation occuring during the processing that results in some samples having better pore channel and ceramic phase alignment than others that, as observed in the results of the modelling study in Section 3, significantly affects the piezoelectric properties. The slight decline in d_{33} observed as relative density increased beyond ~0.55 may be a result of increasing fractions of ceramic in the pore channels, which was shown to be detrimental to the longitudinal piezoelectric properties in the porous network model, see Section 3.

Relative permittivity is plotted in Fig. 12b as a function of relative density. It can be seen that
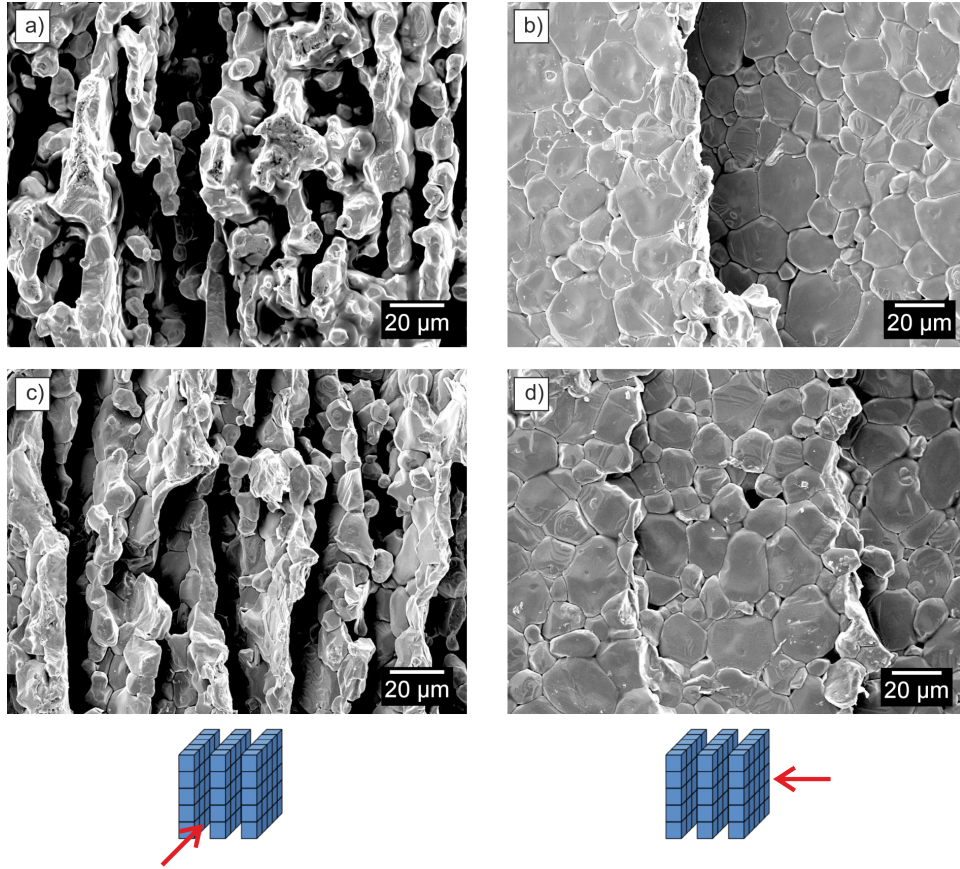
121

Figure 10: SEM images of freeze cast barium titanate with (a) 55 vol.% and (b) 45 vol.% porosity (ρ_{rel} = 0.45 and 0.55, respectively); images (c) and (d) were taken from samples with 55 and 40 vol.% porosity, respectively, showing grain size did not change with porosity or solid loading content of frozen suspension. The freezing direction was vertical in all images; schematic representations of the direction of images with respect to the freeze cast structure are shown below the SEM images.

the aligned freeze cast barium titanate had a slightly lower permittivity than the uniform porous barium titanate, which was not predicted by either finite element model presented in this paper or indeed other models discussed elsewhere [47, 49]. However, these models all assume there is no physical change in the material properties with the introduction of porosity or processing conditions as the input properties are those measured from the fully dense ceramic. As discussed in Section 4.2, the grains in the freeze cast material appeared to be elongated in the freezing direction, whereas the barium titanate formed via the BURPS process that the freeze cast permittivity data are compared to in Fig. 12b had spherical grains [19] and it is known that the microstructure can alter significantly the properties of barium titanate. For example, the dielectric properties of barium titanate are influenced by the grain size of the material, with the permittivity decreasing as grain size increases, thought to be an effect in of changing domain mobility, size and wall with variation in grain size [50, 51, 52]. Single crystal barium titanate has highly anisotropic dielectric properties [53] and texturing the material can also affect the measured permittivity [54]. Any
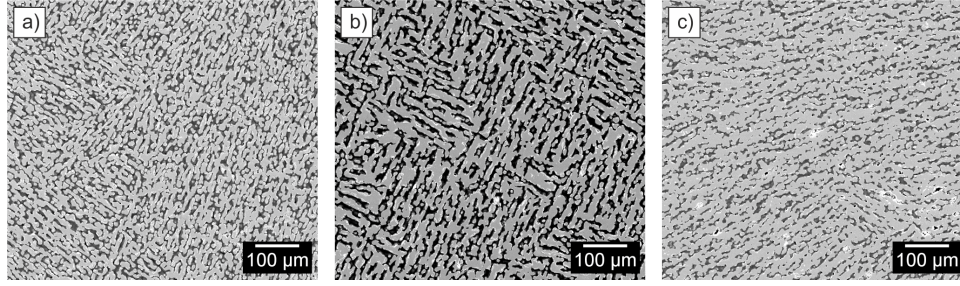
Figure 11: Transverse SEM images (perpendicular to freezing direction) of barium titanate freeze cast with varying solid loadings and different resulting porosities, (a) 20 vol.%, ρ_{rel} = 0.45, (b) 30 vol.%, ρ_{rel} = 0.55 and (c) 32.5 vol.%, ρ_{rel} = 0.45.

grain size or texturing effects are likely also alter the piezoelectric properties of barium titanate [52, 54, 55], however, the model and experimental data suggests that the piezoelectric coefficient is more dependent on the poling behaviour due to the porous structure, which may explain why the d_{33} data in Fig. 12a is closer to what the behaviour predicted by the finite element model. Further work is required to fully understand the experimental permittivity data, however, the lower than expected results are beneficial in terms of the energy harvesting figure of merit, see Eqn. 1.

The high d_{33} coefficients measured in the freeze barium titanate samples led to significantly increased energy harvesting figures of merit compared to uniform porous barium titanate, see Fig. 12c, and coupled with the observed reduction in permittivity yielded a two-fold increase in figure of merit compared to the dense material. A maximum of 3.79 pm^2/N was found in the freeze cast barium titanate at a relative density of 0.55 and many samples were found to have a figure of merit of >3.0 pm^2/N, more than twice that of dense barium titanate. This was higher than was predicted by the finite element model due to the lower than expected permittivity in the experimental results; the model data for an ideal 2-2 structure are shown in Fig. 12c (black dashed line) for comparison with the experimental data. Even if the permittivity was higher, i.e. the upper bound predicted in an ideal 2-2 structure, the figures of merit would still be higher than the uniform porous and dense barium titanate, demonstrating the potential for porous ferroelectric materials manufactured using the freeze casting process.

4.4. Piezoelectric energy harversting demonstrator

A piezoelectric energy harvesting system, shown in Fig. 13, was used to demonstrate the improved harvesting of the porous freeze cast barium titanate compared to the dense material with three samples selected for comparison: a dense pellet with a figure of merit of 1.39 pm^2/N, and two freeze cast samples, with a relative density of 0.55 and 0.60 and figure of merit of 3.24 pm^2/N and 2.19 pm^2/N, respectively; see Table 1 for more details. The thickness of all samples was ~1.8 mm. The piezoelectric samples were fixed to a perspex beam attached to a shaker (*LDS V201*, Brüel & Kjær, Denmark) with conductive silver epoxy (*CircuitWorks Conductive Epoxy*, Chemtronics, USA). The perpendicular distance from the central axis of the shaker to the location of the sample was minimised so as not to induce any bending effects. An end mass
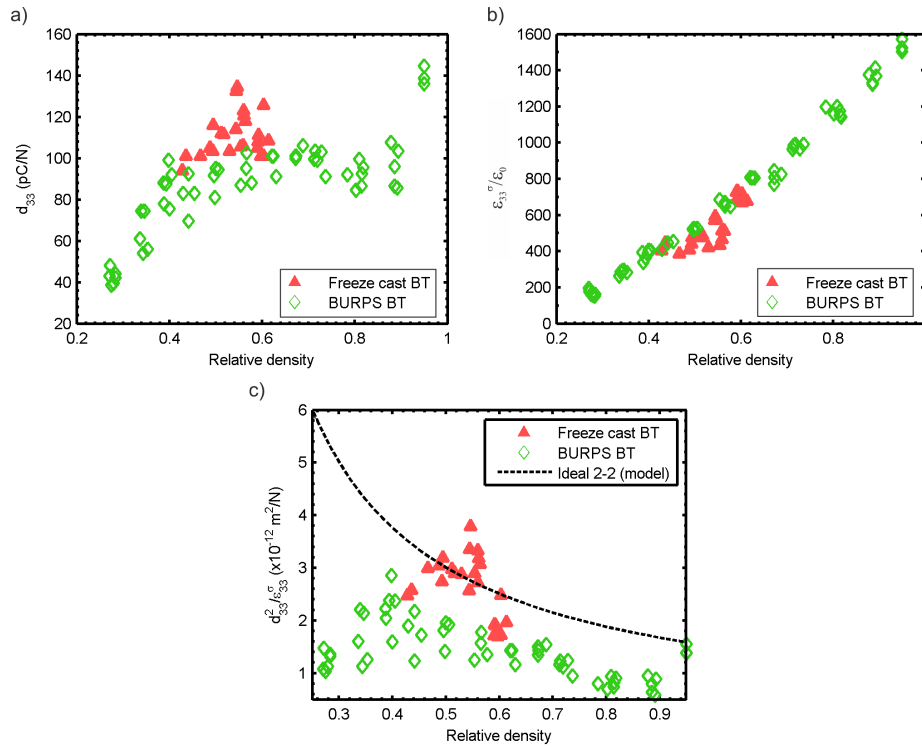
Figure 12: Comparison of freeze cast (red) and uniform porous (green, manufactured using burned out polymer spheres (BURPS) process, from [19]) for (a) longitudinal piezoelectric strain coefficient, d_{33}, (b) relative permittivity, $\varepsilon_{33}^{\sigma}/\varepsilon_0$, and (c) energy harvesting figure of merit ($d_{33}^2/\varepsilon_{33}^{\sigma}$) as a function of relative density.

weighing six grams was attached to the sample with silver epoxy. The samples were excited off-resonance at 97 Hz on the shaker driven at 205 mV by a signal generator passed through an amplifier with the gain set to 20 dB (x10 amplification); calibration using an accelerometer found these conditions to give a maximum acceleration force of approximately 11g. The open circuit voltage (across resistance >1 TΩ) and short circuit current were measured using a Keysight B2987A Electrometer. The voltage (measured across 10 MΩ load resistance) and current were measured after being passed through a full bridge rectifying circuit with four 1n4148 diodes, which enabled calculation of the voltage drop across the rectifier. Finally, a 1 μF capacitor (63 V, Philips 030K0, USA) was charged across a load resistance of 6.67 MΩ. The tests were conducted in a Faraday cage to reduce noise particularly at the 50 Hz frequency. Open circuit voltage and short circuit current experiments were repeated six times for each sample and the data averaged; capacitor charging experiments were repeated three times per sample. The voltage drop across the rectifying bridge was 0.2 V.

The open circuit voltage, V_{oc}, and short circuit current, I_{sc}, are shown in Fig. 14a and b, respectively; data sets have been smoothed and averaged. The open circuit voltage increased with increasing porosity, with a maximum peak-to-peak open circuit voltage, $V_{oc} = 1.15$ V for the barium titanate with $\rho_{rel} = 0.55$ compared to $V_{oc} = 0.62$ V for the dense barium titanate. The
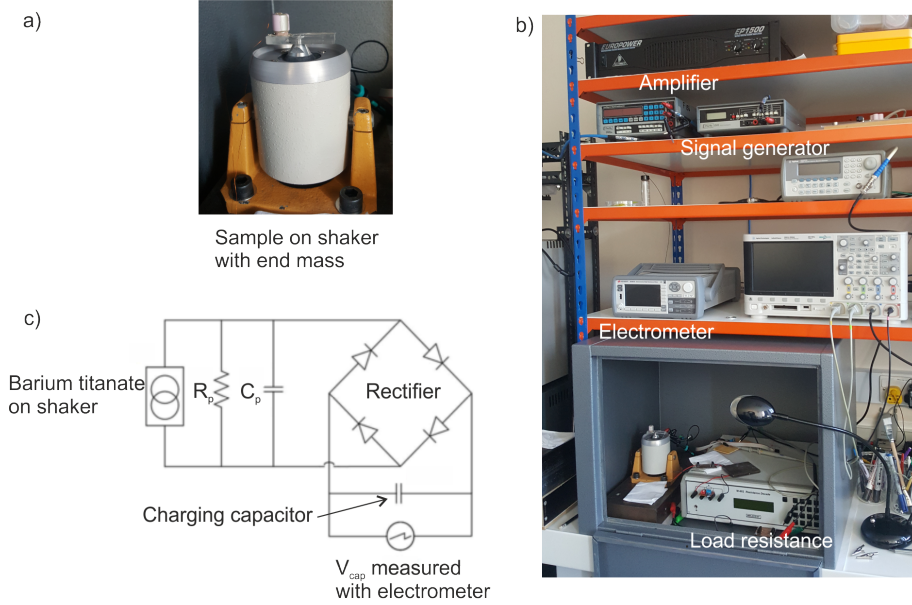
124

Figure 13: Experimental setup for piezoelectric energy harvesting experiments; (a) sample was attached to a perspex beam fixed to a shaker with silver epoxy and a 6 g end mass attached to the other side, (b) shows the full set up with relevant measuring apparatus labelled and (c) is the circuit diagram for the rectifying circuit and measurement of voltage across capacitor that was charged using electrical energy converted from input mechanical energy by the barium titanate samples.

Table 1: Details of samples used in piezoelectric energy harvesting experiments.

ρ_{rel}	d_{33} (pC/N)	ε_r	$d_{33}^2/\varepsilon_{33}^\sigma$ pm^2/N)	V_{oc} (V) (peak-to-peak)	I_{sc} (nA) (peak-to-peak)	V_{cap} (mV)	C (pF)
0.95	136	1504	1.39	0.63	360	96	742
0.60	118	717	2.19	0.97	231	196	256
0.55	129	580	3.24	1.15	213	234	187

theoretical open circuit voltage generated by a piezoelectric due to an applied stress, σ, can be calculated from the following equation [56]:

$$V_{oc} = \frac{d_{33}}{\varepsilon_{33}^\sigma}.t.\sigma \quad (3)$$

where t is the sample thickness. The piezoelectric strain coefficient, d_{33}, and sample thickness was similar in the three tested samples and so under the same loading conditions V_{oc} was expected to be approximately inversely proportional to the permittivity of the sample, as was observed experimentally whereby V_{oc} increased with increasing porosity and decreasing permittivity, see Fig. 14a and Table 1.

The dense sample had the highest peak-to-peak short circuit current, $I_{sc} = 360$ nA, compared to the samples with ρ_{rel} of 0.60 and 0.55, which had peak-to-peak short circuit currents of 231 and 213 nA, respectively. The reason for the fall in current with increasing porosity is thought to
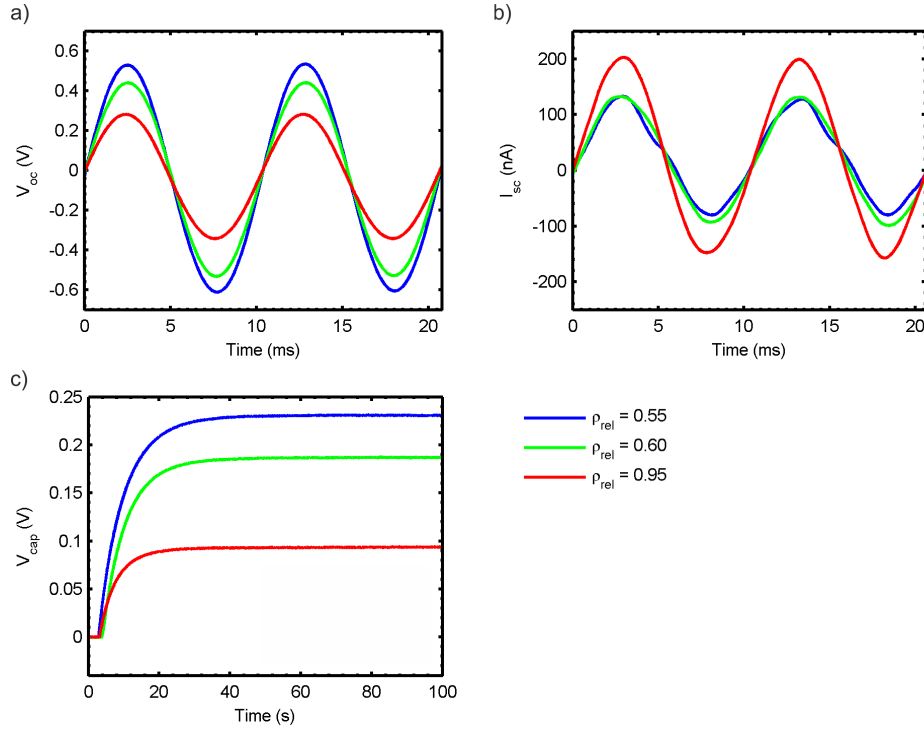
Figure 14: Results from shaker experiment showing comparison between two porous freeze cast barium titanate samples (blue and green lines) and dense barium titanate (red) for (a) open circuit voltage, (b) short circuit current and (c) capacitor charging curve after rectification. Sample details are shown in Table 1.

be an effect of the varying capacitances of the samples. The current produced by the sample due to mechanical excitation, I, is equal to the change in charge, dQ, with time, dt:

$$I = \frac{dQ}{dt} \tag{4}$$

and the change in charge due to a change in voltage, dV, can be written as:

$$dQ = C.dV \tag{5}$$

if we assume constant capacitance, C, of the piezoelectric during the experiment. If we then differentiate with respect to time and rearrange we get the relationship:

$$I = \frac{dQ}{dt} = C.\frac{dV}{dt}. \tag{6}$$

From Eqn. 6 it can be seen that for a given change in voltage with time, dV/dt, the dense sample was expected to produce the most current as it had the highest capacitance, four times greater than the capacitance of the highest porosity sample, see Table 1. However, as the porous samples had a lower permittivity they produced higher voltages per unit stress (for example see Eqn. 3 and Fig. 14a) therefore the peak current of the dense barium titanate due to an applied stress was not four times greater than the barium titanate with $\rho_{rel} = 0.55$, as predicted by their respective

capacitances, but was instead found to be only ~1.7 times greater due to a combination of higher capacitance yielding increased current outputs whilst simultaneously causing a reduction in the voltage generated due to an applied stress.

Fig. 14c shows that the porous barium titanate more effectively charged the capacitor than the dense material with a maximum voltage of $V_{cap} = 234$ mV achieved for the sample with $\rho_{rel} = 0.55$, compared to $V_{cap} = 96$ mV for the dense sample (average V_{cap} from three measurements). The time to achieve the peak voltage in the barium titanate with $\rho_{rel} = 0.55$ was 40 seconds. The results from these experiments indicate that whilst the amount of energy harvested was small for all samples, the rate and magnitude of harvested energy increased with increasing porosity, as was predicted by the piezoelectric energy harvesting figures of merit of the three samples tested, demonstrating proof-of-concept for the use of porous ferroelectric materials in piezoelectric energy harvesters. The reduced capacitance of the porous samples compared to the dense materials may also enable easier resistance matching if this proof-of-concept experiment was to be developed further into a prototype harvesting device.

5. Conclusions

This paper has demostrated the potential for the controlled introduction of porosity into ferroelectric ceramics as a method to improve their longitudinal energy harvesting capabilities. Two finite element models were presented that investigated the effect of pore structure on the poling behaviour and piezoelectric properties of porous ferroelectric materials in varying levels of detail, followed by an experimental study whereby highly aligned porous barium titanate was fabricated via the freeze casting method and found to have improved energy harvesting properties compared to dense barium titanate.

Firstly, a single pore model showed that high aspect ratio pores aligned to the poling direction aided the poling of the porous ferroelectric material through promotion of homogeneous poling fields that yield high fractions of poled ferroelectric phase, compared to pores with lower aspect ratios not aligned to the poling axis. This model provides an explanation for high piezoelectric strain coefficients that have been reported previously in freeze cast ferroelectric ceramics, highlighting the importance of the link between pore morphology and structure and the resulting piezoelectric properties of porous ferroelectric materials.

A second finite element model was then used to more accurately model 2-2 connected porous structures commonly achieved through water-based freeze casting. A porous network approach was used to investigate the effect of porosity in the ceramic channels and ceramic bridges in the pore channels. As expected, increasing the fraction of porosity in the ceramic channels reduced the fraction of material poled and therefore the effective longitudinal piezoelectric strain coefficient, d_{33} of the material. However, of perhaps greater interest was the detrimental effect of the presence of ceramic bridges in the pore channels, which tended to remain unpoled due to their location within the porous structure, whilst acting to restrict the induced strain in the highly poled ceramic channels, leading to lower d_{33} coefficients than similar porosity structures with clear pore channels.

Freeze cast porous barium titanate samples were fabricated and characterised in terms of their piezoelectric and dielectric properties and compared to dense barium titanate and porous barium titanate with spherical, uniformly distributed pores. The freeze cast material had similar d_{33} coefficients as the dense material up to ~50 vol.% porosity, significantly higher than the barium titanate with uniform porosity. The permittivity of the material was found to decrease with increasing porosity in all cases, leading to excellent piezoelectric energy harvesting figures of merit, with a maximum of 3.79 pm^2/N achieved at 45 vol.% porosity (relative density, ρ_{rel} = 0.55), compared to ~1.40 pm^2/N for dense barium titanate.

Finally, the benefits of introducing porosity into ferroelectric materials in terms of the piezoelectric energy harvesting performance were demonstrated experimentally. Dense and freeze cast porous barium titanate samples were mechanically excited on a shaker and the electrical response used to charge a 1 μF capacitor. The porous samples were found to charge the capacitor at a faster rate than the dense material, as predicted by the energy harvesting figures of merit. The maximum measured voltage across the charged capacitor was found to be 234 mV for freeze cast barium titanate with 45 vol.% porosity, compared with 96 mV for dense barium titanate.

References

[1] F. K. Shaikh, S. Zeadally, Energy harvesting in wireless sensor networks: A comprehensive review, Renew. Sustain. Energy Rev. 55 (2016) 1041–1054.

[2] C. R. Bowen, H. A. Kim, P. M. Weaver, S. Dunn, Piezoelectric and ferroelectric materials and structures for energy harvesting applications, Energy Environ. Sci. 7 (2013) 25–44.

[3] C. R. Bowen, J. Taylor, E. LeBoulbar, D. Zabek, A. Chauhan, R. Vaish, Pyroelectric materials and devices for energy harvesting applications, Energy Environ. Sci. 7 (2014) 3836–3856.

[4] R. A. Islam, S. Priya, Realization of high-energy density polycrystalline piezoelectric ceramics, Appl. Phys. Lett. 88 (2006) 032903.

[5] C. R. Bowen, J. Taylor, E. Le Boulbar, D. Zabek, V. Y. Topolov, A modified figure of merit for pyroelectric energy harvesting, Mater. Lett. 138 (2015) 243–246.

[6] J. I. Roscow, Y. Zhang, J. Taylor, C. R. Bowen, Porous ferroelectrics for energy harvesting applications, Eur. Phys. J. Spec. Top. 224 (2015) 2949–2966.

[7] G. H. Haertling, Ferroelectric Ceramics: History and Technology, J. Am. Ceram. Soc. 82 (1999) 797–818.

[8] R. W. C. Lewis, A. C. E. Dent, R. Stevens, C. R. Bowen, Microstructural modelling of the polarization and properties of porous ferroelectrics, Smart Mater. Struct. 20 (2011) 085002.

[9] J. I. Roscow, R. W. C. Lewis, J. Taylor, C. R. Bowen, Modelling and fabrication of porous sandwich layer barium titanate with improved piezoelectric energy harvesting figures of merit, Acta Mater. 128 (2017) 207–217.

[10] E. Mercadelli, A. Sanson, C. Galassi, Porous piezoelectric ceramics, in: E. Suaste-Gomez (Ed.), Piezoelectric Ceramics, InTech Open, 2010, Ch. 6, pp. 111–128.

[11] R. E. Newnham, D. P. Skinner, L. E. Cross, Connectivity and piezoelectric-pyroelectric composites, Mater. Res. Bull. 13 (1978) 525–536.

[12] S. Marselli, V. Pavia, C. Galassi, E. Roncari, F. Cranciun, G. Guidarelli, Porous piezoelectric ceramic hydrophone, J. Acoust. Soc. Am. 106 (1999) 733–738.

[13] H. Kara, R. Ramesh, R. Stevens, C. R. Bowen, Porous PZT ceramics for receiving transducers, IEEE Trans. Ultrason., Ferroelect., Freq. Control 50 (2003) 289–296.

[14] C. R. Bowen, A. Perry, A. C. F. Lewis, H. Kara, Processing and properties of porous piezoelectric materials with high hydrostatic figures of merit, J. Eur. Ceram. Soc. 24 (2004) 541–545.

[15] T. Zeng, X. Dong, S. Chen, H. Yang, Processing and piezoelectric properties of porous PZT ceramics, Ceram. Int. 33 (2007) 395–399.

[16] A.-K. Yang, C.-A. Wang, R. Guo, Y. Huang, C.-W. Nan, Porous PZT Ceramics with High Hydrostatic Figure of Merit and Low Acoustic Impedance by TBA-Based Gel-Casting Process, J. Am. Ceram. Soc. 93 (2010) 1427–1431.

[17] A. Navarro, R. W. Whatmore, J. R. Alcock, Preparation of functionally graded PZT ceramics using tape casting, J. Electroceram. 13 (2004) 413–415.

[18] C. P. Shaw, R. W. Whatmore, J. R. Alcock, Porous, Functionally Gradient Pyroelectric Materials, J. Am. Ceram. Soc. 90 (2007) 137–142.

[19] J. I. Roscow, J. Taylor, C. R. Bowen, Manufacture and characterization of porous ferroelectrics for piezoelectric energy harvesting applications, Ferroelectr. 498 (2016) 40–46.

[20] Y. Zhang, Y. Bao, D. Zhang, C. R. Bowen, Porous PZT Ceramics with Aligned Pore Channels for Energy Harvesting Applications, J. Am. Ceram. Soc. 98 (2015) 2980–2983.

[21] Y. Zhang, M. Xie, J. Roscow, K. Zhou, Y. Bao, D. Zhang, C. Bowen, Enhanced pyroelectric and piezoelectric properties of PZT with aligned porosity for energy harvesting applications, J. Mater. Chem. A 5 (2017) 6569–6580.

[22] R. Guo, C. A. Wang, A. Yang, Effects of pore size and orientation on dielectric and piezoelectric properties of 1-3 type porous PZT ceramics, J. Eur. Ceram. Soc. 31 (2011) 605–609.

[23] S. H. Lee, S. H. Jun, H. E. Kim, Y. H. Koh, Piezoelectric properties of PZT-based ceramic with highly aligned pores, J. Am. Ceram. Soc. 91 (2008) 1912–1915.

[24] S.-H. Lee, S.-H. Jun, H.-E. Kim, Y.-H. Koh, Fabrication of Porous PZT-PZN Piezoelectric Ceramics With High Hydrostatic Figure of Merits Using Camphene-Based Freeze Casting, J. Am. Ceram. Soc. 90 (2007) 2807–2813.

[25] W. Liu, N. Li, Y. Wang, H. Xu, J. Wang, J. Yang, Preparation and properties of 3-1 type PZT ceramics by a self-organization method, J. Eur. Ceram. Soc. 35 (2015) 3467–3474.

[26] W. Liu, L. Lv, Y. Li, Y. Wang, J. Wang, C. Xue, Y. Dong, J. Yang, Effects of slurry composition on the properties of 3-1 type porous PZT ceramics prepared by ionotropic gelation, Ceram. Int. 43 (2017) 6542–6547.

[27] I. S. Grant, W. R. Phillips, Electromagnetics, in: Electromagnetics, 1990.

[28] L. Padurariu, L. P. Curecheriu, L. Mitoseriu, Nonlinear dielectric properties of paraelectric-dielectric composites described by a 3D Finite Element Method based on Landau-Devonshire theory, Acta Mater. 103 (2016) 724–734.

[29] F. Gheorghiu, L. Padurariu, M. Airimioaei, L. Curecheriu, C. Ciomaga, C. Padurariu, C. Galassi, L. Mitoseriu, Porosity-Dependent Properties of Nb-Doped $Pb(Zr,Ti)O_3$ Ceramics, J. Am. Ceram. Soc. 100 (2016) 647–658.

[30] R. Khachaturyan, S. Zhukov, J. Schultheiß, C. Galassi, C. Reimuth, J. Koruza, H. von Seggern, Y. A. Genenko, Polarization-switching dynamics in bulk ferroelectrics with isometric and oriented anisometric pores, J. Phys. D: App. Phys. 50 (2017) 045303.

[31] C. Padurariu, L. Padurariu, L. Curecheriu, C. Ciomaga, N. Horchidan, C. Galassi, L. Mitoseriu, Role of the pore interconnectivity on the dielectric, switching and tunability properties of PZTN ceramics, Ceram. Int. 43 (2017) 5767–5773.

[32] T. Zeng, X. Dong, C. Mao, Z. Zhou, H. Yang, Effects of pore shape and porosity on the properties of porous PZT 95/5 ceramics, J. Eur. Ceram. Soc. 27 (2007) 2025–2029.

[33] H. L. Zhang, J.-F. Li, B.-P. Zhang, Microstructure and electrical properties of porous PZT ceramics derived from different pore-forming agents, Acta Mater. 55 (2007) 171–181.

[34] A. P. Roberts, E. J. Garboczi, Elastic properties of model porous ceramics, J. Am. Ceram. Soc. 83 (2000) 3041–3048.

[35] S. Deville, E. Saiz, R. K. Nalla, A. P. Tomsia, Freezing as a path to build complex composites, Science 311 (2006) 515–518.

[36] J. Seuba, S. Deville, C. Guizard, A. J. Stevenson, Mechanical properties and failure behavior of unidirectional porous ceramics, Sci. Rep. 6 (2016) 24326.

[37] D. Berlincourt, H. A. Krueger, C. Near, Properties of Morgan electro ceramic ceramics, Technical Publication TP-226, Morgan Electroceramics (1999) 1–12.

[38] T. Hang, J. Glaum, Y. A. Genenko, T. Phung, M. Hoffman, Investigation of partial discharge in piezoelectric ceramics, Acta Mater. 102 (2016) 284–291.

[39] S. Deville, E. Saiz, A. P. Tomsia, Ice-templated porous alumina structures, Acta Mater. 55 (2007) 1965–1974.

[40] S. Deville, Freezing Colloids: Observations, Principles, Control, and Use, Springer, 2017.

[41] S. Deville, Freeze-Casting of Porous Ceramics: A Review of Current Achievements and Issues, Adv. Eng. Mater. 10 (2008) 155–169.

[42] T. Waschkies, R. Oberacker, M. J. Hoffmann, Control of lamellae spacing during freeze casting of ceramics using double-side cooling as a novel processing route, J. Am. Ceram. Soc. 92 (2009) 79–84.

[43] S. Deville, E. Maire, G. Bernard-Granger, A. Lasalle, A. Bogner, C. Gauthier, J. Leloup, C. Guizard, Metastable and unstable cellular solidification of colloidal suspensions, Nat. Mater. 8 (12) (2009) 966–972.

[44] N. O. Shanti, K. Araki, J. W. Halloran, Particle redistribution during dendritic solidification of particle suspensions, J. Am. Ceram. Soc. 89 (8) (2006) 2444–2447.

[45] X.-Y. Zhang, Y. Zhang, D. Zhang, Effect of particle size on the lamellar pore microstructure of porous Al_2O_3 ceramics fabricated by the unidirectional freezing, App. Mech. Mater. 184-185 (2012) 818–825.

[46] C. R. Bowen, A. C. Dent, R. Stevens, M. G. Cain, A. Avent, A new method to determine the un-poled elastic properties of ferroelectric materials, Sci. Tech. Adv. Mater. (2017) 253–263.

[47] H. R. Gallantree, Piezoelectric ceramic/polymer composites, British Ceramics Proceedings 41 (1989) 161.

[48] BSI, Advanced technical ceramics Monolithic ceramics General and textural properties, Part 2: Determination of density and porosity.

[49] A. Goncharenko, V. Lozovski, E. Venger, Lichtenecker's equation: applicability and limitations, Optics Communications (January) (2000) 19–32.

[50] G. Arlt, D. Hennings, G. D. With, Dielectric properties of finegrained barium titanate ceramics Dielectric properties of fine-grained barium titanate ceramics, J. Appl. Phys. 58 (1985) 1619–1625.

[51] A. Bell, Grain Size Effects in Barium Titanate - Revisited, IEEE (1991) 14–17.

[52] Y. Tan, J. Zhang, Y. Wu, C. Wang, V. Koval, B. Shi, H. Ye, R. McKinnon, G. Viola, H. Yan, Unfolding grain size effects in barium titanate ferroelectric ceramics, Sci. Rep. 5 (2015) 9953.

[53] D. Berlincourt, H. Jaffe, Elastic and piezoelectric coefficients of single crystal Barium Titanate, Phys. Rev. 111 (1958) 143–148.

[54] S. Wada, K. Takeda, T. Tsurumi, T. Kimura, Preparation of [110] grain oriented barium titanate ceramics by templated grain growth method and their piezoelectric properties, Japan. J. App. Phys. 46 (2007) 7039–7043.

[55] Y. Huan, X. Wang, J. Fang, L. Li, Grain size effects on piezoelectric properties and domain structure of $BaTiO_3$ ceramics prepared by two-step sintering, J. Am. Ceram. Soc. 96 (2013) 3369–3371.

[56] S. Priya, Criterion for Material Selection in Design of Bulk Piezoelectric Energy Harvesters, IEEE Trans. Ultrason., Ferroelect., Freq. Control 57 (2010) 2610–2612.

6.2 Summary

This paper provided another case study on the effect of porous structure on the poling behaviour and piezoelectric properties of porous ferroelectric materials, in this instance those with highly aligned structures orientated to the poling direction. The key findings are summarised as:

1. A single pore model was used to examine the effect of pore shape and orientation with respect to poling field direction on the poling behaviour of the ferroelectric material. Elongated pores aligned to the field yielded the highest fractions of poled material, i.e. they disrupted the field the least relative to the homogeneous fields observed in dense materials, whilst high aspect ratio pores orientated perpendicular to the poling direction resulted in the highest fractions of unpoled material.

2. A porous network model based on 2-2 structures aligned to the poling direction was used to investigate the effect of structural features typical of water-based freeze cast materials. The findings of this model agreed with the observations from the single pore model as the structures with highly defined pore channels, i.e. few ceramic bridges between adjacent ceramic lamellae, were found to have the highest longitudinal piezoelectric strain coefficients, close to that of dense barium titanate. Increasing the alignment of the porous structure in the poling direction also increased permittivity, however, large reductions in permittivity were achieved with the introduction of porosity, regardless of pore alignment, leading to predicted increases in energy harvesting figures of merit.

3. Barium titanate with a range of porosities was produced via the freeze casting method and the piezoelectric energy harvesting properties characterised. As predicted by the finite element model, and reported previously in the literature, the freeze cast materials had excellent longitudinal strain coefficients, with a maximum of $d_{33} = 134.5$ pC/N for barium titanate with 45 vol.% porosity, a fall of only 7% compared to the d_{33} of the dense material. Lower than expected permittivity resulted in excellent energy harvesting figures of merit with a maximum $d_{33}^2/\varepsilon_{33}^\sigma = 3.79$ pm^2/N at 45 vol.% porosity compared to $d_{33}^2/\varepsilon_{33}^\sigma = 1.40$ pm^2/N for the dense barium titanate; the reason for the low permittivity values remains unclear and may warrant further investigation, but is thought to be a microstructural effect. This was slightly higher than the maximum figure of merit for the sandwich layer barium titanate reported in Chapter 5 (3.74 pm^2/N).

4. Porous barium titanate was found to convert mechanical energy into electrical energy more effectively than the dense barium titanate, as shown in the piezoelectric harvesting demonstration discussed in the paper. This shows the benefits of porosity are not just limited to enhancements in figures of merit but can actually improve the energy harvesting capabilities of ferroelectric materials.

Chapter 7

Conclusions and further work

This chapter summarises the findings reported in this thesis and provides a discussion of the importance and novelty of key points with regards to the objectives set out in Chapter 2. The further work section discusses the key findings and how the research may be continued to develop increased understanding of the behaviour of composite ferroelectric materials for a variety of applications.

7.1 Conclusions

The key findings of this thesis can be summarised as:

1. The morphology and connectivity of pores was found to have a significant effect on the poling behaviour of porous ferroelectric ceramics, which enabled tuning of key material properties for longitudinal mode piezoelectric energy harvesting where the relevant figure of merit is $d_{33}^2/\varepsilon_{33}^\sigma$. Finite element models were developed to better understand the effect of pore morphology on the poling behaviour that were then used to design porous ferroelectric structures with improved energy harvesting figures of merit.

    i) Porous ferroelectric materials with high aspect ratio pores aligned to the poling direction resulted in the highest fractions of active material becoming poled and therefore yielded the highest longitudinal piezoelectric strain coefficients (d_{33}), compared to porous materials with equi-axed pores or pores aligned perpendicular to the poling direction.

    ii) Concentrating porosity into a porous layer orientated perpendicular to the poling direction and sandwiched between dense outerlayers resulted in low effective permittivity (ε_{33}^σ) and relative high piezoelectric strain coefficients due to the complex poling behaviour, highlighting another potential method to produce materials with improved energy harvesting figures of merit compared to the dense ferroelectric material.

2. Novel processing routes were used to fabricate porous ferroelectric ceramics with pore structures identified as promising by the finite element models (i.e. those with high figures of merit).

   i) The burned out polymer spheres (BURPS) method was adapted to form barium titanate with high porosity layers sandwiched between dense outerlayers.

   ii) Freeze casting was used to fabricate barium titanate with a 2-2 type lamellar porous structure aligned to the poling direction.

   iii) A comparison of material properties relevant to the piezoelectric energy harvesting performance are shown in Fig. 7-1 for barium titanate with the various pore structures fabricated and discussed throughout this thesis.

3. The introduction of porosity into barium titanate was found to increase the rate at which mechanical energy was converted into electrical energy compared with the dense material, as predicted by calculated energy harvesting merit indices.

   i) This was demonstrated by subjecting both porous and dense barium titanate to mechanical excitation and using the derived electrical current to charge a reference capacitor.

4. Permittivity contrast between phases in composite materials (e.g low permittivity pores in a high permittivity ferroelectric ceramic or a high permittivity filler in a low permittivity matrix) leads to inhomogenous electric field distributions when an external field is applied, with field preferentially concentrating in the low permittivity phase.

   i) For porous ferroelectric materials this can be exploited to yield high piezoelectric coefficients by aligning high aspect pores parallel to the poling direction, resulting in high fractions of the ferroelectric material becoming poled.

   ii) In composites for energy storage this causes field concentrations in the matrix phase that leads to an observed increase in the effective permittivity and reduction in dielectric strength. The highest field concentrations are observed when high aspect ratio fibres are aligned parallel to the applied field.

5. It is concluded that the use of composite materials for energy storage applications is flawed because the reduction in breakdown strength outweighs the beneficial increase in effective permittivity.

7.2 Discussion and further work

The main bulk of work in this thesis relates to the effect porosity has on key material properties for energy harvesting, in particular the longitudinal piezoelectric coefficient, d_{33}, and the relative permittivity, ε_r. The research has demonstrated that both the morphology of pores and the
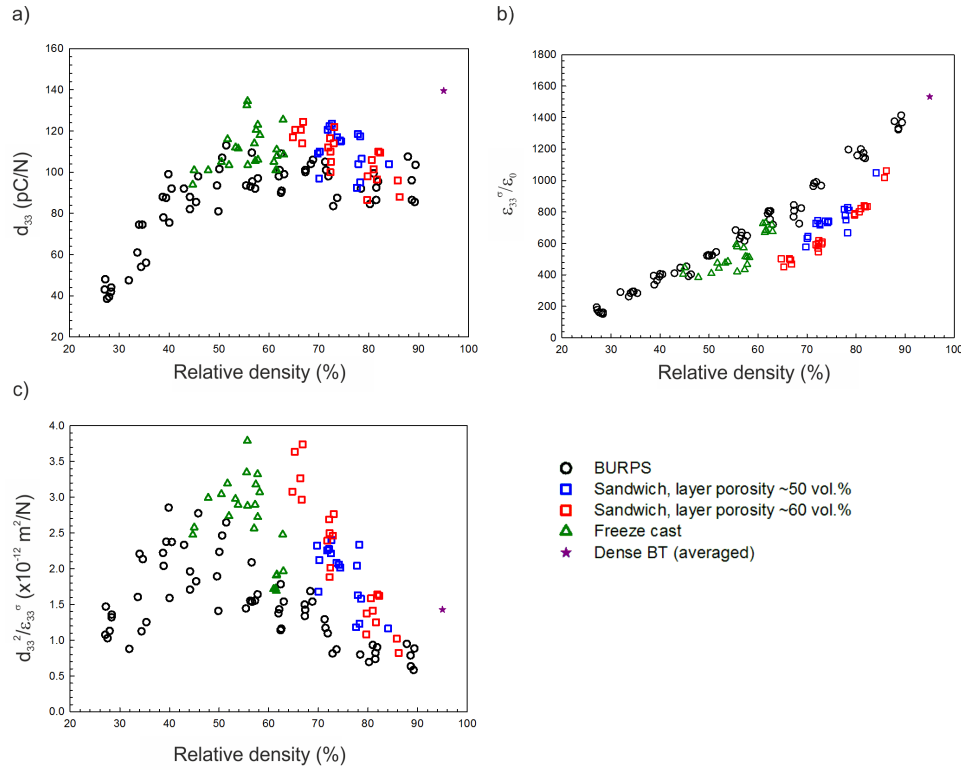
133

Figure 7-1: Comparison of (a) piezoelectric strain coefficient, d_{33}, (b) relative permittivity, $\varepsilon_{33}^{\sigma}/\varepsilon_0$, and (c) energy harvesting figure of merit, $d_{33}^2/\varepsilon_{33}^{\sigma}$ for dense and porous barium titanate with different pore structures.

bulk porous structure can affect significantly the properties of the porous ferroelectric material. For example, anisotropic pores aligned parallel to the poling axis yield high d_{33} coefficients yet also result in a higher permittivity, whereas lower permittivies occur when pores are either concentrated into a layer perpendicular to the applied poling direction, as in Chapter 5, or for example in freeze cast PZT poled perpendicular to the freezing direction, as in the paper by *Zhang et al. (2017)*. For certain material systems or applications it may be that reducing the permittivity is more important than maintaining a high d_{33}, in which case the porous structure and processing route can be selected accordingly with the help of the porous network model. For example, the potential for layered structures for hydrophone applications was presented in the form of a conference paper written for the 2017 Joint IEEE International Symposium on the Applications of Ferroelectrics (ISAF) in which bilayer PZT, formed of a dense and a porous layer, was modelled and predicted to have excellent hydrostatic properties compared to uniform porous and dense PZT. The introduction of porosity also reduces the acoustic impedance of ferroelectric ceramics for operation in water or when in contact with biological tissue (*Ramesh et al. (2005), Zeng et al. (2007), Mercadelli et al. (2010)*), which when coupled with low permittivity and d_{31}, and relatively high d_{33}, makes these bilayer structures promising for hydrophone and medical applications and would therefore be of interest to study further.

The finite element models presented in this work helped to reveal the importance of porous structure with respect to the poling behaviour of ferroelectric materials. However, the models do not take into account the switching dynamics of domains, a field of research that has received some interest in the past two years with several papers published on the subject, including those by *Gheorghiu et al. (2016)* and *Khachaturyan et al. (2017)*. Gaining a further understanding of how domain switching may be influenced by porosity may shed further light of the fundamental physics of these materials and is an area of research that would be interesting in terms of further work. The models presented in this thesis essentially assume that the net polarisation direction of domains within the volume contained in a single element will switch if the field is large enough and contribute to the piezoelectric response with the same properties as the dense ferroelectric ceramic phase, however, this is thought to be an oversimplification, albeit one that facilitated a deeper understanding of the effect of porosity on ferroelectric material properties. Work is currently ongoing to investigate this phenomenon in the form of further modelling studies, and it is hoped future collaborations may provide experimental evidence for this. Related to this is the effect of pore size on the material properties, which has not been studied in detail during this project as the porous network models do not predict size effects on the relevant scale. The literature on the subject of effect of pore size on piezoelectric and dielectric properties is somewhat contradictory (for example, some studies observe no change in behaviour with pore size, e.g. *Khachaturyan et al. (2017)*, while others report differences in the material properties with variation in pore size, e.g. *Bowen et al. (2004)*), perhaps because with change in pore size comes a change in other microstructural features such as pore shape and interconnectivity, and so is another avenue of research that may be of interest.

An additional area of research related to the work contained in this thesis is the design and fabrication of flexible ferroelectric composites for energy harvesting and sensing applications, as they are of particular interest for robotic skins that can both actuate and act as thermal and touch sensors. Typically a piezoelectric ceramic phase is added to a polymer phase, which may or may not be ferroelectric, and porosity may also be introduced. It is envisaged that the modelling methods used here may be able to help better understand the poling behaviour and properties of this type of composites to enable improved design in the future.

The research in this thesis on porous ferroelectrics has focussed on one material system, barium titanate, as it is cleaner and less toxic to process and sinter than PZT, as well as being a stable stoichiometric compound, eliminating concerns regarding change in composition during sintering, which could potentially be more likely to occur in high porosity PZT ceramics due to the volatility of lead at high temperatures. In the final year of the project porous PZT was also manufactured but it was decided not to report in detail these findings so as not to distract from the main research topic into the effect of porosity; barium titanate, although not as piezoelectrically active as PZT, was considered to be a satisfactorily 'ideal' system to study. The results for PZT, whilst demonstrating similar trends in terms of material properties, do not yield the same percentage increases in terms of energy harvesting figure of merit as found for barium titanate with increasing porosity. The reason for this appears to be that the PZT used for the experiments (Noliac NCE-55) had a measured d_{33} when dense of $\sim$550 pC/N and a relative

permittivity of $\sim$4000, which meant that although was permittivity initially high (2.35 times that of the dense barium titanate produced in this study), offering the potential for significant reductions with the introduction of porosity, the d_{33} was almost four times higher than the barium titanate. When porosity was introduced the effect on the piezoelectric coefficients for PZT was relatively more pronounced than for the barium titanate, perhaps because the permittivity contrast between the ceramic and the pore was initially higher, and as the energy harvesting figure of merit depends on the square of d_{33} it requires a rapid fall in permittivity at the same time to increase significantly, which was not seen in the freeze cast PZT where an almost linear relationship with increasing porosity was observed (as found in the porous network model presented in Chapter 6). Therefore, relatively small increases were observed compared to the three-fold increases found in this work porous barium titanate. This has significance for research into state of the art lead-free materials that are intended to replace lead-based ferroelectrics as an environmentally cleaner option; currently they struggle to compete with PZT, however, introducing porosity could increase their performance for certain applications to such an extent that, when coupled with advances in low power electronics, may make them a viable alternative to PZT. This is not to say that the energy harvesting performance of PZT cannot be increased significantly by the controlled introduction of porosity, as can be seen from the reanalysed data from literature in Chapter 2, rather that very precise control of the porous structure is required to maintain a high d_{33} at over 50 vol.% porosity. Ionotropic gelation was highlighted in Chapter 6 as a potential alternative to freeze casting for producing highly aligned 3-1 porous structures with excellent material properties (*Liu et al. (2015, 2017)*). Another area of future work would be to use the model to explore a range of materials with various porous structures to identify promising combinations of materials systems and pore structures for specific applications.

Bibliography

Adhikary, P., Garain, S., Mandal, D. (2015). The co-operative performance of a hydrated salt assisted sponge like P(VDF-HFP) piezoelectric generator: an effective piezoelectric based energy harvester. Phys. Chem. Chem. Phys., 17, 7275-7281.

Ahn, C. W., Amarsanaa, G., Won, S. S., Chae, S. A., Lee, D. S., Kim, I. W. (2015). Antiferroelectric Thin-Film Capacitors with High Energy-Storage Densities, Low Energy Losses, and Fast Discharge Times. ACS Appl. Mater. Interfaces, 7, 26381-26386.

Aisu, K., Osada, M., Suzuki, Y. (2014). Synthesis of $BaTiO_3$ Nanowires via Anodic Aluminum Oxide Template Method Assisted by Vacuum-and-Drop Loading. J. Mater. Sci. Technol., 1, 1-6.

Akdogan, E. K., Allahverdi, M., Safari, A. (2005). Piezoelectric Composites for Sensor and Actuator Applications. IEEE Trans. Ultrason., Ferroelect., Freq. Control, 52, 746-775.

Allahverdi, M., Danforth, S. C., Jafari, M., Safari, A. (2001). Processing of advanced electroceramic components by fused deposition technique. J. Eur. Ceram. Soc., 21, 1485-1490.

Allen, J., Smits, J. (2001). Energy harvesting eel. J. Fluids Struct., 15, 1-13.

Almond, D. P., Bowen, C. R. (2004). Anomalous power law dispersions in ac conductivity and permittivity shown to be characteristics of microstructural electrical networks. Phys. Rev. Lett., 92, 157601-1.

Andrews, C., Lin, Y., Sodano, H. A. (2010). The effect of particle aspect ratio on the electroelastic properties of piezoelectric nanocomposites. Smart Mater. Struct., 19, 25018.

Arai, T., Ayusawa, K., Sato, H., Miyata, T., Kazutami, K., Keiichi, K. (1991). Properties of hydrophone with porous piezoelectric ceramics. Jpn. J App. Phys., 30, 2253-2255.

Araki, K., Halloran, J. W. (2005). Porous Ceramic Bodies with Interconnected Pore Channels by a Novel Freeze Casting Technique. J. Am. Ceram. Soc., 88, 1108-1114.

Araki, K., Halloran, J. W. (2004). Room-temperature freeze casting for ceramics with nonaqueous sublimable vehicles in the naphthalene-camphor eutectic system. J. Am. Ceram. Soc., 87, 2014-2019.

Arlt, G., Hennings, D., With, G. De. (1985). Dielectric properties of fine-grained barium titanate ceramics. J. Appl. Phys., 58, 1619-1625.

Banno, H. (1993). Effects of porosity on dielectric, elastic and electromechanical properties of $Pb(Zr,Ti)O_3$ ceramics with open pores: A theoretical approach. Jpn. J App. Phys., Part 1, 32, 4214-4217.

Beeby, S. P., Tudor, M. J., White, N. M. (2006). Energy harvesting vibration sources for microsystems applications. Meas. Sci. Tech., 17, 175-195.

Bell, A. J. (1991). Grain Size Effects in Barium Titanate - Revisited. IEEE, 1417.

Berlincourt, D., Jaffe, H. (1958). Elastic and piezoelectric coefficients of single crystal Barium Titanate. Phys. Rev., 111, 143148.

Berlincourt, D., Krueger, H. A., Near, C. (1999). Properties of Morgan electro ceramic ceramics. Technical Publication TP-226, Morgan Electroceramics, 1-12.

Bosse, P. W., Challagulla, K. S., Venkatesh, T. A. (2012). Effects of foam shape and porosity aspect ratio on the electromechanical properties of 3-3 piezoelectric foams. Acta Mater., 60, 6464-6475.

Bowen, C. R., Kara, H. (2002). Pore anisotropy in 3-3 piezoelectric composites. Mater. Chem. Phys., 75, 45-49.

Bowen, C. R., Kim, H. A., Weaver, P. M., Dunn, S. (2013). Piezoelectric and ferroelectric materials and structures for energy harvesting applications. Energy Environ. Sci., 7, 25-44.

Bowen, C. R., Perry, A., Lewis, A. C. F., Kara, H. (2004). Processing and properties of porous piezoelectric materials with high hydrostatic figures of merit. J. Eur. Ceram. Soc., 24, 541-545.

Bowen, C. R., Taylor, J., Le Boulbar, E., Zabek, D., Topolov, V. Y. (2015). A modified figure of merit for pyroelectric energy harvesting. Mater. Lett., 138, 243-246.

Bowen, C. R., Taylor, J., Le Boulbar, E., Zabek, D., Chauhan, A., Vaish, R. (2014). Pyroelectric materials and devices for energy harvesting applications. Energy Environ. Sci., 7, 3836-3856.

Bowen, C. R., Topolov, V. Y. (2003). Piezoelectric sensitivity of $PbTiO_3$-based ceramic/polymer composites with 0-3 and 3-3 connectivity. Acta Mater., 51, 4965-4976.

Bowen, C. R., Dent, A. C., Stevens, R., Cain, M. G., Avent, A. (2017). A new method to determine the un-poled elastic properties of ferroelectric materials. Sci. Tech. Adv. Mater., 253-263.

Briscoe, J., Dunn, S. (2015). Piezoelectric nanogenerators - a review of nanostructured piezoelectric energy harvesters. Nano Energy, 14, 15-29.

BSI. (1993). Advanced technical ceramics Monolithic ceramics General and textural properties. Part 2: Determination of Density and Porosity.

Buscaglia, M. T., Harnagea, C., Dapiaggi, M., Buscaglia, V., Pignolet, A., Nanni, P. (2009). Ferroelectric $BaTiO_3$ Nanowires by a Topochemical Solid-State Reaction. Chem. Mater., 21, 5058-5065.

Cha, S. N., Kim, S. M., Kim, H. J., Ku, J. Y., Sohn, J. I. (2011). Porous PVDF as effective sonic wave driven nanogenerators. Nano Lett., 11, 5142-5147.

Challagulla, K. S., Venkatesh, T. A. (2012). Electromechanical response of piezoelectric foams. Acta Mater., 60, 2111-2127.

Chang, H. H. S., Huang, Z. (2010). Laminate composites with enhanced pyroelectric effects for energy harvesting. Smart Mater. Struct., 19, 65018.

Chen, R., Huang, Y., Wang, C. A., Qi, J. (2007). Ceramics with ultra-low density fabricated by gelcasting: An unconventional view. J. Am. Ceram. Soc., 90, 3424-3429.

Chi, Q. G., Li, W. L., Fei, W. D., Zhao, Y. (2009). Enhanced performance of sandwich structure $Pb_{0.8}La_{0.1}Ca_{0.1}T_{0.975}O_3$ thin film for pyroelectric applications. Mater. Lett., 63, 1712-1714.

Chi, Q., Dong, J., Zhang, C., Wang, X., Lei, Q. (2016). Highly (100)-oriented sandwich structure of $(Na_{0.85}K_{0.15})_{0.5}Bi_{0.5}TiO_3$ composite films with outstanding pyroelectric properties. J. Mater. Chem. C, 4, 4442-4450.

Choi, C.-H., Seo, I.-T., Song, D., Jang, M.-S., Kim, B.-Y., Nahm, S., Song, H.-C. (2013). Relation between piezoelectric properties of ceramics and output power density of energy harvester. J. Eur. Ceram. Soc., 33, 1343-1347.

Chu, B., Zhou, X., Ren, K., Neese, B., Lin, M., Wang, Q., Zhang, Q. M. (2006). A dielectric polymer with high energy density and fast discharge speed. Science, 313, 334-336.

Cook-Chennault, K. A., Thambi, N., Sastry, A. M. (2008). Powering MEMS portable devices-a review of non regenerative and regenerative power supply systems with special emphasis on piezoelectric energy harvesting systems. Smart Mater. Struct., (43001).

Craciun, F., Galassi, C., Roncari, E., Filippi, A., Guidarelli, G. (1998). Electro-elastic properties of porous piezoelectric ceramics obtained by tape casting. Ferroelectr., 205, 49-67.

Creedon, M. J., Schulze, W. A. (1994). Axially distorted 3-3 piezoelectric composites for hydrophone applications. Ferroelectr., 153, 333-339.

Dang, Z.-M., Yuan, J.-K., Yao, S.-H., Liao, R.-J. (2013). Flexible Nanodielectric Materials with High Permittivity for Power Energy Storage. Adv. Mater., 25, 6334-6365.

Dent, A. C., Bowen, C. R., Stevens, R., Cain, M. G., Stewart, M. (2007). Effective elastic properties for unpoled barium titanate. J. Eur. Ceram. Soc., 27, 3739-3743.

Deterre, M., Lefeuvre, E., Dufour-Gergam, E. (2012). An active piezoelectric energy extraction method for pressure energy harvesting. Smart Mater. Struct., 21, 85004.

Deville, S. (2008). Freeze-Casting of Porous Ceramics: A Review of Current Achievements and Issues. Adv. Eng. Mater., 10, 155-169.

Deville, S. (2017). Freezing Colloids: Observations, Principles, Control, and Use. Springer.

Deville, S., Maire, E., Bernard-Granger, G., Lasalle, A., Bogner, A., Gauthier, C., Leloup, J., Guizard, C. (2009). Metastable and unstable cellular solidification of colloidal suspensions. Nat. Mater., 8, 966972.

Deville, S., Saiz, E., Nalla, R. K., Tomsia, A. P. (2006). Freezing as a path to build complex composites. Science, 311, 515-518.

Deville, S., Saiz, E., Tomsia, A. P. (2007). Ice-templated porous alumina structures. Acta Mater., 55, 1965-1974.

Dietze, M., Krause, J., Solterbeck, C.-H., Es-Souni, M. (2007). Thick film polymer-ceramic composites for pyroelectric applications. J. Appl. Phys., 101, 54113.

Dorey, R. A. (2014). Integrated Powder-Based Thick Films for Energy Harvesting Devices. IEEE Sensors Journal, 14, 2177-2184.

Du, H., Lin, X., Zheng, H., Qu, B., Huang, Y., Chu, D. (2016). Colossal permittivity in percolative ceramic/metal dielectric composites. J. Alloys Compd., 663, 848-861.

Dunn, M. L., Taya, M. (1993). Electromechanical properties of porous piezoelectric ceramics. J. Am. Ceram. Soc., 76, 1697-1706.

Duxbury, P. M., Beale, P. D., Bak, H., Schroeder, P. A. (1990). Capacitance and dielectric breakdown of metal loaded dielectrics. J. Phys. D: App. Phys., 23, 1546.

Friswell, M. I., Adhikari, S. (2010). Sensor shape design for piezoelectric cantilever beams to harvest vibration energy. J. Appl. Phys., 108, 14901.

Fukasawa, T., Ando, M. (2001). Synthesis of Porous Ceramics with Complex Pore Structure by Freeze Dry Processing. J. Am. Ceram. Soc., 84, 230-232.

Fukasawa, T., Deng, Z., Ando, M. (2002). Synthesis of Porous Silicon Nitride with Unidirectionally Aligned Channels Using Freeze-Drying Process. J. Am. Ceram. Soc., 85, 2151-2155.

Gallantree, H. R. (1989). Piezoelectric ceramic/polymer composites. British Ceramics Proceedings, 41, 161.

George, S., James, J., Sebastian, M. T. (2007). Giant Permittivity of a Bismuth Zinc Niobate–Silver Composite. J. Am. Ceram. Soc., 90, 3522-3528.

Gheorghiu, F., Padurariu, L., Airimioaei, M., Curecheriu, L., Ciomaga, C., Padurariu, C., Mitoseriu, L. (2016). Porosity-Dependent Properties of Nb-Doped $Pb(Zr,Ti)O_3$ Ceramics. J. Am. Ceram. Soc., 100, 647-658.

Grabowski, C. A., Fillery, S. P., Westing, N. M., Chi, C. Z., Meth, J. S., Durstock, M. F., Vaia, R. A. (2013). Dielectric Breakdown in Silica-Amorphous Polymer Nanocomposite Films: The Role of the Polymer Matrix. ACS Appl. Mater. Interfaces, 5, 5486-5492.

Granstrom, J., Feenstra, J., Sodano, H. A., Farinholt, K. (2007). Energy harvesting from a backpack instrumented with piezoelectric shoulder straps. Smart Mater. Struct., 16, 1810-1820.

Grant, I. S., Phillips, W. R. (1990). Electromagnetics. In Electromagnetics. Guo, N., DiBenedetto, S. A., Tewari, P., Lanagan, M. T., Ratner, M. A., Marks, T. J. (2010). Nanoparticle, Size, Shape, and Interfacial Effects on Leakage Current Density, Permittivity, and Breakdown Strength of Metal Oxide-Polyolefin Nanocomposites: Experiment and Theory. Chem. Mater., 22, 1567-1578.

Guo, R., Wang, C. A., Yang, A. (2011). Effects of pore size and orientation on dielectric and piezoelectric properties of 1-3 type porous PZT ceramics. J. Eur. Ceram. Soc., 31, 605-609.

Gyure, M. F., Beale, P. D. (1992). Dielectric breakdown in continuous models of metal-loaded dielectrics. Phys. Rev. B, 46, 3736-3746.

Haertling, G. H. (1999). Ferroelectric Ceramics: History and Technology. J. Am. Ceram. Soc., 82, 797-818.

Hang, T., Glaum, J., Genenko, Y. A., Phung, T., Hoffman, M. (2016). Investigation of partial discharge in piezoelectric ceramics. Acta Mater., 102, 284-291.

Hao, X., Zhai, J., Yao, X. (2009). Improved Energy Storage Performance and Fatigue Endurance of Sr-Doped $PbZrO_3$ Antiferroelectric Thin Films. J. Am. Ceram. Soc., 92, 1133-1135.

He, Z., Ma, J., Zhang, R. (2004). Investigation on the microstructure and ferroelectric properties of porous PZT ceramics. Ceram. Int., 30, 1353-1356.

Homes, C. C., Vogt, T. (2013). Colossal permittivity materials: Doping for superior dielectrics. Nat. Mater., 12, 782-783.

Hou, Y., Deng, Y., Wang, Y., Gao, H. (2015). Uniform distribution of low content $BaTiO_3$ nanoparticles in poly(vinylidene fluoride) nanocomposite: toward high dielectric breakdown strength and energy storage density. RSC Adv., 5, 72090-72098.

Hu, L., Wang, C.-A., Huang, Y., Sun, C., Lu, S., Hu, Z. (2010). Control of pore channel size during freeze casting of porous YSZ ceramics with unidirectionally aligned channels using different freezing temperatures. J. Eur. Ceram. Soc., 30, 3389-3396.

Hu, P., Song, Y., Liu, H., Shen, Y., Lin, Y., Nan, C.-W. (2013). Largely enhanced energy density in flexible P(VDF-TrFE) nanocomposites by surface-modified electrospun $BaSrTiO_3$ fibers. J. Mater. Chem. A, 1, 1688-1693.

Hu, P., Shen, Y., Guan, Y., Zhang, X., Lin, Y., Zhang, Q., Nan, C. W. (2014). Topological-structure modulated polymer nanocomposites exhibiting highly enhanced dielectric strength and energy density. Adv. Funct. Mater., 24, 3172-3178.

Hu, W., Liu, Y., Withers, R. L., Frankcombe, T. J., Norn, L., Snashall, A., Wong-Leung, J. (2013). Electron-pinned defect-dipoles for high-performance colossal permittivity materials. Nat. Mater., 12, 821-826.

Huan, Y., Wang, X., Fang, J., Li, L. (2013). Grain size effects on piezoelectric properties and domain structure of $BaTiO_3$ ceramics prepared by two-step sintering. J. Am. Ceram. Soc., 96, 33693371.

Huang, J., Zheng, H., Chen, Z., Gao, Q., Ma, N., Du, P. (2009). Percolative ceramic composites with giant dielectric constants and low dielectric losses. J. Mater. Chem., 19, 3909-3913.

Huang, X., Iizuka, T., Jiang, P., Ohki, Y., Tanaka, T. (2012). Role of Interface on the Thermal Conductivity of Highly Filled Dielectric Epoxy / AlN Composites. J. Phys. Chem. C, 116, 13629-13636.

Huang, X., Jiang, P., Kim, C., Liu, F., Yin, Y. (2009). Influence of aspect ratio of carbon nanotubes on crystalline phases and dielectric properties of poly(vinylidene fluoride). Eur. Polym. J., 45, 377-386.

Huang, X., Jiang, P., Xie, L. (2009). Ferroelectric polymer/silver nanocomposites with high dielectric constant and high thermal conductivity. Appl. Phys. Lett., 95, 242901.

Huang, X., Zhi, C., Jiang, P., Golberg, D., Bando, Y., Tanaka, T. (2013). Polyhedral oligosilsesquioxane-modified boron nitride nanotube based epoxy nanocomposites: An ideal dielectric material with high thermal conductivity. Adv. Funct. Mater., 23, 1824-1831.

Hunter, S. R., Lavrik, N. V, Mostafa, S., Rajic, S., Datskos, P. G. (2012). Review of pyroelectric thermal energy harvesting and new MEMs-based resonant energy conversion techniques. Proc. Soc. Photo. Opt. Instru. Eng., 8377.

Hur, J., Seo, I.-T., Kim, D.-H., Nahm, S., Ryu, J., Han, S. H., Yoon, S.-J. (2014). Piezo-

electric Ceramics for Use in Multilayer Actuators and Energy Harvesters. J. Am. Ceram. Soc., 97, 3157-3163.

Islam, R. A., Priya, S. (2006). Realization of high-energy density polycrystalline piezoelectric ceramics. Appl. Phys. Lett., 88, 32903.

Iyer, S., Venkatesh, T. A. (2010). Electromechanical response of porous piezoelectric materials: Effects of porosity connectivity. Appl. Phys. Lett., 97, 72904.

Iyer, S., Alkhader, M., Venkatesh, T. A. (2014). Electromechanical Response of Piezoelectric Honeycomb Foam Structures. J. Am. Ceram. Soc., 97, 826-834.

Jiang, C., Zhang, D., Zhou, K. C., Zhou, X. F., Luo, H., Abrahams, I. (2016). Significantly enhanced energy storage density of sandwich-structured $(Na_{0.5}Bi_{0.5})_{0.93}$ $Ba_{0.07}TiO_3$/P(VDF-HFP) composites induced by PVP-modified two-dimensional platelets. J. Mater. Chem. A, 4, 18050-18059.

Johnson, I., William, T., Choate, W. T., Davidson, A. A. (2008). Waste heat recovery: technology and opportunities in US industry. US Department of Energy.

Jung, H. M., Kang, J.-H., Yang, S. Y., Won, J. C., Kim, Y. S. (2010). Barium titanate nanoparticles with diblock copolymer shielding layers for high-energy density nanocomposites. Chem. Mater., 22, 450-456.

Kar-Gupta, R., Venkatesh, T. A. (2007). Electromechanical response of porous piezoelectric materials: Effects of porosity distribution. Appl. Phys. Lett., 91, 62904.

Kara, H., Ramesh, R., Stevens, R., Bowen, C. R. (2003). Porous PZT ceramics for receiving transducers. IEEE Trans. Ultrason., Ferroelect., Freq. Control, 50, 289-296.

Khachaturyan, R., Zhukov, S., Schulthei, J., Galassi, C., Reimuth, C., Koruza, J., Genenko, Y. A. (2017). Polarization-switching dynamics in bulk ferroelectrics with isometric and oriented anisometric pores. J. Phys. D: App. Phys., 50, 45303.

Kim, K., Zhu, W., Qu, X., Aaronson, C., McCall, W. R. (2014). 3D Optical Printing of Piezoelectric Nanoparticle-Polymer Composite Materials. ACS Nano, 8, 9799-9806.

Kim, P., Doss, N. M., Tillotson, J. P., Hotchkiss, P. J., Pan, M.-J., Marder, S. R., Perry, J. W. (2009). High energy density nanocomposites based on surface-modified $BaTiO_3$ and a ferroelectric polymer. ACS Nano, 3, 2581-2592.

Kim, P., Jones, S. C., Hotchkiss, P. J., Haddock, J. N., Kippelen, B., Marder, S. R., Perry, J. W. (2007). Phosphonic acid-modified barium titanate polymer nanocomposites with high permittivity and dielectric strength. Adv. Mater., 19, 1001-1005.

Kisi, E. H., Piltz, R. O., Viola, G., Ning, H., Forrester, J. S., Piltz, R. O. (2002). The piezoelectric effect in $Na_{0.5}Bi_{0.5}TiO_3$ ceramics. J. Phys: Cond. Matt., 14, 5399-5406.

Kotipalli, V., Gong, Z., Pathak, P., Zhang, T., He, Y., Yadav, S., Que, L. (2010). Light and thermal energy cell based on carbon nanotube films. Appl. Phys. Lett., 97, 124102.

Krishnan, S., Ezhilarasi, D., Uma, G., Umapathy, M. (2014). Pyroelectric-based solar and wind energy harvesting system. IEEE Trans. Sustain. Energy, 5, 73-81.

Kumar, B. P., Kumar, H. H., Kharat, D. K. (2005). Study on pore-forming agents in processing of porous piezoceramics. J. Mater. Sci.: Mater. Electron., 16, 681-686.

142

Kwei, G. H., Lawson, A. C. (1993). Structures of the ferroelectric phases of barium titanate. J. Phys. Chem., 97, 2368-2377.

Lang, S. B. (2005). Pyroelectricity : From Ancient Curiosity to Modern Imaging Tool. Phys. Today, 58, 31-36.

Lang, S. B., Das-Gupta, D. K. (2001). Pyroelectricity: Fundamentals and Applications. In Handbook of Advanced Electronic and Photonic Materials and Devices (p. vol. 4, 1-54).

Lang, S. B., Ringgaard, E. (2009). Measurements of the thermal, dielectric, piezoelectric, pyroelectric and elastic properties of porous PZT samples. In IEEE Conference on Electrical Insulation and Dielectric Phenomena (pp. 739-742).

Lee, F. Y., Navid, A., Pilon, L. (2012). Pyroelectric waste heat energy harvesting using heat conduction. Appl. Therm. Eng., 37, 30-37.

Lee, J., Choi, B. (2014). Development of a piezoelectric energy harvesting system for implementing wireless sensors on the tires. Energy Convers. Manage., 78, 32-38.

Lee, S. H., Jun, S. H., Kim, H. E., Koh, Y. H. (2008). Piezoelectric properties of PZT-based ceramic with highly aligned pores. J. Am. Ceram. Soc., 91, 1912-1915.

Lee, S.-H., Jun, S.-H., Kim, H.-E., Koh, Y.-H. (2007). Fabrication of Porous PZT-PZN Piezoelectric Ceramics With High Hydrostatic Figure of Merits Using Camphene-Based Freeze Casting. J. Am. Ceram. Soc., 90, 2807-2813.

Levassort, F., Lethiecq, M., Desmare, R., Tran-Huu-Hue, L. P. (1999). Effective electroelastic moduli of 3-3(0-3) piezocomposites. IEEE Trans. Ultrason., Ferroelect., Freq. Control, 46, 1028-1034.

Lewis, R. W. C., Allsopp, D. W. E., Shields, P., atka, A., Yu, S., Topolov, V. Y., Bowen, C. R. (2012). Nano-Imprinting of Highly Ordered Nano-Pillars of Lithium Niobate (LiNbO$_3$). Ferroelectr., 429, 62-68.

Lewis, R. W. C., Dent, A. C. E., Stevens, R., Bowen, C. R. (2011). Microstructural modelling of the polarization and properties of porous ferroelectrics. Smart Mater. Struct., 20, 85002.

Li, J. Y., Zhang, L., Ducharme, S. (2007). Electric energy density of dielectric nanocomposites. Appl. Phys. Lett., 90, 132901.

Li, J., Khanchaitit, P., Han, K., Wang, Q. (2010). New route toward high-energy-density nanocomposites based on chain-end functionalized ferroelectric polymers. Chem. Mater., 22, 5350-5357.

Li, J., Tan, S., Ding, S., Li, H., Yang, L., Zhang, Z. (2012). High-field antiferroelectric behaviour and minimized energy loss in poly(vinylidene-co-trifluoroethylene)-graft-poly(ethyl methacrylate) for energy storage application. J. Mater. Chem., 22, 23468.

Li, J., Seok, S. Il, Chu, B., Dogan, F., Zhang, Q., Wang, Q. (2009). Nanocomposites of ferroelectric polymers with TiO$_2$ nanoparticles exhibiting significantly enhanced electrical energy density. Adv. Mater., 21, 217-221.

Li, P. I. N., Pu, Y., Dong, Z., Gao, P. A. N. (2014). Kaolinite as a Suspending Agent for Preparation of Porous BaTiO 3 Ceramics via Freeze Casting. J. Electron. Mater., 43, 459-464.

Li, Q., Han, K., Gadinski, M. R., Zhang, G., Wang, Q. (2014). High energy and power

density capacitors from solution processed ternary ferroelectric polymer nanocomposites. Adv. Mater., 26, 6244-6249.

Li, Q., Liu, F., Yang, T., Gadinski, M. R., Zhang, G., Chen, L.-Q., Wang, Q. (2016). Sandwich-structured polymer nanocomposites with high energy density and great charge-discharge efficiency at elevated temperatures. Proc. Nation. Acad. of Sci., 113, 9995-10000.

Li, Y.-Y., Li, L.-T., Li, B. (2015). Direct ink writing of 3-3 piezoelectric composite. J. Alloys Compd., 620, 125-128.

Li, Z., Luo, X., Wu, W., Wu, J. (2017). Niobium and divalent-modified titanium dioxide ceramics: Colossal permittivity and composition design. J. Am. Ceram. Soc., 100, 3004-3012.

Lin, X., Hu, P., Jia, Z., Gao, S. (2016). Enhanced electric displacement induces large energy density in polymer nanocomposites containing core-shell structured BaTiO 3 @TiO$_2$ nanofibers. J. Mater. Chem. A, 4, 2314-2320.

Liu, G., Button, T. W., Zhang, D. (2014). Lamellar BaTiO$_3$ and its composites fabricated by the freeze casting technique. J. Eur. Ceram. Soc., 34, 4083-4088.

Liu, S., Xue, S., Xiu, S., Shen, B., Zhai, J. (2016). Surface-modified Ba(Zr$_{0.3}$Ti$_{0.7}$)O$_3$ nanofibers by polyvinylpyrrolidone filler for poly(vinylidene fluoride) composites with enhanced dielectric constant and energy storage density. Sci. Rep., 6, 26198.

Liu, S., Zhai, J. (2015). Improving the dielectric constant and energy density of poly(vinylidene fluoride) composites induced by surface-modified SrTiO$_3$ nanofibers by polyvinylpyrrolidone. J. Mater. Chem. A, 3, 1511-1517.

Liu, S., Zhai, J., Wang, J., Xue, S., Zhang, W. (2014). Enhanced energy storage density in poly(vinylidene flouride) nanocomposites by a small loading of surface-hydroxylated Ba$_{0.6}$Sr$_{0.4}$TiO$_3$ nanofibers. ACS Appl. Mater. Interfaces, 6, 1533-1540.

Liu, S., Wang, J., Shen, B., Zhai, J., Hao, H., Zhao, L. (2017). Poly(vinylidene fluoride) nanocomposites with a small loading of core-shell structured BaTiO$_3$@Al$_2$O$_3$ nanofibers exhibiting high discharged energy density and efficiency. J. Alloys Compd., 696, 136-142.

Liu, S., Zhai, J. (2015). Improving the dielectric constant and energy density of poly(vinylidene fluoride) composites induced by surface-modified SrTiO$_3$ nanofibers by polyvinylpyrrolidone. J. Mater. Chem. A, 3, 1511-1517.

Liu, W., Du, L., Wang, Y., Yang, J., Xu, H. (2013). Effects of foam composition on the microstructure and piezoelectric properties of macroporous PZT ceramics from ultrastable particle-stabilized foams. Ceram. Int., 39, 8781-8787.

Liu, W., Li, N., Wang, Y., Xu, H., Wang, J., Yang, J. (2015). Preparation and properties of 3-1 type PZT ceramics by a self-organization method. J. Eur. Ceram. Soc., 35, 3467-3474.

Liu, W., Lv, L., Li, Y., Wang, Y., Wang, J., Xue, C., Yang, J. (2017). Effects of slurry composition on the properties of 3-1 type porous PZT ceramics prepared by ionotropic gelation. Ceram. Int., 43, 6542-6547.

Liu, W., Xu, J., Lv, R., Wang, Y., Xu, H., Yang, J. (2014). Effects of sintering behavior on piezoelectric properties of porous PZT ceramics. Ceram. Int., 40, 2005-2010.

Liu, W., Xu, J., Wang, Y., Xu, H., Xi, X., Yang, J. (2013). Processing and Properties of

Porous PZT Ceramics from Particle-Stabilized Foams via Gel Casting. J. Am. Ceram. Soc., 96, 1827-1831.

Lou, X. J. (2009). Why do antiferroelectrics show higher fatigue resistance than ferroelectrics under bipolar electrical cycling? Appl. Phys. Lett., 94, 72901.

Lovinger, A. J. (1983). Ferroelectric Polymers. Science, 220, 1115-1121.

Luna, A., Yuan, J., Nri, W., Zakri, C., Poulin, P., Colin, A. (2015). Giant Permittivity Polymer Nanocomposites Obtained by Curing a Direct Emulsion. Langmuir, 31, 12231-12239.

Luo, H., Chen, C., Zhou, K., Zhou, X., Wu, Z., Zhang, D. (2015). Enhancement of dielectric properties and energy storage density in poly(vinylidene fluoride-co-hexafluoropropylene) by relaxor ferroelectric ceramics. RSC Adv., 5, 68515-68522.

Luo, H., Zhang, D., Jiang, C., Yuan, X., Chen, C., Zhou, K. (2015). Improved dielectric properties and energy storage density of poly(vinylidene fluoride-co-hexafluoropropylene) nanocomposite with hydantoin epoxy resin coated $BaTiO_3$. ACS Appl. Mater. Interfaces, 7, 8061-8069.

Luo, H., Zhang, D., Wang, L., Chen, C., Zhou, J., Zhou, K. (2015). Highly enhanced dielectric strength and energy storage density in hydantoin@$BaTiO_3$-P(VDF-HFP) composites with a sandwich-structure. RSC Adv., 5, 52809-52816.

Luo, H., Roscow, J., Zhou, X., Chen, S., Han, X., Zhou, K., Bowen, C. (2017). Ultra-high Discharged Energy Density Capacitor using High Aspect Ratio $Na_{0.5}Bi_{0.5}TiO_3$ Nanofibers. J. Mater. Chem. A, 5, 7091-7102.

Luo, H., Zhou, K., Bowen, C., Zhang, F., Wei, A., Wu, Z., Zhang, D. (2016). Building Hierarchical Interfaces Using $BaSrTiO_3$ Nanocuboid Dotted Graphene Sheets in an Optimized Percolative Nanocomposite with Outstanding Dielectric Properties. Adv. Mater. Interfaces, 3, 1-6.

Luo, S., Yu, S., Sun, R., Wong, C.-P. (2014). Nano Ag-deposited $BaTiO_3$ hybrid particles as fillers for polymeric dielectric composites: toward high dielectric constant and suppressed loss. ACS Appl. Mater. Interfaces, 6, 176-182.

Marselli, S., Pavia, V., Galassi, C., Roncari, E., Cranciun, F., Guidarelli, G. (1999). Porous piezoelectric ceramic hydrophone. J. Acoust. Soc. Am., 106, 733-738.

Martins, P., Lopes, A. C., Lanceros-Mendez, S. (2014). Electroactive phases of poly(vinylidene fluoride): Determination, processing and applications. Prog. Polym. Sci., 39, 683-706.

Maurya, D., Petkov, V., Kumar, A., Priya, S. (2012). Nanostructured lead-free ferroelectric $Na_{0.5}Bi_{0.5}TiO_3$-$BaTiO_3$ whiskers: synthesis mechanism and structure. Dalton Trans., 41, 5643-5652.

Mccall, W. R., Kim, K., Heath, C., Pierre, G. La, Sirbuly, D. J. (2014). Piezoelectric Nanoparticle Polymer Composite Foams. ACS Appl. Mater. Interfaces, 6, 19504-19509.

McLean, D. A. (1967). Dielectric Materials and Capacitor Miniaturization. IEEE Trans. Parts, Mater. and Packag., 3, 163-169.

Mercadelli, E., Sanson, A., Pinasco, P., Roncari, E., Galassi, C. (2010). Tape cast porosity-graded piezoelectric ceramics. J. Eur. Ceram. Soc., 30, 1461-1467.

Mercadelli, E., Sanson, A., Galassi, C. (2010). Porous piezoelectric ceramics. In E. Suaste-Gomez (Ed.), Piezoelectric Ceramics (pp. 111-128). InTech Open.

Nadagouda, M. N., Varma, R. S. (2007). Green approach to bulk and template-free synthesis of thermally stable reduced polyaniline nanofibers for capacitor applications. Green Chem., 9, 632-637.

Navarro, A., Whatmore, R. W., Alcock, J. R. (2004). Preparation of functionally graded PZT ceramics using tape casting. J. Electroceram., 13, 413-415.

Navid, A., Pilon, L. (2011). Pyroelectric energy harvesting using Olsen cycles in purified and porous poly(vinylidene fluoride-trifluoroethylene) [P(VDF-TrFE)] thin films. Smart Mater. Struct., 20, 25012.

Navid, A., Vanderpool, D., Bah, A., Pilon, L. (2010). Towards optimization of a pyroelectric energy converter for harvesting waste heat. Inter. J. Heat Mass Trans., 53, 4060-4070.

Newnham, R. E., Skinner, D. P., Cross, L. E. (1978). Connectivity and piezoelectric-pyroelectric composites. Mater. Res. Bull., 13, 525-536.

Niu, Y., Bai, Y., Yu, K., Wang, Y., Xiang, F., Wang, H. (2015). Effect of the modifier structure on the performance of barium titanate/poly(vinylidene fluoride) nanocomposites for energy storage applications. ACS Appl. Mater. Interfaces, 7, 24168-24176.

Okazaki, K., Nagata, K. (1973). Effects of grain size effects and porosity on electrical and optical properties of PLZT ceramics. J. Am. Ceram. Soc., 56, 82-86.

Padurariu, C., Padurariu, L., Curecheriu, L., Ciomaga, C., Horchidan, N., Galassi, C., Mitoseriu, L. (2017). Role of the pore interconnectivity on the dielectric, switching and tunability properties of PZTN ceramics. Ceram. Int., 43, 5767-5773.

Padurariu, L., Curecheriu, L. P., Mitoseriu, L. (2016). Nonlinear dielectric properties of paraelectric-dielectric composites described by a 3D Finite Element Method based on Landau-Devonshire theory. Acta Mater., 103, 724-734.

Palmqvist, L., Palmqvist, K., Shaw, C. P. (2007). Porous multilayer PZT materials made by aqueous tape casting. Key Eng. Mater., 333, 215-218.

Pan, Z. B., Yao, L. M., Zhai, J. W., Liu, S. H., Yang, K., Wang, H. T., Liu, J. H. (2016). Fast discharge and high energy density of nanocomposite capacitors using $Ba_{0.6}Sr_{0.4}TiO_3$ nanofibers. Ceram. Int., 42, 14667-14674.

Panteny, S., Bowen, C. R., Stevens, R. (2006). Characterisation of barium titanate-silver composites, part I: Microstructure and mechanical properties. J. Mater. Sci., 41, 3837-3843.

Park, M. H., Kim, H. J., Kim, Y. J., Moon, T., Kim, K. D., Lee, Y. H., Hwang, C. S. (2015). Study on the internal field and conduction mechanism of atomic layer deposited ferroelectric $Hf_{0.5}Zr_{0.5}O_2$ thin films. J. Mater. Chem. C, 3, 6291-6300.

Patil, S. K., Koledintseva, M. Y., Schwartz, R. W., Huebner, W. (2008). Prediction of effective permittivity of diphasic dielectrics using an equivalent capacitance model. J. Appl. Phys., 104, 74108.

Pecharroman, C., Esteban-Betegn, F., Bartolome, J. F., Lpez-Esteban, S., Moya, J. S. (2001). New Percolative $BaTiO_3$ - Ni Composites with a High and Frequency-Independent Dielectric Constant ($\varepsilon = 80,000$). Adv. Mater., 13, 1541-1544.

Pecharromn, C., Moya, J. S. (2000). Experimental evidence of a giant capacitance in insulator-conductor composites at the percolation threshold. Adv. Mater., 12, 294-297.

Piazza, D., Capiani, C., Galassi, C. (2005). Piezoceramic material with anisotropic graded porosity. J. Eur. Ceram. Soc., 25, 3075-3078.

Prateek, Thakur, V. K., Gupta, R. K. (2016). Recent progress on ferroelectric polymer-based nanocomposites for high energy density capacitors: synthesis, dielectric properties, and future aspects. Chem. Rev., 116, 4260-4317.

Priya, S. (2007). Advances in energy harvesting using low profile piezoelectric transducers. J. Electroceram., 19, 165-182.

Priya, S. (2010). Criterion for Material Selection in Design of Bulk Piezoelectric Energy Harvesters. IEEE Trans. Ultrason., Ferroelect., Freq. Control, 57, 2610-2612.

Ramesh, R., Kara, H., Bowen, C. R. (2005). Finite element modelling of dense and porous piezoceramic disc hydrophones. Ultrason., 43, 173-81.

Ramsey, M. J., Clark, W. W. (2001). Piezoelectric energy harvesting for bio-MEMS applications. In Proc. Soc. Photo. Opt. Instru. Eng. (pp. 429-438).

Rice, R. W. (1996). Evaluation and extension of physical property-porosity models based on minimum solid area. J. Mater. Sci., 31, 102-118.

Rittenmyer, K., Shrout, T. R., Schulze, W. A., Newnham, R. E. (1982). Piezoelectric 3-3 composites. Ferroelectr., 41, 189-195.

Roberts, A. P., Garboczi, E. J. (2000). Elastic properties of model porous ceramics. J. Am. Ceram. Soc., 83, 3041-3048.

Roleder, K., Franke, I., Glazer, A. M., Thomas, P. A., Miga, S., Suchanicz, J. (2002). The piezoelectric effect in $Na_{0.5}Bi_{0.5}TiO_3$ ceramics. J. Phys: Cond. Matt., 14, 5399-5406.

Roncari, E., Galassi, C., Craciun, F., Capiani, C., Piancastelli, A. (2001). A microstructural study of porous piezoelectric ceramics obtained by different methods. J. Eur. Ceram. Soc., 21, 409-417.

Roncari, E., Galassi, C., Cranciun, F., Guidarelli, G., Marselli, S., Pavia, V. (1998). Ferroelectric ceramics with included porosity for hydrophone applications. Proceedings of the Eleventh IEEE International Symposium on Applications of Ferroelectrics, 373-376.

Roscow, J. I., Lewis, R. W. C., Taylor, J., Bowen, C. R. (2017). Modelling and fabrication of porous sandwich layer barium titanate with improved piezoelectric energy harvesting figures of merit. Acta Mater., 128, 207-217.

Roscow, J. I., Taylor, J., Bowen, C. R. (2016). Manufacture and characterization of porous ferroelectrics for piezoelectric energy harvesting applications. Ferroelectr., 498, 40-46.

Roscow, J. I., Zhang, Y., Taylor, J., Bowen, C. R. (2015). Porous ferroelectrics for energy harvesting applications. Eur. Phys. J. Spec. Top., 224, 2949-2966.

Safari, A., Akdogan, E. K. (2006). Rapid Prototyping of Novel Piezoelectric Composites. Ferroelectr., 331, 153-179.

Saleem, M., Song, J. S., Jeong, S. J., Kim, M. S., Yoon, S., Kim, I. S. (2015). Dielectric response on microwave sintered $BaTiO_3$ composite with Ni nanopowder and paste. Mater. Res. Bull., 64, 380-385.

Seuba, J., Deville, S., Guizard, C., Stevenson, A. J. (2016). Mechanical properties and failure behavior of unidirectional porous ceramics. Sci. Rep., 6, 24326.

Shaikh, F. K., Zeadally, S. (2016). Energy harvesting in wireless sensor networks: A comprehensive review. Renew. Sustain. Energy Rev., 55, 1041-1054.

Shanti, N. O., Araki, K., Halloran, J. W. (2006). Particle redistribution during dendritic solidification of particle suspensions. J. Am. Ceram. Soc., 89, 24442447.

Shaw, C. P., Whatmore, R. W., Alcock, J. R. (2007). Porous, Functionally Gradient Pyroelectric Materials. J. Am. Ceram. Soc., 90, 137-142.

Shenck, N. S., Paradiso, J. A. (2001). Energy scavenging with shoe-mounted piezoelectrics. IEEE Micro, 21, 30-42.

Sihvola, A. H., Alanen, E. (1991). Studies of mixing formulae in the complex plane. Ieee Trans. Geosci. Remote. Sens, 4, 679-687.

Sihvola, A. H., Kong, J. A. (1988). Effective permittivity of dielectric mixtures. Ieee Trans. Geosci. Remote. Sens, 26, 420-429.

Skinner, D. P., Newnham, R. E., Cross, L. E. (1978). Flexible Composite Transducers. Mater. Res. Bull., 13, 599-607.

Smoker, J., Nouh, M. (2012). Energy harvesting from a standing wave thermoacoustic-piezoelectric resonator. J. Appl. Phys., 111, 104901.

Sodano, H. A. (2005). Comparison of Piezoelectric Energy Harvesting Devices for Recharging Batteries. J. Intell. Mater. Syst. Struct., 16, 799-807.

Sodano, H. A., Inman, D. J., Park, G. (2004). A Review of Power Harvesting from Vibration Using Piezoelectric Materials. The Shock and Vibration Digest, 36, 197-205.

Sodano, H. A., Park, G., Inman, D. J. (2004). Estimation of Electric Charge Output for Piezoelectric Energy Harvesting. Strain, 40, 49-58.

Stewart, M., Weaver, P. M., Cain, M. (2012). Charge redistribution in piezoelectric energy harvesters. Appl. Phys. Lett., 100, 73901.

Stoyanov, H., McCarthy, D., Kollosche, M., Kofod, G. (2009). Dielectric properties and electric breakdown strength of a subpercolative composite of carbon black in thermoplastic copolymer. Appl. Phys. Lett., 94, 232905.

Studart, A. R., Gonzenbach, U. T., Tervoort, E., Gauckler, L. J. (2006). Processing Routes to Macroporous Ceramics: A Review. J. Am. Ceram. Soc., 89, 1771-1789.

Su, R., Luo, Z., Zhang, D., Liu, Y., Wang, Z., Li, J., Yang, Y. (2016). High Energy Density performance of polymer nanocomposites induced by designed formation of $BaTiO_3$@sheet-like TiO_2 hybrid nanofillers. J. Phys. Chem. C, 120, 11769-11776.

Suchanicz, J. (1998). Behaviour of $Na_{0.5}Bi_{0.5}TiO_3$ ceramics in the ac electric field. Ferroelectr., 209, 561-568.

Tan, Y., Zhang, J., Wu, Y., Wang, C., Koval, V., Shi, B., Ye, H., McKinnon, R., Viola, G., Yan, H. (2015). Unfolding grain size effects in barium titanate ferroelectric ceramics. Sci. Rep., 5, 9953.

Tang, H., Lin, Y., Andrews, C., Sodano, H. A. (2011). Nanocomposites with increased energy density through high aspect ratio PZT nanowires. Nanotech., 22, 15702.

Tang, H., Lin, Y., Sodano, H. A. (2013). Synthesis of high aspect ratio $BaTiO_3$ nanowires for high energy density nanocomposite capacitors. Adv. Energy Mater., 3, 451-456.

Tang, H., Lin, Y., Sodano, H. A. (2012). Enhanced energy storage in nanocomposite capacitors through aligned PZT nanowires by uniaxial strain assembly. Adv. Energy Mater., 2, 469-476.

Tang, H., Sodano, H. A. (2013). Ultra high energy density nanocomposite capacitors with fast discharge using $Ba_{0.2}Sr_{0.8}TiO_3$ nanowires. Nano Lett., 13, 1373-1379.

Tang, H., Zhou, Z., Sodano, H. A. (2014). Relationship between $BaTiO_3$ nanowire aspect ratio and the dielectric permittivity of nanocomposites. ACS Appl. Mater. Interfaces, 6, 5450-5455.

Tang, H., Sodano, H. A. (2013). High energy density nanocomposite capacitors using non-ferroelectric nanowires. Appl. Phys. Lett., 102, 63901.

Tang, H., Zhou, Z., Bowland, C. C., Sodano, H. A. (2015). Synthesis of calcium copper titanate ($CaCu_3Ti_4O_{12}$) nanowires with insulating SiO_2 barrier for low loss high dielectric constant nanocomposites. Nano Energy, 17, 302-307.

Tehrani, M. G., Gatti, G., Brennan, M. J., Thompson, D. J. (2013). Energy harvesting from train vibrations. In 11th International Conference on Vibration Problems.

Tiwari, V., Srivastava, G. (2014). Effect of thermal processing conditions on the structure and dielectric properties of PVDF films. J. Polym. Res., 21, 587.

Wada, S., Takeda, K., Tsurumi, T., Kimura, T. (2007). Preparation of [110] grain oriented barium titanate ceramics by templated grain growth method and their piezoelectric properties. Japan. J. App. Phys., 46, 70397043.

Wang, D. R., Zhou, T., Zha, J. W., Zhao, J., Shi, C. Y., Dang, Z. M. (2013). Functionalized graphene-$BaTiO_3$/ferroelectric polymer nanodielectric composites with high permittivity, low dielectric loss, and low percolation threshold. J. Mater. Chem. A, 1, 6162-6168.

Wang, D., Bao, Y., Zha, J.-W., Zhao, J., Dang, Z.-M., Hu, G.-H. (2012). Improved Dielectric Properties of Nanocomposites Based on Poly(vinylidene fluoride) and Poly(vinyl alcohol)-Functionalized Graphene. ACS Appl. Mater. Interfaces, 4, 6273-6279.

Wang, G., Huang, X., Jiang, P. (2015). Tailoring dielectric properties and energy density of ferroelectric polymer nanocomposites by high-k nanowires. ACS Appl. Mater. Interfaces, 7, 18017-18027.

Wang, H., Liu, J., Zhai, J., Shen, B., Xiu, S., Xiao, S., Pan, Z. (2016). Enhanced energy storage density and discharge efficiency in the strontium sodium niobate-based glass-ceramics. J. Alloys Compd., 687, 280-285.

Wang, S., Huang, X., Wang, G., Wang, Y., He, J., Jiang, P. (2015). Increasing the Energy Efficiency and Breakdown Strength of High-Energy-Density Polymer Nanocomposites by Engineering the $Ba_{0.7}Sr_{0.3}TiO_3$ Nanowire Surface via Reversible Addition-Fragmentation Chain Transfer Polymerization. J. Phys. Chem. C, 119, 25307-25318.

Wang, Y., Wang, K. F., Zhu, C., Liu, J.-M. (2006). Polarization fatigue of ferroelectric $Pb(Zr_{0.1}Ti_{0.9})O_3$ thin films: Temperature dependence. J. Appl. Phys., 99, 44109.

Wang, Z. L., Song, J. (2006). Piezoelectric nanogenerators based on zinc oxide nanowire arrays. Science, 312, 242-247.

Waschkies, T., Oberacker, R., Hoffmann, M. J. (2009). Control of lamellae spacing during freeze casting of ceramics using double-side cooling as a novel processing route. J. Am. Ceram. Soc., 92, 7984.

Whatmore, R. W. (1986). Pyroelectric devices and materials. Rep. Prog. Phys., 49, 1335-1386.

Xie, B., Zhang, Q., Zhang, H., Zhang, G., Qiu, S., Jiang, S. (2016). Largely enhanced ferroelectric and energy storage performances of P(VDF-CTFE) nanocomposites at a lower electric field using $BaTiO_3$ nanowires by stirring hydrothermal method. Ceram. Int., 42, 19012-19018.

Xie, L., Huang, X., Li, B.-W., Zhi, C., Tanaka, T., Jiang, P. (2013). Core-satellite Ag@$BaTiO_3$ nanoassemblies for fabrication of polymer nanocomposites with high discharged energy density, high breakdown strength and low dielectric loss. Phys. Chem. Chem. Phys., 15, 17560-17569.

Xie, L., Huang, X., Huang, Y., Yang, K., Jiang, P. (2013). Core-shell Structured Hyper-branched Aromatic Polyamide / $BaTiO_3$ Hybrid Filler for Poly (vinylidene fluoride-tri fluoroethylene - chloro fluoroethylene) Nanocomposites with the Dielectric Constant Comparable to That of Percolative Composites. ACS Appl. Mater. Interfaces, 5, 1747-1756.

Xie, L., Huang, X., Wu, C., Jiang, P. (2011). Core-shell structured poly(methyl methacrylate)/$BaTiO_3$ nanocomposites prepared by in situ atom transfer radical polymerization: A route to high dielectric constant materials with the inherent low loss of the base polymer. J. Mater. Chem., 21, 5897-5906.

Xie, L., Huang, X., Yang, K., Li, S., Jiang, P. (2014). Grafting to route to PVDF-HFP-GMA/$BaTiO_3$ nanocomposites with high dielectric constant and high thermal conductivity for energy storage and thermal management applications. J. Mater. Chem. A, 2, 5244-5251.

Xu, S., Hansen, B. J., Wang, Z. L. (2010). Piezoelectric-nanowire-enabled power source for driving wireless microelectronics. Nat. Comms., 1, 93.

Xu, T., Wang, C.-A. (2014). Piezoelectric Properties of a Pioneering 3-1 Type PZT/Epoxy Composites Based on Freeze-Casting Processing. J. Am. Ceram. Soc., 97, 1511-1516.

Yang, A.-K., Wang, C.-A., Guo, R., Huang, Y. (2011). Effects of porosity on dielectric and piezoelectric properties of porous lead zirconate titanate ceramics. Appl. Phys. Lett., 98, 152904.

Yang, A.-K., Wang, C.-A., Guo, R., Huang, Y. (2010). Microstructure and Electrical Properties of Porous PZT Ceramics Fabricated by Different Methods. J. Am. Ceram. Soc., 1990, 1984-1990.

Yang, A.-K., Wang, C.-A., Guo, R., Huang, Y., Nan, C.-W. (2010). Porous PZT Ceramics with High Hydrostatic Figure of Merit and Low Acoustic Impedance by TBA-Based Gel-Casting Process. J. Am. Ceram. Soc., 93, 1427-1431.

Yang, A.-K., Wang, C.-A., Guo, R., Huang, Y., Nan, C.-W. (2010). Effects of sintering

behavior on microstructure and piezoelectric properties of porous PZT ceramics. Ceram. Int., 36, 549-554.

Yang, J., Zhang, J., C Liang, Wang, M., Zhao, P., Liu, M., Che, R. (2013). Ultrathin BaTiO$_3$ Nanowires with High Aspect Ratio: A Simple One-Step Hydrothermal Synthesis and Their Strong Microwave Absorption. ACS Appl. Mater. Interfaces, 5, 7146-7151.

Young, A. C., Omatete, O. O., Janney, M. A., Menchhofer, P. A. (1991). Gelcasting of Alumina. J. Am. Ceram. Soc., 74, 612-618.

Yuan, J.-K., Yao, S.-H., Dang, Z.-M., Sylvestre, A., Genestoux, M., Bai1, J. (2011). Giant Dielectric Permittivity Nanocomposites: Realizing True Potential of Pristine Carbon Nanotubes in Polyvinylidene Fluoride Matrix through an Enhanced Interfacial Interaction. J. Phys. Chem. C, 115, 5515-5521.

Zeng, T., Dong, X. L., Chen, H., Wang, Y. L. (2006). The effects of sintering behavior on piezoelectric properties of porous PZT ceramics for hydrophone application. Mater. Sci. Eng. B, 131, 181-185.

Zeng, T., Dong, X., Chen, S., Yang, H. (2007). Processing and piezoelectric properties of porous PZT ceramics. Ceram. Int., 33, 395-399.

Zeng, T., Dong, X., Mao, C., Zhou, Z., Yang, H. (2007). Effects of pore shape and porosity on the properties of porous PZT 95/5 ceramics. J. Eur. Ceram. Soc., 27, 2025-2029.

Zhang, C., Chi, Q., Dong, J., Cui, Y., Wang, X., Liu, L., Lei, Q. (2016). Enhanced dielectric properties of poly(vinylidene fluoride) composites filled with nano iron oxide-deposited barium titanate hybrid particles. Sci. Rep., 6, 33508.

Zhang, D., Zhang, Y., Xie, R., Zhou, K. (2012). Freeze gelcasting of aqueous alumina suspensions for porous ceramics. Ceram. Int., 38, 6063-6066.

Zhang, H. L., Li, J.-F., Zhang, B.-P. (2007). Microstructure and electrical properties of porous PZT ceramics derived from different pore-forming agents. Acta Mater., 55, 171-181.

Zhang, L., Shan, X., Bass, P., Tong, Y., Rolin, T. D., Hill, C. W., Cheng, Z.-Y. (2016). Process and microstructure to achieve ultra-high dielectric constant in ceramic-polymer composites. Sci. Rep., 6, 35763.

Zhang, Q., Agbossou, A., Feng, Z., Cosnier, M. (2011). Solar micro-energy harvesting with pyroelectric effect and wind flow. Sens. Actuators, A, 168, 335-342.

Zhang, R., Jiang, B., Cao, W. (2001). Elastic, piezoelectric, and dielectric properties of multidomain 0.67Pb(Mg$_{1/3}$Nb$_{2/3}$)O$_3$-0.33PbTiO$_3$ single crystals. J. Appl. Phys., 90, 3471-3475.

Zhang, X., Chen, W., Wang, J., Shen, Y., Gu, L., Lin, Y., Nan, C. W. (2014). Hierarchical interfaces induce high dielectric permittivity in nanocomposites containing TiO$_2$@BaTiO$_3$ nanofibers. Nanoscale, 6, 6701-6709.

Zhang, X. (2015). Ultrahigh Energy Density of Polymer Nanocomposites Containing BaTiO$_3$ @TiO$_2$ Nanofibers by Atomic - Scale Interface Engineering. Adv. Mater., 27, 819-824.

Zhang, X.-Y., Zhang, Y., Zhang, D. (2012). Effect of particle size on the lamellar pore microstructure of porous Al$_2$O$_3$ ceramics fabricated by the unidirectional freezing. App. Mech. Mater., 184185, 818825.

Zhang, Y., Zhou, K., Zeng, J., Zhang, D. (2013). Control of pore structures and sizes in freeze cast ceramics. Adv. App. Ceram., 112, 405-411.

Zhang, Y., Bao, Y., Zhang, D., Bowen, C. R. (2015). Porous PZT Ceramics with Aligned Pore Channels for Energy Harvesting Applications. J. Am. Ceram. Soc., 98, 2980-2983.

Zhang, Y., Chen, L., Zeng, J., Zhou, K., Zhang, D. (2014). Aligned porous barium titanate/hydroxyapatite composites with high piezoelectric coefficients for bone tissue engineering. Mater. Sci. Eng. C, 39, 143-149.

Zhang, Y., Xie, M., Roscow, J., Zhou, K., Bao, Y., Zhang, D., Bowen, C. (2017). Enhanced pyroelectric and piezoelectric properties of PZT with aligned porosity for energy harvesting applications. J. Mater. Chem. A, 5, 6569-6580.

Zhou, X., Jiang, C., Chen, C., Luo, H., Zhou, K., Zhang, D. (2016). Morphology control and piezoelectric response of $Na_{0.5}Bi_{0.5}TiO_3$ synthesized via a hydrothermal method. Cryst. Eng. Comm., 18, 1302-1310.

Zhu, M., Huang, X., Yang, K., Zhai, X., Zhang, J., He, J., Jiang, P. (2014). Energy storage in ferroelectric polymer nanocomposites filled with core-shell structured polymer@$BaTiO_3$ nanoparticles: understanding the role of polymer shells in the interfacial regions. ACS Appl. Mater. Interfaces, 6, 19644-19654.

Zou, C., Kushner, D., Zhang, S. (2011). Wide temperature polyimide/ ZrO_2 nanodielectric capacitor film with excellent electrical performance. Appl. Phys. Lett., 98, 82905.

Appendix A: Supplementary information: *Ultra-high discarged energy density capacitor using high aspect ratio $Na_{0.5}Bi_{0.5}TiO_3$ nanofibres*

Electronic Supplementary Information

Ultra-high Discharged Energy Density Capacitor using High

Aspect Ratio $Na_{0.5}Bi_{0.5}TiO_3$ Nanofibers

Hang Luo[ab], James Roscow[c], Xuefan Zhou[a], Sheng Chen[d], Xianghui Han[d], Kechao Zhou[a], Dou Zhang*[a], Chris R. Bowen*[c]

[a] State Key Laboratory of Powder Metallurgy, Central South University, Changsha, Hunan 410083, China

[b] College of Chemistry and Chemical Engineering, Central South University, Changsha 410083, Hunan Province, China

[c] Department of Mechanical Engineering, University of Bath, Bath, BA2 7AY, UK

[d] Key Laboratory of Polymeric Materials and Application Technology of Hunan Province, College of Chemistry, Xiangtan University, Xiangtan 411105, Hunan Province, China

*E-mail: dzhang@csu.edu.cn (Dou Zhang)

*E-mail: C.R.Bowen@bath.ac.uk (Chris R. Bowen)

Electronic supplementary information (ESI) available.
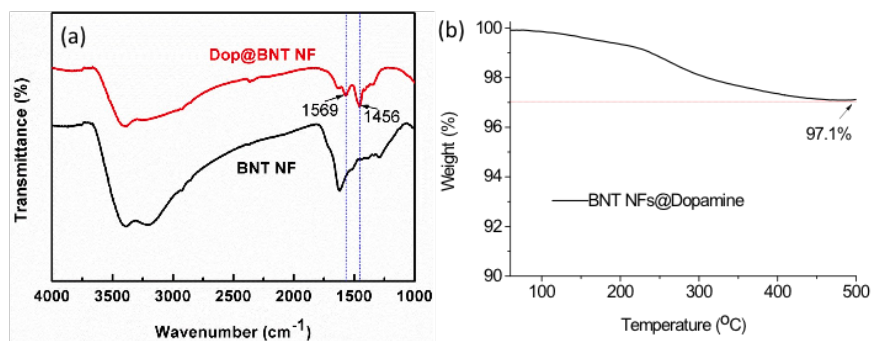
Authors contributed equally.

Figure A1 (a) FT-IR spectra of dopamine modified and pristine BNT nanofibres (NFs). It can be seen that two new peaks were formed after the BNT NFs were modified by dopamine; the peaks at 1456 and 1569 cm^{-1} originate from $-NH_3^+$ deformation and amide band, NH bending, respectively.[1] (b) TGA curve of BNT NFs@Dopamine.
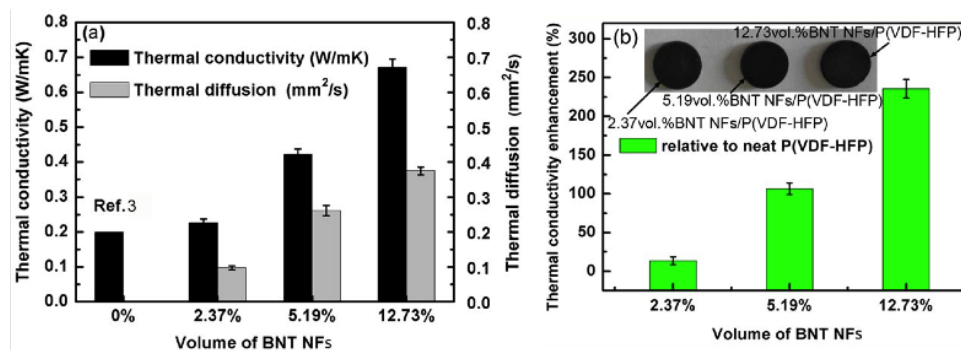
Figure A2 (a) Thermal conductivity and thermal diffusion, and (b) Thermal conductivity enhancement of the BNT nanofiber/P(VDF-HFP) composites with filler loading, a photo of the samples is shown in the insert. The room temperature thermal conductivity of the pure P(VDF-HFP) is approximately 0.2 W m^{-1} K^{-1}, as previously reported.[2] It is clear that the thermal conductivity of the composites depends on the BNT nanofiber loading, which increases with the degree of loading; a similar phenomenon is exhibited with respect to thermal diffusion. For example, the thermal conductivity of the nanocomposite with 12.73 vol% BNT nanofibers increased to 0.67 W m^{-1} K^{-1}, which increased by more than two times compared to the pure P(VDF-HFP) matrix. The enhancement of thermal conductivity is shown in Figure S5b, and the insert shows the test sample of the BNT nanofiber/P(VDF-HFP) composites. The increased thermal conductivity and thermal diffusion is attributed to the high thermal conductivity and thermal diffusion of the BNT nanofiber phase and the homogeneous dispersion of BNT nanofiber

155

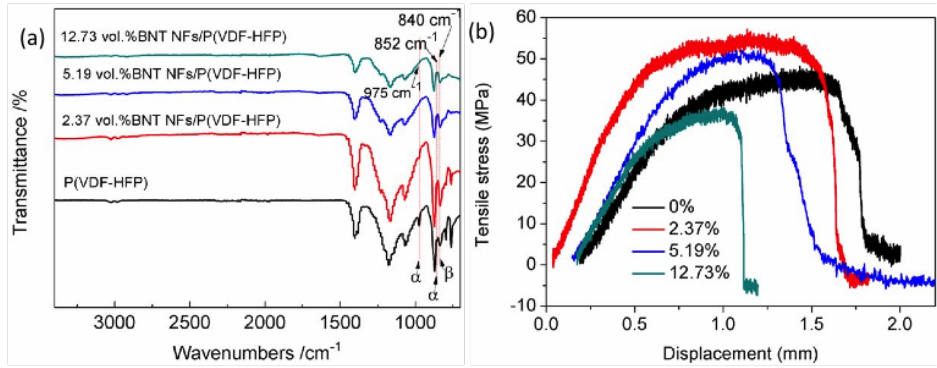in the polymer matrix as well as the high density achieved via hot pressing.

Figure A3 (a)　FT-IR spectra of the P(VDF-HFP) nanocomposites with different BNT NFs loadings, (b) The tensile stress-displacement curve of BNT Nanofibers/P(VDF-HFP) nanocomposites with BNT loading level in vol.%.

Table A1 Characteristic breakdown strength and shape factor of the breakdown strength data for the samples

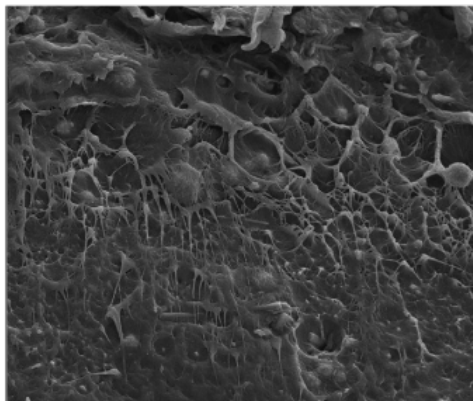| Sample (BNT vol.%)	β	E_0 (kV/mm)
0	8.24	397
2.37	4.30	458
5.19	5.50	337
12.73	5.96	302

156

Figure A 4 Cross-sectional SEM image of BNT nanofiber/P(VDF-HFP) composites. BNT

nanofibres were aligned to the direction of the nanocomposite film, which was perpendicular to

the direction of the electric field.
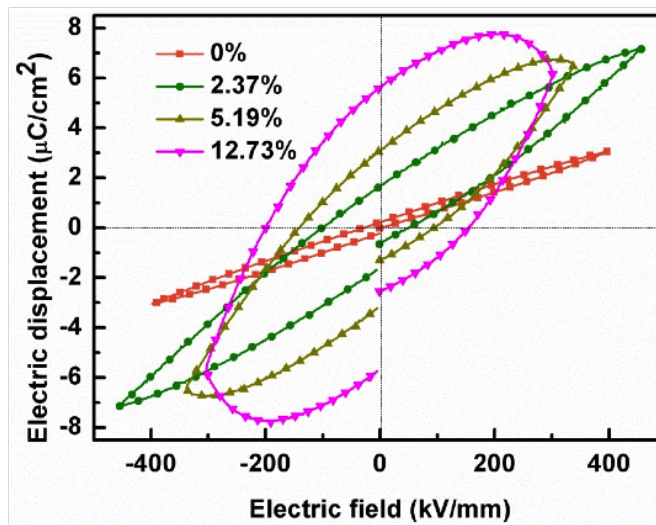
Figure A5 D-E loops of the BNT nanofiber/P(VDF-HFP) nanocomposites with various filler loadings at the maximum electric field. The saturated polarization was continuously increased with the BNT nanofiber content, while the remanent polarization showed a faster increase trend than saturated polarization of the nanocomposite with 12.73 vol% BNT NFs.
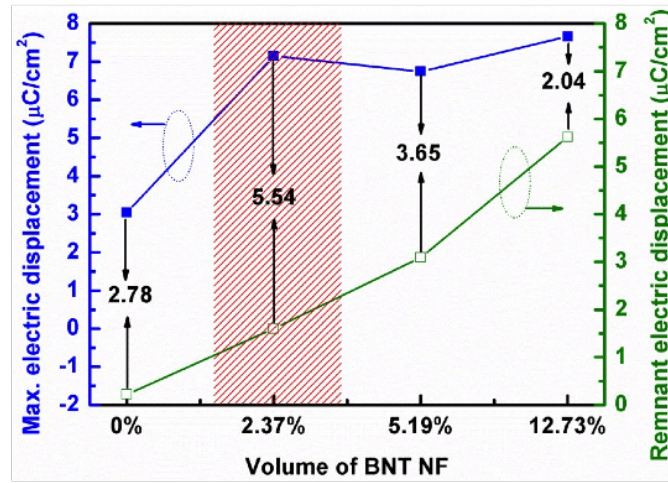
Figure A6 Max. and remnant electric displacement of the BNT nanofiber/P(VDF-HFP)

nanocomposites with various filler loadings at the largest electric field.
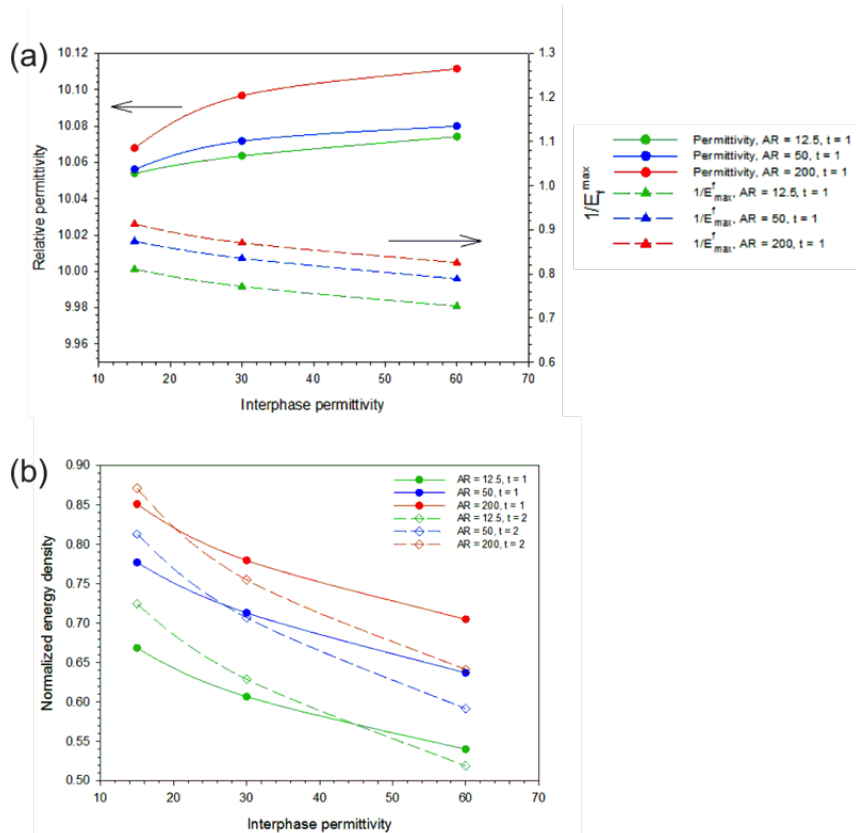
Figure A7 (a) Effect of interphase permittivity (solid line, left axis) and electric field concentration factor, $1/E_r^{max}$ (dashed line, right axis), on relative permittivity of composite for constant composite layer thickness (t = 1), varying aspect ratio (AR = 12.5, 50, 200); (b) effect of interphase permittivity on normalised energy density for interlayer thickness t = 1 (solid lines) and t = 2 (dashed lines) for varying aspect ratio (AR = 12.5, 50, 200) of high permittivity phase. Increasing the permittivity of the interphase past ε_r = 15 is detrimental in terms of energy storage properties due to an increase in electric field concentration.

Reference:

1 V. KumaráThakur, E. JináTan, P. SeeáLee, *RSC Adv.*, 2011, 1, 576

2 Y. Li, X. Huang, Z. Hu, P. Jiang, S. Li and T. Tanaka, *ACS Appl. Mater. Interfaces*, 2011, 3, 4396.

3 X. Huang, T. Iizuka, P. Jiang, Y. Ohki and T. Tanaka, J. Phys. Chem. C, 2012, 116, 13629.

Appendix B: Single inclusion model script

```
!!! SINGLE INCLUSION MODEL SCRIPT !!!


FINISH

/CLEAR,ALL

!/INPUT,RUN,TXT              !copy and paste into command line in Ansys to run

/UIS,MSGPOP,3               ! Turns Off note & warning messages

/UIS,ABORT,OFF             ! Turns Off status & cancellation messages

KEYW,PR_SGUI,1            ! Prevent 'Solution Done' message (affects image
                           plotting)

!/WINDOW,1,OFF            ! Turn graphics window off while running iterations


/PREP7                    ! Enter preprocessor

ET,1,PLANE13,7            ! Select element type i.e. 2D coupled field element


! Matrix properties

MP,DENS,1,1000

MP,PERX,1,1

MP,PERY,1,1

MP,PERZ,1,1

! High permittivity / conductive inclusion properties

MAT,11

MP,DENS,,1.3

MP,PERX,,1000000

MP,PERY,,1000000

MP,PERZ,,1000000


angle = 0        !rotation angle w.r.t. field
```

```
!Topological degeneracy error will show if slice goes exactly along diagonal of
cylinder

!i.e. max aspect ratio ellipse, solve by increasing cyclinder length (won't change
aspect ratio)



BLC4,-10,-10,20,20                  ! Form matrix

! aspect = 1:10 (comment out as necessary)

WPROTA,angle,0,0 $ WPOFFS,0,0,-6 $ CYL4,0,0,1,,,,12 $ aspect = 1

!WPROTA,angle,0,60  $ WPOFFS,0,0,-6 $ CYL4,0,0,0.707107,,,,12 $ aspect = 2

!WPROTA,angle,0,70.52877937 $ WPOFFS,0,0,-6 $ CYL4,0,0,0.57735,,,,12 $ aspect = 3

!WPROTA,angle,0,75.52248781 $ WPOFFS,0,0,-6 $ CYL4,0,0,0.5,,,,12 $ aspect = 4

!WPROTA,angle,0,78.46304097 $ WPOFFS,0,0,-6 $ CYL4,0,0,0.447214,,,,12 $ aspect = 5

!WPROTA,angle,0,80.40593177 $ WPOFFS,0,0,-6 $ CYL4,0,0,0.408248,,,,12 $ aspect = 6

!WPROTA,angle,0,81.7867893 $ WPOFFS,0,0,-6 $ CYL4,0,0,0.377964,,,,12 $ aspect = 7

!WPROTA,angle,0,82.81924422 $ WPOFFS,0,0,-6 $ CYL4,0,0,0.353553,,,,12 $ aspect = 8

!WPROTA,angle,0,83.62062979 $ WPOFFS,0,0,-6 $ CYL4,0,0,0.333333,,,,12 $ aspect = 9

!WPROTA,angle,0,84.26082952 $ WPOFFS,0,0,-6 $ CYL4,0,0,0.316228,,,,12 $aspect = 10



filename = 'conductor_composite_asp%aspect%_angle%angle%'



ASBV,1,1,,KEEP,DELETE     !subtract inclusion volume from matrix, delete volume

APLOT,ALL                 !plot all, selects all

AOVLAP,ALL                !overlap remaining inclusion area from subtract function
onto matrix



ASEL,S,,,2                !select matrix

AATT,11,,1,0              !assign matrix properties

ASEL,S,,6                 !select inclusion

AATT,1,,1,0               !assign inclusion properties

ASEL,ALL                  !select all
```

```
! smart mesh function - fine mesh using GUI

SMRT,1

MSHAPE,1,2D

MSHKEY,0

FLST,5,2,5,ORDE,2

FITEM,5,2

FITEM,5,6

CM,_Y,AREA

ASEL, , , ,P51X

CM,_Y1,AREA

CHKMSH,'AREA'

CMSEL,S,_Y

AMESH,_Y1

CMDELE,_Y

CMDELE,_Y1

CMDELE,_Y2


! apply loads to boundary lines

DL,4,21,VOLT,20

DL,2,21,VOLT,0


! solve

/SOLU

SOLVE
```

Appendix C: Supplementary information: *A breakdown in the case for materials with giant permittivity?*
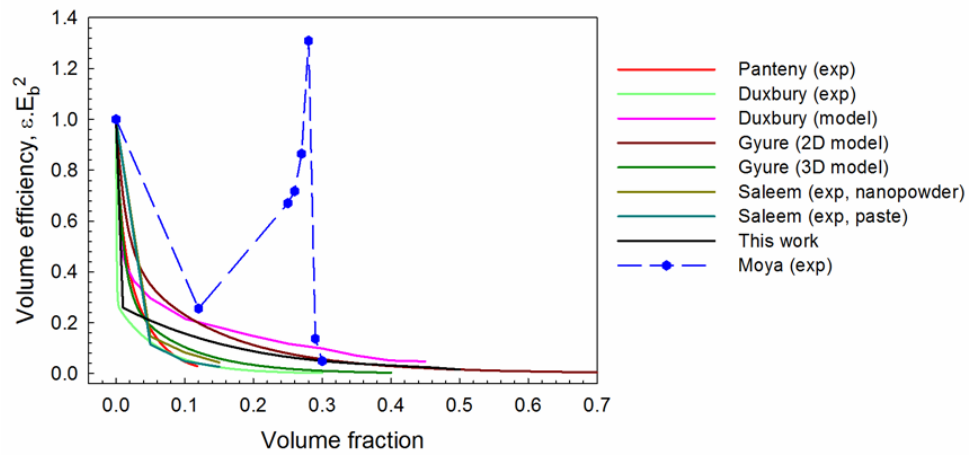
Figure C1. Energy storage material merit index for energy density, $\varepsilon_r.(E_{dielectric})^2$, for data from literature including Moya (Pecharroman et al.) data excluded from Fig. 2 in main text.

Appendix D: Supplementary information: *Modelling and fabrication of porous sandwich layer barium titanate with improved energy harvesting figures of merit*
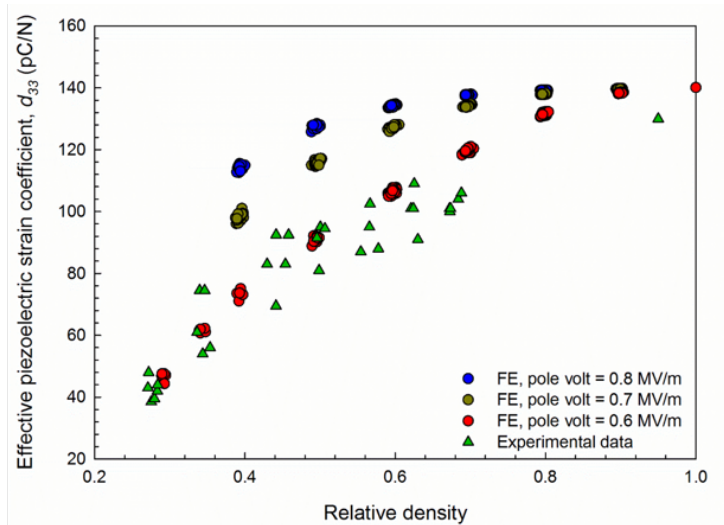
Figure D1: Effect of poling electric field used in FE model on effective piezoelectric strain coefficient, d_{33}, for BaTiO$_3$ with uniformly distributed porosity. A poling field of 0.6MV/m gave the best fit to experimental data and was therefore used for modelling sandwich layer structures.
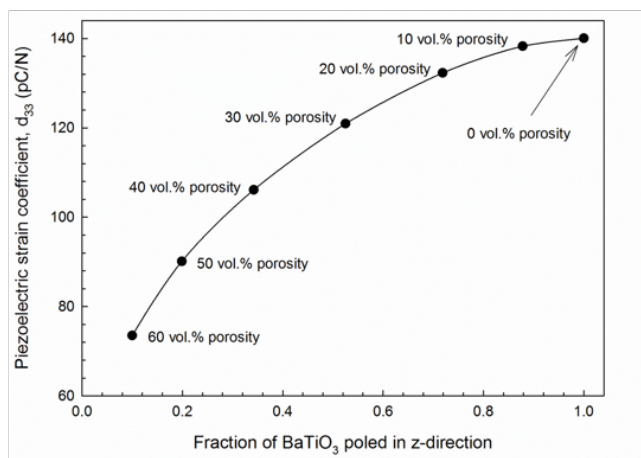
Figure D2: Relationship between the fraction of BaTiO$_3$ poled in the z-direction and the effective longitudinal piezoelectric strain coefficient, d_{33}, for structures with uniformly distributed porosity, obtained via finite element modelling.
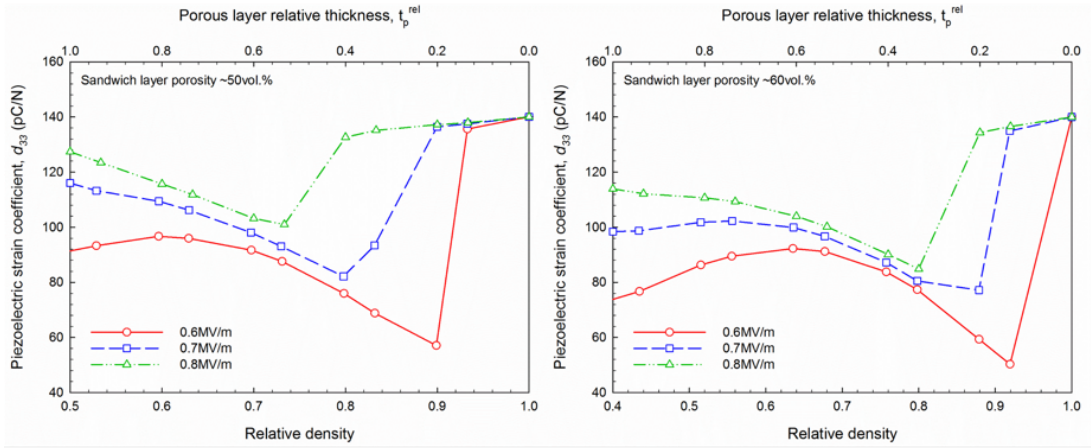
Figure D3: FE modelled data of $BaTiO_3$ with sandwich layer porosity of (a) 50vol.% and (b) 60vol.% for different poling voltages (0.6, 0.7 and 0.8MV/m). In all cases increasing the poling field leads to an increase in d_{33} as more of the sandwich structure becomes poled.
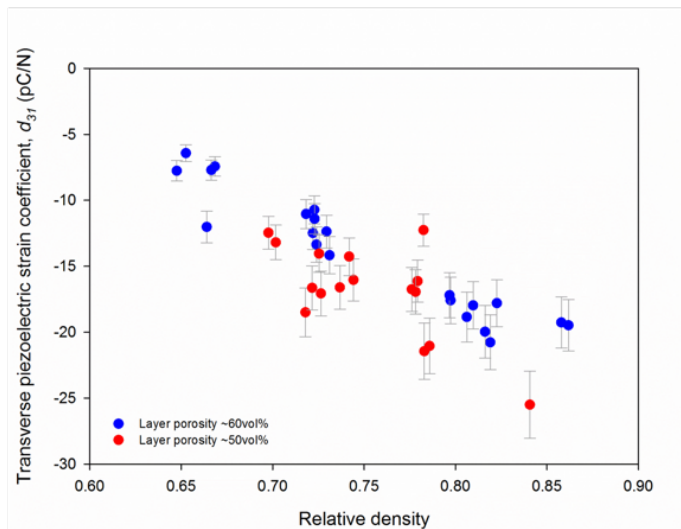
Figure D4: Effect of introducing high porosity sandwich layer on transverse piezoelectric strain coefficient, d_{31}. The significant reduction in d_{31} when $\rho_{rel} < 0.7$ indicates the potential for hydrostatic transducer applications. Error bars at +-10% (accuracy of measurement device).

Appendix E: Porous sandwich layer network model script

```
!!! Porous sandwich layer poling model script !!!

FINISH                              ! Exits from previous work

*DEL,ALL                            ! Deletes previous
                                    variables/arrays

/CLEAR,START                        ! Clears current data and
                                    reads default start.ans file

/CONFIG,NORSTGM,1                   ! Do not store geometry data
                                    in results file (faster)

/CONFIG,NOELDB,1                    ! Do not store results in
                                    database after solution
                                    (faster)

/FDELE,EMAT,DELE                    ! Delete file after use /
                                    don't create if possible
                                    (element matrices)

/FDELE,ESAV,DELE                    ! Delete file after use /
                                    don't create if possible
                                    (element save data)

/FDELE,FULL,DELE                    ! Delete file after use / don't
                                    create if possible (stiffness & mass
                                    matrices)

/FILNAME, sandwich,1                ! Job name (32char) and Job details

/TITLE, Piezoelectric Polarised Porous Structure

/STITLE,1, R.W.C. Lewis 2015

/UNITS, SI

/WINDOW,1,OFF

/com,stage1
```

```
! ---------------------------------------

! Variables controlling the model run

! ---------------------------------------

density = 40                              ! Porous layer density

meshdivs = 30                             ! Mesh size

lz = 5e-3                                 ! Dimension in z-axis

lx = lz                                   ! Dimension in x-axis

ly = lz                                   ! Dimension in y-axis

td_calc = 0.3                             ! Total dense layer thickness

td=lz*(td_calc/2)                         ! Single dense layer thickness

pole_volt = 3E3                           ! Poling voltage

con_no                                    ! Used for results array

area = lx*ly

*DIM,res,ARRAY,iterations,12

*DIM,por_res,ARRAY,iterations,3

! Initialize variables

d33 = 0

d31 = 0

d32 = 0

per33 = 0

a = 0                                     ! Stores corner node reference to
                                          find strain

! Define composition

pzcomp = 100 - airpore                    ! Calculations to find volume
                                          fractions of tri-phasic system

phaseone = (pzcomp/100)*density

phasetwo = pzcomp – phaseone


! Defining Arrays

*DIM,con_res,ARRAY,con_no,4

! Pre-calculate constants
```

```
field=5/lz                              ! Field is Voltage applied (V)
                                        across separation (m)

permconst=(lx*ly*field*8.854E-12)

! ****************************************

! Enter pre-processor mode

! ****************************************

/PREP7

SHPP,ON                                 ! Shape checking on (will produce
                                        warnings)

ET,1,SOLID5,3                           ! Define Element1 as 3D piezo
                                        'brick' with X,Y,Z,V DOF

EMUNIT,EPZRO,8.854E-12                   ! Set more accurate value for free-
                                        space permittivity

! ---------------------------------------

! Define material properties

! ---------------------------------------

! --- Material (1): BaTiO3 Unpoled ---

! Elastic properties from literature

MAT,1

MP,DENS,,5500

MP,PERX,,1187.5

MP,EX,,128E9

MP,PRXY,,0.30

! --- Material (2): BaTiO3 (Berlincourt, Curran, and Jaffe) Poled Z°-Z' (Nrm) ---

! Material is same as theoretically modelled by Topolov et al, 2006

MP,DENS,2,5700

MP,PERX,2,1115 $ MP,PERY,3,1115 $ MP,PERZ,3,1260

TB,PIEZ,2

TBDATA,03,-4.35,,,-4.35

TBDATA,09,17.50

TBDATA,14,11.40,,11.40
```

170

```
TB,ANEL,2,1,,0

TBDATA,01,150.0E9,68.0E9,57.0E9

TBDATA,07,150.0E9,57.0E9

TBDATA,12,171.0E9,,,,57.0E9

TBDATA,19,57.0E9,,57.0E9
```

! --- Material (11) Air : Dry, at 0°C and 1 atm pressure ---

! 'Soft Air' approach for coupled/structural element

! Density: Cutnell & Johnson. 'Physics' 3rd Edn, New York: Wiley. 1995: p315 {Ref:29}

```
MAT,11

MP,DENS,,1.3

MP,PERX,,1

MP,EX,,1e-12

MP,PRXY,,1e-12
```

! ---------------------------------------

! Create model

! ---------------------------------------

BLC4,0,0,lx,ly,lz	! Create block volume from origin with side of 5mm
VSEL,S,,,1	! Select volume 1
VATT,1,,1,0	! Set selected volume attributes to MAT=1,ET=1,Cartesian
MSHKEY,2	! Mesh type: Mapped where possible, no smart size.
ALLSEL,ALL	
ESIZE,,meshdivs	! Mesh (element) size: no size set, meshdivs div's per boundary line
VMESH,ALL	! Mesh all selected volumes

! ***************************************

! Run Simulation(s) and Record data

! ***************************************

```
! Warning: Disables pop-up information messages while in the main loop

/UIS,MSGPOP,3                            ! Turns Off note & warning
                                         messages

/UIS,ABORT,OFF                           ! Turns Off status & cancellation
                                         messages

KEYW,PR_SGUI,1                           ! Prevent 'Solution Done'
                                         message (Affects image
                                         plotting!)

/WINDOW,1,OFF                            ! Turn graphics window off while
                                         running iterations

/PNUM,MAT,1

/NUMBER,1


ALLSEL,ALL                               ! Select all entities (effectively
                                         removes selection)

*DO,it,1,iterations                      ! Main loop- each iteration creates
                                         a different microstructure

/PREP7

*IF,it,GT,1,THEN

DDELE,ALL

CPDELE,ALL

*ENDIF

NSEL,S,LOC,Z,0                           ! Select nodes at location Z=0
                                         (~Electrode 1)

CP,1,VOLT,ALL                            ! Couple selected nodes in voltage
                                         DOF (Set1)

D,ALL,VOLT,0                             ! DOF constraint for selected nodes:
                                         V=0


NSEL,S,LOC,Z,lz                          ! Select nodes at location Z=lz
                                         (~Electrode 2)

CP,2,VOLT,ALL                            ! Couple selected nodes in voltage
                                         DOF (Set2)

D,ALL,VOLT,pole_volt                     ! DOF constraint for selected nodes:
                                         E=-1kV/cm
```

172

```
*GET,charge_node,CP,2,TERM,1,NODE         ! Finds the master node of
                                           the 2nd coupled set
                                           (Electrode 2)

NSEL,S,LOC,X,0 $ DSYM,SYMM,X               ! Select nodes at X=0, then
                                           constrain DOF by symmetry

NSEL,S,LOC,Y,0 $ DSYM,SYMM,Y               ! Select nodes at Y=0, then
                                           constrain DOF by symmetry

NSEL,S,LOC,Z,0 $ DSYM,SYMM,Z               ! Select nodes at Z=0, then
                                           constrain DOF by symmetry

NSEL,S,LOC,X,lx $ CP,3,UX,ALL              ! Select nodes on exterior
                                           'X' face and couple
                                           displacements

NSEL,S,LOC,Y,ly $ CP,4,UY,ALL              ! Select nodes on exterior
                                           'Y' face and couple
                                           displacements

NSEL,S,LOC,Z,lz $ CP,5,UZ,ALL              ! Select nodes on exterior
                                           'Z' face and couple
                                           displacements

ALLSEL,ALL                                 ! Select all entities
                                           (effectively removes
                                           selection)

*SET,a,NODE(lx,ly,lz)                      ! Get the corner node ref.
                                           number for displacement

*GET,element_1,ELEM,,NUM,MIN               ! Read the number of the
                                           first selected element

*GET,element_n,ELEM,,NUM,MAX               ! Read the number of the last
                                           selected element

*GET,starttime,ACTIVE,0,TIME,WALL          ! Start time for benchmarking


/SOLU                                      ! Solution mode

ANTYPE,STATI

EQSLV,JCG,1E-6                             ! Select JCG solver,
                                           with 1e-6 tolerance (faster)

pores=0                                    ! Reset counter for number
                                           of pores

aircontent=0

pzcontent=0
```

```
*DO, grain, element_1, element_n, 1

*IF,RAND(1,100),LE,airpore,THEN        ! Set grains to the
                                        porous air content
                                        (random)

MPCHG,11,grain

aircontent=aircontent+1

*ELSE

*IF,RAND(1,100),LE,density,THEN

MPCHG,1,grain                          ! Assign each solid
                                        'grain' a random
                                        (unpoled) polarization

pzcontent=pzcontent+1                  ! For porous solid,
                                        randomly determine
                                        whether solid or pore

*ELSE

MPCHG,11,grain                         ! Second phase of
                                        piezocomposite (random)

pores=pores+1                          ! Counts the number of
                                        pores for density
                                        calculation

*ENDIF

*ENDIF

*ENDDO

denstru=pzcontent/element_n            ! Calculate true volume
                                        density of
                                        material (first phase)

airdens=aircontent/element_n           ! Calculate true volume
                                        of air porosity

denspore=pores/element_n               ! Calculate true volume
                                        density of material (second
                                        phase)

!*********************************************

NSEL,S,LOC,Z,0,td

NSEL,A,LOC,Z,lz-td,lz

ESLN,S,ALL
```

```
MPCHG,1,ALL

ALLSEL,ALL

!***********************************************

*DO,icon,1,con_no,1

/SOLU

/com,*SOLUTION 1

/com,*SOLUTION 1

/com,*SOLUTION 1

/com,*SOLUTION 1

/com,*SOLUTION 1

EQSLV,SPARSE,1E-6

SOLVE

FINISH

/POST1

SET,1

*GET,elem_1,ELEM,0,NUM,MIN

*GET,elem_no,ELEM,0,NUM,MAX

vf_air_post = 0

vf_poled_post = 0

vf_unpoled_post = 0

elem_mat = 0

ETABLE,field_sum,EF,Z

/com,*ETABLE

/com,*ETABLE

/com,*ETABLE

/com,*ETABLE

/com,*ETABLE

/PREP7

*DO,m,elem_1,elem_no,1

/com,*****DO LOOP*****
```

```
*GET,elec_field,ELEM,m,ETAB,field_sum

elec_field = ABS(elec_field)

*GET,elem_mat,ELEM,m,ATTR,MAT

*IF,elem_mat,NE,11,THEN

*IF,elec_field,GE,0.5E6,THEN

MPCHG,2,m

*ENDIF

*ENDIF

*ENDDO

ESEL,S,MAT,,1

*GET,elem_unpoled_post,ELEM,0,COUNT

ESEL,S,MAT,,2

*GET,elem_poled_post,ELEM,0,COUNT

ESEL,S,MAT,,11

*GET,elem_air_post,ELEM,0,COUNT

ALLSEL,ALL

vf_air_post = elem_air_post/elem_no

vf_poled_post = elem_poled_post/elem_no

vf_unpoled_post = elem_unpoled_post/elem_no

con_res(icon,1) = vf_air_post

con_res(icon,2) = vf_poled_post

con_res(icon,3) = vf_unpoled_post

*IF,icon,GE,2,THEN

ic = icon - 1

*VOPER,con_res(icon,4),con_res(ic,2),DIV,con_res(icon,2)

*IF,con_res(icon,4),GT,0.95,AND,con_res(icon,4),LT,1.05,EXIT

*ENDIF

*ENDDO

/PREP7

DDELE,ALL
```

```
CPDELE,ALL

NSEL,S,LOC,Z,0                              ! Select nodes at location Z=0
                                            (~Electrode 1)

CP,1,VOLT,ALL                               ! Couple selected nodes in voltage
                                            DOF (Set1)

D,ALL,VOLT,0                                ! DOF constraint for selected nodes:
                                            V=0

NSEL,S,LOC,Z,lz                             ! Select nodes at location Z=lz
                                            (~Electrode 2)

CP,2,VOLT,ALL                               ! Couple selected nodes in voltage
                                            DOF (Set2)

D,ALL,VOLT,-5                               ! DOF constraint for selected nodes:
                                            E=-1kV/cm

field = 5/lz

permconst = 8.854E-12

NSEL,S,LOC,X,0 $ DSYM,SYMM,X                ! Select nodes at X=0, then
                                            constrain DOF by symmetry

NSEL,S,LOC,Y,0 $ DSYM,SYMM,Y                ! Select nodes at Y=0, then
                                            constrain DOF by symmetry

NSEL,S,LOC,Z,0 $ DSYM,SYMM,Z                ! Select nodes at Z=0, then
                                            constrain DOF by symmetry

NSEL,S,LOC,X,lx $ CP,3,UX,ALL               ! Select nodes on exterior 'X' face
                                            and couple displacements

NSEL,S,LOC,Y,ly $ CP,4,UY,ALL               ! Select nodes on exterior 'Y' face
                                            and couple displacements

NSEL,S,LOC,Z,lz $ CP,5,UZ,ALL               ! Select nodes on exterior 'Z' face
                                            and couple displacements

ALLSEL,ALL                                  ! Select all entities (effectively
                                            removes selection)

*SET,a,NODE(lx,ly,lz)                       ! Get the corner node ref. number
                                            for displacement

EQSLV,JCG,1E-6                              ! Select JCG solver, with 1e-6
                                            tolerance (faster)

/SOLU

SOLVE

/POST1
```

```
SET,1

*SET,d33,(UZ(a)/lz)/field                ! Calculate d33

*SET,d31,(UX(a)/lx)/field                ! Calculate d31

*SET,d32,(UY(a)/ly)/field                ! Calculate d32

ETABLE,energy,SENE                       ! Use to calculate permittivity

SSUM

*GET,W,SSUM,,ITEM,energy

K33 = (2*W)/(8.854E-12*25*lz)            !applied voltage for d33 etc is 5V

res2 = vf_air_post                       ! Store results, can change if
                                         different data required

res3 = vf_poled_post

res4 = vf_unpoled_post

res5 = d33

res6 = K33

*DIM,ef_res,ARRAY,6,it

*CFOPEN,results,csv,,append              ! Open results spreadsheet

*VWRITE,it,res2,res3,res4,res5,res6

%I,%0.4G,%0.4G,%0.4G,%0.4G,%0.4G

*CFCLOS                                  ! Close results spreadsheet

*ENDDO

FINISH
```

Appendix F: Freeze casting experimental set-up

Freeze casting was used to produce highly aligned porous barium titanate, as discussed in Chapter 6, due to the potential for these types of materials to be beneficial for energy harvesting applications, which is highlighted in Chapter 2. For ease of design a single-sided freeze casting approach was used whereby a suspension of ceramic powder in water was poured into a PDMS mould and cooled from one side so as to create a temperature gradient. As the temperature of the cold surface reduces below 0°C the water in the suspension begins to nucleate into ice crystals at this surface. The presence of the temperature gradient drives preferential growth of this ice along the direction of the temperature gradient. As the ice forms the ceramic particles are forced into the channels between the ice crystals, in theory forming dense lamellar channels. Changing the rate of freezing affects the coarseness of the microstructure, with slower freezing rates yielding wider pore channels and by freezing faster a fine porous structure can be achieved. If the freezing rate is too fast, however, ceramic particulates are liable to be trapped in the pore channels, and if it is too slow the porous material after sintering often has low mechanical strength due to a low frequency of bridging channels between the ceramic channels. Adjusting the solid loading of the ceramic suspension gave control over porosity. Polyethylene glycol and polyacrylic acid were used as binder and dispersant, respectively. A binder content of 1 wt.% of the solid mass was found sufficient for all suspensions and less than 0.5 wt.% dispersant was used as too much caused some foaming of the suspension, trapping bubbles that resulted in randomly distributed microporosity in the sintered samples.
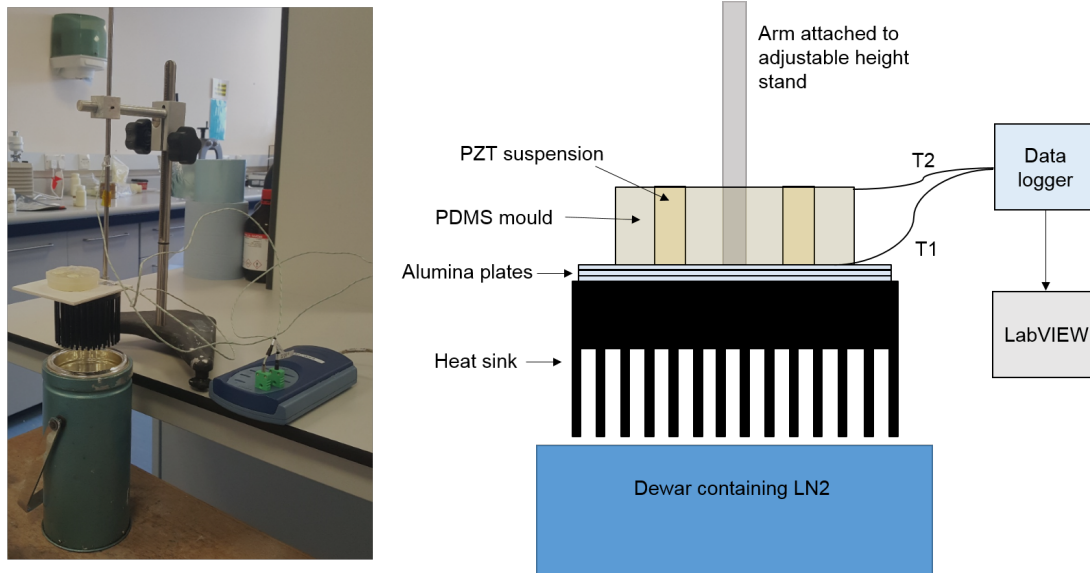
Figure F1: (left) photograph and (right) schematic diagram of single sided freeze casting set up.

An aluminium heat sink (83 mm diameter) on a height-adjustable stand was used as the freezing surface. Liquid nitrogen contained in a dewer (90 mm inner diameter) was used as the freezing agent. Depending on the desired freezing conditions the prongs of the heat sink could be submerged in the liquid nitrogen gradually or, if the dewer was partially filled, above the liquid nitrogen but encased within the dewer. Two K-type thermocouples (RS Components) were used to measure the temperature of the heat sink during the process and the ambient temperature at the top surface of the mould. A Pico USB TC-08 thermocouple data logger was used in conjuction with LabView to record the data during the freeze casting process. Aluminium tape was used on the bottom surface of the mould to contain the suspension, which was pipetted in prior to casting. Care was taken not to introduce bubbles and the filled moulds were gently tapped to remove air bubbles prior to freezing.

Frozen samples were then freeze dried (Mini Lyotrap, LTE Scientific) to remove the ice whilst preserving the ice-templated structure of the ceramic powder formed during freeze casting. The ice is removed via sublimation at low pressure (<600 Pa) over a period of 24-36 hours. The water vapour then recondenses as ice at the cold trap in the freeze dryer, which was at -55°C. Once the ice was completely removed the samples were sintered under the conditions discussed in Chapter 6.

Appendix G: Matlab script for generating 2-2 structures

```matlab
%%% Matlab script for generating 2-2 structures %%%

clc
clear all

n = 30;                           %mesh size (single dimension)
A = rand(n,n,n);                  %network
W = 4;                            %ceramic channel width
p = 0.9;                          %pore fraction in pore channel
c = 0.05;                         %pore fraction in ceramic channel

for M = 2 : W : n;                %generates pore channel
    for k = 1 : n;
        for j = 1 : n;
            for i = 1 : n;
                if i == M && A(i,j,k) >= p;
                    A(i,j,k) = 1;
                end
                if i == M && A(i,j,k) < p;
                    A(i,j,k) = 0;
                end
            end
        end
    end
end

for M = 2 : W : n;
    for k = 1 : n;
        for j = 1 : n;
            for i = 1 : n;
                if i ~= M && A(i,j,k) < c;
                    A(i,j,k) = 0;
                end
                if i ~= M && A(i,j,k) > c;
                    A(i,j,k) = 1;
                end
            end
        end
    end
end
```

```
%remove floating elements unless larger than 6^3

for i = 2:n-1;
    for j = 2:n-1;
        for k = 2:n-1;
            if A(i,j,k) == 1 && A(i-1,j,k) == 0 && A(i,j-1,k) == 0 &&
A(i,j,k-1) == 0 && ...
                    A(i+1,j,k) == 0 && A(i,j+1,k) == 0 && A(i,j,k+1) == 0
                A(i,j,k) = 0;
            end
        end
    end
end

for i = 3:n-2;
    for j = 3:n-2;
        for k = 3:n-2;
            if A(i,j,k) == 1 && A(i-2,j,k) == 0 && A(i,j-2,k) == 0 &&
A(i,j,k-2) == 0 && ...
                    A(i+2,j,k) == 0 && A(i,j+2,k) == 0 && A(i,j,k+2) == 0
                A(i,j,k) = 0;
            end
        end
    end
end

for i = 4:n-3;
    for j = 4:n-3;
        for k = 4:n-3;
            if A(i,j,k) == 1 && A(i-3,j,k) == 0 && A(i,j-3,k) == 0 &&
A(i,j,k-3) == 0 && ...
                    A(i+3,j,k) == 0 && A(i,j+3,k) == 0 && A(i,j,k+3) == 0
                A(i,j,k) = 0;
            end
        end
    end
end
```

Appendix H: Full publication list

J. I. Roscow, Y. Zhang, J. Taylor, & C. R. Bowen, Porous ferroelectrics for energy harvesting applications, *European Physical Journal: Special Topics* **224** (2015) 2949-2966.

J. I. Roscow, J. Taylor, & C. R. Bowen, Manufacture and characterisation of porous ferroelectrics for energy harvesting applications, *Ferroelectrics* **498** (2016) 40-46.

J. I. Roscow, V. Yu. Topolov, C. R. Bowen, J. Taylor, & A. E. Panich Understanding the peculiarities of the piezoelectric effect in macro-porous BaTiO$_3$, *Science and Technology of Advanced Materials* **17** (2016) 769-776.

J. I. Roscow, R. W. C. Lewis, J. Taylor, & C. R. Bowen, Modelling and fabrication of porous sandwich layer barium titanate with improved energy harvesting figures of merit, *Acta Materialia* **128** (2017) 207-217.

J. I. Roscow, V. Yu. Topolov, J. Taylor, & C. R. Bowen, Piezoelectric anisotropy and energy-harvesting characteristics of novel sandwich layer BaTiO$_3$ structures, *Smart Materials and Structures* **26** (2017) 105006.

J. I. Roscow, R. W. C. Lewis, J. Taylor, & C. R. Bowen, Finite element modelling of bilayer porous PZT structures with improved hydrostatic figures of merit, *Proceedings of the 2017 Joint IEEE International Symposium on the Applications of Ferroelectrics (ISAF)/International Workshop on Acoustic Transduction Materials and Devices (IWATMD)/Piezoresponse Force Microscopy (PFM)*, 7-11 May (2017) 78-82.

Y. Zhang, M. Xie, **J. I. Roscow**, Y. Bao, K. Zhou, D. Zhang, & C. R. Bowen, Enhanced pyroelectric and piezoelectric properties of PZT with aligned porosity for energy harvesting applications, *Journal of Materials Chemistry A* **5** (2017) 6569-6580.

H. Luo, **J. I. Roscow**, X. Zhou, S. Chen, X. Han, K. Zhou, D. Zhang, & C. R. Bowen, Ultrahigh discharged energy density capacitor using high aspect ratio Na$_{0.5}$Bi$_{0.5}$TiO$_3$ nanofibers, *Journal of Materials Chemistry A* **5** (2017) 7091-7102.

D. Zhang, X. Zhou, **J. I. Roscow**, K. Zhou, L. Wang, H. Luo, & C. R. Bowen, Significantly enhanced energy storage density by modulating the aspect ratio of BaTiO$_3$ nanofibers, *Scientific Reports* **7** (2017) 45179